https://doi.org/10.15388/vu.thesis.627
https://orcid.org/0000-0002-9280-5919

VILNIUS UNIVERSITY
CENTER FOR PHYSICAL SCIENCES AND TECHNOLOGY

Paulius Šlevas

Methods for the Formation of Structured Light Beams and their Application for Laser Microprocessing

DOCTORAL DISSERTATION

Natural Sciences,
Physics (N 002)

VILNIUS 2024

This dissertation was prepared between 2019 and 2023 in the Center for Physical Sciences and Technology.

Academic supervisor – Dr. Sergej Orlov (Center for Physical Sciences and Technology, Natural Sciences, Physics – N 002).

This doctoral dissertation will be defended in a public meeting of the Dissertation Defence Panel:

Chairman – Prof. Dr. Aidas Matijošius (Vilnius University, Natural Sciences, Physics – N 002).
Members:
Prof. Dr. Mangirdas Malinauskas (Vilnius University, Natural Sciences, Physics – N 002),
Dr. Kęstutis Regelskis (Center for Physical Sciences and Technology, Natural Sciences, Physics – N 002),
Prof. Dr. Kęstutis Staliūnas (Universitat Politècnica de Catalunya (UPC), Natural Sciences, Physics, N 002),
Assoc. Prof. Dr. Viktorija Tamulienė (Vilnius University, Natural Sciences, Physics – N 002).

The dissertation shall be defended at a public meeting of the Dissertation Defense Panel at 14:00 on 28th June 2024 in Room D401 of the Center for Physical Sciences and Technology.
Address: Saulėtekio av. 3, NFTMC, Room D401, Vilnius, Lithuania.
Tel. +370 5 264 9211; email: office@ftmc.lt.

The text of this dissertation can be accessed at the libraries of the Center for Physical Sciences and Technology and Vilnius University, as well as on the website of Vilnius University:
www.vu.lt/naujienos/ivykiu-kalendorius

https://doi.org/10.15388/vu.thesis.627
https://orcid.org/0000-0002-9280-5919

VILNIAUS UNIVERSITETAS
FIZINIŲ IR TECHNOLOGIJOS MOKSLŲ CENTRAS

Paulius Šlevas

Struktūrinių šviesos pluoštų formavimo metodai ir jų taikymas lazeriniam mikroapdirbimui

DAKTARO DISERTACIJA

Gamtos mokslai,
Fizika (N 002)

VILNIUS 2024

Disertacija rengta 2019–2023 metais Fizinių ir technologijos mokslų centre.

Mokslinis vadovas – Dr. Sergejus Orlovas (Fizinių ir technologijos mokslų centras, fizika – N 002).

Gynimo taryba:
Pirmininkas – prof. dr. Aidas Matijošius (Vilniaus universitetas, gamtos mokslai, fizika – N 002).
Nariai:
prof. dr. Mangirdas Malinauskas (Vilniaus universitetas, gamtos mokslai, fizika – N 002),
dr. Kęstutis Regelskis (Fizinių ir technologijos mokslų centras, gamtos mokslai, fizika – N 002),
prof. dr. Kęstutis Staliūnas (Katalonijos politechnikos universitetas (UPC), gamtos mokslai, fizika, N 002),
doc. dr. Viktorija Tamulienė (Vilniaus universitetas, gamtos mokslai, fizika – N 002).

Disertacija ginama viešame Gynimo tarybos posėdyje 2024 m. birželio mėn. 28 d. 14 val. Nacionalinio fizinių ir technologijos mokslų centro D401 auditorijoje. Adresas: Saulėtekio al. 3, NFTMC, D401 aud., Vilnius, Lietuva.
Tel. +370 5 264 9211; el. paštas: office@ftmc.lt.

Disertaciją galima peržiūrėti Fizinių ir technologijos mokslų centro bei Vilniaus universiteto bibliotekose ir VU interneto svetainėje adresu:
www.vu.lt/naujienos/ivykiu-kalendorius

CONTENTS

LIST OF ABBREVIATIONS

CCD	Charge-coupled device
CGH	Computer generated hologram
CMOS	Complementary metal–oxide–semiconductor
CO_2	Carbon dioxide
DMD	Digital micromirror device
DOE	Diffractive optical element
GP	Geometric phase
HG	Hermite-Gaussian
IG	Ince-Gaussian
LC	Liquid crystal
LCoS	Liquid crystal on silicon
LG	Laguerre-Gaussian
OAM	Orbital angular momentum
PAN	Parallel-aligned nematic
PBP	Pancharatnam-Berry phase
SLM	Spatial light modulator
STED	Stimulated emission depletion
TEM	Transverse Electro-Magnetic

1. INTRODUCTION

Light is an important part of nature, providing people with energy and visual information about their surroundings and the universe. The notion of structured light refers to its modulation in all degrees of freedom. This includes control of spatial degrees of freedom, such as phase, amplitude, or polarization, as well as temporal degrees of freedom, such as pulse length and frequency. A magnifying glass could be considered as a form of incoherent light shaping used by people for several millennia [1]. Such optics could be used not only for magnification purposes but also to start fires by concentrating solar energy into a small area. One could regard this as an early material modification by non-coherent light.

A few decades after the development of the laser, a field now known as laser beam shaping took off. Advances in optical technology allowed us to improve lithographic techniques, which led to faster computers that could calculate the new optical designs required to create new structured laser beams [2]. In practice, various light patterns can be formed by diffractive optical elements (DOEs), which are manufactured according to the computer generated holograms (CGHs) [3]. Such elements are usually designed and made to generate a specific beam shape using a laser emitting a certain wavelength. Versatile phase and amplitude modulation of light can be achieved with devices such as a liquid crystal on silicon (LCoS) spatial light modulator (SLM) and a digital micromirror device (DMD), which, respectively, work on the basis of liquid crystals (LCs) or controllable micromirrors [4, 5]. These devices facilitate the development of structured fields by allowing quick change of CGHs to experimentally verify designed beams. LC arrays can also be implemented to localize the polarization states in the light field to create vector beams [6, 7]. In the experiments presented here, SLM was an important tool used to investigate propagation dynamics of the designed beams. Subwavelength structures within the transparent material or on metasurfaces are also used to modulate amplitude, phase, and polarization [7, 8]. This type of optics is known as geometrical phase elements (GPEs). In the case when nanogratings are inscribed in a transparent sample, GPEs can have transmittance higher than 90% in a broad spectral region and their damage threshold is comparable to that of clear

fused silica [9]. Such GPEs enable the generation of high-quality, high-energy beams and can be used in high power setups. Because of this, fabrication tasks of this work require some CGHs to be made as GPEs.

Generally, the most common shape of the laser beam has an intensity distribution shaped like a Gaussian function, also known as the TEM_{00} (transverse electromagnetic) mode. Using the aforementioned methods, other forms of structured light can be created. For instance, Hermite-Gaussian (HG) [10], Laguerre-Gaussian (LG) [11], and Ince-Gaussian (IG) [12] are some of the prominent laser beam modes. Another category, which has gained particular interest in recent years, is nondiffractive beams. For example, a notorious Bessel beam [13], has a central region that seems to propagate without spreading. Another well-known Airy beam has a main lobe that appears to accelerate transversely while propagating on a curved trajectory [14]. Some forms of structured light, such as higher-order Bessel beams or LG modes, are able to carry orbital angular momentum (OAM). These beams have a spiraling phase front and phase singularity with no intensity at the center. Similarly, zero-intensity regions form in vector beams that possess polarization singularities. Many intensity patterns reminiscent of flowers [15], stars [16], or other shapes can be formed by shaping various degrees of freedom of light. Some of the structured light fields even acquired peculiar names such as photonic wheels [17], hooks [18], optical bottles [19], needles [20], drills [21], knives [22] and shovels [22]. Nevertheless, more efficient methods, that allow a flexible focal zone control are desirable as these types of laser beams, combined with high power setup, could find use in various fields of physics.

Many advances have been made in numerous laser applications as a result of the developing field of structured light. In Stimulated emission depletion (STED) microscopy the use of a hollow core beam allows the super resolution to be reached [23]. In the field of optical trapping, beams carrying OAM can rotate particles [24], and Airy beams can be used to relocate particles [25]. In laser manufacturing, the use of different spatial intensity or polarization distributions of the laser beam can offer better process quality or increased processing speeds. Vector beams have been shown to be beneficial for cutting metal sheets [26], while the use of nondiffracting beams offers a tremendous advantage for transparent material processing.

This work focuses on the development of beam structuring methods used for the formation of fields with complex transverse and longitudinal intensity distributions. All of the main results are described in the publications that are also provided in this work. Particular attention is paid to the shaping of nondiffractive beams such as optical needles, which are long beams possessing a uniform longitudinal intensity profile. Experimental conditions can have an influence on the formed beam, therefore, one of the works is dedicated to the exploration of these effects. For some applications, it could also be desirable to have a controllable transverse intensity profile together with an optical needle beam. In this work, Airy beams were employed to create high aspect ratio beams with controllable main lobe ellipticity. More elaborate light structures are constructed by adding several Bessel beams. This approach also allows to create parallel optical needles and is covered in this work as well. Some selected intensity patterns of the considered beams were used to modify transparent materials. Full details of all the experiments are given in the supplied articles.

1.1. The aim of this thesis

Investigate the latest beam shaping methods, design and produce efficient optical elements for the creation of spatially structured light beams having continuous intensity distributions that are relevant for laser micromachining applications.

To achieve this aim, several tasks were set:

1.2. Tasks of this work

1. Investigate methods to obtain Bessel-Gauss beam superpositions. Perform Bessel ring phase modulation to form combined Bessel beams with different vortical charges. Obtain and characterize surface and bulk modifications in a transparent medium using the combined beam.

2. Experimentally form the superpositions of Bessel beams with different vortical charges and cone angles. Experimentally determine the positions of individual optical vortices in the combined beam. Compare numerical and experimental results.

3. Investigate the possibility of generating an optical needle with a smooth axial intensity distribution using geometrical phase elements. Perform the required experiments to generate such an optical needle and benchmark its stability under imperfect experimental conditions.

4. Investigate the possibility of generating transversely elongated optical needles using Airy beams. Evaluate the possibility of controlling the transverse ellipticity of the beam by varying the parameters of the binary phase mask. Generate these beams experimentally and compare them with numerical simulation. Describe the impact of this beam when it is focused on the surface and most of the transparent media.

5. Create an array of optical needles with individual topological charges, axial intensity distributions, and positions in the transverse and longitudinal coordinates. Describe the influence of the distance between optical needles on the total intensity distribution of an array.

6. Experimentally form a top-hat beam using geometrical phase element. Characterize the propagation in free space of this beam. Determine the influence of imperfect experimental conditions on the characteristics of the top-hat beam. Compare numerical and experimental data.

1.3. Novelty and relevance

1. A method to experimentally produce a superposition of several Bessel-Gauss beams of different topologies using a pair of axicon and a geometrical phase element was introduced. This method was also used in high-power laser applications. This is relevant for the creation of multiple microchannels within glass at higher speeds.

2. A geometric phase element was used to shape the amplitude of the beam entering an axicon to create an optical needle with a uniform intensity distribution on the propagation axis. The generation stability of the optical needle under imperfect placement of the shaping element was also benchmarked.

3. The position of the top-hat beam depending on the incident beam diameter was numerically and experimentally benchmarked when the top-hat beam is generated by a geometrical phase element. It is important to know the tolerable deviations when designing optical systems.

4. Airy beams were used to create an optical needle with flexibly adjustable main lobe ellipticity in the transverse plane. This beam was also used to produce directional modifications inside the glass.

5. The generation of an array of optical needles with a controllable axial intensity distribution and distinct topological charge at each position was demonstrated. This method facilitates the creation of various spatial intensity distributions in three dimensions. Flexible beam positioning is desirable in laser micromachining applications.

1.4. Statements to be defended

1. Azimuthal modulation of the spatial spectrum of a Bessel-Gauss beam using two helical phase distributions of different topologies, creates a superposition of Bessel-Gauss beams that is applicable for the single shot modification inscription in glass volume.

2. In a superposition of Bessel-Gauss beams with different topological charges, the transverse and longitudinal intensity distributions of a complex light field are determined by the positions of single charged optical vortices.

3. The longitudinal intensity distribution of the optical needle formed by a geometrical phase element, polarizer, and an axicon remains constant within the Bessel zone.

4. Superposition of Airy beams, produced by a binary phase mask in the +1 and -1 diffraction orders, is eligible for the formation of an elliptical optical needle.

5. The direction of the microcracks, induced by the elliptical optical needle inside EXG glass, is controlled through the mechanical rotation of the geometrical phase element around its axis.

The author was responsible for the experimental part of all the papers provided in this thesis. This includes designing and assembling experimental setups, obtaining, analyzing, and describing experimental results, as well as comparing them with numerically modeled results.

In [**P1**], author performed numerical simulations, designed a GPE with 180 zones, assembled the experimental setup, made the samples and beam measurements, analyzed the data, and wrote most of the text. E. Nacius designed a GPE with 6 zones. O. Ulčinas fabricated GPEs. S. Orlov wrote Theoretical background, supervised the work, and edited the text.

In [**P2**], author assembled the setup, performed experimental measurements, and wrote an experimental description. P. Gotovski numerically modeled optical needle, prepared illustrations, wrote most of the text. O. Ulčinas fabricated GPE. S. Orlov, supervised the work and edited the text.

In [**P3**], author assembled the setup, experimentally obtained the required data, and described the results. P. Gotovski performed numerical simulations, prepared illustrations, and wrote most of the text. O. Ulčinas fabricated GPE. S. Orlov supervised the work and edited the text.

In [**P4**], author assembled both experimental setups, performed experimental measurements, sample fabrication, analyzed the data, and wrote most of the text. K. Mundrys performed numerical simulations. O. Ulčinas fabricated GPE. S. Orlov, supervised the work and edited the text.

In [**P5**], author performed numerical simulations, assembled the experimental setup, performed all measurements, analyzed, and described the theoretical and experimental data, edited the text. S. Orlov wrote introduction and theoretical background sections, edited the text.

In [**P6**], the author assembled the optical setup. performed experimental measurements, analyzed the data, prepared data for publication, and edited the text. S. Orlov did theoretical calculations, prepared the original manuscript, and edited the text.

2. LITERATURE OVERVIEW

2.1. Non-diffracting beams

The most well-known beam profile emitted by a typical laser source is known as a Gaussian beam. During propagation, it diverges as a result of diffraction. Microprocessing applications require a tight focus. However, the divergence angle of a Gaussian beam is inversely proportional to the beam waist; therefore, when focused it can maintain a small diameter only for short distances.

The concept of nondiffractive beams in optics was introduced by Durnin in 1987 [13, 27]. As the name suggests, such beams would remain invariant during propagation. This is contrary to the most common transverse Gaussian profile. Durnin's suggested solution to the wave equation included a Bessel function; therefore, such a beam is now called a Bessel beam. In theory, the ability to remain impervious to spreading requires the ideal Bessel beam to carry infinite power. This is impossible to achieve in practice. Shortly after its theoretical introduction, the finite energy approximation known as the Bessel-Gauss beam with a limited nondiffractive zone was experimentally realized using ring apertures, computer-generated holograms, and conical lenses [3, 27–30]. In the literature, the terms Bessel-Gauss and Bessel beam are often used to refer to experimentally realizable beams to simplify terminology.

During the years, variations of the nondiffractive beams, which can be regarded as Bessel-like beams, have been proposed. A common property is a high aspect ratio of longitudinal to transverse dimensions, whereas the difference is the shaped transverse or longitudinal intensity distribution. Mathieu beams, for example, are solutions to the wave equation in cylindrical elliptical coordinates [14, 31–33]. They have a transversely elongated intensity distribution and maintain their shape over long distances. Solutions of the Helmholtz equation expressed in terms of parabolic cylinder functions are known as parabolic beams, as they have a transverse intensity distribution of this form [34, 35]. Because of their unique properties, such as long focal zone, narrow high intensity peak, and ability to carry orbital angular momentum, Bessel beams and their variations found their place in a variety of applications, which are discussed later in this chapter.

The nondiffractive Airy beam was proposed by Berry and Balazs [36] in 1979 as a solution to the Schrödinger equation. However, only in 2007 Siviloglou introduced the concept of the Airy beam in optics [14, 37] and showed the experimental generation of such beams [38]. Apart from their ability to resist diffraction, they also possess a unique ability to propagate in a curved parabolic trajectory, which also makes the beam interesting for a number of applications, also described later in this chapter.

2.2. Bessel beams

Bessel beams were found by Durnin [13] by investigating solutions to a scalar wave equation for free space:

$$\left(\nabla^2 - \frac{1}{c^2}\frac{\partial^2}{\partial t^2}\right) E(\mathbf{r}, t) = 0. \tag{2.1}$$

Durnin's solution representing a non-diffracting scalar field, propagating in free space is:

$$E(\mathbf{r}, t) = \exp\left[i(\beta z - \omega t)\right] J_0(\alpha\rho), \tag{2.2}$$

where $\rho^2 = x^2 + y^2$, $\alpha^2 + \beta^2 = (\omega/c)^2$, J_0 is a zero-order Bessel function of the first kind. When β is real, the intensity does not depend on z. In the case when $\alpha = 0$, the solution represents the plane wave, but when $0 < \alpha \leq (\omega/c)$, the solution is a nondiffracting beam that has an intensity profile that decays at a rate inversely proportional to $\alpha\rho$ [13]. A more general representation of equation (2.2) is presented in [39, 40]:

$$E(\mathbf{r}, t) = \exp\left[i(\beta z - \omega t)\right] \sum_n p_n \exp(-in\varphi) J_n(\alpha\rho), \tag{2.3}$$

where φ is an azimuthal coordinate, p_n are coefficients and J_n is n-th order Bessel function of the first kind, which can be expressed as [41]:

$$J_n(x) = \sum_m^{\infty} \frac{(-1)^m}{m!\Gamma(n+m+1)} \left(\frac{x}{2}\right)^{n+2m}, \tag{2.4}$$

where $\Gamma()$ is the gamma function. Equation (2.3) is a discrete-mode representation of the solution represented in Equation (2.2). A 0-th-

order Bessel beam has a high intensity peak at the center and the phase shifts by a value of π between adjacent rings (see Figure 2.1 (a,d)). Higher-order Bessel beams have a minimum intensity in the center (see Figure 2.1). As the topological charge increases, the diameter of the central core increases. Higher-order Bessel beams also have a helical wavefront [42] because of which the phase in the center of the beam is not defined and the intensity minimum is formed. Such beams also carry OAM [43, 44] and are known in the literature as Bessel vortices [45].

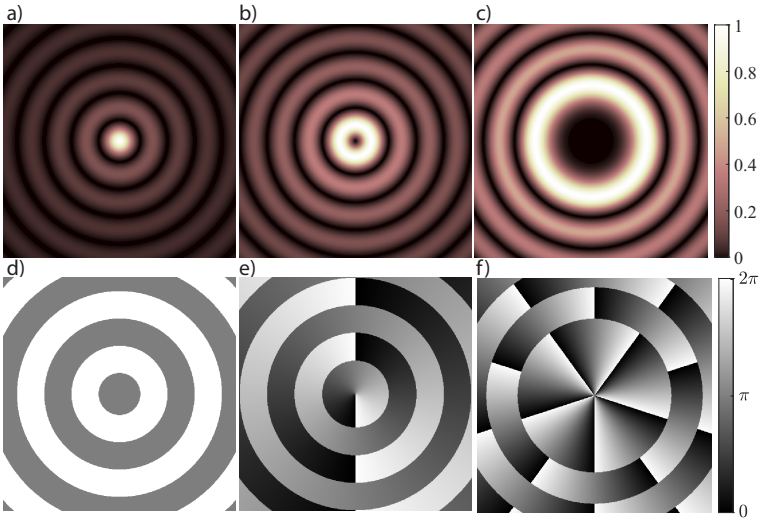

Figure 2.1: Intensity distributions of Bessel beams having topological charge 0, 1, 5 in (a), (b), (c) respectively. Phase distributions of Bessel beams having topological charge 0, 1, 5 in (d), (e), (f).

The perfect Bessel beam has infinite power, while its spatial spectrum is an infinitely narrow ring. In practice such a beam does not exist, and only finite power and dimension approximations, known as Bessel-Gauss beams, can be experimentally generated. A complex amplitude of such a beam is as follows:

$$A(r,\varphi) = a_n J_n(k_\rho \rho) \exp(in\varphi) \exp\left(-\frac{\rho^2}{d^2}\right), \tag{2.5}$$

where a_n is an amplitude, $k_\rho = k \sin\theta = (\omega/c)\sin\theta$, θ is an angle between propagation axis z and a wave vector $\mathbf{k}$, also known as a Bessel beam cone angle, which can also be expressed as $\theta = \text{atan}(k_r/k_z)$. d is a Gaussian beam radius at the intensity level $1/e^2$. If $d \to \infty$, then

the Bessel-Gauss beam is an ideal Bessel beam. Instead of comparing the diffraction characteristics of a central lobe of a Bessel beam with a Gaussian beam, in [46] the authors included the size of the ring structure when estimating the diameter of a truncated Bessel beam and then compared it with a Gaussian beam of the same diameter. They concluded that in this case the Bessel beam diffracts faster than the Gaussian as the rings diffract sequentially starting from an outer one, whereas the central lobe persists as long as there are off-axis rings to replenish its diffraction losses [46]. However, comparing the central lobe of a Bessel-Gauss beam shows that it is more resistant to diffraction and transports power more efficiently than a regular Gaussian beam [47]. The central core diameter of a Bessel beam can be calculated as follows: [48]:

$$r_0 = \frac{2.405}{k_r}. \tag{2.6}$$

The experimental demonstration of a Bessel beam was first demonstrated by Durnin *et. al.* [27]. In their work, the authors used collimated light to illuminate a circular slit, which was placed in the focal plane of a lens as shown in Figure 2.2 (a). Each point along the slit acts as a point source, which the lens transforms into a plane wave. The set of plane waves formed this way has wave vectors lying on the surface of a cone, which is a defining characteristic of a Bessel beam [27]. The maximum propagation distance (Z_{max}) of a beam formed in this way can be determined using geometrical optics by finding the location where a shadow zone begins:

$$z_{max} = \frac{R}{\tan\theta}, \tag{2.7}$$

where R is the radius of the imaging lens. Such method of modulating an amplitude of an incoming light is not very efficient. Most of the power is lost at the aperture.

Another common and very popular method for generating Bessel beams is the use of a conical lens known as an axicon (see Figure 2.2 (b)). The thickness of the axicon increases or decreases along the radial direction from the center; therefore, a plane wave propagating through an axicon experiences a linear phase shift in the radial direction. In this way, most of the power of an incident wave is converted to a Bessel beam. If the axicon is transparent to the laser wavelength, then losses

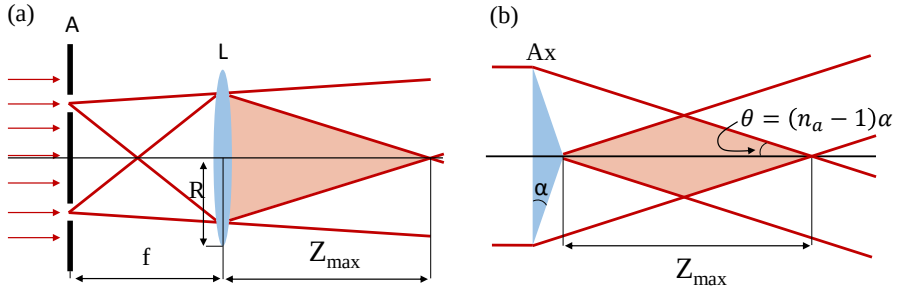

Figure 2.2: Examples of Bessel beam formation method. (a) Using a circular aperture, (b) using a conical lens – axicon.

occur due to reflections from surfaces only, which can be minimized using antireflective coatings. The main specifications of an axicon are its base angle (marked α in Figure 2.2 b) and its refractive index n_a. The cone angle of the generated Bessel beam is related to the base angle of the axicon by the relation $\theta = (n_a - 1)\alpha$. The maximum propagation length of a Bessel beam formed by an axicon can be expressed as [48]:

$$z_{max} = \frac{k}{k_r} d \approx \frac{d}{\theta}. \tag{2.8}$$

It is worth mentioning that, in addition to the long and narrow intensity peak at the center, Bessel beams have another interesting property, which is to reconstruct after propagating through the obstacle. Bouchal has studied the interaction of the beam with an obstacle of the 2D on the axis and showed that the phase topology and intensity pattern regenerate after further propagation in the free space [49].

Axicon transforms a Gaussian beam into a 0-th order Bessel beam. Using Laguerre-Gaussian modes to illuminate an axicon, higher-order Bessel beams can be obtained [30,50,51]. Jarutis *et. al.* found a complex amplitude of a Laguerre-Gaussian beam focused by an axicon [51]:

$$\begin{aligned} c_1(\rho, \phi, z) = a_0 \sqrt{2\pi k_\rho d} \left(\frac{z}{z_{max}} \right)^{l+\frac{1}{2}} \exp\left(-\frac{z^2}{z_{max}^2} \right) \\ \exp\left[i \left(l\phi - \frac{l\pi}{2} - \frac{\pi}{4} \right) \right] J_l(k_\rho \rho), \end{aligned} \tag{2.9}$$

where l is the azimuthal mode index of the Laguerre-Gaussian beam, ρ, ϕ and z denote cylindrical beam coordinates. The spatial spectrum of

higher-order Bessel beams has the same shape of a ring as a 0-th order beam, but the phase of this ring varies along the azimuth. Interfering two Bessel beams of different topologies produces interesting non-diffracting patterns [52–55]. This interference, also known as a superposition of two vortical Bessel beams, can be expressed as:

$$E(\rho,\varphi,z,t) = \left[a_m J_m\left(\frac{k_{\rho 1}\rho}{Z}\right)\exp\left(-\mathrm{i}\frac{k_{\rho 1}^2}{2k}\frac{z}{Z}\right)\exp(\mathrm{i}m\varphi+\mathrm{i}k_{z1}z)\right.$$
$$\left.+\, a_n J_n\left(\frac{k_{\rho 2}\rho}{Z}\right)\exp\left(-\mathrm{i}\frac{k_{\rho 2}^2}{2k}\frac{z}{Z}\right)\exp(\mathrm{i}n\varphi+\mathrm{i}k_{z2}z)\right]$$
$$\times\,\frac{1}{Z}\exp\left(-\frac{\rho^2}{d_0^2 Z}\right)\exp(-\mathrm{i}\omega t), \tag{2.10}$$

where $Z = 1+\mathrm{i}z/z_0$, $z_0 = kd_0^2/2$ is the Rayleigh length, d_0 is the radius of Gaussian aperture, m and n are topological charges of the first and the second beam respectively. The two main degrees of freedom that affect the intensity distribution of a combined beam are the topological charge and the cone angle of the individual beam. Some examples of the superpositions of two Bessel beams with different topological charges and cone angles are shown in Figure 2.3. Many phase singularities can be observed in the phase maps of Figure 2.3 (f, g, h). Orlov *et. al*

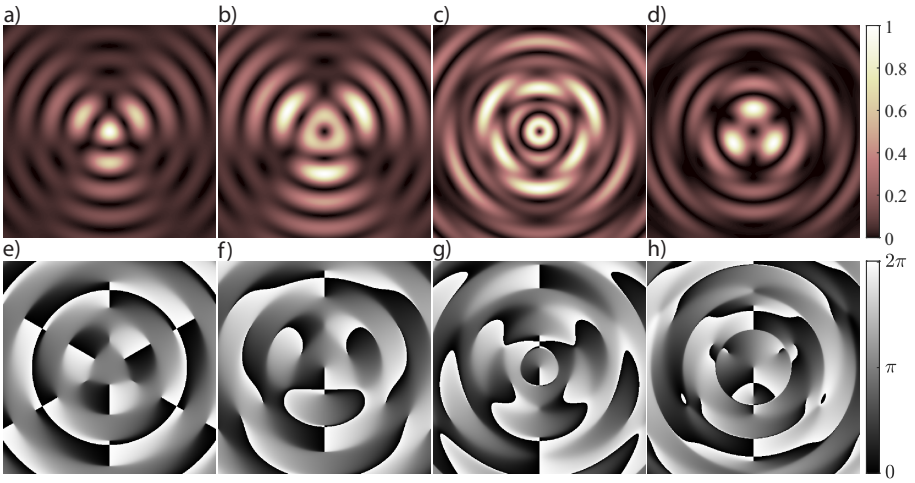

Figure 2.3: Transverse intensity and phase distributions of a combined Bessel beam with topological charge pair $m = 0$, $n = 3$ in (a, e), $m = 1$, $n = 4$ in (b, c, d, f, g, h) and cone angle ratio $\theta_1/\theta_2 = 1$ in (a, b, e, f), $\theta_1/\theta_2 = 2$ in (c,g), $\theta_1/\theta_2 = 0.5$ in (d, h).

showed that such structured beams carrying optical vortices has richer vortex structure in the near field (Bessel beam) than in the far field (a ring shaped Bessel spectrum) [54]. During propagation of such a structured field, individual single charged positive and negative vortices move in the field, rotate under diffraction, are being created, and are being annihilated. Such vortice braiding was reported in Bessel beams in superposition with Gaussian mode [56, 57].

A single vortex is a dark spot of light with a phase singularity in its core. Thus, its three-dimensional trajectory can be considered as a single entity, especially given the fact that the time reversal would change signs of single vortices in the beam. For this reason, a negatively charged optical vortex can be interpreted as a positively charged backward propagating vortex, and the creation and annihilation of positive and negative vortices in pairs under diffraction can be seen as a dark knot of light [58–60]. This interpretation of the complex evolution of vortical structures with rich topologies has caused the appearance of terminology such as knots, braids, and bundles of dark light [61].

The experimental formation of superimposed Bessel beams of different topologies and the same cone angles was demonstrated using computer-generated holograms [52]. They have also been generated using a spatial light modulator (SLM) to shape the phase of the incoming Gaussian beam and, in addition using a ring-slit aperture to form a ring spectrum, which can then be Fourier transformed into a combined beam by a lens [62]. Rotation rate measurements of a superposition of two Bessel beams with the same magnitude but different sign topologies are provided in [63]. In **[P1]**, a method for the generation of superimposed higher order Bessel beams with different topologies using GPEs is presented and the ability to use such beams in high power applications to create surface and volume modifications is demonstrated. Paper **[P5]** expands the discussion further by considering individual Bessel vortices with different cone angle and how the vortical dynamics influence the three-dimensional pattern of the combined beam. An extended review of the beams, which incorporate angular momentum, is presented in [64].

Because of their non-diffracting properties, Bessel beams are used in various fields. For example, they have been used successfully in light sheet microscopy [65–67], terahertz imaging to improve focal depth and contrast [68, 69], and optical trapping [24, 70, 71].

In laser micromachining, there are two main advantages to using Bessel beams. First, because of the propagation invariance, the technical issue of maintaining the surface of a workpiece within the laser focus can be alleviated. Second, the nonlinear propagation of the Bessel beam inside the transparent material can also be invariant, in contrast to the non-linear propagation of Gaussian beams [72, 73]. Because of the second property, high aspect ratio nanostructures can be inscribed using a single laser pulse. The nonlinear propagation of Bessel beams is described in [74] where the authors distinguish three regimes of Bessel beam filamentation. The first is a weakly non-linear regime when the power at the central peak of the beam is sufficient to induce self-focusing, but not sufficient to induce significant multiphoton absorption [75]. The second regime is an unsteady Bessel filamentation, where multiphoton absorption and material damage occur. Gaižauskas *et. al.* used this to obtain periodically arranged damage traces in borosilicate glass [76]. The third is a steady Bessel filamentation regime in which strong self-focusing of the central peak of the Bessel beam occurs, which triggers multiphoton absorption. Therefore, the peak intensity in the core starts to reduce and the process can occur again because Kerr self-focusing of the external ring periodically brings energy to the core [74, 77]. Using a Bessel beam with moderately high fluence (typ. 10^{13} W/cm^2) and low to moderate focus conditions ($\theta < 15°$ in transparent material) can induce structural rearrangements that can result in positive or negative modifications of the refraction index [72, 78–80]. In [81, 82] the authors used the Bessel beam to inscribe Bragg gratings inside fused silica glass at a significantly higher speed compared to the Gaussian beam due to reduced scanning repetitions. In [83] the authors demonstrated a technique employing Bessel beams that allows the fabrication of photonic crystal filters in inorganic glass, with a transmission passband of nearly 100% and a transmission stopband of nearly 0%.

When the high-energy Bessel beam is focused strongly on the transparent material, a high aspect ratio nanovoid will be inscribed inside the bulk [84]. This process was demonstrated in materials such as fused silica [85–87], borosilicate glass [84], and sapphire [88]. However, a modification produced in a transparent material is not always a void. After initial heating with a laser pulse, the material can be redistributed during cooling, and bubbles can form that can split or close the void [89].

In [90] the authors investigated material responses (fused silica) in the surface and subsurface regions triggered by the impinging Bessel beam. Irradiation of material with a pulse of high energy density creates temperatures and pressures that are high enough, exceeding the bulk modulus of the solid, to form a void in the center of a beam [91]. The diameter of a void is smaller than the diameter of the central peak of a Bessel beam. Around the void, where the material experiences exposure to photons, no apparent crack is found because of laser-induced local melting. Outside the laser irradiated region, microcracks have a radial direction due to laser-induced mechanical stress that exceeds the critical mechanical strength [90]. The appearance of the microcracks depends on the irradiation parameters, and it is crucial for a transparent material dicing application.

Dicing glass using non-diffracting Bessel beams offers several advantages compared to mechanical methods such as saw dicing, scribe, and breaking, or laser methods such as ablation. The technique allows one to achieve high processing speeds, near zero kerf, and low chipping while also allowing one to process arbitrary shapes. Depending on the glass sample thickness, it can be modified all the way through by a single pass of the laser beam. At first, it was demonstrated on 100 µm thin flexible glass at a low speed of 1 mm/s [92] but the process was quickly improved to be applicable to thicker glasses at a significantly higher speed [93]. To reach higher processing depths, several repetitions of the same trajectory can be done together with a change of focus position, moving it from the bottom to the top. However, the use of high-energy pulses (several mJ) and optical setups comprised of several axicons allows the processing of thick glass with a single pass of a laser [94–97]. This allows us to maintain a good dicing speed. In [96], for example, the entire depth of a 10 mm thick glass sample was modified by scanning the laser only once. To achieve complete glass separation, two processing steps are needed. The first step is the creation of defects within the depth of the material by an ultrashort pulse laser. The second step is an application of stress that would lead to fracture through the defects. A second step can be completed by mechanical flexure or applying a CO_2 laser to heat the surface to induce thermal stress due to the temperature gradient [98, 99]. The surface quality of a sidewall is relatively rough after such a process (approximately 1 µm) [100]. This might be related to

the fact that microcracks obtained by an ordinary Bessel beam have an irregular direction [90]. Shaping the transverse beam profile allows one to control their behavior. In [101] Dudutis *et.al.* reported that using an imperfect axicon with an elliptical cross section, or by tilting the axicon perpendicular to its optical axis [102,103] results in directional cracking of glass, which can be controlled by the rotation of the axicon. Similarly, shaping the amplitude or phase of the Bessel beam spectrum [104–106] or designing specific diffractive optical elements [107] allows the creation of asymmetric transverse Bessel beam profiles that can induce a preferred direction microcrack inside transparent material. Better material separability and bending strength are achieved with this technique [108]. It is worth mentioning that glass dicing at an angle can be utilized using aberration-corrected Bessel beams [99,109]. In article **[P4]** an elongated in-transverse-plane high aspect ratio beam is created using a method that employs two diffraction orders of Airy beam, created by a binary phase mask. Glass modifications were made using this beam revealed the potential of this beam-shaping approach. An overview of different glass cutting technologies with a quantitative comparison of their edge qualities is given in [110].

Another field of laser micromachining that benefits from the use of structured light is multiphoton polymerization, where the length of the voxel can be increased using high aspect ratio beams [111]. In [112] higher-order Bessel beams were used to create cylindrical structures without the need to scan the beam in circles. The diameter of the structures can be controlled by choosing a topological charge of the beam. A superposition of Bessel beams of the same cone angle was used to create a grid of high intensity cores that was applied for the parallel polymerization of several high aspect ratio structures [113, 114], while in [115] the authors demonstrated a technique to manufacture 3D helical structures using a single exposure.

Laser surface nanostructuring requires very high precision. By controlling the sample area in which fluence exceeds the ablation threshold, nanostructures can be created with dimensions below the laser wavelength [116]. Precise control of the longitudinal position is required when processing nanostructures with a Gaussian beam. The use of Bessel beams with longitudinally elongated focus allows us to compensate for thickness variation of the sample or even process non-flat sur-

faces [117–120]. The intensity distribution of a regular Bessel beam slightly varies along the axis. However, for such sensitive applications, it would be beneficial to have a nearly constant longitudinal intensity distribution. Beam with a flat on-axis intensity profile, can also help stabilize the propagation of the Bessel beam in a nonlinear medium as shown in [121]. Such type of beams are know as optical needles. To create them, various methods were developed. For example, it can be done using logarithmic axicon [122, 123], however the transverse width of such a Bessel-like beam is increasing during the propagation. It can also be done by creating a spatial spectrum of a Bessel beam with the desired amplitude and phase [124–126], but efficiency of this method is low. Different transverse profile beams can be input to the axicon to shape axial intensity distribution [127]. In **[P2]** a GPE, polarizer and an axicon is used to form an optical needle with efficiency of around 50%. The shape of the optical needle can be influenced by ellipticity of the incident Gaussian beam, the misalignment of optical axes, misadjustment of the polarizer, and the GPE. These effects are also considered in **[P2]**. Authors of [126] demonstrated a generation of optical needle array with controllable needle positions. Paper **[P6]** expands on this by also studying topological charge influence to the overall formation of the array.

2.3. Airy beams

In 1979 Berry and Balaz noticed that a wavepacket described by the Airy function could be a solution to the Schrödinger equation for a free particle [36, 38]:

$$i\frac{\partial u}{\partial \xi}+\frac{1}{2}\frac{\partial^2 u}{\partial s^2}=0. \tag{2.11}$$

This equation is very similar to the paraxial diffraction equation when $u(s,\xi)$ is a function of the electrical field envelope, $s = x/x_0$ – dimensionless transverse coordinate, $\xi = z/(kx_0^2)$ – dimensionless longitudinal coordinate. A solution to equation 2.11 that describes a nondispersive Airy wavepacket is given as [38]:

$$u(s,\xi)=Ai\left(s-\frac{\xi^2}{4}\right)\exp\left[i\left(-\frac{\xi^3}{12}+\frac{s\xi}{2}\right)\right], \tag{2.12}$$

where $Ai()$ is the Airy function. It can be seen that $u(s,0) = Ai(s)$ at the beginning of the beam propagation. Similarly to Bessel beams, an ideal Airy beam remains invariant during propagation and also contains infinite power. The term $\xi^2/4$ in Eq. (2.12) reveals that the intensity profile experiences constant acceleration while propagating on a parabolic trajectory (see Figure 2.4 (b)). To describe real Airy beams and ensure containment of the infinite Airy tail, an exponential aperture function is introduced as described in [36]:

$$u(s,\xi=0) = Ai(s)\exp(as), \tag{2.13}$$

where a is a damping parameter with typical values $a << 1$. Solving equation 2.11, using Eq. 2.13 as initial condition, a solution of Airy beam with one transverse and one longitudinal coordinate can be expressed as [36–38]:

$$u(s,\xi) = Ai\left(s - \frac{\xi^2}{4} + ia\xi\right)\exp\left[as - \frac{a\xi^2}{2} + i\left(\frac{a^2\xi}{2} - \frac{\xi^3}{12} + \frac{s\xi}{2}\right)\right]. \tag{2.14}$$

Another beam dimension can be added by multiplication, therefore, electric field envelope of an Airy beam with two transverse coordinates can be expressed as:

$$\begin{aligned} u(s_x,s_y,\xi) = {} & Ai\left(s_x - \tfrac{\xi^2}{4} + ia\xi\right)\exp\left[as_x - \tfrac{a\xi^2}{2} + i\left(\tfrac{a^2\xi}{2} - \tfrac{\xi^3}{12} + \tfrac{s_x\xi}{2}\right)\right] \\ & \times Ai\left(s_y - \tfrac{\xi^2}{4} + ia\xi\right)\exp\left[as_y - \tfrac{a\xi^2}{2} + i\left(\tfrac{a^2\xi}{2} - \tfrac{\xi^3}{12} + \tfrac{s_y\xi}{2}\right)\right], \end{aligned} \tag{2.15}$$

where, $s_x = x/x_0$ and $s_y = y/y_0$. Examples of transverse and longitudinal intensity distributions, obtained using Eq. 2.15, with $x_0 = 1$, $y_0 = 1$ and $a = 0.02$, are depicted in Figure 2.4. A main lobe and multiple side lobes that have exponentially decaying intensity is visible in transverse intensity distribution (Fig. 2.4 (a)). Applying a Fourier transform to Eq. 2.14 gives the spatial spectrum of the wavepacket.

$$\tilde{u}\,(k_t) = \exp\Big[(a_t + ik_t)^3/3\Big], \tag{2.16}$$

where k_t denotes the normalized (i.e. proportional to x_0 or y_0) x or y component of the wave vector, a_t is the exponential truncation factor (either a_x or a_y) [128]. Consequently, the spatial spectrum of the three-dimensional Airy beam is $\tilde{u}\,(k_x,k_y) = \tilde{u}\,(k_x)\,\tilde{u}\,(k_y)$. So, the general

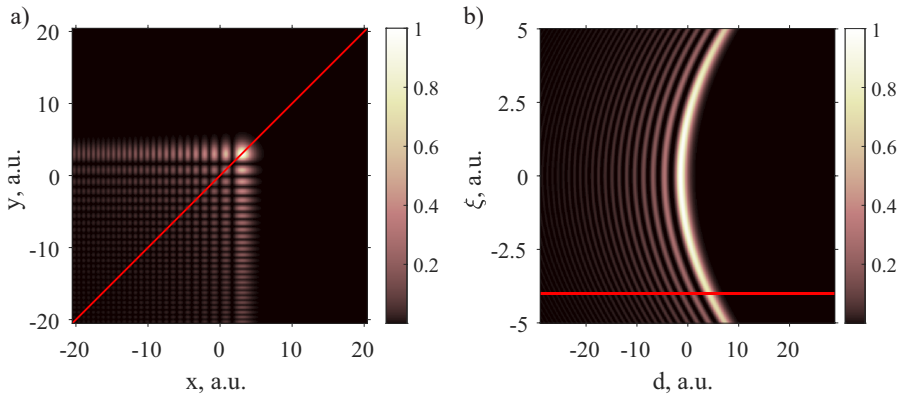

Figure 2.4: An example of Airy beam transverse intensity distribution in (a). Red line marks a cross section used to obtain a longitudinal intensity distribution in (b). Red line in (b) marks longitudinal coordinate at which distribution in (a) is calculated. In (b) axis denoted d represents a diagonal coordinate of a red line in (a).

expression of the spatial spectrum is:

$$\tilde{u}\left(k_x, k_y\right) = A_0 \exp\left[-\left(a_x k_x^2 + a_y k_y^2\right)\right] \times \exp\left[-i\frac{k_x^3+k_y^3}{3} + i\left(a_x^2 k_x + a_y^2 k_y\right)\right], \tag{2.17}$$

here the spatial coordinates are normalized with respect to x_0 and y_0. The number of parameters in this expression is commonly reduced to achieve a Gaussian envelope with an additional cubic phase [129]:

$$\tilde{u}\left(k_x, k_y\right) = A_0 \exp\left[-a\left(k_x^2 + k_y^2\right)\right] \exp\left(i\frac{k_x^3+k_y^3}{3}\right), \tag{2.18}$$

where A_0 is a constant, k_x and k_y are Fourier spectrum coordinates. This equation shows that to obtain Airy beam, a Gaussian beam has to be modulated by a cubic phase and then Fourier transformed with a lens. This way Airy beam was experimentally generate by Siviloglou *et. al.* [38].

Airy beams are usually generated using SLM by modulating the phase and/or amplitude of the beam [130, 131]. However, other methods, such as cubic phase plates made on a lithographic basis [132], or

a combination of negative and positive cylindrical lenses [133] were also demonstrated. It was also shown that Airy beams can carry an optical vortex. When close to the core, the vortex follows a parabolic trajectory, but eventually is pushed to the center of the beam by a reconstructed main lobe [134–136].

There are a variety of applications in which Airy beams are used. For example, a plasma channel with a curved trajectory can be generated by a high-intensity 2D Airy beam in air or water [137,138]. Because of the curved trajectory, the supercontinuum radiation generated by the filament is angularly resolved in the far field. In the field of imaging, a self-bending point spread function based on Airy beams was introduced to achieve high resolution fluorescence imaging [139]. The main reason for using Airy beams as point spread functions is that they can propagate over several Rayleigh lengths without experiencing significant diffraction and are self-healing after being obscured in scattering media [140]. In [141] the authors demonstrate the use of Airy beam in light sheet microscopy and also compare it to the Bessel beam. Because of the ring structure, illumination by a Bessel beam produces background fluorescence. An asymmetric excitation pattern induced by the Airy beam helps to increase the contrast of the image. In [69] the authors demonstrated the THz imaging technique using Airy beams and found that, compared to other illumination methods, it offers better performance when there is an obstacle that covers part of the image. Yet another application for Airy beams is small particle transportation and manipulation. In [25], an Airy wave packet was utilized to achieve optically mediated particle clearing. The beam drags the particles into the main lobe, which vertically guides them along parabolic trajectories.

The curved beam trajectory and nondiffractive properties of the Airy beam were also used in laser material processing. A big challenge is the machining of structures that have longitudinally varying dimensions. Mathis et al. employed accelerating beams to ablate curved trenches and rounded edges in silicon [142,143] and inscribe curved modifications within glass [144]. However, the beams used in [142–144] could curve only over a distance of 50 to 70 µm [72]. In [145] curved modifications of 0.7 mm radius were inscribed inside 525 µm thick glass and then etched in potassium hydroxide solution to obtain complete glass separation with rounded edges.

A beam shaping element can be any transparent material with varying thickness and/or curved surfaces. A beam of light passing through this material will experience refraction and a phase delay of different magnitude depending on the spatial position of the beam-shaping element. The most simple example for this is a spherical lens, which is a piece of glass that has one or two surfaces shaped as a sphere. It allows the beam light to be focused or spread depending on the curvature of the surfaces. Another example is the already discussed implementation of the conical prism (axicon) used for the creation of Bessel beams (see section 2.2). Reflective surfaces having similar geometry are also used for the same purpose [146]. However, such optics are bulky and the manufacturing of free-form surfaces or delicate parts like the axicon tip is a challenge. Because of this, the quality of the generated beam is reduced [147]. For example, the use of diffractive optics helps overcome these challenges. These types of elements and the use of spatial light modulators and geometrical phase elements are discussed in this section.

Diffractive optical elements

The role of diffractive optical elements (DOEs) is to modulate light. Usually a DOE surface is divided into many subelements with each subelement modulating only a local part of the beam. There are two methods to shape light using DOEs: amplitude modulation and phase modulation. Sometimes, these methods are combined [148]. The transfer function of an amplitude modulation-based element (also called a mask) is as follows.

$$T(x,y) = A(x,y), \tag{2.19}$$

where $A(x,y)$ is an amplitude with possible values from 0 to 1, while the phase remains constant. A light beam interferes with itself after propagating through such mask to create a diffraction pattern. One disadvantage of using such element is that intensity of the passing light is attenuated. Such mask can be quantized. For instance, when the number of values is 2 a DOE is called binary a transfer function is expressed as [3]:

$$T_B(x,y) = \begin{cases} 1, \text{ for} & 0 \leq A(x,y) \leq b \\ 0, \text{ for} & b < A(x,y) \leq 1 \end{cases}, \tag{2.20}$$

where $b = A_{0max}/2$ for the case considered by Vasara *et. al.* [3].

Phase shaping DOEs (phase masks) allow one to modulate the phase of the incoming beam. The transfer function in this case is expressed as

$$T(x,y) = A_0 e^{i\varphi(x,y)}, \tag{2.21}$$

where A_0 is constant, while the phase $\varphi(x,y)$ depends on spatial coordinates. After propagating through a phase mask, light beam does not lose intensity which is an advantage compared to amplitude masks. For a binary phase mask transfer function can be expressed as:

$$T_B(x,y) = A \begin{cases} e^{i\pi}, \text{ for} & \pi < \varphi(x,y) \leq 2\pi \\ e^{i0}, \text{ for} & 0 < \varphi(x,y) \leq \pi. \end{cases} \tag{2.22}$$

It is possible to have amplitude modulation with phase-only modulating DOE by encoding the following transfer function [149]:

$$T(x,y) = \frac{1}{2}\left\{e^{i[\varphi + \arccos(A)]} + e^{i[\varphi - \arccos(A)]}\right\} = \frac{1}{2}\left(e^{i\varphi_1} + e^{i\varphi_2}\right). \tag{2.23}$$

For this to work, a subelement of the DOE has to be divided in to 4 parts, then φ_1 and φ_2 has to be calculated and placed in checkerboard pattern [150]. Because of this pattern, light is diffracted away to realize amplitude modulation. There is also a method to obtain a result of a phase shaping mask using only amplitude modulation that mathematically can be described [151]:

$$T(x,y) = \frac{1}{2}\{1 + \cos[\varphi(x,y)]\}. \tag{2.24}$$

One can note that this function values can vary from 0 to 1.

Spatial light modulators

The spatial light modulator (SLM) is a dynamic DOE that allows one to modulate or manipulate properties of light, such as phase, amplitude, or polarization. This technology uses unique properties of LCs that

can be implemented to work with the reflection or transmission of light. Reflective SLMs have their LCs assembled on a high-performance silicon complementary metal–oxide–semiconductor (CMOS) [4, 152] to make a pixelated display formed by cells filled with LCs. Each of these pixels can be individually addressed and controlled by an electronic circuit located beneath the pixel arrays. An important characteristic of the LC display is the molecular alignment within the pixels, which determines how the beam is modulated: amplitude only, phase only, or both [148]. Some of the most common LC display types are those that are electro-optical, which means that the molecular alignment is controlled by an electric field. In the case of amplitude modulation, the light signal is modified by controlling the direction of polarization of incident light passing through a linear polarizer. In the case of phase-only modulation, light passes through the LC, where it experiences a phase delay, then is reflected by the mirror, and passes through the LC layer again. The most important property for which LCs are used in SLMs is birefringence. This means that the refractive index of the material depends on the direction of polarization and propagation of light. The magnitude of birefringence is the following:

$$\Delta n = n_e - n_o, \tag{2.25}$$

where n_o is ordinary and n_e is extraordinary indices of refraction for the incident beam. Most LCs have a positive birefringence ($\Delta n > 0$) [4, 153–155].

LCs are phases of matter with intermediate properties of solid and liquid. There are many types of LC phases, but the smectic and nematic phases are the most widely used [4]. Smectic LC have a higher degree of degree of order which means their state is more 'solid-like'. They have a viscosity higher than that of nematic LCs, which leads to slower response times when the crystals are placed in an electric field. Therefore, they are not suitable for phase-only SLMs. However, arranged in a specific order [156], they can be used in a binary phase-only light modulation [157]. Nematic LCs are less viscous and can be easily and continuously manipulated in an electric field. A big advantage of using them in devices like phase-only SLM is that multilevel phase modulation can be achieved. When the crystals are aligned in a PAN (parallel aligned nematic) configuration, the molecules of LC are parallel to each other when no electric field is applied. When an electric field is used,

the LC molecules rotate at an angle θ. The effective extraordinary refractive index $n_e(\theta)$ depends on this rotation angle and can be expressed as [158]:

$$n_e(\theta) = \frac{n_e n_o}{\sqrt{n_e^2 \cos^2\theta + n_o^2 \sin^2\theta}}, \tag{2.26}$$

where n_e is extraordinary refractive index in the off state of the LC pixel, when no voltage is applied. The total phase retardation of the LC can be expressed as follows:

$$\delta = \frac{2\pi d |n_e(\theta) - n_o|}{\lambda}, \tag{2.27}$$

where d is the thickness of LC layer. Dielectric anisotrpoty is another important property of LCs. Electrical properties of the nematic phase are described by 3×3 dielectric tensor of the form [159]:

$$\varepsilon_{ij} = \varepsilon_\perp \delta_{ij} + \Delta\varepsilon L_i L_j, \tag{2.28}$$

where $\Delta\varepsilon = \varepsilon_{||} - \varepsilon_\perp$, $i, j = x, y, z$, $\mathbf{L}$ is a LC director, which shows the mean direction of the long axis of the molecules. Because of the dielectric anisotropy, molecular orientation can change when electric field is applied. Torque that acts the LC molecule is equal to [159]:

$$\mathbf{\Gamma} = \varepsilon_0 \Delta\varepsilon (\mathbf{L} \cdot \mathbf{E})(\mathbf{L} \times \mathbf{E}). \tag{2.29}$$

When the angle between the electric field applied to LCs ($\mathbf{E}$) and the director is 0 or 90 deg torque is 0, while the maximum torque for positive $\Delta\varepsilon$ is achieved at an angle of 45 deg. In this way, the director is aligned with the direction of the electric field. LCs in SLMs are arranged on a matrix of controlled electrodes; therefore, modulation can be controlled by varying the voltage applied on an individual pixel [159, 160]. By applying a specific phase mask to the SLM screen and illuminating it with a laser beam, it is possible to generate various modes of light [161]. They can be changed relatively quickly, making SLM a versatile, although expensive, tool for beam shaping. It was shown that the use of SLM in an optical setup can improve the quality and speed of such processes as holographic imaging [162], multiphoton polymerization [112–114], foil drilling [163], optical aberration compensation [99], etc.

The concept of geometrical phase (GP), also known as the Pancharatnam-Berry phase (PBP), is associated with the polarization of light. Polarization states can be depicted on the Poincaré sphere with circular polarizations of the right and left at the poles, linear polarization on the equator, and points on the hemisphere representing right- or left-handed elliptical polarizations [164]. When the polarization of the light wave creates a closed loop on the sphere, the final state differs from the initial state by a phase that is proportional to the area of the closed loop on the sphere [165–167]. The final polarization state is the same, but the wave gained additional phase. This was shown in the experiment by inserting several waveplates into one of the arm of the Mach-Zehner interferometer. Even when the polarization of light entering and exiting a stack of waveplates is the same, the intensity pattern depends on the intermediate states of polarization in the stack [168]. A typical waveplate is a birefringent crystal with an optical axis parallel to the surface of the plate. Due to birefringence, there are two axes on the surface plane: the ordinary axis with the refraction index n_o that is perpendicular to the extraordinary axis with the refraction index n_e. Depending on n_o and n_e, these axes are also called the slow or fast axis. The polarization change induced on a light beam by a wave plate depends on the angle between the electric field and the crystal optical axis.

A GPE can be viewed as an array of wave plates with spatially varying axis angles. To design a GPE, it is necessary to calculate the required optical axis distribution $\theta(x, y)$ within the element. This can be done by using the Jones matrix formalism [169]. An electric field passing through an optical retarder will result in a field [170]:

$$\mathbf{E}_{out} = \mathbf{M}\mathbf{E}_{in}, \tag{2.30}$$

where $\mathbf{M}$ is a matrix of an optical retarder, $\mathbf{E}_{in}$ is a Jones vector of an incoming light field. For example Jones vectors for horizontal, vertical, circular right and left handed polarizations respectively are:

$$E_H = \begin{bmatrix} 1 \\ 0 \end{bmatrix}, E_V = \begin{bmatrix} 0 \\ 1 \end{bmatrix}, E_{CRP} = \frac{1}{\sqrt{2}} \begin{bmatrix} 1 \\ -i \end{bmatrix}, E_{CLP} = \frac{1}{\sqrt{2}} \begin{bmatrix} 1 \\ i \end{bmatrix} \tag{2.31}$$

A matrix of a wave plate with a spatially varying axis distribution can be expressed [167]:

$$\mathbf{M}(x,y) = \mathbf{R}[(\theta(x,y))]\mathbf{J}(\delta)\mathbf{R}^{-1}[\theta(x,y)], \tag{2.32}$$

where $\mathbf{J}(\delta)$ is the waveplate operator with retardance δ, $\mathbf{R}$ is the operator for optical rotator, θ is the local orientation of the axis at each point (x,y). Rotation operator is expressed as:

$$R(\theta) = \begin{bmatrix} \cos\theta & \sin\theta \\ -\sin\theta & \cos\theta \end{bmatrix}, \tag{2.33}$$

With everything considered, a general form of a Jones matrix for an arbitrary retarder is expressed as [171]:

$$\mathbf{M}(x,y) = e^{-\frac{i\delta}{2}} \begin{bmatrix} \cos^2\theta + e^{i\delta}\sin^2\theta & (1-e^{i\delta})e^{-i\phi}\cos\theta\sin\theta \\ (1-e^{i\delta})e^{-i\phi}\cos\theta\sin\theta & \sin^2\theta + e^{i\delta}\cos^2\theta. \end{bmatrix} \tag{2.34}$$

Here ϕ is the circularity. For linear retarders it has a value of $\phi = 0$, for elliptical retarders ϕ takes values between $-\pi/2$ and $\pi/2$.

To make a GPE, one needs to create a birefringent optical element with a space-varying optical axis. Very small structures with dimensions below the wavelength of light act as birefringent materials. An example of this could be a grating with a sub-wavelength period. Controlling the depth and direction of a grating allows us to produce a GPE [167]. Such small structures can be produced on optical surfaces by a photolithographic process, for example [172,173]. Another way is to deposit nanoparticles of various shapes and sizes to create metasurfaces [174]. GPEs used in this research were created by inscribing nanogratings inside fused silica glass by femtosecond laser pulses [170]. During the inscription process, such gratings align perpendicular to the polarization of the inscribing beam. The slow axis of these gratings is perpendicular to the corrugation of the grating. Therefore, controlling the polarization

of the incident beam during the inscription process allows us to produce an optical element with a space-variable optical axis. The resistance of the inscribed structures depends on the pulse energy used, the duration of the pulse, the laser wavelength, the writing speed [170,175]. Depending on the design, these elements can be used as polarization converters or phase retarders [8,176] when a certain incident beam polarization is chosen. For example, in [8], a described GPE acts as a radial or azimuthal polarization converter when linear polarization is used, but it can also generate an optical vortex beam if a circularly polarized beam passes through an element.

3. EXPERIMENTAL METHODS

3.1. Calculations of the DOE

In this work, beam shaping was performed using two different techniques: beam generation with SLM and beam generation using GPEs. In both cases, a phase mask is required to load onto the screen of SLM or to inscribe inside a fused silica sample. These masks can be calculated according to a specific transfer function. For example, for an axicon, this transfer function is:

$$T(\rho,\theta) = \exp(\mathrm{i}k\theta\rho)\exp(\mathrm{i}m\varphi). \tag{3.1}$$

Cone angle θ is related to a base angle of refractive axicon by $\theta = (n_a - 1)\alpha$ relation. Examples of a phase masks for generation of Bessel beams with topological charge 0 and 3 are given in Figure 3.1 (a) and (b) respectively. It is also possible to add two transfer functions together to obtain a mask for generation of Bessel beams superpositions. More details about this approach can be found in paper **[P5]**, where superposed masks were used for the formation of complex light structures. An example of a phase mask when same cone angle transfer functions with topological charges 0 and 3 are added together, is depicted in Figure 3.1 (c).

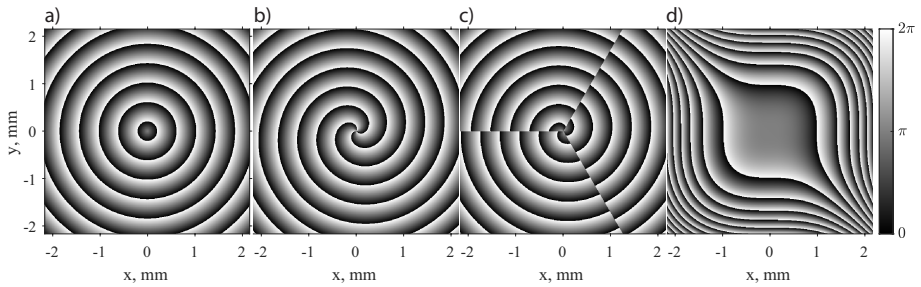

Figure 3.1: Examples of phase masks needed to generate a) Bessel beam with topological charge 0, b) Bessel beam with topological charge 3, c) a superposition of Bessel beams of topological charges 1 and 3, d) an Airy beam.

The phase mask for Airy beam generation is calculated using the following transfer function:

$$T = e^{-i(a(x^3+y^3)+b(x+y))}, \tag{3.2}$$

and the example of a cubic phase mask is given in Figure 3.1 (d). In the experiments described in **[P4]** such phase patterns were loaded to the SLM to verify the designed beams. Afterwards one of the masks was made as a GPE to be used in high energy laser setup.

Phase-only modulation can also be obtained using GPEs. When the retardance of a GPE is set to be equal to $\delta = \pi$ (or $\lambda/2$), the general Jones matrix equation 2.34 simplifies to the following:

$$M = \begin{bmatrix} \cos 2\theta & \sin 2\theta \\ \sin 2\theta & -\cos 2\theta \end{bmatrix}. \tag{3.3}$$

If the polarization of an incident beam is circular, then the output electric field is:

$$E_{out} = ME_{in} = ME_0 \begin{bmatrix} 1 \\ \pm i \end{bmatrix} = E_0 e^{i2\theta} \begin{bmatrix} 1 \\ \mp i \end{bmatrix}. \tag{3.4}$$

We see that phase modulation of the GPE is $e^{i2\theta}$. Therefore, by controlling the angle of the local optical axis, it is possible to modulate the phase of the incident beam. GPEs were extensively used in this work (see papers **[P1]**, **[P2]**, **[P3]**, **[P4]**).

3.2. Beam focusing systems

After a Bessel beam is formed with an axicon or DOE, a beam with a rather long central peak is created. For example, using the equation 2.8 for a Bessel beam with a cone angle of 2 deg and an incident Gaussian beam radius of 4 mm, the length of the Bessel zone would be $4/(2\pi/180) \approx 115$ mm, while the diameter of the central spot would be around 11 µm for 1 µm irradiation. The energy density in such a large volume is far from sufficient for laser micromachining applications. To increase the energy density, a Bessel beam is demagnified by a $4f$ imaging setup such as the one shown in Figure 3.2. A primary Bessel beam enters the set of lenses, is demagnified, and creates a secondary Bessel beam after the last lens. The magnification coefficient of such a setup is $M = f_2/f_1$ with f_1 and f_2 being focal lengths of the first and second

lenses, respectively.

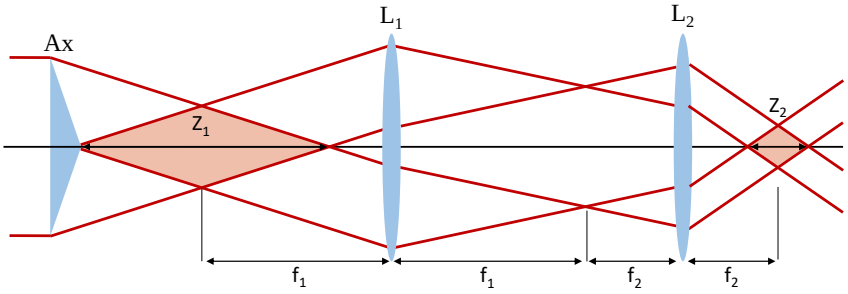

Figure 3.2: Examples of Bessel beam demagnification by a $4f$ imaging system

The cone angle, length and central core radius of the secondary beam are expressed as follow [109, 177, 178]:

$$\theta_2 = \frac{\theta_1}{M}; \quad Z_2 = \frac{Md}{\theta_2}; \quad r_2 = Mr_1, \tag{3.5}$$

where, d is the Gaussian beam radius entering an axicon. It can be seen that transverse dimensions scales linearly, while longitudinal dimensions scales as a square of magnification. If the beam is entering a transparent material, then the cone angle of a secondary beam should be divided by a refraction index of the sample, which means that the beam in elongated when entering transparent material. Imaging setups of various magnifications were used in the experiments presented in **[P1]**, **[P2]**, **[P4]**, **[P5]** **[P6]**.

3.3. Detection of optical vortices

To detect optical vortices, a setup containing two optical branches is used. In one branch, a beam containing an optical vortex is generated, while in another branch a reference plane wave is propagating. These two beams are then coupled at an angle to create an interference pattern. An example of such interference is depicted in Figure 3.3.

At the location of the optical vortex, the interference fringes fork. The number by which fringes increased on the one side of the fork is equal to the magnitude of a topological charge of the analyzed beam. This can be seen by comparing Figures 3.3 (a) and (b). The sign of topological

charge can be determined by the direction of forking (see Figure 3.3 (a) and (c)). More complex interference patterns are analyzed in [**P5**].

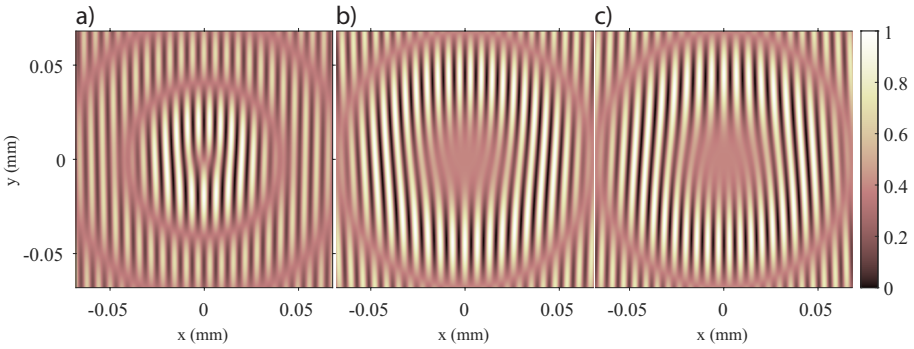

Figure 3.3: Examples of higher order Bessel beam interference with a plane. Topological charges of the Bessel beam are 1, 3 and -3 in (a), (b) and (c) respectively.

4. OVERVIEW OF THE INVESTIGATION

In this work, several instances of light structuring were investigated. From the family of nondiffractive beams, the ability to generate optical needles with a controllable longitudinal and transverse intensity distribution using Bessel and Airy beams was studied. The use of Bessel beam superpositions for generation of braided beams with complex transverse and longitudinal intensity structures was also considered. The case of top-hat beam generation using the same beam-shaping methods was also studied. The results obtained during this work have been published in six scientific papers, and a short overview of them is presented in this chapter.

Bessel beam superpositions

Paper P1 "Azimuthally modulated axicon vortical beams for laser microprocessing"

A way to create high aspect ratio nondiffracting beams with complex transverse intensity distribution patterns was introduced. It is done by using an axicon together with a geometrical phase element (GPE) that is used to azimuthaly modulate a spatial spectrum of the beam. GPE also introduces a topology to create a vortical beam structure. The resulting beam is a superposition of two Bessel beams with the same angle but different topologies. Two designs were selected to produce GPEs that azimuthaly modulate the beam spectrum to obtain multiple high aspect ratio intensity peaks in the Bessel zone. The high damage threshold of the GPE and phase-only modulation used in this method allow one to use such beams in a high-power optical setup to induce volume and surface modifications on a transparent sample with a single pulse of a laser. These modifications were characterized for different irradiation conditions. When short pulse durations are used, the surface damage resembles the beam profile. Increasing the pulse duration results in only the most intense peaks that affect the surface of the material. Volume modifications were less pronounced when the axicon beam was constructed from beams of high topological charges because their length was shorter than that of a beam constructed of smaller topological charges.

Paper P5 "Braiding of vortices in superpositions of Bessel-Gaussian beams for creation of high-contrast intensity structures"

The impact of the topological charge, as well as the cone angle of each constituent beam, on the topology of the vortical structure and the overall shape of the superposition was investigated both theoretically and experimentally. The difference in the modulus of topological charges controls the number of single charged optical vortices created in ever-increasing circles around the central peak or the central vortical void. The presence of an azimuthally symmetric vortical matrix influences the shape of the high-intensity regions. The ratio of cone angles influences the angular rotation of the vortical structure and the accompanying high-contrast intensity shapes. It also affects the individual position of the vortices and the contrast of the intensity areas surrounding them. Braided vortical and intensity structures are created only when the cone angles of the constituent beams are not equal, and the number of braids in the combined beam depends on the difference in topological charges. The presence of optical vortices and their positions were experimentally determined by interfering a structured beam with a plane wave to confirm numerical findings.

Optical needles

Paper P2 "Generation of an optical needle beam with a laser-inscribed Pancharatnam-Berry phase element under imperfect conditions"

An amplitude-based optical geometrical phase element was introduced for the modification of the beam profile entering the axicon to generate a Bessel-like optical needle with a smooth and constant on-axis intensity profile. The stability of the generation of an optical needle under various imperfect conditions was investigated both numerically and experimentally. After investigating the effect that a different-size incident beam has on the optical needle, it was determined that the optical needle was preserved for small deviations of $|\Delta w_0|/w_0 \approx 0.05$ from the beam of ideal dimensions. In the case of azimuthal misalignment of the GPE and the linear polarizer, it was concluded that the optical needle remains smooth for angular misalignments of $|\beta| < 5^\circ$. The transverse displacement of the GPE can result in a convex axial intensity profile, but the optical needle is insensitive to displacements of $\Delta x/w_0 < 0.125$.

Paper P4 "An optical needle with elongated transversal profile created using Airy beams for laser processing of glasses"

A method was proposed to create an elliptical optical needle with controllable elongation in the transverse profile using binary phase masks containing cubic and linear phases with carefully selected coefficients. The selection of these coefficients allows one to control the spatial position of two diffraction maxima independently, and placing them close to each other results in creation of an elliptical optical needle. Its characteristics such as the ratio of energy in the main lobe compared to the entire beam, the ratio of the semi-major and semi-minor axes of the main lobe, the length of the optical needle, the homogeneity length, and the directionality length were studied for different combinations of linear phase coefficients. An elliptical optical needle with a ratio of the major to minor axis of 1.7, good homogeneity, propagation length can be formed when two independent linear phase coefficients are $b_1 = -1400\pi$, $b_2 = -300\pi$. This case was realized experimentally using SLM as well as a GPE. Surface and volume modifications of the transparent material were obtained using this GPE in an optical setup with a high-energy laser. Investigations of volume modifications showed that directional cracking of glass is obtained around the center of the optical needle, where an elliptical main lobe is formed. However, this control is maintained only in a short distance around the focus plane of the lens, and direction control is lost when the beam defocuss and the two lobes of the Airy beam split apart.

Paper P6 "Creating an Array of Parallel Vortical Optical Needles"

The paper describes a method for the creation of an array of optical needles. A plane wave is directed into a phase-only SLM that shapes the phase and amplitude of a wave according to the uploaded phase mask. This phase mask is designed to create a spectrum of an optical needle array that is comprised of two spectra: one containing a function of longitudinal intensity of an optical needle array and another containing transverse positions and topological charges of the Bessel beams. Amplitude modulation is encoded in the final phase mask by using a checkerboard method. An array of optical needles is created by a Fourier lens. The interplay between the separation of optical needles is analyzed according to their individual length and distance between adjacent needles. Destructive interference is observed when the optical

needles are generated close to each other. This destruction is less pronounced when the length of the optical needle is short. The preliminary findings suggest that this phenomenon was caused by distinct spatial modulation in the Fourier space associated with optical needles of different lengths. The distortion between neighboring optical needles was the result of spatial overlap, emphasizing the importance of minimizing such overlap for optimal results.

Top-hat beam

Paper P3 "Investigation of the Pancharatnam-Berry phase element for the generation of the top-hat beam"

A method to control the incident beam amplitude via the Pancharatnam-Berry geometrical phase was presented, and the application of Gaussian to the top-hat converter was analyzed. The phase profile required to generate a top-hat beam from a Gaussian beam is presented. It was shown that the quality of the top-hat beam increases with the waist of the top-hat for distances closer to the PBP element. The formation dynamics of the top-hat beam with a PBP element was investigated numerically. The mismatch of the incident Gaussian beam waist by 16% will result mainly in a change of the top-hat beam formation position either further or closer to the element by $\approx 10\%$. The small transverse shift (around 10%) of the element does not affect the intensity profile of the top-hat beam, but this tolerance to shifts is more pronounced if the incident Gaussian beam is smaller than intended. For larger incident beams, the element shift produces a distinct C-shaped intensity modulation on the edge of the beam. The experimental results were in good agreement with the numerical estimations.

CONCLUSIONS

During this work, several conclusions were drawn.

1. Azimuthal modulation of the spatial spectrum of a Bessel-Gauss beam using two helical phase distributions of different topologies, creates a superposition of Bessel-Gauss beams that is continuous along propagation axis and is suitable to inscribe volume modifications inside glass using a single laser pulse.

2. In a superposition of Bessel-Gauss beams with different topological charges, the transverse and longitudinal intensity distributions of a complex light field are determined by the positions of single charged optical vortices, which is determined by the cone angle ratio and topological charge difference of the constituent Bessel beams. The creation of braided vortical and intensity structures is possible only for uneven cone angles and the period of braids in the combined beam increases with increasing cone angle ratio and decreasing topological charge difference.

3. The longitudinal intensity distribution of the optical needle formed by a geometrical phase element, polarizer, and an axicon remains constant within the Bessel zone when the intensity distribution of the beam impinging the axicon is shaped by reducing the amplitude in the center and within the radius of a Gaussian beam.

4. Superposition of Airy beams, produced by a binary phase mask in the +1 and -1 diffraction orders, is eligible for the formation of an elliptical optical needle.

5. An elliptical optical needle is formed by a superposition of Airy beams which is produced by the overlapping +1 and -1 diffraction orders that are formed by a binary phase mask.

6. The direction of the microcracks, induced by the elliptical optical needle inside EXG glass, is controlled through the geometrical phase element mechanical rotation which determines the parabolic trajectory of the individual Airy beam.

SANTRAUKA LIETUVIŲ KALBA

Įvadas

Struktūrinės šviesos sąvoka suprantama kaip šviesos valdymas visais laisvės laipsniais. Erdvinių laisvės laipsnių: fazės, amplitudės ar poliarizacijos, bei laikinių charakteristikų: impulso ilgio, dažnio kontrolė yra laikoma šviesos struktūrizavimu. Jau kelis tūkstantmečius žmonės naudoja vieną paprasčiausių nemonochromatinės šviesos formavimo būdų – vaizdo didinimą didinamuoju stiklu [1]. Šis optinis elementas, taip pat buvo naudojamas primityviai medžiagų modifikacijai. Juo galima sukoncentruoti saulės spindulius į mažą tašką ir uždegti toje vietoje esančią medžiagą.

Keli dešimtmečiai po to kai Maiman sukonstravo pirmąjį lazerį, pradėjo vystytis ir lazerinių pluoštų formavimo sritis. Besivystančios optinės technologijos skatino pažangą litografijos srityje, o tai leido tobulinti kompiuterius, kuriais buvo galima projektuoti optiką, reikalingą įvairių lazerinių pluoštų struktūrizavimui [2]. Daug įvairių pluošto intensyvumo skirstinių galima suformuoti panaudojus difrakcinius optinius elementus, kurie yra gaminami pagal tam tikras kompiuteriu suskaičiuotas hologramas [3]. Vienas toks optinis elementas yra skirtas suformuoti tam tikro bangos ilgio ir erdvinės struktūros pluoštui. Erdviniai šviesos moduliatoriai (EŠM) ir skaitmeniniai mikro veidrodžių įrenginiai (DMD) gali būti naudojami gretai moduliuoti krintančios šviesos fazę ir amplitudę, pagal hologramas, atvaizduotas ant prietaisų ekrano [4, 5]. Šiame darbe pristatomų tyrimų metu EŠM buvo svarbus įrenginys, kurio dėka buvo eksperimentiškai įvertinami sumodeliuotų pluoštų sklidimai. Naudojant tam tikrus metodus įmanoma moduliuoti ne tik pluošto fazę ir amplitudę, bet ir jo poliarizaciją. Pavyzdžiui, panaudojus skystųjų kristalų masyvą, metapaviršius arba į skaidrios medžiagos tūrį įrašytas mažo periodo struktūras, galima lokaliai keisti poliarizacijos kryptis kiekviename pluošto taške ir taip formuoti vektorinius pluoštus [6–8]. Tokio tipo optika yra vadinama geometrinės fazės elementais (GFE). Kai GFE gaminami į skaidrios medžiagos tūrį įrašant nano gardeles, tokių elementų lazerinės spinduliuotės pralaidumas gali siekti daugiau nei 90% plačiame spektriniame diapozone [9]. Taip pat jie pasižymi aukštu optinio pažeidimo slenksčiu ir gali būti naudojami didelės energijos lazerinių pluoštų

formavimui. Dėl šios priežasties daliai šio darbo uždavinių atlikti buvo naudojami GFE.

Tipiniai lazeriniai šaltiniai kuria vieną populiariausių Gauso pluoštą, kitaip vadinamą TEM_{00} modą. Naudojant paminėtas technologijas galima suformuoti įvairias intensyvumo struktūras turinčius pluoštus, pavyzdžiui, HG [10], LG [11] ir IG [12] modas. Sklindant laisva erdve šios modos dėl difrakcijos plečiasi. Daugumoje mikroapdirbimo taikymų reikalingi mažų skersinių, ir santykinai ilgų išilginių matmenų pluoštai. Gauso pluošto plitimo kampas yra atvirkščiai proporcingas pluošto sąsmaukos matmenims. Dėl to mažas pluošto diametras galimas tik trumpuose sklidimo atstumuose. Įdomi sąvoka optikos srityje yra nedifraguojantys pluoštai. Iš jų vienas populiariausių – Beselio pluoštas turi centrinę smailę, kuri, sklidimo metu, tam tikru atstumu išlaiko savo matmenis [13]. Kitas taip pat gerai žinomas yra Airy nedifraguojantis pluoštas [14]. Intensyviausia jo smailė sklinda lenkta trajektorija, o skersinėse koordinatėse atrodo, jog ji sklinda su pagreičiu. Tam tikri struktūriniai pluoštai, pavyzdžiui, aukštesnės eilės Beselio pluoštai, LG modos turi įdomią savybę pernešti orbitinį judesio kiekio momentą. Šie pluoštai turi sraigtinį bangos frontą susuktą apie centrinį nulinio intensyvumo tašką, kurio fazė nėra apibrėžta. Poliarizacijos singuliarumai taip pat sukuria intensyvumo minimumus vektoriniuose pluoštuose. Taigi, valdant šviesos laisvės laipsnius, galima gauti įvairių intensyvumo skirstinių, kartais primenančių gėles [15], žvaigždes [16] ar kitokias formas. Kai kurie pluoštai vadinami gana keistais vardais, pavyzdžiui, fotininiais ratas [17] ir kabliais [18], optiniais buteliais [19], adatomis [20], grąžtais [21], peiliais [22] ir kastuvais [22].

Struktūrinė šviesa yra naudojama įvairiuose taikymuose. Stimuliuoto emisijos gesinimo mikroskopijoje pluošto su intensyvumo minimumu centre panaudojimas leidžia pagerinti vaizdavimo skyrą [23]. Pluoštai turintys orbitinį judesio kiekio momentą, naudojami optiniuose pincetuose, leidžia sukioti daleles [24], o Airy pluoštai gali būti naudojami dalelių pernašai [25]. Lazerinio apdirbimo srityje, įvairių intensyvumo struktūrų bei poliarizacijų pluoštai dažnai leidžia pagerinti procesų kokybę ir greitį. Vektoriniai pluoštai yra efektyvesni metalų pjovime [26], o nedifraguojantys pluoštai yra naudingi skaidrių medžiagų apdirbimui.

Šioje disertacijoje yra aprašomi metodai skirti kurti struktūrinius šviesos pluoštus, turinčius sudėtingus skersinius ir išilginius intensyvu-

mo skirstinius. Pagrindiniai šio darbo rezultatai yra aprašyti publikacijose, kurios pateikiamos kartu su disertacijos tekstu. Didelis dėmesys skiriamas nedifraguojančių pluoštų – optinių adatų formavimui. Praktikoje formuojant šiuos pluoštus, gaunamas intensyvumo skirstinys gali priklausyti nuo eksperimentinių sąlygų, o dėl šių sąlygų netobulumo atsirandtantis pokytis yra nagrinėjamas vienoje iš pateikiamų publikacijų. Tam tikriems taikymams reikia valdyti ne tik išilginį, bet ir skersinį pluošto intensyvumo skirstinį, tad kitas darbo uždavinys buvo suformuoti optinę adatą su valdomo elipsiškumo intensyvumo smaile skersinėse koordinatėse. Tai buvo atlikta panaudojant Airy pluoštą. Sudėjus kelis nedifraguojančius Beselio pluoštus, gaunamos sudėtingos šviesos struktūros. Šis metodas taip pat buvo nagrinėjamas tyrimų metu ir jį naudojant buvo suformuojami lygegriačių optinių adatų masyvai. Galiausiai, pasirinkti struktūriniai pluoštai buvo panaudoti skaidrių terpių modifikavimui, o detalesnė eksperimentų informacija pateikiama pridėtose publikacijose.

Darbo tikslas

Ištirti naujus lazerinių kompleksinių pluoštų formavimo metodus ir kurti efektyvius optinius elementus, kurie formuotų pluoštus turinčius erdvinius ir tolydžius intensyvumo skirstinius, aktualius lazerinio mikro apdirbimo srityje, galinčius modifikuoti skaidrias terpes vienetiniu lazerio impulsu.

Sprendžiami uždaviniai

Darbo tikslui įgyvendinti buvo iškelti šie uždaviniai:

- Išnagrinėti galimus metodus Beselio-Gauso pluoštų superpozicijos formavimui. Suformuoti erdvinę šviesos struktūrą, sudarytą iš kelių topologinių krūvių Beselio pluoštų, moduliuojant spektro fazę. Gauti pažaidas skaidrioje terpėje panaudojant sudėtinius pluoštus.

- Eksperimentiškai realizuoti Beselio-Gauso pluoštų superpozicijas, sudarytas iš pluoštų su skirtingais topologiniais krūviais ir kūgio kampais. Eksperimentiškai nustatyti tokioje erdvinėje šviesos struktūroje esančių optinių sūkurių padėtis. Palyginti eksperimentinius rezultatus su skaitmeninio modeliavimo rezultatais.

- Išnagrinėti galimybę formuoti optinę adatą Beselio-Gauso pluoštu, pasitelkiant geometrinės fazės elementus. Eksperimentiškai realizuoti optinę adatą ir ištirti eksperimente pasitaikančių netobulumų įtaką optinės adatos formavimo stabilumui.

- Ištirti elipsinės adatos formavimo galimybę Airy pluoštais. Įvertinti binarinės Airy fazinės kaukės parametrų įtaką elipsinės optinės adatos charakteristikoms. Eksperimentiškai suformuoti šį pluoštą, palyginti eksperimentinius rezultatus su skaitmeninio modeliavimo rezultatais. Ištirti elipsinės Airy pluošto adatos poveikį skaidrioje terpėje.

- Suformuoti optinių adatų masyvą, kuriame būtų galima valdyti kiekvienos atskiros optinės adatos topologinį krūvį, bei adatos padėtį išilginėse ir skersinėse koordinatėse. Ištirti pluoštų masyvo skersinio intensyvumo skirstinio kokybę priklausomai nuo individualių pluoštų ilgių, bei parinkto atstumo tarp pluoštų.

- Suformuoti plokščios intensyvumo viršūnės pluoštą geometrinės fazės elementu. Charakterizuoti šio pluošto sklidimą laisva erdve. Įvertinti galimų eksperimentinių netobulumų įtaką šio pluošto formavimui ir palyginti rezultatus su skaitmeninio modeliavimo rezultatais.

Darbo naujumas ir aktualumas

- Pademonstruotas metodas eksperimentiškai suformuoti kelių topologinių krūvių Beselio-Gauso pluoštų superpoziciją naudojant kūginį lęšį ir geometrinės fazės elementą, bei pademonstruotas šio metodo panaudojimas didelės impulso energijos reikalaujantiems taikymams. Tai yra aktualu norint greičiau formuoti mikrokanalus skaidrioje terpėje.

- Geometrinės fazės elementas buvo panaudotas moduliuoti į kūginį lęšį krintančio pluošto amplitudę, ir suformuoti lygaus ašinio intensyvumo profilio optinę adatą. Taip pat buvo įvertintas optinės adatos formavimo stabilumas, kai šio elemento pozicija optinėje schemoje nėra tobula.

- Skaitmeniškai ir eksperimentiškai įvertinta plokščios viršūnės

pluošto formavimosi atstumo priklausomybė nuo pluošto, krintančio į geometrinės fazės elementą, diametro. Galimų pluošto netobulumų žinojimas yra aktualus projektuojant optines sistemas.

- Pademonstruotas metodas iš Airy pluoštų suformuoti optinę adatą su lanksčiai valdomu pagrindinės intensyvumo smailės elipsiškumu skersinėje plokštumoje. Parodyta, kad stiklo tūrį paveikus tokios erdvinės struktūros impulsu, galima gauti kryptingus mikro įtrūkius.

- Pademonstruotas optinių adatų masyvo formavimas, kuriame galima ne tik laisvai pasirinkti individualios optinės adatos padėtį, bet ir jos topologinį krūvį.

Ginamieji teiginiai

- Azimutiškai moduliuojant Beselio-Gauso pluošto erdvinį spektrą dviejų skirtingų topologinių krūvių sūkurinių pluoštų faziniais skirstiniais, gaunama šių topologinių krūvių Beselio-Gauso pluoštų superpozicija, tinkama "vienašūviam" modifikacijų įrašymui stiklo tūryje.

- Skersiniai ir išilginiai kompleksinio šviesos pluošto intensyvumo skirstiniai priklauso nuo vienetinio topologinio krūvio sūkurių padėčių įvairių eilių Beselio-Gauso pluoštų superpozicijoje.

- Geometrinės fazės elementu, poliarizatoriumi ir eksikonu suformuotos optinė adatos išilginis intensyvumo skirstinys išlieka pastovus Beselio zonoje.

- Binarine fazine kauke formuojamų +1 ir -1 eilės difrakcinių maksimumų Airy pluoštų superpozicija tinkama elipsinės optinės adatos formavimui.

- Eplipsinėmis optinėmis adatomis formuojamų mikroįtrūkimų kryptys EXG stikle valdomos geometrinės fazės elemento sukimu aplink jo ašį.

Autoriaus indelis

Visose prie šios disertacijos pridėtose publikacijose, autorius buvo atsakingas už eksperimentinę dalį. Autorius atliko tokius darbus kaip: eksperimentinių stendų projektavimas ir surinkimas, eksperimentinių rezultatų gavimas, jų analizė, aprašymas ir palyginimas su teoriniais duomenimis.

Darbe [**P1**], autorius atliko skaitmeninį modeliavimą, suprojektavo 180-ies zonų geometrinės fazės elementą, surinko eksperimentinį stendą, gavo pažeidas stikle, išanalizavo rezultatus, parašė didžiąją dalį teksto. E. Nacius suprojektavo 6-ių zonų elementą. O. Ulčinas pagamino geometrinės fazės elementus. S. Orlovas parašė teorinį įvadą, kuravo darbą, koregavo tekstą.

Darbe [**P2**], autorius surinko eksperimentinį stendą, atliko eksperimentinius matavimus ir juos aprašė. P. Gotovski skaitmeniškai sumodeliavo optinę adatą, parengė iliustracijas, parašė didžiąją dalį teksto. O. Ulčinas pagamino geometrinės fazės elementą. S. Orlovas kuravo darbą, koregavo tekstą.

Darbe [**P3**], autorius surinko eksperimentinį stendą, atliko eksperimentinius matavimus ir juos aprašė. P. Gotovski atliko skaitmeninio modeliavimo darbus, parašė didžiąją dalį teksto. O. Ulčinas pagamino geometrinės fazės elementą. S. Orlovas kuravo darbą, koregavo tekstą.

Darbe [**P4**], autorius surinko abu eksperimentinius stendus, atliko eksperimentinius matavimus, bandinių gamybą, išanalizavo rezultatus, parašė didžiąją dalį teksto. K. Mundrys atliko skaitmeninio modeliavimo darbus. S. Orlovas kuravo darbą, koregavo tekstą.

Darbe [**P5**], autorius atliko skaitmeninio modeliavimo darbus, surinko eksperimentinį stendą, atliko eksperimentinius matavimus, išanalizavo ir aprašė modeliavimo ir eksperimento rezultatus. S. Orlovas parašė įvadą, teorinį įvadą, koregavo tekstą.

Darbe [**P6**], autorius surinko eksperimentinį stendą, atliko matavimus, paruošė rezultatus publikacijai, bei koregavo tekstą. S. Orlovas atliko skaičiavimus, parašė didžiąją dalį publikacijos teksto.

Rezultatų apžvalga

Darbo metu buvo atliktas lazerinių pluoštų struktūrizavimas įvairiais pluoštų formavimo metodais. Dauguma tyrimų buvo atlikti naudojant

nedifraguojančius pluoštus: optinių adatų su valdomu skersiniu ir išilginiu intensyvumo skirstiniu formavimas naudojant Beselio ir Airy pluoštus; Beselio optinių adatų masyvo formavimas; Beselio pluoštų superpozicijos panaudojimas formuoti pluoštus turinčius sudėtingus skersinio ir išilginio intensyvumo skirstinius. Taip pat buvo nagrinėjamas plokščio intensyvumo pluošto formavimas. Doktorantūros metu atliktų tyrimų rezultatai buvo atspausdinti 6-uose moksliniuose straipsniuose, o trumpa straipsnių apžvalga pateikiama žemiau.

Beselio pluoštų superpozicijos

Straipsnis P1 "Azimuthally modulated axicon vortical beams for laser microprocessing"

Straipsnyje pristatomas metodas sudėtingos skersinės intensyvumo struktūros pluoštų, su dideliu ašinių ir skersinių matmenų santykiu, formavimui. Tai buvo įgyvendinta panaudojant kūginio lęšio ir geometrinės fazės elemento (GFE) porą. GFE buvo naudojamas Beselio pluošto spektro fazės moduliacijai, Gautas struktūrinis pluoštas yra dviejų skirtingų topologinių krūvių Besselio pluoštų superpozicija. Straipsnyje pristatomi du GFE, kuriais moduliuojant Beselio pluošto spektrą, gaunamas struktūrinis pluoštas su keliomis aukšto intensyvumo smailėmis. Dėl aukšto GFE pažeidimo slenksčio ir gero fazinės moduliacijos efektyvumo suformuotos superpozicijos buvo panaudotos stiklo paviršiaus ir tūrio modifikacijoms gauti. Tam buvo panaudoti skirtingi lazerio pluošto parametrai, o gautos modifikacijos buvo apibūdintos pagal pažaidos formą ir jos ilgį. Naudojant trumpus impulsus, paviršiaus modifikacijų struktūra atkartoja pluošto skersinio intensyvumo pasiskirstymą, o parinkus ilgesnes impulso trukmes tik intensyviausios smailės pažeidžia paviršių. Kai naudojamo pluošto struktūra yra sudaryta iš aukštų topologinių krūvių Besselio-Gauso pluoštų, tūrinės modifikacijos yra trumpesnės lyginant su tūrinėmis modifikacijomis gautomis esant žemesnio topologinio krūvio pluoštų superpozicijoms.

Straipsnis P5 "Braiding of vortices in superpositions of Bessel beams for creation of high-contrast intensity structures"

Straipsnyje teoriniu ir eksperimentiniu metodu buvo nagrinėjama sudedamų pluoštų topologinių krūvių ir kūgių kampų įtaka sudėtinio pluošto sūkurinei struktūrai ir bendram pluošto intensyvumo pasiskirs-

tymui. Topologinių krūvių skirtumo modulis nusako pirmojo topologinio krūvio sūkurių skaičių, kurie formuojasi aplink centrinį intensyvumo minimumą arba maksimumą. Šių sūkurių pozicijos lemia bendrą aukšto intensyvumo smailių struktūrą. Sklidimo metu stebimas kampinis struktūrinio pluošto sukimasis priklauso nuo sudedamų Beselio pluoštų kūgio kampų santykio. Nuo šio santykio taip pat priklauso ir individualių optinių sūkurių pozicijos ir sudėtinio pluošto intensyvumo skirstinio forma. Aukšto intensyvumo smailių pynė susiformuoja tik tuo atveju kai sudedamų pluoštų kūgio kampai nėra lygūs. Darbe buvo eksperimentiškai nustatytos optinių sūkurių padėtys kelių Beselio-gauso pluoštų superpozicijoje.

Optinės adatos

Straipsnis P2 "Generation of an optical needle beam with a laser inscribed Pancharatnam-Berry phase element under imperfect conditions"

Šiame darbe buvo pristatytas geometrinės fazės (GF) optinis elementas, leidžiantį formuoti didelės galios optinę adatą su glotniu ir pastoviu ašinio intensyvumo profiliu. Darbe tiek skaitmeniškai, tiek eksperimentiškai buvo ištirtas GF elemento ir poliarizatoriaus poros formuojamos optinės adatos sklidimas esant tokiems eksperimentinių sąlygų netobulumams, kaip į elementą krintančio pluošto matmenų neatitikimas, GF elemento ir tiesinio poliarizatoriaus kampinis išderinimas, bei elemento skersinis poslinkis nuo optinės ašies centro. Buvo nustatyta, kad geriausios sąlygos optinės adatos formavimui yra kai: į elementą krintančio pluošto diametro nuokrypio ir idealaus pluošto diametro santykis <0.05, elemento ir poliarizatoriaus kampinis išderinimas $<5°$, skersinio elemento poslinkio santykis su pluošto spinduliu <0.125. Taigi, esant nedideliems sistemos iškraipymas, formuojama optinė adata yra stabili.

Straipsnis P4 "An optical needle with elongated transversal profile created using Airy beams for laser processing of glasses"

Straipsnyje pristatomas metodas formuoti elipsinę optinę adatą naudojant binarines kubinės fazinės kaukes su papildoma tiesine fazės moduliacija. Parenkant kubinės ir tiesinės fazių koeficientus galima valdyti dviejų difrakcijos maksimumų, kuriuose formuojasi Airy pluoštai, pozicijas. Kai šie maksimumai yra arti vienas kito, formuojama optinė

adata. Buvo ištirtos šios adatos charakteristikos: energijos pagrindinėje smailėje santykis su energija likusiame pluošte, pagrindinės smailės ilgosios ir trumposios elipsės ašių santykis, optinės adatos ilgis, homogeniškumo ilgis, kryptingumo ilgis. Parinkus binarinės kaukės tiesinės fazės koeficientus $b_1 = -1400\pi$, $b_2 = -300\pi$, kaukė formuoja elipsinę optinę adatą su ilgosios ir trumposios ašies santykiu 1.7, sąlyginai ilgu sklidimo ir homogeniškumo ilgiu. Ši optinė adata buvo panaudota paviršinių ir tūrinių pažaidų gavimui stikle. Židinio plokštumoje suformuoti mikroįtrūkiai yra kryptingai išdėstyti lygiagrečiai pluošto ilgąjai ašiai, tačiau tokia mikroįtrūkių kontrolė galima tik trumpame sklidimo atstume.

Straipsnis P6 "Creating an Array of Parallel Vortical Optical Needles"

Straipsnyje aprašomas metodas lygiagrečių optinių adatų masyvo formavimui. Struktūrinių pluoštų masyvas yra formuojamas erdviniu šviesos moduliatoriumi (EŠM), jį apšviečiant plokščiąja banga. EŠM moduliuoja bangos fazę ir amplitudę pagal ant jo ekrano atvaizduotą fazinę kaukę, kuri yra apskaičiuota taip, kad sukurtų optinių adatų masyvo spektrą. Šis spektras yra apskaičiuojamas sudedant išilginio intensyvumo spektro funkciją ir skersinio intensyvumo spektro funkciją, kurioje yra Beselio pluoštų pozicijų ir topologinių krūvių informacija. Reikalinga amplitudinė moduliacija yra gaunama užkoduojant galutinę fazinę kaukę šachmatų lentos metodu. Optinių adatų masyvas yra formuojamas lęšiu atliekant spektro Furje transformaciją. Straipsnyje yra nagrinėjama sąveika tarp gretimų optinių adatų priklausomai nuo parinkto adatų ilgio, bei atstumo tarp jų. Kai parinkti atstumai tarp optinių adatų yra nedideli (iki 40 bangos ilgių) –stebima destruktyvi interferencija, individualios optinės adatos neišskiriamos. Parinkus trumpesnius individualių optinių adatų ilgius, destruktyvi interferencija yra silpnesnė ir adatas galima formuoti arčiau viena kitos. Skersinio intensyvumo iškraipymai tarp optinių adatų atsiranda dėl individualių optinių adatų erdvinių spektrų persiklojimo. Norint pasiekti optimalius rezultatus reikėtų mažinti šį persiklojimą.

Straipsnis P3 "Investigation of the Pancharatnam-Berry phase element for the generation of the top-hat beam"

Straipsnyje aptartas metodas Pancharatnam-Berry geometrinės fazės elementu valdyti kritusio Gauso pluošto amplitudę ir paversti jį plokščios viršūnės pluoštu. Tam pasiekti reikalinga fazės moduliacija specifiniu fazės portretu, kuris yra pristatytas straipsnyje. Skaitmeniškai bei eksperimentiškai buvo ištirta plokščios viršūnės pluošto formavimosi dinamika kai į elementą krinta netikslių matmenų pluoštas ir kai elemento centras nesutampa su į jį krintančio pluošto centru. Kai į elementą krintančio pluošto diametro neatitikimas yra iki 16% nuo idealaus, keičiasi atstumas, kuriame susiformuoja plokščios viršūnės pluoštas. Nedidelis skersinis elemento poslinkis (apie 10 %) neiškreipia plokščios viršūnės intensyvumo profilio. Jeigu skersinis elemento poslinkis yra didelis, tuomet formuojamo pluošto intensyvumo skirstinys tampa C formos.

Išvados

Atliekant darbą buvo padarytos tokios išvados:

1. Azimutiškai moduliuojant Beselio-Gauso pluošto erdvinį spektrą dviejų skirtingų topologinių krūvių sūkurinių pluoštų faziniais skirstiniais, gaunama šių topologinių krūvių Beselio-Gauso pluoštų superpozicija tolydi trimatėje erdvėje bei tinkama modifikacijų įrašymui stiklo tūryje paveikus vienu lazerio impulsu.

2. Skersiniai ir išilginiai kompleksinio šviesos pluošto intensyvumo skirstiniai priklauso nuo vienetinio topologinio krūvio sūkurių padėčių įvairių eilių Beselio-Gauso pluoštų superpozicijoje dėl sudedamų skirtingų sūkurinių Beselio pluoštų kūgio kampų. Pynių persipynimo periodas didėja mažėjant sudedamų pluoštų topologinių krūvių skirtumui ir didėjant kūgio kampų santykiui, o esant santykiniam kūgio kampui 1 – pynių nelieka.

3. Geometrinės fazės elementu, poliarizatoriumi ir eksikonu suformuotos optinė adatos išilginis intensyvumo skirstinys išlieka pastovus Beselio zonoje, dėl prieš eksikoną suformuojamo intensyvu-

mo skirstinio, sumažinant jo amplitudę ne tik centre, bet Gauso pluošto spindulio atstume.

4. Dėl binarine fazine kauke formuojamų +1 ir -1 eilės persiklojančių difrakcinių maksimumų – Airy pluoštų – superpozicijos sukuriama elipsinė optinė adata.

5. Eplipsinėmis optinėmis adatomis formuojamų mikroįtrūkimų kryptys EXG stikle valdomos geometrinės fazės elemento sukimu aplink jo ašį, lemiančiu individualaus Airy pluošto parabolinę sklidimo trajektoriją.

LIST OF PUBLICATIONS

On the dissertation topic

[P1] **P. Šlevas**, S. Orlov, E. Nacius, O. Ulčinas, Azimuthally modulated axicon vortical beams for laser microprocessing, Optics Communications **50**, 127509 (2021).

DOI: 10.1016/j.optcom.2021.127509

[P2] P. Gotovski, **P. Šlevas**, S. Orlov, O. Ulčinas, A. Urbas, Generation of an optical needle beam with a laser inscribed Pancharatnam-Berry phase element under imperfect conditions, Opt. Express **29**(21), 33331-33345 (2021).

DOI: 10.1364/OE.438709

[P3] P. Gotovski, **P. Šlevas**, S. Orlov, O. Ulčinas, V. Jukna, A. Urbas, Investigation of the Pancharatnam–Berry phase element for the generation of the top-hat beam, J. Opt. **24**, 035607 (2022).

DOI: 10.1088/2040-8986/ac4317

[P4] **P. Šlevas**, K. Mundrys, O. Ulčinas, S. Orlov, An optical needle with elongated transversal profile created using Airy beams for laser processing of glasses, Optics & Laser Technology, **174**, 110558 (2024).

DOI: 10.1016/j.optlastec.2024.110558

[P5] **P. Šlevas**, S. Orlov, Braiding of vortices in superpositions of Bessel–Gaussian beams for creation of high-contrast intensity structures, Optik, **300**, 171676 (2024).

DOI: 10.1016/j.ijleo.2024.171676

[P6] **P. Šlevas**, S. Orlov, Creating an Array of Parallel Vortical Optical Needles, Photonics, **11**(3), 203 (2024).

DOI: doi.org/10.3390/photonics11030203

Conference proceedings

[PR1] **P. Šlevas**, S. Orlov, E. Nacius, O. Ulcinas, P. Gotovski, J. Baltrukonis, V. Jukna, Laser induced modifications in transparent materials using azimuthally modulated axicon beams," Proc. SPIE 11267, Laser Applications in Microelectronic and Optoelectronic Manufacturing (LAMOM) XXV, 112670B, 2020. DOI: 10.1117/12.2546580

[PR2] P. Gotovski, **P. Šlevas**, E. Nacius, V. Jukna, S. Orlov, O. Ulcinas, J. Baltrukonis, T. Gertus, Design of efficient Gauss to top-hat converters using geometrical phase elements inscribed in the glass by femtosecond laser pulses, Proc. SPIE 11266, Laser Resonators, Microresonators, and Beam Control XXII, 112661J, 2020. DOI: 10.1117/12.2546620

[PR3] P. Gotovski, **P. Šlevas**, E. Nacius, V. Jukna, S. Orlov, J. Baltrukonis, O. Ulčinas, T. Gertus, Formation of optical needles by Pancharatnam-Berry phase element for laser-induced modifications in transparent materials, Proc. SPIE 11268, Laser-based Micro- and Nanoprocessing XIV, 112681Y, 2020. DOI: 10.1117/12.2544925

[PR4] P. Gotovski, **P. Šlevas**, S. Orlov, O. Ulčinas, A. Urbas, Inscription in the glass of efficient Gauss to top-hat converters based on Pancharatnam-Berry phase by high power femtosecond laser pulses, Proc. SPIE 11673, Laser Applications in Microelectronic and Optoelectronic Manufacturing (LAMOM) XXVI, 116730H, 2021. DOI: 10.1117/12.2578318

[PR5] **P. Šlevas**, E. Kozlovskis, S. Orlov, P. Gotovski, O. Ulčinas, Creation of high-contrast structures in superpositions of higher order Bessel beams for laser processing of glasses, 2021 Conference on Lasers and Electro-Optics Europe & European Quantum Electronics Conference (CLEO/Europe-EQEC), 2021. DOI: 10.1109/CLEO/Europe-EQEC52157.2021.9542280

[PR6] P. Gotovski, **P. Šlevas**, S. Orlov, O. Ulšinas, A. Urbas, Effects of various misalignments and beam impurities on creation of optical needle using Pancharatnam–Berry phase elements, 2021

Conference on Lasers and Electro-Optics Europe & European Quantum Electronics Conference (CLEO/Europe-EQEC), 2021. DOI: 10.1109/CLEO/Europe-EQEC52157.2021.9542214

Conference presentations

[C1] **P. Šlevas**, S. Orlov, E. Nacius, O. Ulcinas, P. Gotovski, J. Baltrukonis, V. Jukna, Laser induced modifications in transparent materials using azimuthally modulated axicon beams, 11267-9, SPIE Photonics West 2020, February 3-7, San Francisco, USA, oral presentation.

[C2] P. Gotovski, **P. Šlevas**, E. Nacius, V. Jukna, S. Orlov, J. Baltrukonis, O. Ulčinas, T. Gertus, Formation of optical needles by Pancharatnam-Berry phase element for laser-induced modifications in transparent materials, 11268-69, SPIE Photonics West 2020, February 3-7, San Francisco, USA, poster presentation.

[C3] P. Gotovski, **P. Šlevas**, E. Nacius, V. Jukna, S. Orlov, O. Ulcinas, J. Baltrukonis, T. Gertus, Design of efficient Gauss to top-hat converters using geometrical phase elements inscribed in the glass by femtosecond laser pulses, 11266-55, SPIE Photonics West 2020, February 3-7, San Francisco, USA, poster presentation.

[C4] P. Gotovski, **P. Šlevas**, O. Ulčinas, E. Nacius, B. Stanionis, S. Orlov, V. Jukna, T. Gertus, Flat axial intensity profile in the Bessel beam for beam shaping applications in laser systems, We-P2.9, Europhoton, 2020, virtual poster presentation.

[C5] S. Orlov, P. Gotovski, **P. Šlevas**, O. Ulčinas, E. Nacius, E. Kozlovskis, V. Jukna, T. Gertus, Incription of efficient top-hat elements in the glass using high power femtosecond laser system, Th-P3.6, Europhoton, 2020, virtual poster presentation.

[C6] P. Gotovski, **P. Šlevas**, S. Orlov, O. Ulčinas, A. Urbas, Inscription in the glass of efficient Gauss to top-hat converters based on Pancharatnam-Berry phase by high power femtosecond laser pulses, SPIE Photonics West 2021, March 5, 2021, virtual poster presentation.

[C7] **P. Šlevas**, E. Kozlovskis, S. Orlovas, O. Ulčinas, Superimposed Bessel beams for transparent material modification, E-MRS spring meeting, June 1, 2021, virtual poster presentation.

[C8] P. Gotovski, **P. Šlevas**, S. Orlov, O. Ulčinas, V. Jukna, A. Urbas, Incription in the glass of Pancharatnam-Berry phase elements for efficient for generation of Gauss to top-hat converters, E-MRS spring meeting, June 1, 2021, virtual poster presentation.

[C9] P. Gotovski, **P. Šlevas**, S. Orlov, O. Ulčinas, V. Jukna, A. Urbas, Stability of optical needle generation using geometrical phase elements to misalignments and impurities, E-MRS spring meeting, June 1, 2021, virtual poster presentation.

[C10] **P. Šlevas**, P. Gotovski, S. Orlovas, O. Ulčinas, A. Urbas, Effects of various misalignments and beam impurities on creation of optical needle using Pancharatnam–Berry phase element, Lasers in Manufacturing, June 23, 2021, virtual oral presentation.

[C11] **P. Šlevas**, E. Kozlovskis, S. Orlovas, P. Gotovski, O. Ulčinas, Creation of high-contrast structures in superpositions of higher order Bessel beams for laser processing of glasses, CLEO Europe, June 25, 2021, virtual poster presentation.

[C12] S. Orlovas, P. Gotovski, **P. Šlevas**, V. Jukna, O. Ulčinas, A. Urbas, Generation of the optical needle with geometric phase elements under imperfect conditions, LNFK 44, October 7, 2021, Vilnius, Lithuania, oral presentation.

[C13] **P. Šlevas**, E. Kozlovskis, E. Nacius, S. Orlovas, O. Ulcinas, Beselio pluoštų superpozicijų formavimas geometrinės fazės elementais, FizTech, October 20, 2021, Vilnius, Lithuania, oral presentation.

[C14] **P. Šlevas**, K. Mundrys, S. Orlovas, Spatially controlled Airy beams for glass processing, E-MRS spring meeting, May 30, 2022, virtual poster presentation.

[C15] P. Kizevicius, E. Nacius, R. Ivaskeviciute-Povilauskiene, D. Jakubauskis, L. Minkevicius, S. Orlov, G. Valusis, **P. Šlevas**, Investigation of laser-ablated Si phase elements for generation of

THz Bessel beams, E-MRS spring meeting, May 30, 2022, virtual poster presentation.

[C16] **P. Šlevas**, P. Gotovski, S. Orlov, O. Ulčinas, A. Urbas, Optinės adatos formavimas geometrinės fazės elementu neidealiomis sąlygomis, FizTech, October 19, 2022, Vilnius, Lithuania, oral presentation.

ACKNOWLEDGEMENTS

First of all, I would like to thank my academic supervisor Sergejus Orlovas for all the counseling, encouragement to maintain a steady pace of improvement throughout the doctoral studies, and the help to navigate bureaucratic pathways.

Furthermore, I am grateful to all the co-authors of the papers included in this thesis. Special thanks goes to Pavel Gotovski and Karolis Mundrys for all the theoretical modeling and the help to understand the math behind it. To Orestas Ulčinas for his collaboration and all the optical elements he provided. Also, my thanks goes to Vytautas Jukna for all the questions and remarks that he has in every group meeting.

Lastly, I am grateful to my family and to my incredible friends for their kindness, support, all sorts of advice, jokes and adventures, that helped me to recharge my batteries.

REFERENCES

[1] G. Sines, Y. A. Sakellarakis, Lenses in antiquity, American Journal of Archaeology **91**(2), 191–196 (1987).

[2] A. Forbes, Structured light: tailored for purpose, Opt. Photon. News **31**(6), 24–31 (2020).

[3] A. Vasara, J. Turunen, A. T. Friberg, Realization of general nondiffracting beams with computer-generated holograms, J. Opt. Soc. Am. A **6**(11), 1748–1754 (1989), https://doi.org/10.1364/JOSAA.6.001748.

[4] Z. Zhang, Z. You, D. Chu, Fundamentals of phase-only liquid crystal on silicon (LCOS) devices, Light: Science & Applications **3**(10), e213 (2014).

[5] Y.-X. Ren, R.-D. Lu, L. Gong, Tailoring light with a digital micromirror device, Annalen der physik **527**(7-8), 447–470 (2015).

[6] P. Chen, W. Ji, B.-Y. Wei, W. Hu, V. Chigrinov, Y.-Q. Lu, Generation of arbitrary vector beams with liquid crystal polarization converters and vector-photoaligned q-plates, Applied Physics Letters **107**(24) (2015).

[7] M. J. Escuti, J. Kim, M. W. Kudenov, Controlling light with geometric-phase holograms, Optics and Photonics News **27**(2), 22–29 (2016).

[8] M. Beresna, M. Gecevičius, P. G. Kazansky, T. Gertus, Radially polarized optical vortex converter created by femtosecond laser nanostructuring of glass, Applied Physics Letters **98**(20) (2011).

[9] P. Gotovski, P. Šlevas, E. Nacius, V. Jukna, S. Orlov, J. Baltrukonis, O. Ulčinas, T. Gertus, Formation of optical needles by Pancharatnam-Berry phase element for laser-induced modifications in transparent materials, in *Laser-based Micro-and Nanoprocessing XIV* (International Society for Optics and Photonics, 2020), volume 11268, 112681Y.

[10] A. E. Siegman, Hermite–Gaussian functions of complex argument as optical-beam eigenfunctions, JOSA **63**(9), 1093–1094 (1973).

[11] L. Allen, M. W. Beijersbergen, R. Spreeuw, J. Woerdman, Orbital angular momentum of light and the transformation of Laguerre-Gaussian laser modes, Physical review A **45**(11), 8185 (1992).

[12] M. A. Bandres, J. C. Gutiérrez-Vega, Ince–Gaussian beams, Optics letters **29**(2), 144–146 (2004).

[13] J. Durnin, Exact solutions for nondiffracting beams. I. the scalar theory, JOSA A **4**(4), 651–654 (1987).

[14] J. C. Gutiérrez-Vega, M. D. Iturbe-Castillo, S. Chávez-Cerda, Alternative formulation for invariant optical fields: Mathieu beams, Opt. Lett. **25**(20), 1493–1495 (2000), https://doi.org/10.1364/OL.25.001493.

[15] T. Lu, T. Huang, J. Wang, L. Wang, R. R. Alfano, Generation of flower high-order Poincaré sphere laser beams from a spatial light modulator, Scientific reports **6**(1), 39657 (2016).

[16] X. Gao, T. Geng, X. Dong, H. Guo, S. Zhuang, Experimental generation of tunable star-shape laser beam from Gaussian beam, Optik **124**(10), 915–918 (2013).

[17] A. Aiello, P. Banzer, M. Neugebauer, G. Leuchs, From transverse angular momentum to photonic wheels, Nature Photonics **9**(12), 789–795 (2015).

[18] L. Yue, O. V. Minin, Z. Wang, J. N. Monks, A. S. Shalin, I. V. Minin, Photonic hook: a new curved light beam, Optics letters **43**(4), 771–774 (2018).

[19] J. Arlt, M. J. Padgett, Generation of a beam with a dark focus surrounded by regions of higher intensity: the optical bottle beam, Optics letters **25**(4), 191–193 (2000).

[20] J. Wang, W. Chen, Q. Zhan, Engineering of high purity ultra-long optical needle field through reversing the electric dipole array radiation, Optics express **18**(21), 21965–21972 (2010).

[21] G. Kontenis, D. Gailevičius, N. Jiménez, K. Staliūnas, Optical drills by dynamic high-order Bessel beam mixing, Physical Review Applied **17**(3), 034059 (2022).

[22] S. Orlov, V. Vosylius, P. Gotovski, A. Grabusovas, J. Baltrukonis, T. Gertus, Vector beams with parabolic and elliptic cross-sections for laser material processing applications, Journal of Laser Micro Nanoengineering **13**(3), 280–286 (2018).

[23] G. Vicidomini, P. Bianchini, A. Diaspro, Sted super-resolved microscopy, Nature methods **15**(3), 173–182 (2018).

[24] V. Garcés-Chávez, D. McGloin, M. Padgett, W. Dultz, H. Schmitzer, K. Dholakia, Observation of the transfer of the local angular momentum density of a multiringed light beam to an optically trapped particle, Physical review letters **91**(9), 093602 (2003).

[25] J. Baumgartl, M. Mazilu, K. Dholakia, Optically mediated particle clearing using Airy wavepackets, Nature photonics **2**(11), 675–678 (2008).

[26] V. Niziev, A. Nesterov, Influence of beam polarization on laser cutting efficiency, Journal of Physics D: Applied Physics **32**(13), 1455 (1999).

[27] J. Durnin, J. Miceli Jr, J. H. Eberly, Diffraction-free beams, Physical review letters **58**(15), 1499 (1987).

[28] M. Lapointe, Review of non-diffracting Bessel beam experiments, Optics & Laser Technology **24**(6), 315–321 (1992), https://doi.org/https://doi.org/10.1016/0030-3992(92)90082-D.

[29] R. M. Herman, T. A. Wiggins, Production and uses of diffractionless beams, J. Opt. Soc. Am. A **8**(6), 932–942 (1991), https://doi.org/10.1364/JOSAA.8.000932.

[30] J. Arlt, K. Dholakia, Generation of high-order Bessel beams by use of an axicon, Optics Communications **177**(1), 297–301 (2000), https://doi.org/https://doi.org/10.1016/S0030-4018(00)00572-1.

[31] S. Chávez-Cerda, J. C. Gutiérrez-Vega, G. H. C. New, Elliptic vortices of electromagnetic wave fields, Opt. Lett. **26**(22), 1803–1805 (2001), https://doi.org/10.1364/OL.26.001803.

[32] J. Gutiérrez-Vega, M. Iturbe-Castillo, G. Ramırez, E. Tepichın, R. Rodrıguez-Dagnino, S. Chávez-Cerda, G. New, Experimental demonstration of optical Mathieu beams, Optics Communications **195**(1), 35–40 (2001), https://doi.org/https://doi.org/10.1016/S0030-4018(01)01319-0.

[33] R. J. Hernández-Hernández, R. A. Terborg, I. Ricardez-Vargas, K. Volke-Sepúlveda, Experimental generation of Mathieu–Gauss beams with a phase-only spatial light modulator, Appl. Opt. **49**(36), 6903–6909 (2010), https://doi.org/10.1364/AO.49.006903.

[34] M. A. Bandres, J. C. Gutiérrez-Vega, S. Chávez-Cerda, Parabolic nondiffracting optical wave fields, Opt. Lett. **29**(1), 44–46 (2004), https://doi.org/10.1364/OL.29.000044.

[35] J. C. Gutiérrez-Vega, M. A. Bandres, Helmholtz–Gauss waves, J. Opt. Soc. Am. A **22**(2), 289–298 (2005), https://doi.org/10.1364/JOSAA.22.000289.

[36] M. V. Berry, N. L. Balazs, Nonspreading wave packets, American Journal of Physics **47**(3), 264–267 (1979), https://doi.org/10.1119/1.11855.

[37] G. A. Siviloglou, D. N. Christodoulides, Accelerating finite energy Airy beams, Optics letters **32**(8), 979–981 (2007).

[38] G. A. Siviloglou, J. Broky, A. Dogariu, D. N. Christodoulides, Observation of accelerating Airy beams, Phys. Rev. Lett. **99**, 213901 (2007), https://doi.org/10.1103/PhysRevLett.99.213901.

[39] G. Indebetouw, Nondiffracting optical fields: some remarks on their analysis and synthesis, J. Opt. Soc. Am. A **6**(1), 150–152 (1989), https://doi.org/10.1364/JOSAA.6.000150.

[40] R. Piestun, J. Shamir, Generalized propagation-invariant wave fields, JOSA A **15**(12), 3039–3044 (1998).

[41] K. F. Riley, M. P. Hobson, S. J. Bence, *Special functions* (Cambridge University Press, 2006), 602–614, 3 edition.

[42] P. L. Overfelt, Scalar optical beams with helical symmetry, Phys. Rev. A **46**, 3516–3522 (1992), https://doi.org/10.1103/PhysRevA.46.3516.

[43] S. M. Barnett, L. Allen, Orbital angular momentum and nonparaxial light beams, Optics communications **110**(5-6), 670–678 (1994).

[44] K. Volke-Sepulveda, V. Garcés-Chávez, S. Chávez-Cerda, J. Arlt, K. Dholakia, Orbital angular momentum of a high-order Bessel light beam, Journal of Optics B: Quantum and Semiclassical Optics **4**(2), S82 (2002).

[45] A. Matijošius, A. Piskarskas, V. Smilgevièius, A. Stabinis, Second harmonic generation of Bessel vortex, in *Conference on Lasers and Electro-Optics Europe* (Optica Publishing Group, 2000), CMG2.

[46] P. Sprangle, B. Hafizi, Comment on nondiffracting beams, Physical review letters **66**(6), 837 (1991).

[47] F. Bloisi, L. Vicari, Comparison of nondiffracting laser beams, Optics communications **75**(5-6), 353–357 (1990).

[48] D. McGloin, K. Dholakia, Bessel beams: diffraction in a new light, Contemporary physics **46**(1), 15–28 (2005).

[49] Z. Bouchal, Resistance of nondiffracting vortex beam against amplitude and phase perturbations, Optics communications **210**(3-6), 155–164 (2002).

[50] N. E. Andreev, S. S. Bychkov, V. V. Kotlyar, L. Y. Margolin, L. N. Pyatnitskii, P. Serafimovich, Formation of high-power hollow Bessel light beams, Quantum Electronics **26**(2), 126 (1996).

[51] V. Jarutis, R. Paškauskas, A. Stabinis, Focusing of Laguerre–Gaussian beams by axicon, Optics communications **184**(1-4), 105–112 (2000).

[52] J. A. Davis, E. Carcole, D. M. Cottrell, Nondiffracting interference patterns generated with programmable spatial light modulators, Applied optics **35**(4), 599–602 (1996).

[53] D. McGloin, V. Garcés-Chávez, K. Dholakia, Interfering Bessel beams for optical micromanipulation, Optics letters **28**(8), 657–659 (2003).

[54] S. Orlov, K. Regelskis, V. Smilgevičius, A. Stabinis, Propagation of Bessel beams carrying optical vortices, Optics communications **209**(1-3), 155–165 (2002).

[55] S. Orlov, A. Stabinis, Propagation of superpositions of coaxial optical Bessel beams carrying vortices, Journal of Optics A: Pure and Applied Optics **6**(5), S259 (2004).

[56] S. Orlov, A. Stabinis, Free-space propagation of light field created by Bessel–Gauss and Laguerre–Gauss singular beams, Optics communications **226**(1-6), 97–105 (2003).

[57] A. A. Voitiv, J. M. Andersen, M. E. Siemens, M. T. Lusk, Optical vortex braiding with Bessel beams, Optics Letters **45**(6), 1321–1324 (2020).

[58] J. Leach, M. R. Dennis, J. Courtial, M. J. Padgett, Knotted threads of darkness, Nature **432**(7014), 165–165 (2004).

[59] M. R. Dennis, R. P. King, B. Jack, K. O'holleran, M. J. Padgett, Isolated optical vortex knots, Nature Physics **6**(2), 118–121 (2010).

[60] D. Sugic, M. R. Dennis, Singular knot bundle in light, JOSA A **35**(12), 1987–1999 (2018).

[61] B. Bode, M. R. Dennis, D. Foster, R. P. King, Knotted fields and explicit fibrations for lemniscate knots, Proceedings of the Royal Society A: Mathematical, Physical and Engineering Sciences **473**(2202), 20160829 (2017).

[62] R. Vasilyeu, A. Dudley, N. Khilo, A. Forbes, Generating superpositions of higher–order Bessel beams, Optics express **17**(26), 23389–23395 (2009).

[63] R. Rop, A. Dudley, C. López-Mariscal, A. Forbes, Measuring the rotation rates of superpositions of higher-order Bessel beams, Journal of Modern Optics **59**(3), 259–267 (2012).

[64] Y. Shen, X. Wang, Z. Xie, C. Min, X. Fu, Q. Liu, M. Gong, X. Yuan, Optical vortices 30 years on: OAM manipulation from topological charge to multiple singularities, Light: Science & Applications **8**(1), 90 (2019).

[65] F. O. Fahrbach, V. Gurchenkov, K. Alessandri, P. Nassoy, A. Rohrbach, Light-sheet microscopy in thick media using scanned Bessel beams and two-photon fluorescence excitation, Optics express **21**(11), 13824–13839 (2013).

[66] O. E. Olarte, J. Licea-Rodriguez, J. A. Palero, E. J. Gualda, D. Artigas, J. Mayer, J. Swoger, J. Sharpe, I. Rocha-Mendoza, R. Rangel-Rojo, et al., Image formation by linear and nonlinear digital scanned light-sheet fluorescence microscopy with Gaussian and Bessel beam profiles, Biomedical optics express **3**(7), 1492–1505 (2012).

[67] H. Jia, X. Yu, Y. Yang, X. Zhou, S. Yan, C. Liu, M. Lei, B. Yao, Axial resolution enhancement of light-sheet microscopy by double scanning of Bessel beam and its complementary beam, Journal of biophotonics **12**(1), e201800094 (2019).

[68] L. Minkevičius, D. Jokubauskis, I. Kašalynas, S. Orlov, A. Urbas, G. Valušis, Bessel terahertz imaging with enhanced contrast realized by silicon multi-phase diffractive optics, Optics express **27**(25), 36358–36367 (2019).

[69] R. Ivaškevičiūtė-Povilauskienė, P. Kizevičius, E. Nacius, D. Jokubauskis, K. Ikamas, A. Lisauskas, N. Alexeeva, I. Matulaitienė, V. Jukna, S. Orlov, et al., Terahertz structured light: nonparaxial Airy imaging using silicon diffractive optics, Light: science & applications **11**(1), 326 (2022).

[70] Y. A. Ayala, A. V. Arzola, K. Volke-Sepúlveda, Comparative study of optical levitation traps: focused Bessel beam versus Gaussian beams, JOSA B **33**(6), 1060–1067 (2016).

[71] A. S. Desyatnikov, V. G. Shvedov, A. V. Rode, W. Krolikowski, Y. S. Kivshar, Photophoretic manipulation of absorbing aerosol particles with vortex beams: theory versus experiment, Optics Express **17**(10), 8201–8211 (2009).

[72] F. Courvoisier, Nonstandard light for ultrafast laser microstructuring and nanostructuring, Ultrafast Laser Nanostructuring: The Pursuit of Extreme Scales 581–621 (2023).

[73] A. Couairon, A. Mysyrowicz, Femtosecond filamentation in transparent media, Physics reports **441**(2-4), 47–189 (2007).

[74] P. Polesana, M. Franco, A. Couairon, D. Faccio, P. Di Trapani, Filamentation in kerr media from pulsed Bessel beams, Phys. Rev. A **77**, 043814 (2008), https://doi.org/10.1103/PhysRevA.77.043814.

[75] D. Roskey, M. Kolesik, J. Moloney, E. Wright, Self-action and regularized self-guiding of pulsed Bessel-like beams in air, Optics express **15**(16), 9893–9907 (2007).

[76] E. Gaizauskas, E. Vanagas, V. Jarutis, S. Juodkazis, V. Mizeikis, H. Misawa, Discrete damage traces from filamentation of Gauss-Bessel pulses, Optics letters **31**(1), 80–82 (2006).

[77] P. Polesana, A. Couairon, D. Faccio, A. Parola, M. Porras, A. Dubietis, A. Piskarskas, P. Di Trapani, Observation of conical waves in focusing, dispersive, and dissipative kerr media, Physical review letters **99**(22), 223902 (2007).

[78] R. Stoian, M. K. Bhuyan, A. Rudenko, J.-P. Colombier, G. Cheng, High-resolution material structuring using ultrafast laser nondiffractive beams, Advances in Physics: X **4**(1), 1659180 (2019).

[79] A. Marcinkevičius, S. Juodkazis, S. Matsuo, V. Mizeikis, H. Misawa, Application of Bessel beams for microfabrication of dielectrics by femtosecond laser, Japanese Journal of Applied Physics **40**(11A), L1197 (2001).

[80] P. K. Velpula, M. Bhuyan, F. Courvoisier, H. Zhang, J.-P. Colombier, R. Stoian, Spatio-temporal dynamics in nondiffractive Bessel ultrafast laser nanoscale volume structuring, Laser & Photonics Reviews **10**(2), 230–244 (2016).

[81] M. Mikutis, T. Kudrius, G. Šlekys, D. Paipulas, S. Juodkazis, High 90% efficiency Bragg gratings formed in fused silica by femtosecond Gauss-Bessel laser beams, Optical Materials Express **3**(11), 1862–1871 (2013).

[82] D. Paipulas, M. Mikutis, V. Sirutkaitis, S. Juodkazis, Volumetric modifications in fused silica using Gaussian and Bessel femtosecond laser beams, in *Pacific Rim Laser Damage 2013: Optical Materials for High Power Lasers* (SPIE, 2013), volume 8786, 66–73.

[83] D. Gailevičius, V. Purlys, K. Staliūnas, Photonic crystal spatial filters fabricated by femtosecond pulsed Bessel beam, Optics letters **44**(20), 4969–4972 (2019).

[84] M. Bhuyan, F. Courvoisier, P. Lacourt, M. Jacquot, R. Salut, L. Furfaro, J. Dudley, High aspect ratio nanochannel machining using single shot femtosecond Bessel beams, Applied Physics Letters **97**(8) (2010).

[85] M. K. Bhuyan, P. K. Velpula, M. Somayaji, J.-P. Colombier, R. Stoian, 3D nano-fabrication using controlled Bessel-glass interaction in ultra-fast modes, Journal of Laser Micro Nanoengineering **12**(3), 274–280 (2017).

[86] M. Bhuyan, P. K. Velpula, J.-P. Colombier, T. Olivier, N. Faure, R. Stoian, Single-shot high aspect ratio bulk nanostructuring of fused silica using chirp-controlled ultrafast laser Bessel beams, Applied Physics Letters **104**(2) (2014).

[87] T. Chen, G. Zhang, Y. Wang, X. Li, R. Stoian, G. Cheng, Reconstructing of embedded high-aspect-ratio nano-voids generated by ultrafast laser Bessel beams, Micromachines **11**(7), 671 (2020).

[88] L. Rapp, R. Meyer, R. Giust, L. Furfaro, M. Jacquot, P.-A. Lacourt, J. M. Dudley, F. Courvoisier, High aspect ratio microexplosions in the bulk of sapphire generated by femtosecond Bessel beams, Scientific Reports **6**(1), 34286 (2016).

[89] C. Vetter, R. Giust, L. Furfaro, C. Billet, L. Froehly, F. Courvoisier, High aspect ratio structuring of glass with ultrafast Bessel beams, Materials **14**(22), 6749 (2021).

[90] G. Zhang, R. Stoian, R. Lou, T. Chen, G. Li, X. Wang, Y. Pan, P. Wu, J. Wang, G. Cheng, Thermal and mechanical limitations to processing resolution in volume non-diffractive ultrafast laser structuring, Applied Surface Science **570**, 151170 (2021).

[91] R. Beuton, B. Chimier, J. Breil, D. Hébert, P.-H. Maire, G. Duchateau, Thermo-elasto-plastic simulations of femtosecond laser-induced structural modifications: Application to cavity formation in fused silica, Journal of Applied Physics **122**(20) (2017).

[92] W.-J. Tsai, C.-J. Gu, C.-W. Cheng, J.-B. Horng, Internal modification for cutting transparent glass using femtosecond Bessel beams, Optical Engineering **53**(5), 051503–051503 (2014).

[93] M. Bhuyan, O. Jedrkiewicz, V. Sabonis, M. Mikutis, S. Recchia, A. Aprea, M. Bollani, P. D. Trapani, High-speed laser-assisted cutting of strong transparent materials using picosecond Bessel beams, Applied Physics A **120**, 443–446 (2015).

[94] B. Chebbi, S. Minko, N. Al-Akwaa, I. Golub, Remote control of extended depth of field focusing, Optics communications **283**(9), 1678–1683 (2010).

[95] K. Bergner, M. Müller, R. Klas, J. Limpert, S. Nolte, A. Tünnerman, Scaling ultrashort laser pulse induced glass modifications for cleaving applications, Applied optics **57**(21), 5941–5947 (2018).

[96] R. Meyer, L. Froehly, R. Giust, J. Del Hoyo, L. Furfaro, C. Billet, F. Courvoisier, Extremely high-aspect-ratio ultrafast Bessel beam generation and stealth dicing of multi-millimeter thick glass, Applied Physics Letters **114**(20) (2019).

[97] A. Feuer, J.-U. Thomas, C. Freitag, R. Weber, T. Graf, Single-pass laser separation of 8 mm thick glass with a millijoule picosecond pulsed Gaussian–Bessel beam, Applied Physics A **125**(5), 332 (2019).

[98] F. Werr, A. Veber, M. Brehl, M. Bergler, D. Werner, U. Eppelt, L. Müllers, D. de Ligny, Surface probing of ultra-short-pulse laser filament cut window glass and the impact on the separation behavior, Advanced Engineering Materials **22**(9), 2000471 (2020).

[99] C. Ungaro, N. Kaliteevskiy, P. Sterlingov, V. V. Ivanov, A. B. Ruffin, R. J. Terbrueggen, N. Savidis, Using phase-corrected Bessel beams to cut glass substrates with a chamfered edge, Applied Optics **60**(3), 714–719 (2021).

[100] K. Liao, W. Wang, X. Mei, B. Liu, High quality full ablation cutting and stealth dicing of silica glass using picosecond laser Bessel beam with burst mode, Ceramics International **48**(7), 9805–9816 (2022).

[101] J. Dudutis, P. Gečys, G. Račiukaitis, Non-ideal axicon-generated Bessel beam application for intra-volume glass modification, Optics express **24**(25), 28433–28443 (2016).

[102] J. Dudutis, R. Stonys, G. Račiukaitis, P. Gečys, Aberration-controlled Bessel beam processing of glass, Optics express **26**(3), 3627–3637 (2018).

[103] J. Dudutis, R. Stonys, G. Račiukaitis, P. Gečys, Glass dicing with elliptical Bessel beam, Optics & Laser Technology **111**, 331–337 (2019).

[104] R. Meyer, M. Jacquot, R. Giust, J. Safioui, L. Rapp, L. Furfaro, P.-A. Lacourt, J. M. Dudley, F. Courvoisier, Single-shot ultrafast laser processing of high-aspect-ratio nanochannels using elliptical Bessel beams, Optics letters **42**(21), 4307–4310 (2017).

[105] M. Jenne, D. Flamm, K. Chen, M. Schäfer, M. Kumkar, S. Nolte, Facilitated glass separation by asymmetric Bessel-like beams, Optics express **28**(5), 6552–6564 (2020).

[106] J. Dudutis, M. Mackevičiūtė, J. Pipiras, R. Stonys, V. Stankevič, G. Račiukaitis, P. Gečys, Transversal and axial modulation of axicon-generated Bessel beams using amplitude and phase masks for glass processing applications, Optics Express **30**(2), 1860–1874 (2022).

[107] E. Nacius, P. Gotovski, O. Ulčinas, S. Orlov, A. Urbas, V. Jukna, Spatially displaced and superposed Bessel beams for transparent material laser microprocessing, JOSA B **38**(12), 3886–3895 (2021).

[108] R. Meyer, R. Giust, M. Jacquot, J. M. Dudley, F. Courvoisier, Submicron-quality cleaving of glass with elliptical ultrafast Bessel beams, Applied Physics Letters **111**(23) (2017).

[109] M. Jenne, D. Flamm, T. Ouaj, J. Hellstern, J. Kleiner, D. Grossmann, M. Koschig, M. Kaiser, M. Kumkar, S. Nolte, High-quality tailored-edge cleaving using aberration-corrected Bessel-like beams, Optics letters **43**(13), 3164–3167 (2018).

[110] J. Dudutis, J. Pipiras, R. Stonys, E. Daknys, A. Kilikevičius, A. Kasparaitis, G. Račiukaitis, P. Gečys, In-depth comparison of conventional glass cutting technologies with laser-based methods by volumetric scribing using Bessel beam and rear-side machining, Optics Express **28**(21), 32133–32151 (2020).

[111] M. Manousidaki, D. G. Papazoglou, M. Farsari, S. Tzortzakis, Long-scale multiphoton polymerization voxel growth investigation using engineered Bessel beams, Optical Materials Express **9**(7), 2838–2845 (2019).

[112] L. Yang, A. El-Tamer, U. Hinze, J. Li, Y. Hu, W. Huang, J. Chu, B. N. Chichkov, Two-photon polymerization of cylinder microstructures by femtosecond Bessel beams, Applied Physics Letters **105**(4) (2014).

[113] L. Yang, D. Qian, C. Xin, Z. Hu, S. Ji, D. Wu, Y. Hu, J. Li, W. Huang, J. Chu, Two-photon polymerization of microstructures by a non-diffraction multifoci pattern generated from a superposed Bessel beam, Optics letters **42**(4), 743–746 (2017).

[114] L. Yang, D. Qian, C. Xin, Z. Hu, S. Ji, D. Wu, Y. Hu, J. Li, W. Huang, J. Chu, Direct laser writing of complex microtubes using femtosecond vortex beams, Applied Physics Letters **110**(22) (2017).

[115] H. Cheng, P. Golvari, C. Xia, M. Sun, M. Zhang, S. M. Kuebler, X. Yu, High-throughput microfabrication of axially tunable helices, Photonics Research **10**(2), 303–315 (2022).

[116] A. P. Joglekar, H.-h. Liu, E. Meyhöfer, G. Mourou, A. J. Hunt, Optics at critical intensity: Applications to nanomorphing, Proceedings of the National Academy of Sciences **101**(16), 5856–5861 (2004).

[117] X. Tsampoula, V. Garces-Chavez, M. Comrie, D. Stevenson, B. Agate, C. Brown, F. Gunn-Moore, K. Dholakia, Femtosecond cellular transfection using a nondiffracting light beam, Applied Physics Letters **91**(5) (2007).

[118] D. H. Doan, R. Iida, B. Kim, I. Satoh, K. Fushinobu, Bessel beam laser-scribing of thin film silicon solar cells by ns pulsed laser, Journal of Thermal Science and Technology **11**(1), JTST0011–JTST0011 (2016).

[119] B. Wetzel, C. Xie, P.-A. Lacourt, J. M. Dudley, F. Courvoisier, Femtosecond laser fabrication of micro and nano-disks in single layer graphene using vortex Bessel beams, Applied Physics Letters **103**(24) (2013).

[120] X. Li, Z. Xu, L. Jiang, Y. Shi, A. Wang, L. Huang, Q. Wei, Creating a three-dimensional surface with antireflective properties by

using femtosecond-laser Bessel-beam-assisted thermal oxidation, Optics Letters **45**(11), 2989–2992 (2020).

[121] I. Ouadghiri-Idrissi, J. M. Dudley, F. Courvoisier, Controlling nonlinear instabilities in Bessel beams through longitudinal intensity shaping, Optics Letters **42**(19), 3785–3788 (2017).

[122] Z. Jaroszewicz, J. Sochacki, A. Kołodziejczyk, L. R. Staronski, Apodized annular-aperture logarithmic axicon: smoothness and uniformity of intensity distributions, Optics letters **18**(22), 1893–1895 (1993).

[123] I. Golub, B. Chebbi, D. Shaw, D. Nowacki, Characterization of a refractive logarithmic axicon, Optics letters **35**(16), 2828–2830 (2010).

[124] T. Čižmár, K. Dholakia, Tunable Bessel light modes: engineering the axial propagation, Optics express **17**(18), 15558–15570 (2009).

[125] S. Orlov, A. Juršėnas, E. Nacius, Optical Bessel-like beams with engineered axial phase and intensity distribution, Journal of Laser Micro Nanoengineering **13**(3), 244–248 (2018).

[126] S. Orlov, A. Juršėnas, J. Baltrukonis, V. Jukna, Controllable spatial array of Bessel-like beams with independent axial intensity distributions for laser microprocessing, Journal of Laser Micro Nanoengineering **13**(3), 324–329 (2018).

[127] R. Dharmavarapu, S. Bhattacharya, S. Juodkazis, Diffractive optics for axial intensity shaping of Bessel beams, Journal of Optics **20**(8), 085606 (2018).

[128] J. Berškys, S. Orlov, Accelerating Airy beams with particle-like polarization topologies and free-space bimeronic lattices, Optics Letters **48**(5), 1168–1171 (2023).

[129] B.-Y. Wei, P. Chen, W. Hu, W. Ji, L.-Y. Zheng, S.-J. Ge, Y. Ming, V. Chigrinov, Y.-Q. Lu, Polarization-controllable Airy beams generated via a photoaligned director-variant liquid crystal mask, Scientific reports **5**(1), 17484 (2015).

[130] G. Siviloglou, J. Broky, A. Dogariu, D. Christodoulides, Ballistic dynamics of Airy beams, Optics Letters **33**(3), 207–209 (2008).

[131] J. Broky, G. A. Siviloglou, A. Dogariu, D. N. Christodoulides, Self-healing properties of optical Airy beams, Optics express **16**(17), 12880–12891 (2008).

[132] J. Wang, J. Bu, M. Wang, Y. Yang, X. Yuan, Generation of high quality Airy beams with blazed micro-optical cubic phase plates, Applied optics **50**(36), 6627–6631 (2011).

[133] B. Yalizay, B. Soylu, S. Akturk, Optical element for generation of accelerating Airy beams, JOSA A **27**(10), 2344–2346 (2010).

[134] H. Dai, Y. Liu, D. Luo, X. Sun, Propagation dynamics of an optical vortex imposed on an Airy beam, Optics letters **35**(23), 4075–4077 (2010).

[135] H. Dai, Y. Liu, D. Luo, X. Sun, Propagation properties of an optical vortex carried by an Airy beam: experimental implementation, Optics letters **36**(9), 1617–1619 (2011).

[136] C. Chen, X. Peng, B. Chen, Y. Peng, M. Zhou, X. Yang, D. Deng, Propagation of an Airy–Gaussian vortex beam in linear and nonlinear media, Journal of Optics **18**(5), 055505 (2016).

[137] P. Polynkin, M. Kolesik, J. V. Moloney, G. A. Siviloglou, D. N. Christodoulides, Curved plasma channel generation using ultraintense Airy beams, Science **324**(5924), 229–232 (2009).

[138] P. Polynkin, M. Kolesik, J. Moloney, Filamentation of femtosecond laser Airy beams in water, Physical review letters **103**(12), 123902 (2009).

[139] S. Jia, J. C. Vaughan, X. Zhuang, Isotropic three-dimensional super-resolution imaging with a self-bending point spread function, Nature photonics **8**(4), 302–306 (2014).

[140] N. K. Efremidis, Z. Chen, M. Segev, D. N. Christodoulides, Airy beams and accelerating waves: an overview of recent advances, Optica **6**(5), 686–701 (2019).

[141] T. Vettenburg, H. I. Dalgarno, J. Nylk, C. Coll-Lladó, D. E. Ferrier, T. Čižmár, F. J. Gunn-Moore, K. Dholakia, Light-sheet microscopy using an Airy beam, Nature methods **11**(5), 541–544 (2014).

[142] A. Mathis, F. Courvoisier, L. Froehly, L. Furfaro, M. Jacquot, P.-A. Lacourt, J. M. Dudley, Micromachining along a curve: Femtosecond laser micromachining of curved profiles in diamond and silicon using accelerating beams, Applied Physics Letters **101**(7) (2012).

[143] A. Mathis, L. Froehly, L. Furfaro, M. Jacquot, J. M. Dudley, F. Courvoisier, Direct machining of curved trenches in silicon with femtosecond accelerating beams, Journal of the European Optical Society-Rapid publications **8** (2013).

[144] L. Froehly, F. Courvoisier, A. Mathis, M. Jacquot, L. Furfaro, R. Giust, P. Lacourt, J. Dudley, Arbitrary accelerating micron-scale caustic beams in two and three dimensions, Optics express **19**(17), 16455–16465 (2011).

[145] D. Sohr, J. U. Thomas, S. Skupin, Shaping convex edges in borosilicate glass by single pass perforation with an Airy beam, Optics letters **46**(10), 2529–2532 (2021).

[146] P. Boucher, J. Del Hoyo, C. Billet, O. Pinel, G. Labroille, F. Courvoisier, Generation of high conical angle Bessel–Gauss beams with reflective axicons, Applied optics **57**(23), 6725–6728 (2018).

[147] O. Brzobohatỳ, T. Čižmár, P. Zemánek, High quality quasi-Bessel beam generated by round-tip axicon, Optics express **16**(17), 12688–12700 (2008).

[148] C. Rosales-Guzmán, A. Forbes, How to shape light with spatial light modulators (Society of Photo-Optical Instrumentation Engineers (SPIE), 2017).

[149] V. Arrizón, Optimum on-axis computer-generated hologram encoded into low-resolution phase-modulation devices, Optics letters **28**(24), 2521–2523 (2003).

[150] A. Dudley, R. Vasilyeu, V. Belyi, N. Khilo, P. Ropot, A. Forbes, Controlling the evolution of nondiffracting speckle by complex amplitude modulation on a phase-only spatial light modulator, Optics Communications **285**(1), 5–12 (2012).

[151] W.-H. Lee, III computer-generated holograms: Techniques and applications, in *Progress in optics* (Elsevier, 1978), volume 16, 119–232.

[152] Z. Zhang, A. M. Jeziorska-Chapman, N. Collings, M. Pivnenko, J. Moore, B. Crossland, D. P. Chu, B. Milne, High quality assembly of phase-only liquid crystal on silicon (LCOS) devices, Journal of Display Technology **7**(3), 120–126 (2010).

[153] S.-T. Wu, U. Efron, L. D. Hess, Birefringence measurements of liquid crystals, Applied optics **23**(21), 3911–3915 (1984).

[154] P. Kohns, J. Schirmer, A. A. Muravski, S. Y. Yakovenko, V. Bezborodov, R. Dãbrowski, Birefringence measurements of liquid crystals and an application: An achromatic waveplate, Liquid crystals **21**(6), 841–846 (1996).

[155] P. Dasgupta, M. K. Das, B. Das, Physical properties of three liquid crystals with negative dielectric anisotropy from x-ray diffraction and optical birefringence measurements, Molecular Crystals and Liquid Crystals **540**(1), 154–161 (2011).

[156] N. A. Clark, S. T. Lagerwall, Submicrosecond bistable electro-optic switching in liquid crystals, Applied Physics Letters **36**(11), 899–901 (1980).

[157] M. O'Callaghan, M. Handschy, Diffractive ferroelectric liquid-crystal shutters for unpolarized light, Optics letters **16**(10), 770–772 (1991).

[158] S. Panezai, D. Wang, J. Zhao, Y. Wang, L. Rong, S. Ma, Study of oblique incidence characterization of parallel aligned liquid crystal on silicon, Optical Engineering **54**(3), 037109–037109 (2015).

[159] J. Beeckman, K. Neyts, P. J. Vanbrabant, Liquid-crystal photonic applications, Optical Engineering **50**(8), 081202–081202 (2011).

[160] S. Reichelt, Spatially resolved phase-response calibration of liquid-crystal-based spatial light modulators, Applied optics **52**(12), 2610–2618 (2013).

[161] S. Ngcobo, I. Litvin, L. Burger, A. Forbes, A digital laser for on-demand laser modes, Nature communications **4**(1), 2289 (2013).

[162] A. Hussain, J. Martínez, J. Campos, Holographic superresolution using spatial light modulator, Journal of the European Optical Society-Rapid publications **8** (2013).

[163] Z. Kuang, W. Perrie, S. P. Edwardson, E. Fearon, G. Dearden, Ultrafast laser parallel microdrilling using multiple annular beams generated by a spatial light modulator, Journal of Physics D: Applied Physics **47**(11), 115501 (2014).

[164] G. Deschamps, P. Mast, Poincaré sphere representation of partially polarized fields, IEEE Transactions on Antennas and Propagation **21**(4), 474–478 (1973).

[165] S. Pancharatnam, Generalized theory of interference, and its applications: Part I. coherent pencils, in *Proceedings of the Indian*

Academy of Sciences-Section A (Springer, 1956), volume 44, 247–262.

[166] M. V. Berry, Quantal phase factors accompanying adiabatic changes, Proceedings of the Royal Society of London. A. Mathematical and Physical Sciences **392**(1802), 45–57 (1984).

[167] Z. Bomzon, G. Biener, V. Kleiner, E. Hasman, Space-variant Pancharatnam–Berry phase optical elements with computer-generated subwavelength gratings, Optics letters **27**(13), 1141–1143 (2002).

[168] P. Kurzynowski, W. A. Woźniak, M. Szarycz, Geometric phase: two triangles on the Poincaré sphere, JOSA A **28**(3), 475–482 (2011).

[169] R. C. Jones, A new calculus for the treatment of optical systems I. description and discussion of the calculus, JOSA **31**(7), 488–493 (1941).

[170] M. Beresna, M. Gecevičius, P. G. Kazansky, Polarization sensitive elements fabricated by femtosecond laser nanostructuring of glass, Optical Materials Express **1**(4), 783–795 (2011).

[171] J. J. Gil, E. Bernabeu, Obtainment of the polarizing and retardation parameters of a non-depolarizing optical system from the polar decomposition of its mueller matrix, Optik (Stuttgart) **76**(2), 67–71 (1986).

[172] Z. Bomzon, G. Biener, V. Kleiner, E. Hasman, Radially and azimuthally polarized beams generated by space-variant dielectric subwavelength gratings, Optics letters **27**(5), 285–287 (2002).

[173] G. Biener, A. Niv, V. Kleiner, E. Hasman, Formation of helical beams by use of Pancharatnam–Berry phase optical elements, Optics letters **27**(21), 1875–1877 (2002).

[174] H.-T. Chen, A. J. Taylor, N. Yu, A review of metasurfaces: physics and applications, Reports on progress in physics **79**(7), 076401 (2016).

[175] W. Yang, E. Bricchi, P. G. Kazansky, J. Bovatsek, A. Y. Arai, Self-assembled periodic sub-wavelength structures by femtosecond laser direct writing, Optics Express **14**(21), 10117–10124 (2006).

[176] R. Drevinskas, P. G. Kazansky, High-performance geometric phase elements in silica glass, APL Photonics **2**(6) (2017).

[177] Y. Matsuoka, Y. Kizuka, T. Inoue, The characteristics of laser micro drilling using a Bessel beam, Applied Physics A **84**, 423–430 (2006).

[178] P. Balage, T. Guilberteau, M. Lafargue, G. Bonamis, C. Hönninger, J. Lopez, I. Manek-Hönninger, Bessel beam dielectrics cutting with femtosecond laser in GHz-burst mode, Micromachines **14**(9), 1650 (2023).

CURRICULUM VITAE

Name: Paulius

Surname: Šlevas

Date of birth: 1994-03-02

Place of birth: Kaunas, Lithuania

E-mail: paulius.slevas@gmail.com

Education:

2019 – 2023	Center for Physical Sciences and Technology *Ph.D. studies.*
2017 – 2019	Vilnius University, Faculty of Physics *Master's degree in Technological Science.*
2013 – 2017	Vilnius University, Faculty of Physics *Bachelor's degree in Physics.*
2009 – 2013	KTU Gymnasium.

Work experience:

2023-04 – now	Center for Physical Sciences and Technology, *Junior researcher.*
2020-01 – 2021-12	Center for Physical Sciences and Technology, *Junior researcher.*
2019-01 – 2019-12	Center for Physical Sciences and Technology, *Engineer.*
2017-02 – now	Workshop of Photonics, *Researcher.*

APIE AUTORIŲ

Vardas: Paulius

Pavardė: Šlevas

Gimimo data: 1994-03-02

Gimimo vieta: Kaunas, Lietuva

Išsilavinimas:

2019 – 2023 Fizinių ir technologijos mokslų centras

Doktorantūros studijos.

2017 – 2019 Vilniaus Universitetas, Fizikos fakultetas

Technologijos mokslų magistro kvalifikacinis laipsnis.

2013 – 2017 Vilniaus Universitetas, Fizikos fakultetas

Fizikos bakalauro kvalifikacinis laipsnis.

2009 – 2013 KTU Gimnazija.

Profesinė veikla:

2023-04 – dabar Fizinių ir technologijos mokslų centras,

Jaunesnysis mokslo darbuotojas.

2020-01 – 2021-12 Fizinių ir technologijos mokslų centras,

Jaunesnysis mokslo darbuotojas.

2019-01 – 2019-12 Fizinių ir technologijos mokslų centras,

Inžinierius.

2017-02 – dabar Workshop of Photonics,

Tyrėjas.

COPIES OF PUBLICATIONS

P1

Azimuthally modulated axicon vortical beams for laser microprocessing

P. Šlevas, S. Orlov, E. Nacius, O. Ulčinas

Optics Communications 505, 127509 (2021)
DOI: 10.1016/j.optcom.2021.127509
https://www.sciencedirect.com/science/article/abs/pii/S0030401821007586?via%3Dihub

Optics Communications 505 (2022) 127509

Contents lists available at ScienceDirect

Optics Communications

journal homepage: www.elsevier.com/locate/optcom

Azimuthally modulated axicon vortical beams for laser microprocessing

Paulius Šlevas [a,b,*], Sergej Orlov [a], Ernestas Nacius [a,b], Orestas Ulčinas [a,b]

[a] Center for Physical Sciences and Technology, Sauletekio Ave. 3, Vilnius, Lithuania
[b] Workshop of Photonics, Mokslininku st. 6A, Vilnius, Lithuania

ARTICLE INFO

Keywords:
Optical vortex
Bessel beam
Non-diffracting beam
Geometrical phase
Laser microprocessing

ABSTRACT

Non-diffracting beams have contributed greatly to recent developments in high power applications such as laser micromachining. Well known for their elongated focal region (also known as a focal line) are zeroth-order Bessel and Bessel vortical beams which allow achieving high aspect ratio modifications inside transparent materials. A superposition of several optical Bessel vortices of different topological charges allows generating high aspect ratio beams with complexly engineered transverse intensity patterns. Non-diffracting Bessel vortices commonly are created using a conical prism — an axicon. Therefore, they can be referred to as axicon beams. In this work, we have studied the formation of high power and energy axicon vortical beams both numerically and experimentally. We have inscribed sub-wavelength birefringent structures inside fused silica glass to create geometrical phase elements for the azimuthal modulation of the spatial spectra of a zeroth-order axicon (Bessel) beam which allows creating a high power superposition of several Bessel vortices. To prove the concept, we apply azimuthally modulated axicon vortical beams to create modifications inside fused silica glass samples.

1. Introduction

Laser technology is a rapidly progressing research field developing new ideas to improve laser average output power, maximum pulse energy, shorten pulse duration, or enhance other parameters of this device [1]. Therefore, methods to utilize these improvements in practice are desirable. A conventional laser outputs a Gaussian beam which is versatile and perfect for most applications such as laser ablation [2], welding [3], waveguide inscription [4], polymerization [5] and more. However, because of a short Rayleigh length and simple transverse intensity distribution, Gaussian beam can limit speeds for some applications. For instance, in Bragg grating inscription Gaussian beam must be scanned for several layers to obtain a required length of a grating [6]. This requires precise alignment of the beam, so the consecutive layer would match the previous one.

The engineering of the focal spot has evolved since then to control the axial behavior of the laser beam. The so-called non-diffracting Bessel beams [7] exhibit a large ratio between the transverse and longitudinal widths of the focal spot [8]. They have stipulated ongoing research into a variety of non-diffracting beams — Mathieu [9], Weber [10], and Airy beams [11]. Bessel beams can be generated using a circular aperture [7] or a conical prism (axicon) [12]. Among others methods, diffractive holograms [13], spatial light modulators [14–16] and geometrical phase elements (GPEs) [17,18] are also used and in some cases they offer a better quality of a beam [19,20].

Bessel beams have an elongated focal region (focal line) located along the propagation direction, which is desirable in many high-power laser applications. For example, microchannel fabrication [21,22], a glass cutting [23] and a variety of other applications [24]. Generation of Bessel beams using an aperture is inefficient due to the high energy losses [25] and the axicon usually creates axial profiles with high pitch oscillations due to the imperfect tip [26]. A variety of approaches were used to improve the quality of the Bessel zone: the creation of optical needles [27], engineering of the focal line [28,29] etc.

Higher-order non-diffracting Bessel beams J_m have a helical wavefront, described by a topological charge m. They possess some fascinating qualities such as carrying orbital angular momentum [30] and are usually referred to as optical vortices [31,32], which find their applications nowadays everywhere [33]. A linear superposition of several Bessel vortices enables the creation of beams of high aspect ratio and elaborate transverse intensity distribution [34,35]. The nonlinear superposition of Bessel vortices produces an even richer structure [36]. They can be successfully applied in high-power applications [37].

Vortical non-diffracting Bessel beams can be represented as a superposition of plane waves with vectors lying on a cone [38,39]. An axicon is known as a conical prism [40], which converts beams with homogeneous spatial spectra into optical beams with a ring-like shaped spatial spectral distribution [12]. In practice, the main difference between individual Bessel beams and their linear superposition is the azimuthal modulation in the ring-shaped spectra.

In this work, we extend our previous findings [41] and present a method for generation of superimposed higher-order Bessel beams with

* Corresponding author at: Center for Physical Sciences and Technology, Sauletekio Ave. 3, Vilnius, Lithuania.
E-mail address: paulius.slevas@ftmc.lt (P. Šlevas).

https://doi.org/10.1016/j.optcom.2021.127509
Received 2 September 2021; Received in revised form 25 September 2021; Accepted 27 September 2021
Available online 2 October 2021

different topologies using geometrical phase elements (GPEs). We first form a Bessel beam using a diffractive axicon. We then modify the beam in its' spectral region using a GPE and create in such way superimposed Bessel vortical beams. In our experimentations we have used GPEs which were manufactured by Altechna R&D with the transmittance being higher than 90% in a broad spectral region [42]. Such elements routinely beam shape high energy pulses, because they can withstand 1.5 mJ energy, 158 fs FWHM duration pulses at 1030 nm [19,43] or even higher [42].

We check the agreement of our experimental results with numerical expectations. Lastly, we demonstrate the ability to use such beams in high power applications and create surface and volume modifications inside a fused silica sample.

2. Theoretical background

The main idea of the theoretical considerations is closely related to the problem studied in Ref. [34], where propagation of superposition of two Bessel vortices was analyzed

$$E(\rho,\varphi,z=0)=\left[a_1 J_m\left(k_\rho\rho\right)\mathrm{e}^{\mathrm{i}m\varphi}+a_2 J_n\left(k_\rho\rho\right)\mathrm{e}^{\mathrm{i}n\varphi}\right]\mathrm{e}^{-\frac{\rho^2}{d_0^2}}, \tag{1}$$

where $k_\rho = k\sin\alpha$ is the radial frequency of BG beam. α is the half-angle of the Bessel cone and d_0 is an aperture radius. Here, m and n are integer topological charges, a_1, a_2 are the amplitudes of the respective order Bessel beams. This field creates a rather rich vortical structure, which was in great detail analyzed in Ref. [34]. However, at that time it was not realized that this field has also a potentially interesting intensity distribution for laser applications. First of all, the azimuthal angles of vortex cores are determined by

$$\varphi_k=\frac{\pi k}{(m-n)},\ k=0,1,2,\ldots,2(m-n)-1. \tag{2}$$

Vortices are singular zero-intensity points where the phase is undetermined [12,34,35]. Because of their presence, the intensity distribution of the superposition has a distinct azimuthal modulation. Areas with dark vortex cores interchange with higher intensity bright spots and the number of dark and bright azimuthal areas is always $|m-n|$. A few examples are presented in Fig. 1. Here we fix the difference of topological charges m and n and plot intensity distributions of the superposition for different values of m and n, and amplitude ratio a_2/a_1. Although the azimuthal modulation is in all cases the same ($m-n=6$), the structure depends not only on the amplitude ratio but also on the smallest topological charge. The central part of the beam either has a maximum or void of different sizes. The peaks surrounding the central spot are either separated or interconnected.

The complex amplitude of a vortical Bessel–Gaussian beam is obtained in the paraxial approximation from the parabolic diffraction equation [34,35]

$$E(\rho,\varphi,z)=\frac{1}{Z}J_m\left(\frac{k_\rho\rho}{Z}\right)\mathrm{e}^{-\frac{\rho^2}{d_0^2 Z}-\mathrm{i}\frac{k_\rho^2 z}{2kZ}+\mathrm{i}m\varphi+\mathrm{i}k_z z}, \tag{3}$$

where $Z=1+\mathrm{i}z/z_0$ and $z_0=kd_0^2/2$ – Rayleigh length, d_0 – is the radius of Gaussian aperture.

The spatial spectrum of the scalar Bessel–Gaussian beam is given by:

$$g(k_r,\phi,m)=\frac{d_0^2}{2}\mathrm{e}^{-(k_r^2+k_\rho^2)d_0^2/4}I_m(k_r k_\rho d_0^2/2)\mathrm{e}^{\mathrm{i}m\phi}, \tag{4}$$

where I_m - is modified Bessel function and $k_r=(k_x+k_y)^{1/2}$ is a radial vector in Fourier space. The spatial spectrum of Bessel–Gaussian beam is a ring of radius k_ρ and has a width of $1/d_0$. When $m>0$, the spectrum is azimuthally modulated with phase modulation of $2\pi m$.

Therefore, the spatial spectrum of the superposed field is

$$S(k_r,\phi)=a_1 g(k_r,\phi,m)+a_2 g(k_r,\phi,n), \tag{5}$$

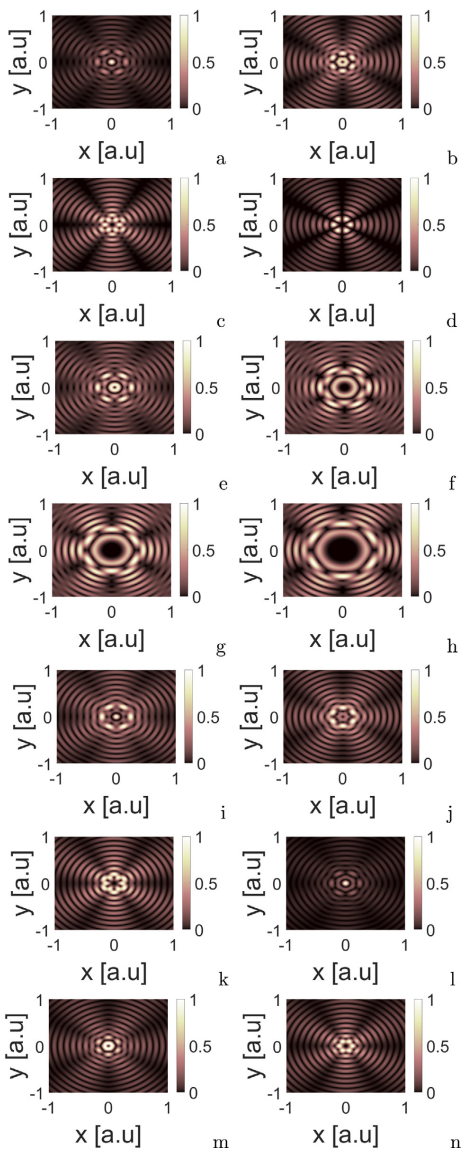

Fig. 1. Intensity distributions of superpositions of Bessel vortex pairs for topological charges $m=6$ and $n=0$ (a, i, l), $m=5$ and $n=-1$ (b, j, m), $m=4$ and $n=-2$ (c, k, n), $m=3$ and $n=-3$ (d), $m=7$ and $n=1$ (a), $m=10$ and $n=4$ (b), $m=13$ and $n=7$ (c), $m=16$ and $n=10$ (d). The amplitude ratio a_2/a_1 is 1 (a–h), 0.5 (i–k) and 2 (l–n).

Usually, Bessel–Gaussian vortices are obtained from LG_0^m (Laguerre–Gaussian) vortices by focusing them with an axicon [12]. As a result, the spatial spectrum of the LG mode is transformed into a ring with azimuthal phase modulation.

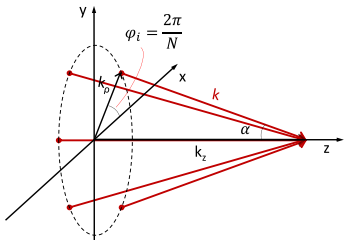

Fig. 2. Representation of an individual plane wave wavevector traveling at cone half angle α.

In what follows we will analyze Bessel vortices as superpositions of N (ideally $N \to \infty$) plane waves (or Gaussian beams). First of all, the ring-shaped spatial spectrum means that each individual spectral component propagates in a such way, that its wavevector is located on a 2α angle cone. For the sake of brevity, let us assume that N individual waves are azimuthally equilocated, i.e. $\varphi = \frac{2\pi}{N} i$, where $i = 0, 1, \ldots, N-1$ (see Fig. 2). So, let us assume that we have N equilocated points in the plane $z = -z_0$ on the radius $\rho = r_0$. Let us point vectors e_{zN} from these points to the point $(0, 0, 0)$. Coordinates for these vectors are $\mathrm{e}_{zN} = (r_0 \cos\varphi, r_0 \sin\varphi, z_0)$. The radius r_0 is $r_0 = z_0 \tan\alpha$, so $\mathrm{e}_{zN} = z_0(\tan\alpha \cos\varphi, \tan\alpha \sin\varphi, 1)$.

Now, we define two orthogonal directions e_{xN} and e_{yN} which are orthogonal to e_{zN}. The plane containing those two vectors is $x \tan\alpha \cos\varphi + y \tan\alpha \sin\varphi + z = 0$. Let us choose e_{xN} as $\mathrm{e}_{xN} = (x_a, y_a, 0)$ and e_{yN} as $\mathrm{e}_{yN} = (-y_a, a_a, z_a)$. As those two new orthogonal directions belong to the plane, it holds true

$$\begin{cases} x_a \tan\alpha \cos\varphi + y_a \tan\alpha \sin\varphi = 0, \\ z_a = -y_a \tan\alpha \cos\varphi + x_a \tan\alpha \sin\varphi \end{cases}, \tag{6}$$

We choose here wisely $x_a = \sin\phi$ and we get $y_a = -\cos\phi$ and $z_a = \tan\alpha$.

Thus, we did end up with three orthogonal directions, which can build new coordinate orts. After normalizing, we end up with a local coordinates system for the ith beam on the cone

$$\begin{aligned} \mathbf{e}_{1i} &= \{\sin\alpha \cos\varphi, \sin\alpha \sin\varphi, \cos\alpha\} \\ \mathbf{e}_{2i} &= \{\sin\varphi, -\cos\varphi, 0\}, \\ \mathbf{e}_{3i} &= \{-\cos\alpha \cos\varphi, -\cos\alpha \sin\varphi, \sin\alpha\} \end{aligned} \tag{7}$$

These are the local coordinates of ith local component of the spatial spectrum. In a trivial way, we end up with the following expressions for local coordinates x_i, y_i, z_i in the coordinate system of the Bessel beam x, y, z

$$\begin{pmatrix} z_i \\ y_i \\ x_i \end{pmatrix} = \begin{pmatrix} \cos\alpha & \sin\alpha \sin\varphi & \sin\alpha \cos\varphi \\ 0 & -\cos\varphi & \sin\varphi \\ \sin\alpha & -\cos\alpha \sin\varphi & -\cos\alpha \cos\varphi \end{pmatrix} \begin{pmatrix} z \\ y \\ x \end{pmatrix}. \tag{8}$$

Now, having this in mind, we recall that the amplitude of a Gaussian beam traveling along the cone is [44]

$$E(\mathbf{r}_i) = \frac{1}{(1 + \mathrm{i} z_i / k\rho_0^2)} \mathrm{e}^{-\frac{x_i^2 + y_i^2}{2\rho_0^2 (1 + \mathrm{i} z_i / k\rho_0^2)}} \mathrm{e}^{\mathrm{i} k z_i}, \tag{9}$$

where ρ_0 is the beam width. The resulting electric field is

$$E_\Sigma(\mathbf{r}, k, \rho_0, \theta) = \sum_{i=0}^{N-1} \frac{E(\mathbf{r}_i)}{N}. \tag{10}$$

These considerations enable us to estimate the effects caused by the discretization of the spatial spectra of the Bessel beam, see Fig. 3. Here we investigate a superposition of Bessel beams with topological charges

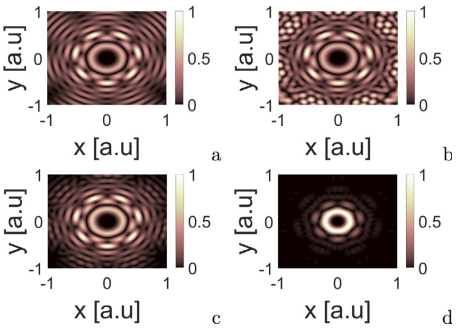

Fig. 3. Intensity distributions of superpositions of Bessel vortex pairs for topological charges $m = 6$ and $n = 13$ created using $N = 180$ (a), $N = 40$ (b–d) plane waves (a, b), Gaussian beams with width $\rho_0 = 0.5$ (c) and $\rho_0 = 0.05$ (d).

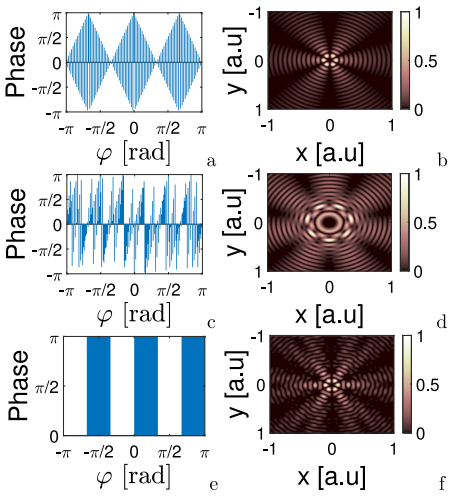

Fig. 4. Dependency of the phase distributions on azimuthal angle in geometrical phase elements for topological charges $m = -3$ and $n = 3$ (a), and $m = 6$ and $n = 13$ (c) and binary $m = -3$ and $n = 3$ (e). Resulting azimuthally modulated axicon beams are depicted in the transverse plane, (b), (d), and (f) respectively.

$m = 6$ and $n = 13$, which was created using Eq. (10). As the number of plane waves is $N = 180$, the electric field intensity closely resembles the field expressed by Eq. (1). However, as the number of plane waves decreases to $N = 40$, we start to notice an appearance of new structures further away from the center, see Fig. 3(b). When we additionally switch from plane waves to Gaussian beams with $\rho_0 = 0.5$, the intensity of these new structures diminishes, see Fig. 3(c), and disappears, when the beam width reaches $\rho_0 = 0.05$, see Fig. 3(d).

3. Geometrical phase elements

Conventional refraction-based optical elements such as lenses or conical prisms modify the wavefront of a beam by controlling the length of the optical path. The phase shift that is introduced by these optical elements is known as a static phase shift and it relies on the

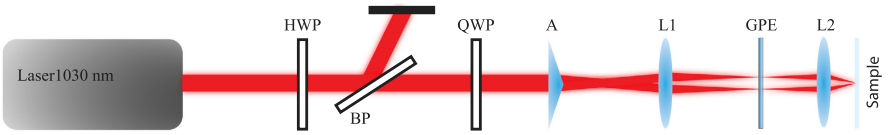

Fig. 5. Experimental setup. HWP — half wave-plate, BP — Beam Polarizer, QWP — quarter wave-plate, A — Axicon, L1 and L2 — lenses $f = 150$ mm and $f = 8$ mm respectively, GPE — geometrical phase element.

refractive index of the material (n) and its' thickness (d) $\delta = \frac{2\pi nd}{\lambda}$, where λ is the wavelength of a beam. In contrast, the geometrical phase, also known as the Pancharatnam–Berry phase [45] depends only on the geometry of the pathway through an anisotropic medium [46]. For example, in a homogeneous birefringent plate, the geometrical phase shift is proportional to twice the orientation angle θ of a fast axis [46]:

$$\delta = \frac{\pi}{\lambda}(n_e + n_o) \pm 2\theta \tag{11}$$

where n_o and n_e are refraction indices for ordinary and extraordinary waves, respectively.

There are several ways to use the geometrical phase for beam shaping element manufacturing, which require the formation of periodic nanostructures of small size compared to the wavelength of light. These can be metasurfaces [47], based on dielectrics [48] or nano-gratings inscribed in fused silica glass [49] as it is in our case. These nano-gratings are self-assembling structures which are created in fused silica glass by irradiating it with a certain set of laser emission parameters [50]. Their birefringence is characterized by two parameters: retardance τ and azimuth θ of the fast axis, which is respectively controlled by adjusting the fluence and polarization direction of the incident beam [50]. The effect that a GPE would have on an incident beam can be evaluated using the Jones matrix [51]. At any point of the GPE, the output polarization can be described as $E_{out} = M(x, y)E_{in}$ where E_{in} is the Jones vector of the incident polarization [52]. In what follows, we consider mainly geometrical phase elements of retardance $\tau = \lambda/2$. In this case, the Jones matrix $M(x, y)$ is expressed as

$$M(x,y) = \begin{pmatrix} \cos^2(\theta) + \mathrm{i}\sin^2(\theta) & (1-\mathrm{i})\cos(\theta)\sin(\theta) \\ (1-\mathrm{i})\cos(\theta)\sin(\theta) & \mathrm{i}\cos^2(\theta) + \sin^2(\theta) \end{pmatrix}, \tag{12}$$

where θ is the angle of the fast axis of a local birefringent nano-grating. For a circularly polarized incident beam E_{in} the modulation of the output beam E_{out} is:

$$E_{out} = M(x,y)E_{in} = \mathrm{e}^{2\mathrm{i}\theta}\begin{pmatrix} 1 \\ \pm\mathrm{i} \end{pmatrix}. \tag{13}$$

In this section, we implement the theoretical considerations described previously and devise a number of GPEs for azimuthal modulation of the spatial spectrum of the axicon beam. The performance of this GPEs was evaluated numerically for different topological charges m and n (see Fig. 4(a), (c), (e)). Numerically obtained intensity distributions of the resulting beams are depicted in Fig. 4(b), (d), (f).

We note here that in Fig. 4(a–d) the number of plane wave components $N = 180$. As we know from our previous experience that a GPE with such a large number of azimuthal sectors might be difficult to produce, we additionally devise a binary GPE element where the phase changes 6 times over the azimuthal angle 2π (see Fig. 4(e)). Surprisingly, this binary element creates an intensity distribution (Fig. 4(f)) that strongly resembles the initial one obtained with a continuously changing phase (Fig. 4(b)). As expected, a distinct azimuthal modulation remains — several (six) intensity peaks are observed. The main differences are observed in small intensity regions further away from the center. This can be explained considering the azimuthal phase modulation on the ring, which can be expressed as $\exp(im\varphi) + \exp(-im\varphi) = 2\cos(m\varphi)$. As the cosine function does not change very rapidly it can be approximated in a binary fashion. For case (d), these (seven) peaks are also elongated.

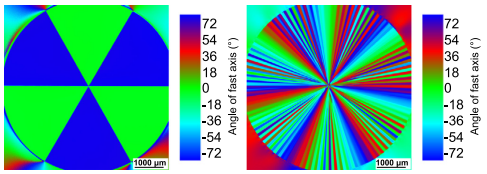

Fig. 6. Experimentally obtained fast axis angle distributions of the manufactured geometrical phase elements. On the left — the binary element for the generation of the $m = -3$ and $n = 3$ superposition, on the right — the GPE for the generation of the $m = 6$ and $n = 13$ superposition.

We have selected a pair of particular designs of GPE for experimental verification. Their azimuthal phase modulation is depicted in Fig. 4(c) and (e). Those two elements represent two radically opposite implementations of the axicon beam azimuthal modulation. In the first case, the number of zones with constant phase on the cone is large and they are relatively small. Thus, in (c) the zones have a fine modulation of vortex beams. Half of the zones represent a topological charge of $n = 6$ and another half – a topological charge of $m = 13$. In the second case, the number of zones with constant phase on the cone is low and they are large. Thus, in (e) every second zone has a modulation of π.

4. Experimental setup

We have used a Yb:KGW oscillator and a regenerative amplifier system "Pharos" (Light Conversion) which can deliver pulses up to 1.5 mJ with the shortest pulse duration of 158 fs which can be increased up to 13 ps. A simplified picture of the experimental setup is given in the diagram of Fig. 5. The laser power was controlled using an external attenuator composed of a half-wave plate (HW) and a beam polarizer (BP). Afterward, the polarization of the beam was changed to circular using a quarter wave-plate (QWP) and the Gaussian beam was delivered to a Bessel beam forming GPE, which is equivalent to a 176-degree Axicon lens. The beam is then focused on the sample with the help of $4f$ de-magnifying telescope consisting of lenses L1 ($f = 150$ mm) and L2 ($f = 8$ mm) while at a focal position of the first lens (L1) a GPE was used to introduce Bessel beam spatial spectrum phase modulation.

The sample was mounted on motorized XYZ translational stages perpendicular to the beam propagation direction. A camera together with a 40x magnifying objective was also placed on the same stage. This allowed us to inspect the focal region of the beam and made the alignment procedure easier.

The selected designs for fixed pairs of topological charges (m, n) of GPEs were manufactured in *the Workshop of Photonics*.

We devise such an element and encode it as a GPE with the transmittance being higher than 90% in a broad spectral region [42]. Such GPEs enable the generation of high-quality, high-energy beams and can be used in high power setups, where they withstand 1.5 mJ energy, 158 fs FWHM duration pulses at 1030 nm [19,53]. Even higher-energy intensity pulses can be transformed into Bessel-like beams by scaling the optical elements used in the experimental setup [42].

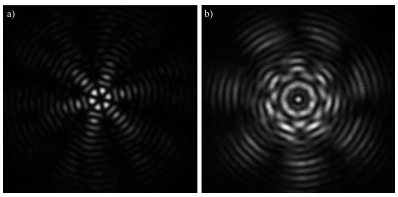

Fig. 7. Experimentally obtained transverse intensity profiles of superimposed Bessel beams of topological charges (a) $m = -3$, $n = 3$ and (b) $m = 6$, $n = 13$.

The fast axis distribution of these GPEs is depicted in Fig. 6. In general, the quality of the manufactured elements is high and their performance, transmittance was as expected [42]. As the orientation of the nano-grating cannot change very rapidly, designs of the GPEs with many sectors might be problematic as we move to the center of the element. On the other hand, these areas are larger in numbers so effectively this should introduce undesirable phases in these small areas, see Fig. 6.

5. Experimental results

In this section, we present experimental verification of the generation of azimuthally modulated beams. We start our experiments by investigating beam intensity profiles. In the first set of experiments, we study the performance of a binary design of the GPE. Here, we superimpose Bessel beams of topological charges $m = -3$ and $n = 3$, so we obtain a beam with 6 intensity maxima which are triangularly shaped, see Fig. 7(a). The recorded intensity profile demonstrates a good agreement with the theoretical predictions.

The second set of experiments is devoted to the investigation of a finely modulated axicon beam. For this, the topological charge $m = 6$ was superimposed with $n = 13$. As a result, 7 intensity maxima are observed. They are azimuthally elongated, as expected in the theoretical section. Results are shown in Fig. 7(b). In this case, the main difference compared to the numerical simulation (see Fig. 4(d)) is a visible zeroth-order intensity maximum in the center of the beam.

This could be explained as a result of GPE manufacturing process. The jump-like transition between one nanograting angle to another in adjacent pixels is not achievable — orientations of nano-gratings cannot be perpendicular. Therefore, it is not possible to inscribe a sharp phase transition. As this design has many zones, subsequently, it means that there may be situations in the design when the phase makes a sharp jump. While implementing this design, many transition regions appear. This leads to the appearance of a small background zeroth-order Bessel beam. This situation is avoided in the previous design as the azimuthally modulated zones are large and there are few transition regions. No central maximum is observed in Fig. 7(a).

As the azimuthally modulated axicon beam can achieve high fluence, our aim in the last set of experiments is to investigate a few laser microprocessing scenarios. For this, we continue the experiment and investigate the interaction of the beams with a transparent material. A polished fused silica sample was used and the surface, as well as the bulk modifications of the sample were performed. This fabrication experimentation was executed with varying energy (from 150 μJ to 250 μJ) and with varying pulse (FWHM) duration (from 158 fs to 10 ps).

For this range of parameters, surface modifications were produced after focusing the beam on the surface. These modifications are depicted in Fig. 8. When the pulse duration is short, the surface damages resemble the beam profile with many azimuthally modulated rings around the main peaks. When the pulse duration increases to 10 ps while maintaining the pulse energy, only the most intense peaks of the beam modify the surface.

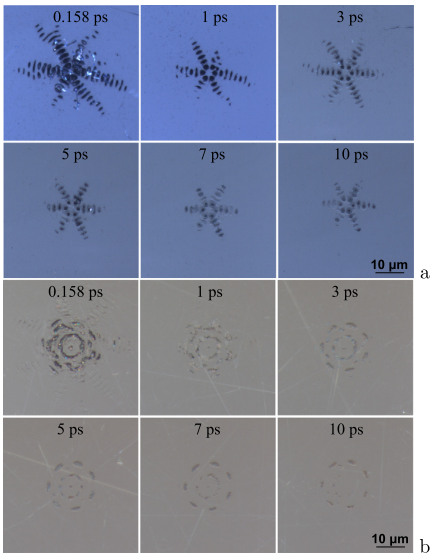

Fig. 8. Microscope images of surface modifications on fused silica samples using azimuthally modulated axicon beams. The pulse energy of 200 μJ was used. Pulse durations are given in pictures. (a) Modifications with a superposition of Bessel beams of topological charges $m = -3$ and $n = 3$, (b) topological charges are $m = 6$ and $n = 13$.

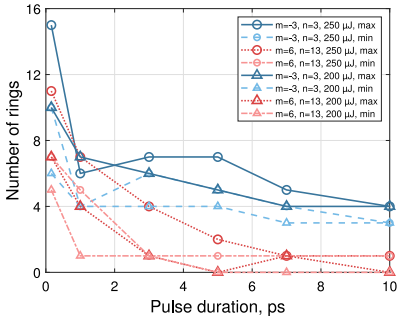

Fig. 9. Dependency on pulse duration of the minimum and maximum number of rings around main peaks visible on a surface of fused silica sample after modifying it with azimuthally modulated axicon beams of topological charges $m = -3$, $n = 3$ and $m = 6$, $n = 13$. Lines with circle and triangles mark energy used: 250 μJ and 200 μJ respectively.

These findings are summarized in Fig. 9, where the minimum and the maximum number of rings appearing in the surface modification around the main peaks is plotted. Most peripheral azimuthally modulated rings appear on the surface when sub-picosecond duration is used. This number gradually decreases, when the pulse duration increases.

Lastly, we investigate volume modifications produced by superimposed azimuthally modulated axicon beams. In this experiment, we have focused superimposed Bessel beams below the surface of a sample. As a result, long bulk modifications were produced by the main peaks of the beams. A side view of a sample is presented in Fig. 10.

The length of volume modifications was larger for the first GPE element than for a second one, see Fig. 11. We observe that a superposition

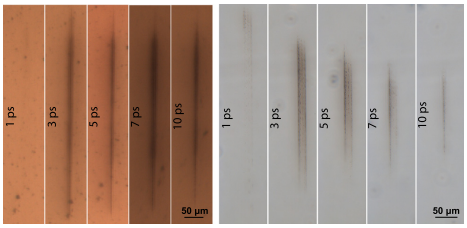

Fig. 10. Microscope images of bulk modifications inside fused silica sample using azimuthally modulated axicon beams. Pulse energy is 250 μJ. Pulse durations are specified in pictures. On the left volume modification produced by superimposed Bessel beams of topological charges, $m = -3$ and $n = 3$ are shown. On the right topological charges are $m = 6$ and $n = 13$.

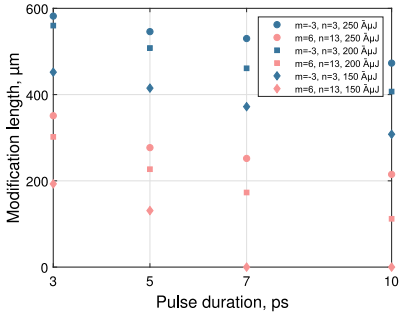

Fig. 11. Dependency on pulse duration of the length of volume modifications in the bulk of fused silica produced with azimuthally modulated axicon beams of topological charges $m = -3$, $n = 3$ and $m = 6$, $n = 13$. Circle, square, and rhombus represent different pulse energy: 250 μJ, 200 μJ, and 150 μJ respectively.

of Bessel beams with $m = -3$ and $n = 3$ topological charges produce relatively long channels. A superposition of Bessel vortices with charges $m = 6$ and $n = 13$ results in a smaller length of volume modifications. This can be well understood given the fact that the topological charges are different and the number of azimuthal modulations is $|m - n|$. For the first GPE, this number is 6 and for the second one it is 7, so the energy is redistributed in a larger number of intensity peaks. Secondly, the energy density in a ring is linearly decreasing as the ring radius increases. For the first GPE, the center of the beam is taken by a vortex of topological charge $m = -3$ and for the second one a vortex with a topological charge of $m = 6$. This means that the first ring does appear in the second case relatively further away from the center than for the first case. As a result, the intensity of the material modifying peaks is further decreased. For this reason, the region in the material where the threshold for modification is exceeded is smaller in the second case. A summarizing graph is presented in Fig. 11.

As expected the increase in the pulse duration results in even shorter modifications. No changes in the sample exposed to a 158 fs pulses were observed under an optical microscope as most of the absorption happens on the sample surface.

6. Conclusions

In conclusion, a superposition of two optical Bessel vortices of different topological charges was investigated. It allows the generation of high aspect ratio non-diffracting beams with complexly transverse intensity patterns. In this work, we have studied a way to create such patterns using an axicon with a discrete spatial spectrum. Because of the intrinsic use of the conical prism in the generation of such beams, we refer to them as azimuthally modulated axicon beams.

As the spatial spectrum of a vortex Bessel beam is a ring, the spatial spectrum of vortex axicon beam is also a ring comprised of N azimuthally equilocated plane wave (or Gaussian beam) components. As our investigation reveals, the central part of such beams, in general, resembles the complex transverse intensity pattern of the superposed Bessel beams. However, as the number of the plane wave components N decreases, some discrepancies start to appear in the periphery of the axicon beam. Of course, plane waves are merely a theoretical construct. A realistic spatial spectrum has a width, so axicon beams are implemented by the superposition of Gaussian beams with spectral widths coinciding with the width of the ring. In this consideration, the width of the Gaussian beams starts to influence the central part of the complex pattern, when the impinging beams become smaller.

We propose to implement a vortical axicon beam using a geometrical phase element. We do so by inscribing subwavelength birefringent structures inside fused silica glass to create spatially varying structures for the azimuthal modulation of the spatial spectra of a zeroth-order Bessel beam. These optical elements are commonly used to produce various high-power beams for laser applications. We theoretically investigate a few selected designs of the GPEs. Based on this investigation, we manufacture two GPEs — one with continuously varying azimuthal phase and one with binary variation in the phase. We observe a good quality of manufacturing as the experimentally observed axicon beams are in good agreement with the numerical simulation.

We demonstrate the ability to use such beams in high-power applications and create surface and volume modifications inside a fused silica sample. To prove the concept, we investigate different pulse durations of azimuthally modulated axicon vortical beams for the creation of modifications inside fused silica glass samples.

For a short pulse duration, the surface damages resemble the axicon beam profile. Increasing pulse duration to 10 ps results in only the most intense peaks affecting the surface.

The volume damage was observed to be rather nontrivial. In this experimentation, the spatial structure of the axicon beams is important. In general, the central part of the beam has a vortex of lesser topological charge [34]. This means that the size of the vortex core depends on the charge. Larger topological charges affect the radius of first intensity spikes. For this reason, volume modifications are less pronounced when the axicon beam is constructed with charges $m = 6$ and $n = 13$. The length of volume modifications is smaller than for an axicon beam with charges $m = -3$ and $n = 3$. Moreover, the intensity pattern is more complex in the first case, so the relative intensity in a single hotspot is smaller than in the second case.

As a summary, this implementation of non-diffracting vortical Bessel beams is useful in various laser microfabrication scenarios such as inscription of long structured volume modifications [17,19].

Declaration of competing interest

The authors declare that they have no known competing financial interests or personal relationships that could have appeared to influence the work reported in this paper.

Acknowledgments

This research is funded by the European Social Fund according to the activity ‘Improvement of researchers’ qualification by implementing world-class R&D projects’ of Measure No. 09.3.3-LMT-K-712.

References

[1] F.M. Dickey, T.E. Lizotte, Laser Beam Shaping Applications, Vol. 1, CRC Press, 2017.

[2] M.D. Shirk, P.A. Molian, A review of ultrashort pulsed laser ablation of materials, J. Laser Appl. 10 (1998) 18–28.

[3] B. Fotovvati, S.F. Wayne, G. Lewis, E. Asadi, A review on melt-pool characteristics in laser welding of metals, Adv. Mater. Sci. Eng. 2018 (2018) 4920718.

[4] J.-P. Bérubé, A.L. Camus, S.H. Messaddeq, Y. Petit, Y. Messaddeq, L. Canioni, R. Vallée, Femtosecond laser direct inscription of mid-ir transmitting waveguides in bgg glasses, Opt. Mater. Express 7 (2017) 3124–3135.

[5] R. Brighenti, M.P. Cosma, L. Marsavina, A. Spagnoli, M. Terzano, Laser-based additively manufactured polymers: a review on processes and mechanical models, J. Mater. Sci. 56 (2021) 961–998.

[6] M. Mikutis, T. Kudrius, G. Šlekys, D. Paipulas, S. Juodkazis, High 90% efficiency bragg gratings formed in fused silica by femtosecond gauss-bessel laser beams, Opt. Mater. Express 3 (2013) 1862–1871.

[7] J. Durnin, J. Micel Jr., J.H. Eberly, Diffraction-free. beams, Diffraction-free beams, Phys. Rev. Lett. 58 (1987) 1499.

[8] J. Durnin, Exact solutions for nondiffracting beams. i. the scalar theory, J. Opt. Soc. Amer. A 4 (1987) 651–654.

[9] J.C. Gutiérrez-Vega, M. Iturbe-Castillo, S. Chávez-Cerda, Alternative formulation for invariant optical fields: Mathieu beams, Opt. Lett. 25 (2000) 1493–1495.

[10] M.A. Bandres, J.C. Gutiérrez-Vega, S. Chávez-Cerda, Parabolic nondiffracting optical wave fields, Opt. Lett. 29 (2004) 44–46.

[11] G. Siviloglou, J. Broky, A. Dogariu, D. Christodoulides, Observation of accelerating airy beams, Phys. Rev. Lett. 99 (2007) 213901.

[12] V. Jarutis, R. Paškauskas, A. Stabinis, Focusing of Laguerre–Gaussian beams by axicon, Opt. Commun. 184 (2000) 105–112.

[13] A. Vasara, J. Turunen, A.T. Friberg, Realization of general nondiffracting beams with computer-generated holograms, J. Opt. Soc. Amer. A 6 (1989) 1748–1754.

[14] C. Rosales-Guzmán, A. Forbes, How To Shape Light with Spatial Light Modulators, SPIE, 2017, pp. 19–21.

[15] S. Orlov, A. Jurš, J. Baltrukonis, V. Jukna, Controllable spatial array of bessel-like beams with independent axial intensity distributions for laser microprocessing, J. Laser Micro Nanoeng. 13 (2018) 324–329.

[16] S. Orlov, A. Jurš, E. Nacius, Optical bessel-like beams with engineered axial phase and intensity distribution, J. Laser Micro Nanoeng. 13 (2018) 244–248.

[17] E. Nacius, P. Gotovski, V. Jukna, O. Ulčinas, T. Gertus, S. Orlov, Generation of bessel type beams via phase shifted axicons encoded in geometrical phase elements, in: A.V. Kudryashov, A.H. Paxton, V.S. Ilchenko, A.M. Armani (Eds.), Laser Resonators, Microresonators, and Beam Control XXII, Vol. 11266, International Society for Optics and Photonics, SPIE, 2020, pp. 98–106, http://dx.doi.org/10.1117/12.2546561.

[18] P. Gotovski, P. Šlevas, E. Nacius, V. Jukna, S. Orlov, J. Baltrukonis, O. Ulčinas, T. Gertus, Formation of optical needles by pancharatnam-berry phase element for laser-induced modifications in transparent materials, in: U. Klotzbach, A. Watanabe, R. Kling (Eds.), Laser-Based Micro- and Nanoprocessing XIV, Vol. 11268, International Society for Optics and Photonics, SPIE, 2020, pp. 357–365, http://dx.doi.org/10.1117/12.2544925.

[19] J. Baltrukonis, O. Ulčinas, S. Orlov, V. Jukna, Void and micro-crack generation in transparent materials with high-energy first-order vector bessel beam, J. Opt. Soc. Amer. B 37 (2020) 2121–2127.

[20] J. Baltrukonis, O. Ulcinas, P. Gotovski, S. Orlov, V. Jukna, Realization of higher order vector bessel beams for transparent material processing applications, in: Laser-Based Micro-and Nanoprocessing XIV, Vol. 11268, International Society for Optics and Photonics, 2020, 112681D.

[21] M.K. Bhuyan, F. Courvoisier, P.-A. Lacourt, M. Jacquot, L. Furfaro, M.J. Withford, J.M. Dudley, High aspect ratio taper-free microchannel fabrication using femtosecond bessel beams, Opt. Express 18 (2010) 566–574.

[22] F. Courvoisier, J. Zhang, M. Bhuyan, M. Jacquot, J.M. Dudley, Applications of femtosecond Bessel beams to laser ablation, Appl. Phys. A Mater. Sci. Process. 112 (2013) 29–34.

[23] K. Mishchik, R. Beuton, O.D. Caulier, S. Skupin, B. Chimier, G. Duchateau, B. Chassagne, R. Kling, C. Hönninger, E. Mottay, J. Lopez, Improved laser glass cutting by spatio-temporal control of energy deposition using bursts of femtosecond pulses, Opt. Express 25 (2017) 33271–33282.

[24] S.N. Khonina, N.L. Kazanskiy, S.V. Karpeev, M.A. Butt, Bessel beam: Significance and applications—a progressive review, Micromachines 11 (2020) 997.

[25] J. Durnin, J. Miceli, J.H. Eberly, Comparison of bessel and gaussian beams, Opt. Lett. 13 (1988) 79–80.

[26] O. Brzobohatý, T. Čižmár, P. Zemánek, High quality quasi-bessel beam generated by round-tip axicon, Opt. Express 16 (2008) 12688–12700.

[27] P. Gotovski, P. Šlevas, E. Nacius, V. Jukna, S. Orlov, J. Baltrukonis, O. Ulčinas, T. Gertus, Formation of optical needles by pancharatnam-berry phase element for laser-induced modifications in transparent materials, in: Laser-Based Micro-and Nanoprocessing XIV, Vol. 11268, International Society for Optics and Photonics, 2020, 112681Y.

[28] S. Orlov, A. Juršenas, E. Nacius, Optical bessel-like beams with engineered axial phase and intensity distribution, J. Laser Micro Nanoeng. 13 (2018) 244–248.

[29] S. Orlov, A. Juršenas, J. Baltrukonis, V. Jukna, Controllable spatial array of bessel-like beams with independent axial intensity distributions for laser microprocessing, J. Laser Micro Nanoeng. 13 (2018) 324–329.

[30] L. Allen, M.W. Beijersbergen, R.J.C. Spreeuw, J.P. Woerdman, Orbital angular momentum of light and the transformation of Laguerre-Gaussian laser modes, Phys. Rev. A 45 (1992) 8185–8189.

[31] P. Coullet, L. Gil, F. Rocca, Optical vortices, Opt. Commun. 73 (1989) 403–408.

[32] K. Gahagan, G.J. Swartzlander, Optical vortex trapping of particles, Opt. Lett. 21 (1996) 827–829.

[33] Y. Shen, X. Wang, Z. Xie, C. Min, X. Fu, Q. Liu, M. Gong, X. Yuan, Optical vortices 30 years on: Oam manipulation from topological charge to multiple singularities, Light: Sci. Appl. 8 (2019) 1–29.

[34] S. Orlov, K. Regelskis, V. Smilgevičius, A. Stabinis, Propagation of Bessel beams carrying optical vortices, Opt. Commun. 209 (2002) 155–165.

[35] S. Orlov, A. Stabinis, Propagation of superpositions of coaxial optical bessel beams carrying vortices, J. Opt. A: Pure Appl. Opt. 6 (2004) S259.

[36] A. Stabinis, S. Orlov, V. Jarutis, Interaction of bessel optical vortices in quadratic nonlinear medium, Opt. Commun. 197 (2001) 419–429.

[37] V. Jukna, J. Baltrukonis, P. Gotovski, S. Orlov, Analysis of higher order vector bessel-gauss beam applicability to transparent material processing, in: Laser-Based Micro-and Nanoprocessing XV, Vol. 11674, International Society for Optics and Photonics, 2021, 116740L.

[38] C.W. McCutchen, Generalized aperture and the three-dimensional diffraction image, J. Opt. Soc. Amer. 54 (1964) 240–244.

[39] G. Indebetouw, Nondiffracting optical fields: some remarks on their analysis and synthesis, J. Opt. Soc. Amer. A 6 (1989) 150–152.

[40] J.H. McLeod, The axicon: a new type of optical element, JOSA 44 (1954) 592–597.

[41] P. Slevas, S. Orlov, E. Nacius, O. Ulcinas, P. Gotovski, J. Baltrukonis, V. Jukna, Laser induced modifications in transparent materials using azimuthally modulated axicon beams, in: Laser Applications in Microelectronic and Optoelectronic Manufacturing (LAMOM) XXV, Vol. 11267, International Society for Optics and Photonics, 2020, 112670B.

[42] Laser-induced damage threshold (lidt) measurement report, 2020, https://wophotonics.com/wp-content/uploads/2020/07/LIDT-result-fs-regime.pdf, (Accessed: 23 july 2021).

[43] J. Baltrukonis, O. Ulčinas, S. Orlov, V. Jukna, High-order vector bessel-gauss beams for laser micromachining of transparent materials, Phys. Rev. A (2021).

[44] A.E. Siegman, Lasers University Science Books, Vol. 37, Mill Valley, CA, 1986, p. 169.

[45] E. Cohen, H. Larocque, F. Bouchard, F. Nejadsattari, Y. Gefen, E. Karimi, Geometric phase from Aharonov–Bohm to Pancharatnam–Berry and beyond, Nat. Rev. Phys. 1 (2019) 437–449.

[46] M.J. Escuti, J. Kim, M.W. Kudenov, Controlling light with geometric-phase holograms, Opt. Photonics News 27 (2016) 22–29.

[47] D. Neshev, I. Aharonovich, Optical metasurfaces: new generation building blocks for multi-functional optics, Light: Sci. Appl. 7 (2018) 58.

[48] B. Desiatov, N. Mazurski, Y. Fainman, U. Levy, Polarization selective beam shaping using nanoscale dielectric metasurfaces, Opt. Express 23 (2015) 22611–22618.

[49] R. Drevinskas, P.G. Kazansky, High-performance geometric phase elements in silica glass, APL Photonics 2 (2017) 066104.

[50] M. Beresna, M. Gecevičius, P.G. Kazansky, Polarization sensitive elements fabricated by femtosecond laser nanostructuring of glass, Opt. Mater. Express 1 (2011) 783–795.

[51] R.C. Jones, A new calculus for the treatment of optical systemsi. description and discussion of the calculus, Josa 31 (1941) 488–493.

[52] Z. Bomzon, V. Kleiner, E. Hasman, Pancharatnam–Berry phase in space-variant polarization-state manipulations with subwavelength gratings, Opt. Lett. 26 (2001) 1424–1426.

[53] J. Baltrukonis, O. Ulčinas, S. Orlov, V. Jukna, High-order vector Bessel-Gauss beams for laser micromachining of transparent materials, Phys. Rev. A 16 (2021) 034001.

P2

Generation of an optical needle beam with a laser inscribed Pancharatnam-Berry phase element under imperfect conditions

P. Gotovski, **P. Šlevas**, S. Orlov, O. Ulčinas, A. Urbas

Optics Express, 29(21), 33331-33345 (2021)
DOI: 10.1364/OE.438709
https://opg.optica.org/oe/fulltext.cfm?uri=oe-29-21-33331&id=460009

Research Article | Vol. 29, No. 21 / 11 Oct 2021 / Optics Express 33331
Optics EXPRESS

Generation of an optical needle beam with a laser inscribed Pancharatnam-Berry phase element under imperfect conditions

PAVEL GOTOVSKI,[1] PAULIUS ŠLEVAS,[1,2] SERGEJ ORLOV,[1,*] ORESTAS ULČINAS,[1,2] AND ANTANAS URBAS[1,2]

[1] Center for Physical Sciences and Technology, Sauletekio av. 3, LT-10257 Vilnius, Lithuania
[2] Workshop of Photonics, Mokslininku st. 6A, LT-08412 Vilnius, Lithuania
[*] sergejus.orlovas@ftmc.lt

Abstract: Beams exhibiting long focal lines and small focal spot sizes are desired in a variety of applications and are called optical needles, with Bessel beams being a common example. Conical prisms are regularly used to generate Bessel beams, however, this method is usually plagued by an appearance of on-axis oscillations. In this work, we consider an optical element based on the space-domain Pancharatnam-Berry phase (PBP) to generate a high-power optical needle with a smooth and constant on-axis intensity profile. The phase in PBP elements is not introduced through optical path differences but results from the geometric phase that accompanies space-variant polarization manipulation. Our implementation is based on a type 2 modification of bulk transparent glass material, resulting in the formation of nanogratings with slow axes aligned perpendicular to the grating corrugation. We investigate both numerically and experimentally the stability of an optical needle generation under imperfect conditions. Influences of misalignments in the optical schema are investigated numerically and experimentally.

1. Introduction

Structuring the light for various applications is becoming a hot topic nowadays. This subject has started from shaping the transverse intensity profile of laser beams (beam shaping) [1]. The engineering of the focal spot has evolved since then to the control of the on-axis behavior. This was caused by the introduction of the so-called non-diffracting Bessel beams [2], which exhibit a large ratio between the transverse and longitudinal widths of the focal spot [3]. Such non-diffracting beams can be generated using a circular aperture or a conical prism (axicon) [4]. In practice, the first method is inefficient due to the high energy losses and the second method is plagued by the appearance of the on-axis high pitch oscillations due to the imperfect axicon tip [5]. These oscillations are also present in implementations of Bessel beams using diffractive optical elements [6]. Due to the geometry of these methods, the on-axis intensity of the Bessel beam is increasing when moving away from the element. This was counteracted by the logarithmic axicon (logaxicon), however, the transverse width of such a Bessel-like beam is increasing [7,8].

The introduction of nonhomogeneous polarization states (radial and azimuthal) has not only enabled the sharp focus of light [9] and also has allowed the creation of very long optical needles [10]. The generation of these polarization states requires vectorial diffractive elements such as q-plates [11], s-wave plates [12] or metasurfaces [13,14]. The desire to control the axial intensity profile of vector and linearly polarized Bessel-like beams has resulted in various techniques being proposed [15–18]. The proper description of such beam-shaping vectorial elements becomes possible after the introduction of the Jones matrix formalism [19,20]. This approach has not only enabled a better understanding of Pancharatnam-Berry phase elements [21] but also has contributed to the design of various metasurface-based elements [22,23].

#438709 https://doi.org/10.1364/OE.438709
Journal © 2021 Received 27 Jul 2021; revised 9 Sep 2021; accepted 10 Sep 2021; published 29 Sep 2021

Optics EXPRESS

Practical implementation of such metasurface-based elements has a broad range of underlying techniques: from dielectric to metallic meta-atoms, from discrete to continuous structures, from orientation induced to size-controlled sub-elements, etc [24–27]. In this work, we implement a Pancharatnam-Berry phase element using a type 2 modification of bulk transparent dielectric material [28–30]. We use a femtosecond laser system to form nanogratings with slow axes aligned perpendicular to the corrugation of the gratings. In such a way we create a metasurface inside the dielectric with continuously varying Pancharatnam-Berry phase (PBP) [31,32].

The main idea of this work is to implement a vectorial diffractive element to shape the axial intensity of the Bessel beam without any change in the width of the transverse profile. We devise such an element and encode it as a PBP element produced by Altechna R&D with the transmittance being higher than 90% in a broad spectral region [33]. Such PBP elements enable the generation of high-quality, high-energy beams and can be used in high power setups, where they withstand 1.5 mJ energy, 158 fs FWHM duration pulses at 1030 nm [34,35]. Even higher-energy intensity pulses can be transformed into Bessel-like beams by scaling the optical elements used in the experimental setup [36]. These high-power beams could find use in various fields of physics.

We systematically investigate the performance of the element both theoretically and experimentally under various imperfect conditions. The ellipticity of the incident Gaussian beam, the misalignment of optical axes, misadjustment of the polarizer, and the PBP element - all these parameters are affecting the quality of the focal line. The structure of the paper is as follows: We start with the methods that describe the underlying theory for the generation of the optical needle; next, we introduce various misalignments and estimate numerically their impact; lastly, we verify our numerical predictions in the experiment. We report on a good agreement between the theory and the experiment.

2. Methods

2.1. Optical needle beam with a constant on-axis intensity

We will consider the case when a laser emits a TEM_{00} mode, its electric field is defined as $E = \exp\left(-r^2/w_0^2\right)$. For the generation of a Bessel-Gaussian beam, we consider a general optical element (GOE), modulating the phase front of the incoming beam with $\exp\left(-ik\sin\alpha_0 r\right)$ where α_0 is the Bessel angle. It transforms the wavefront in a such manner that the projection of the k vector onto the optical z axis is $k_z = k\cos\alpha_0$. In this case, a high-intensity zone known as the Bessel zone is formed right after the GOE, the zone is extending up to $z_{max} = w_0\cot\alpha_0$. If we consider an infinitesimally small ring-shaped illuminating area with radius r' incident on to the GOE as depicted in Fig. 1(a), this region focuses in such a way that its rays are crossing the z axis at the distance $z' = r'\cot\alpha_0$. Similarly, a second infinitesimally small ring-shaped area with a radius that is twice as big as the previous one focuses its rays on the z axis at distance $z'' = 2r'\cot\alpha_0$. However, in the second case, the on-axis intensity is twice as big as in the first case because the ring area $dS = 2\pi r dr$ is proportional to the radius r. With this in mind, we treat the action of GOE on the incident TEM_{00} mode as the focusing of many infinitesimally small ring-shaped areas and thus the on-axis intensity profile is estimated as [5,15]

$$I\left(r=0,z\right) \propto z\exp\left(-2\frac{z^2}{z_{max}^2}\right). \tag{1}$$

The transverse intensity distribution solely depends on the phase modulation introduced by the GOE and is proportional to the zero-order Bessel function [5] as $I(r) \propto J_0^2\left(kr\sin\alpha_0\right)$. We aim to create a constant intensity profile along the optical axis (in a certain range $z_1<z<z_2$) which is usually called the optical needle beam [10]. This kind of intensity profile is formed when the GOE is illuminated with a beam that has an intensity profile I inversely proportional to the radius

Optics EXPRESS

r of the GOE: $I(r) \propto a/r$, see Fig. 1(b). This is achieved by spatially varying the transmittance to shape the intensity of the incoming TEM_{00} mode in the following way

$$I_{inc}(r) = \begin{cases} \exp\left(-2r^2/w_0^2\right), & 0<r<r_1 \cup r_2<r<D/2, \\ a/r, & r_1<r<r_2, \end{cases} \tag{2}$$

where D is the diameter of the GOE. The on-axis intensity in the predefined range $z_1<z<z_2$ can be considered constant as demonstrated in Fig. 1(c).

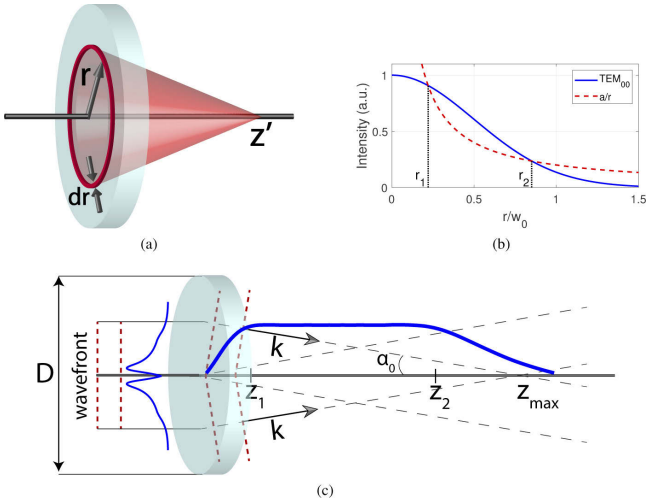

Fig. 1. (a) Schematical depiction of the GOE. An infinitesimal ring-shaped area of radius r and width dr is depicted in red with the rays coming from it being focusing at the distance z'. (b) An exemplary graph of the incident beams TEM_{00} profile (blue solid) and the desired intensity profile (red dashed) for the generation of an optical needle. (c) Schematical depiction of the optical needle generation.

2.2. *Estimation of parameter a*

In this subsection, we will investigate how the proportionality coefficient a influences the efficiency of the optical needle generation. First, we choose a particular value for the parameter a and find corresponding intersection points r_1 and r_2 by solving an equation

$$\exp\left(-2\frac{r^2}{w_0^2}\right) - \frac{a}{r} = 0, \tag{3}$$

which gives two solutions (for the case when values of a/r are smaller than TEM_{00} in the range from r_1 to r_2) as depicted in Fig. 1(b). The analytical solution is very cumbersome to obtain, so we use numerical methods for the estimation of approximate values of r_1 and r_2 instead. Next, we determine a single root $r_0 = w_0/2$ for $a = w_0/(2\sqrt{e})$. This root indicates the upper limit of a, which it cannot exceed. As a consequence, the corresponding points of the start and the end

of the optical needle are bound as $r_1 < w_0/2$ and $r_2 > w_0/2$. It indicates that the solution of the Eq. (3) depends on the ratio a/w_0. We define the efficiency of the element as the ratio between the energy stored in the optical needle and the initial energy of the TEM_{00} mode

$$\eta(a) = \frac{\int_{r_1}^{r_2} \frac{a}{r} r dr}{\int_0^{D/2} \exp\left(-2\frac{r^2}{w_0^2}\right) r dr} = \frac{a[r_2(a) - r_1(a)]}{\frac{1}{4}w_0^2\left[1 - \exp\left(-\frac{D^2}{2w_0^2}\right)\right]} \approx 4\frac{a}{w_0}\left[\frac{r_2(a)}{w_0} - \frac{r_1(a)}{w_0}\right]. \quad (4)$$

Expression in Eq. (4) is further simplified for $D >> w_0$, for small values of a the dependency is linear. The point $a/w_0 = 1/(2\sqrt{e})$ is the limiting point for the generation of an optical needle. Efficiency η is presented in Fig. 2. The efficiency η reaches the maximum value of $\eta \approx 50.6\%$ for $a \approx 5.3w_0$ and the corresponding coordinates for the start $r_1(a = 5.3w_0) \approx 0.19w_0$ and for the end $r_2(a = 5.3w_0) \approx 0.89w_0$ of the optical needle, when $w_0 = 2$mm. This dependency of the efficiency can be well understood considering that the amplitude of the TEM_{00} mode is modified.

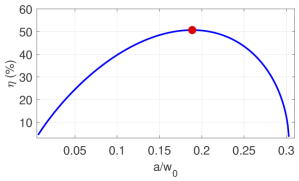

Fig. 2. Dependency of the efficiency η of the element on the parameter a, $w_0 = 2$ mm and $D = 4w_0$.

2.3. *Implementation of the Pancharatnam-Berry phase*

In our further investigation, we implement the optical needle using a combination of the GOE and a Pancharatnam-Berry phase (PBP) element. The GOE is a diffractive axicon with a Bessel angle α_0. The PBP element is encoded in such a way that its transmittance spatially varies and the intensity distribution of the incident TEM_{00} mode is transformed according to the Eq. (2). The principal schema is given in Fig. 3. The PBP element is implemented using birefringent nanogratings induced by direct femtosecond micromachining of glass [37]. This element is considered as a space-variant phase retarder and described using the Jones matrix formalism [19,33]. The general expression for the Jones matrix of the element is [12,37,38]

$$M = \begin{bmatrix} \cos^2\theta - \exp(i\,k\tau)\sin^2\theta & [1 - \exp(i\,k\tau)]\cos\theta\sin\theta \\ [1 - \exp(i\,k\tau)]\cos\theta\sin\theta & \exp(i\,k\tau)\cos^2\theta + \sin^2\theta \end{bmatrix}, \quad (5)$$

where $\theta = \theta(x, y)$ is the slow axis angle of the local birefringent nanograting and τ is the retardance. In the case when the retardance is equal to $\lambda/2$ and the incident TEM_{00} mode is linearly polarized (along the x axis), the output beam is

$$E' = ME\begin{bmatrix}1\\0\end{bmatrix} = \exp\left(-\frac{r^2}{w_0^2}\right)\begin{bmatrix}\cos\theta(x,y)\\ \sin\theta(x,y)\end{bmatrix}. \quad (6)$$

A linear polarizer whose optical axis coincides with the y axis is placed right after the PBP element, so the electric field is given by

$$E_{\text{out}} = \begin{bmatrix}0 & 0\\ 0 & 1\end{bmatrix}E' = \exp\left(-\frac{r^2}{w_0^2}\right)\begin{bmatrix}0\\ \sin\theta(x,y)\end{bmatrix}. \quad (7)$$

Optics EXPRESS

From the Eq. (6) we conclude that by locally changing the nanograting's slow axis angle $\theta(x, y)$ we locally alter the beam intensity distribution of the E_y component and filter out the E_x component. Finally, when a particular parameter a value is chosen, the locally varying slow axis of the PBP element is defined as

$$\theta(x, y) = \frac{\pi}{4} - \frac{1}{2}\arccos\left[\sqrt{\frac{I_{des}(x, y)}{\exp\left(-2\frac{x^2+y^2}{w_0^2}\right)}}\right]. \tag{8}$$

Here, the I_{des} is the desired intensity distribution, see Eq. (2). In our implementation, nevertheless, we alter the intensity distribution in Eq. (2) and rewrite it as

$$I_{des}(r) = \begin{cases} \frac{a}{r_1}\exp\left[-\frac{(r-r_1)^2}{(w_0/7)^2}\right], & 0<r<r_1-\Delta r, \\ \text{spline}, & r_1-\Delta r<r<r_1+\Delta r, \\ \frac{a}{r}, & r_1+\Delta r<r<r_2-\Delta r, \\ \text{spline}, & r_2-\Delta r<r<r_2+\Delta r, \\ \exp\left(-2\frac{r^2}{w_0^2}\right), & r_2+\Delta r<r<D/2, \end{cases} \tag{9}$$

where $\Delta r = w_0/12.5$. Here we have introduced two additional regions - designated as spline - specific sections, where smoothing using the basic spline method is performed [39]. This is important due to the fact, that on-axis intensity oscillations happen when abrupt intensity changes are present in the profile of the beam, which is incident on the axicon. An illustration of such modifications in the beam profile is given in Fig. 4(a). As a result of Eq. (9) the desired intensity I_{des} appears as in Fig. 4(a). The locally varying slow axis $\theta(x, y)$ of the PBP element is depicted in Fig. 4(b).

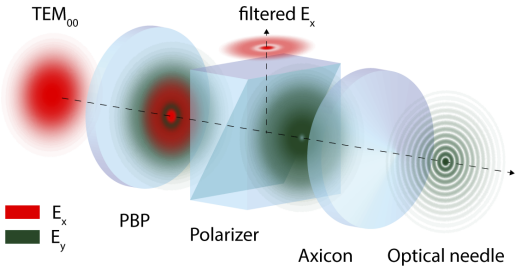

Fig. 3. A schema of the optical setup for the generation of an optical needle using a PBP element. The PBP element, a linear polarizer, and a diffractive axicon are denoted in the graph. Linearly polarized constituents E_x, E_y are depicted in red and green, respectively. Optical axes with their directions are shown in dashed black.

Optics EXPRESS

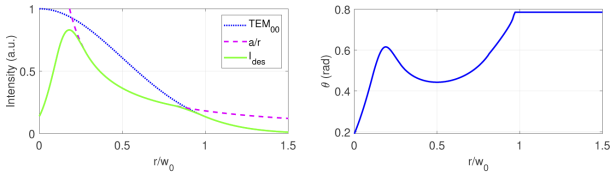

(a) (b)

Fig. 4. (a) A particular example depicting the intensity of the incident TEM_{00} mode (blue, dotted), the beam profile required for the generation of an optical needle (red, dashed), and the desired intensity profile used in this work (green, solid). (b) A radial dependency of the slow axis angle θ distribution of the PBP element on the ratio r/w_0.

3. Stability of the optical needle to imperfect conditions

In this section, we numerically investigate the stability of the formation of the optical needle under various imperfect conditions. As the optical setup, Fig. 3 contains three crucial elements – the PBP element, the linear polarizer, and an axicon – the setup is sensitive to various misplacements and misadjustments. Since the PBP element is rotationally symmetric the main cause of possible imperfections in the generated optical needle is the beam size mismatch and the transverse displacement of the element. The linear polarizer is non-sensitive to the transverse displacements, however, it has its own spatial orientation. When the orientation of the polarizer is mismatched with the orientation of the PBP element additional imperfections in the optical needle are introduced. Additionally, the axicon can be also displaced transversely, but it has no predefined orientation as its transmission function is azimuthally uniform.

These imperfect conditions can be characterized using the beamwidth of the TEM_{00} mode, the ellipticity of the incident beam, the angle β between the optical axis of the PBP and the linear polarizer, the displacement of the center of the PBP element in a relation to the optical axis of the incident beam in the transverse XY plane.

First, we investigate the stability of the optical needle to mismatches of the incident beam width w_0. We have designed an optical element that generates the optical needle when the beamwidth of the TEM_{00} mode is $w_0 = 2$ mm. Here, we introduce two smaller and two larger nonoptimal beam widths and numerically investigate both effects on the spatial filtering of the TEM_{00} modes and the on-axis intensity profile of the needle, see Fig. 5. We note that the constant intensity zone gains a positive tilt for beam waists that are bigger and negative for the beam waists that are smaller than the initial value ($w_0 = 2$ mm) as depicted in Fig. 5. Our numerical investigation reveals that the on-axis profile remains stable for $\Delta w_0 \approx \pm 0.1$ mm. Here we introduce an ellipticity parameter $\gamma = w_{0x}/w_{0y}$ - a ratio between the beam sizes (w_x, w_y) of the TEM_{00} mode in the x and y directions, respectively. Results are presented in the Fig. 5(c). We observe a similar, although less pronounced, effect on the axial profile of the optical needle.

As a next step, we investigate a scenario when the inner direction of the PBP element does not coincide with the axis of the linear polarizer. This situation is among the common ones as it might be difficult to ensure the perfect alignment of those orientations. As we assume that the optical axes coincide, the only possible mismatch is described by the angle β between those two directions. In our simulations the β angle is varying from $-60°$ to $+60°$, see Fig. 6. We additionally include two graphs showcasing this influence with a fine-grained change in the angle β, see Fig. 6(a,b). The numerical modeling reveals that a stable optical needle is generated when β angle is within the range of $\beta \pm 5°$.

Optics EXPRESS

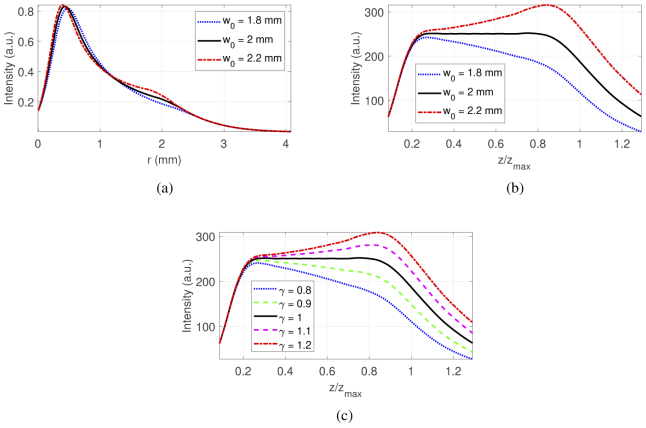

Fig. 5. Investigation of the effect caused by the mismatch of the incident beam width w_0 on the on-axis intensity profile of the optical needle. (a) The intensity distribution of the beam which enters the axicon (i.e. filtered by the PBP element and the linear polarizer) for different values of the incident beam widths w_0. The optimal beam width is w_0 = 2mm. (b) The intensity distribution of the optical needle for different values of the incident beam widths w_0. (c) The intensity distribution of the optical needle for different values of the ellipticity γ of the incident beam.

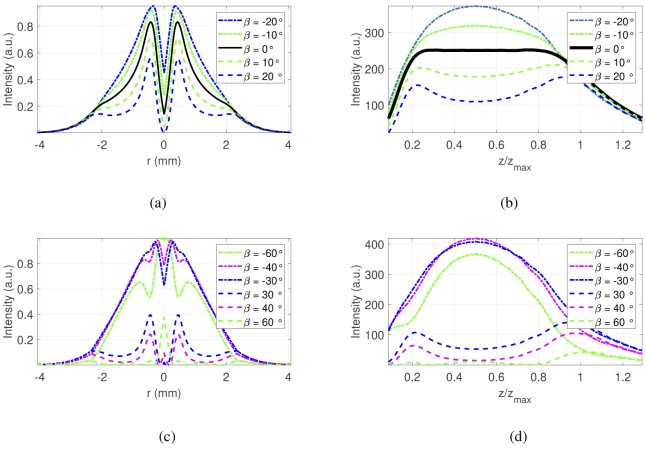

Fig. 6. Distortions in the optical needle are caused by the azimuthal misalignment angle β between the polarizer and the PBP element. (a,c) The transverse intensity distribution of the beam entering the axicon for different values of the angle β. (b,d) On-axis intensity distributions of the optical needle for different values of the angle β.

Optics EXPRESS

Here we note that the rotation of the PBP element has a two times larger effect than the rotation of the polarizer because the PBP element acts as a half-wave plate. When it rotates by 45 degrees the polarization of the exiting beam rotates by 90 degrees.

Lastly, we look into the effects caused by the displacement Δx between the center of the PBP element and the axis of the optical system. This situation is a common one because of the misadjustment of optical mounts holding elements. Therefore, we numerically calculate the spatial filtering of the incident beam, see Fig. 7(a,b). Expectedly, we observe the break of the radial symmetry, which has a strong effect on the axial intensity profile of the optical needle, see Fig. 7(c,d). Here, we additionally look at the whole transverse profile of the beam entering the axicon, see the first row in Fig. 7(e). Nevertheless, as the investigation reveals

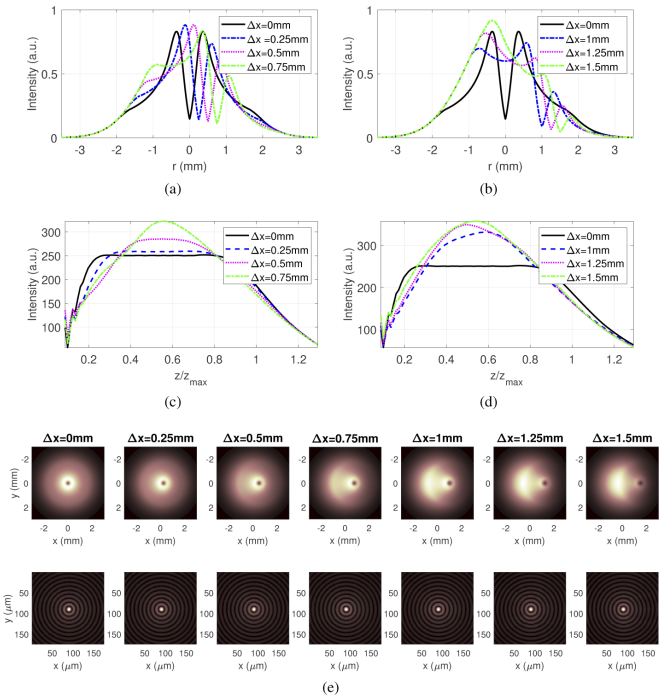

Fig. 7. Effects on the axial profile of the optical needle caused by the displacement Δx between the center of the PBP element and the axis of the optical system. (a,b) The intensity distribution of the beam enters the axicon for different values of the displacement Δx. (c,d) On-axis intensity distribution of the optical needle for different values of the displacement Δx. (e) An array of pictures demonstrating the effect of the displacement Δx on the spatial profile of the beam entering the axicon (first row) and on the transverse profile of the optical needle (second row) for different values of the displacement Δx. Pictures depict the cross-section of the corresponding beams.

the transverse profile of the optical needle remains pretty much the same, see the second row in Fig. 7(e). This means that the Bessel-like profile is stable, however, the on-axis intensity is strongly affected. At first, this result comes as a surprise, because the beam entering the axicon is axially non-symmetric, see Fig. 7(e, first row). However, it turns out that the azimuthal dependency is only slightly affected and the average intensity on the infinitesimally small ring of radius r changes more or less uniformly so the transverse beam profile is retained, but the on-axis amplitude changes.

Additionally, to explain these counter-intuitive results we have prepared Visualization 1, where an animated sequence compares non-displaced transverse intensity distribution of the optical needle with the displaced one. The third distribution which we present in the animated sequence the difference $(I_{\Delta x} - I_{\Delta x=0mm})$ for three values of Δx and several propagation distances z. As this investigation reveals, there is a small asymmetry caused by the transverse displacement of the PBP element. However, it affects mostly the outer-part of the optical needle, where the intensity is relatively low.

From this, we conclude that the optical needle stays stable up to displacement values of $\Delta x \pm 0.25$ mm.

4. Experimental verification

In this section, we experimentally verify the performance of a manufactured Pancharatnam-Berry phase element. Parameters of the PBP element were selected for further experimentation in high-power laser microprocessing. We have used an optical setup depicted in Fig. 8. A beam from a 1030 nm femtosecond laser "Pharos" (Light Conversion) operating at 5 ps, 100kHz, and 2W was attenuated with a half-waveplate (HWP) and a polarizer (Pol1) pair to 40mW (to avoid camera damage), then the size of the beam was adjusted with a variable beam expander (BE). The polarization of the Gaussian beam was modulated using a Pancharatnam-Berry phase element (PBPE presented in Fig. 9(a)) and one polarization component filtered out by a polarizer (Pol2). The resulting beam was recorded with a camera (CCD1) after routing it with a flipping mirror (FM). An optical needle was formed by sending a transformed beam (see Eq. (9)) into a diffractive axicon with a Bessel angle of 1.8° (Holo/Or, DA-030-I-Y-A). The exit beam was demagnified using a $4f$ setup consisting of lenses L1 (f = 150 mm) and L2 (f = 12 mm). Both an axicon and a $4f$ setup were mounted on a translational stage (z) which allowed to scan the exit beam along its propagation axis. The focal region of the system was scanned with an imaging setup comprising of 60x, NA 0.85 microscope objective, and a CCD camera which were mounted on a XY stage for easier navigation around the focal region. The transverse resolution was limited by the size of the pixel of the CCD camera. In the further investigation, it was about 0.5 µm.

The retardance of the PBP element is $\tau \approx \lambda/2$ and its diameter is $D \approx 6$ mm, see Fig. 9(a). The slow axis distribution θ was devised from Eq. (8) and is in good agreement with the experimentally determined one, see Fig. 9(a). The proposed approach can generate optical needles with high energy and quality because the PBP element has a high damage threshold of 63.4 J/cm^2 at 1064 nm in the nanosecond regime (10 ns) and 2.2 J/cm^2 at 1030 nm in the femtosecond regime (212 fs) [36]. Thus, the optical setup can be used in high-power experimentation if the attenuating part is removed.

From resulting scan images of the optical needle a three-dimensional intensity distribution was obtained, see Fig. 9(b). The length of the optical needle is around 600λ and its width is about 20λ. In general, the quality of the optical needle is good, we observe some non-uniformity and fluctuations due to the vibrations of the positioning stage and the noise from other experimental imperfections. Other causes of the non-uniformity are due to the discretization of the scan space, the camera exposure, mechanical shocks in the imaging setup during the measurement, and the step-size of the positioning stage (which is around 6 µm). We assume

Optics EXPRESS

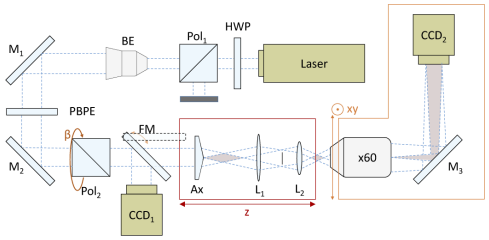

Fig. 8. An experimental setup for the generation of the optical needle under various imperfect conditions. In this schema: a half-waveplate (HWP), polarizers (Pol1, Pol2), a variable beam expander (BE), Pancharatnam-Berry phase element (PBPE), cameras (CCD1, CCD2), a flipping mirror (FM), lenses L1 (f = 150 mm) and L2 (f = 12 mm), mirrors (M1, M2, M3), a diffractive axicon (Ax), a femtosecond laser "Pharos" (Laser).

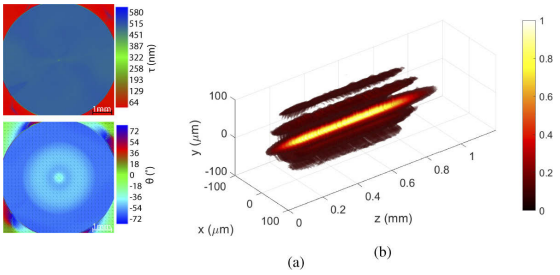

Fig. 9. (a) Distribution of the retardance τ and the slow axis θ in the PBP element manufactured by Altechna R&D. (b) 3D intensity distribution in the optical needle created by a combination of the PBP element, a linear polarizer, and an axicon.

slight misalignment of secondary optical elements and some small deviations in the PBP element due to the manufacturing process inaccuracy.

Similarly as in the theoretical section, first we analyze the influence of the mismatch in the beam width w_0. In this experiment, 3 different beam diameters were introduced: 3.6 mm, 4 mm, and 4.4 mm at the $1/e^2$ of the beam peak intensity. We have used an optical telescope to change the beam diameter, therefore amplitudes are changing too. The intensity distribution of the optical needle was mapped in the focal region by recording its transverse profile at different longitudinal coordinates. In total, 200 images of the transverse profiles were taken, each separated by Δz = 6μm. Maximal values of the central peak intensities were detected and are presented in Fig. 10. For the correct incident beam of diameter $2w_0$ = 4 mm, the on-axis profile was constant. As expected, in the case of a wider ($2w_0$ = 4.4 mm) entering beam, the optical needle loses its shape as the intensity towards the end increases. A smaller ($2w_0$ = 3.6 mm) beam at the entrance results in an opposite effect, the intensity towards the end decreases. This behavior is in accordance with the theoretical expectations, see Fig. 5(b). We observe small differences due to the experimental implementation of the beam size control. We proceed now to the analysis of the misalignment of the polarizer and the PBP element. In the experiment, we change the angle (β) between the PBP element and the polarizer. Here, the PBP position and the orientation

Optics EXPRESS

are fixed and the polarizing cube is rotated instead. We note again that due to the properties of nano-gratings (the PBP element behaves as a half-wave plate) if the PBP element is rotated instead of the polarizer, a half-angle rotation of the PBP element gives the same effect as a whole-angle rotation of the polarizer. The transverse intensity distributions of the beam before the axicon (after shaping it with the PBP element and the polarizer) for several different mismatch angles β are depicted in Fig. 11. When the angle β is zero, the intensity in the beam center drops in the same manner as in the Eq. (9), where the a/r dependency changes, see Fig. 4(a). When the angle β decreases to -40° the beam becomes similar to a Gaussian beam, see Fig. 11.

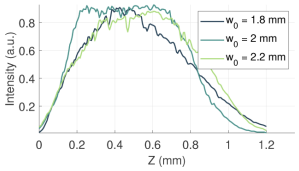

Fig. 10. Experimental investigation of the effect caused by the mismatch of the incident beam width w_0 on the axial intensity profile of the optical needle. The optimal beam width is w_0 = 2mm.

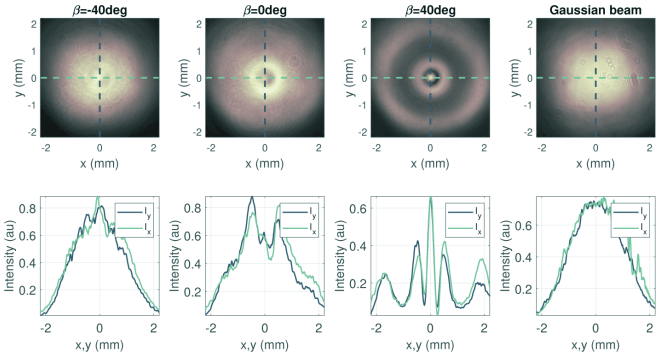

Fig. 11. Experimental investigation of distortions in the beam impinging the axicon caused by the azimuthal misalignment between the polarizer and the PBP element. (first row) Intensity distributions of the beam entering the axicon for different values of the angle β. (second row) Cross-sections of the pictures in the first row. The beamwidth w_0 = 2mm.

Experimentally detected on-axis intensity distributions usually are concave or convex depending on the value of the mismatch angle β, see Fig. 12. This behavior of the on-axis intensity distribution is in accordance with the theoretical expectations as in Fig. 6(b,d).

Lastly, we investigate experimentally the effects caused by the mismatch between the center point of the PBP element and the optical axis of the system. A Gaussian beam of $2w_0$ = 4 mm impinges onto the PBP element which is shifted from the axis up to Δx = 1.5 mm with a 0.25 mm step. The resulting transverse beam profiles registered after the polarizer are shown in Fig. 13(a). Comparing with simulation results (Fig. 7(e) first row), diffraction fringes are present in experimental results. They are caused by the edge of the inscribed structure which is only 6

Optics EXPRESS

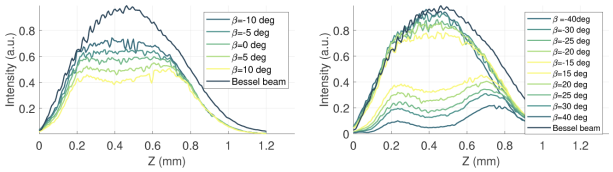

Fig. 12. Experimental investigation of distortions in the optical needle caused by the azimuthal misalignment between the polarizer and the PBP element. Axial intensity distributions for various values of the mismatch angle $\beta = 0°, \pm 5°, \pm 10°$ (a) and $\beta = \pm 15°, \pm 20°, \pm 25°, \pm 30°, \pm 40°$ (b). For a comparison, the on-axis distribution of the Bessel beam is provided (blue star). The beam width $w_0 = 2$mm.

mm in diameter. As expected, the transverse profiles of the optical needle are in line with the numerical simulations and prove that the asymmetry in the Bessel beam is indeed very small for values of the transversal displacements under consideration Fig. 13(b). It seems, that the non-uniform azimuthal modulation disturbs only the very periphery of the beam. Cross-section

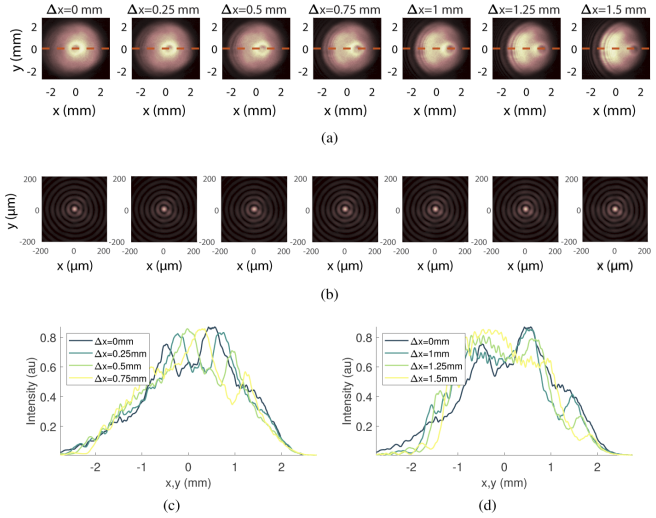

Fig. 13. Experimentally observed effects on the beam profile before the axicon caused by the displacement Δx between the center of the PBP element and the optical axis. (a) The intensity distribution of the beam which enters the axicon for different values of the displacement Δx. (b) Transverse profiles of the optical needle. (c, d) Cross-sections of the beam profile in the first row for different values of the displacement Δx. The beamwidth $w_0 = 2$mm.

intensity distributions presented in Fig. 13(c) and (d) are predominantly on par with the theoretical estimations (Fig. 7(a) and (b)).

We verify experimentally the influence of the lateral shift of the PBP element on the formation of the optical needle. Results are presented in Fig. 14. The optical needle is preserved when the displacement is small (less than 0.25 mm). Starting from $\Delta x = 0.3$ mm axial intensity distribution gradually gains steepness as it develops a convex shape. This behavior is in accordance with the simulation results depicted in Fig. 7(c) and (d). Of course, some sporadic values in the axial intensity profile are present due to the reasons already discussed above. Our experimental investigation reveals that the transverse intensity profile of the optical needle sustains its Bessel-like beam shape for all values of the displacement Δx as in the theoretical consideration.

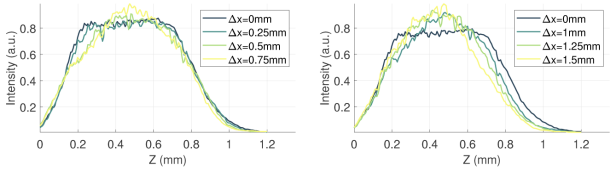

Fig. 14. Experimentally observed axial profiles of the optical needle for different values of displacement $\Delta x = 0, 0.25, 0.5, 0.75$ mm (a) and 1.0, 1.25, 1.5 mm (b). The beam width $w_0 = 2$mm.

5. Conclusions

We have introduced an amplitude-based optical element for the modification of the beam profile entering the axicon to generate a Bessel-like optical needle with a smooth and constant on-axis intensity profile. We implement this element by introducing the space-domain Pancharatnam-Berry phase (PBP). Our implementation is based on transparent nanogratings inscribed in the glass by femtosecond laser pulses. Elements produced this way withstand very high laser beam powers both in nanosecond and femtosecond regimes. This makes such an optical setup attractive for high-power applications of Bessel beams with smooth and flat axial profiles.

In particular, we have fabricated a PBP element generating an optical needle with the length of 600λ and the width of 20λ. The efficiency of the PBP element is 50%, for the $a = 5.3w_0$. In this case the optical needle is created in the region $z_1 = 0.19z_{max}$ and $z_2 = 0.89z_{max}$, where $z_{max} = w_0 \cot \alpha_0$. This PBP element was successfully manufactured by Altechna R&D and the experiment is in good agreement with theoretical expectations. The element was being tested in a high-power laser microfabrication setup, results will be presented elsewhere.

We have both numerically and experimentally investigated the stability of an optical needle generation under various imperfect conditions. It turns out that a wider beam entering the system results in a Bessel-like needle with steadily increasing on-axis intensity. When the beam is smaller the on-axis intensity decreases. The ellipticity of the beam has the same but less pronounced effect - when one of the beam widths is larger the on-axis intensity rises, when one of the beam widths is smaller - it drops. Surprisingly for the ellipticities of the incoming beam we have considered the transverse profile of the needle remains Bessel-like. This can be understood by keeping in mind that the azimuthal asymmetry is averaged. The optical needle was preserved for $|\Delta w_0|/w_0 \approx 0.05$.

The azimuthal misalignment of the PBP element and the linear polarizer has a more complicated effect since the polarizer is responsible for filtering out unwanted components and ensuring the

proper functioning of the PBP element. In this case, for the values of the azimuthal misalignment $\beta = \in -40°, 40°$ the optical needle is distorted - the axial dependency becomes concave or convex. For values of β>40°, the optical needle splits into few parts with rather complicated axial intensity. We conclude that the optical needle stays smooth for $|\beta|$<5°.

Lastly, the effect caused either by the transverse displacement of the PBP element or by the transverse displacement of the beam was looked into. The displacement of the beam gives in general a steadily rising axial intensity profile. However, as this situation is not a common one, we have presented only results for the displacement of the PBP element as in our opinion it is a more common misalignment. In this case, the axial intensity profile becomes convex. The optical needle is insensitive to the displacements of $\Delta x/w_0$<0.125. Surprisingly the transverse profile preserves its Bessel-like shape.

Funding. Lietuvos Mokslo Taryba (09.3.3-LMT-K-712-01-0167).

Acknowledgments. This research is funded by the European Social Fund according to the activity 'Improvement of researchers' qualification by implementing world-class R&D projects' of Measure No. 09.3.3-LMT-K-712.

Disclosures. The authors declare no conflicts of interest

Data availability. Data underlying the results presented in this paper are not publicly available at this time but may be obtained from the authors upon reasonable request.

References

1. F. M. Dickey and T. E. Lizotte, *Laser beam shaping applications*, vol. 1 (CRC, 2017).
2. J. Durnin, J. Miceli Jr, and J. H. Eberly, "Diffraction-free beams," Phys. Rev. Lett. **58**(15), 1499–1501 (1987).
3. J. Durnin, "Exact solutions for nondiffracting beams. i. the scalar theory," J. Opt. Soc. Am. A **4**(4), 651–654 (1987).
4. V. Jarutis, R. Paškauskas, and A. Stabinis, "Focusing of laguerre–gaussian beams by axicon," Opt. Commun. **184**(1-4), 105–112 (2000).
5. O. Brzobohatý, T. Čižmár, and P. Zemánek, "High quality quasi-bessel beam generated by round-tip axicon," Opt. Express **16**(17), 12688–12700 (2008).
6. A. Vasara, J. Turunen, and A. T. Friberg, "Realization of general nondiffracting beams with computer-generated holograms," J. Opt. Soc. Am. A **6**(11), 1748–1754 (1989).
7. J. Sochacki, Z. Jaroszewicz, L. R. Staroński, and A. Kołodziejczyk, "Annular-aperture logarithmic axicon," J. Opt. Soc. Am. A **10**(8), 1765–1768 (1993).
8. Z. Jaroszewicz, J. Sochacki, A. Kołodziejczyk, and L. R. Staronski, "Apodized annular-aperture logarithmic axicon: smoothness and uniformity of intensity distributions," Opt. Lett. **18**(22), 1893–1895 (1993).
9. R. Dorn, S. Quabis, and G. Leuchs, "Sharper focus for a radially polarized light beam," Phys. Rev. Lett. **91**(23), 233901 (2003).
10. M. Zhu, Q. Cao, and H. Gao, "Creation of a 50, 000 λ long needle-like field with 0.36 λ width," J. Opt. Soc. Am. A **31**(3), 500–504 (2014).
11. A. Rubano, F. Cardano, B. Piccirillo, and L. Marrucci, "Q-plate technology: a progress review," J. Opt. Soc. Am. B **36**(5), D70–D87 (2019).
12. M. Beresna, M. Gecevičius, P. G. Kazansky, and T. Gertus, "Radially polarized optical vortex converter created by femtosecond laser nanostructuring of glass," Appl. Phys. Lett. **98**(20), 201101 (2011).
13. C. Pfeiffer and A. Grbic, "Controlling vector bessel beams with metasurfaces," Phys. Rev. Appl. **2**(4), 044012 (2014).
14. F. Aieta, P. Genevet, M. A. Kats, N. Yu, R. Blanchard, Z. Gaburro, and F. Capasso, "Aberration-free ultrathin flat lenses and axicons at telecom wavelengths based on plasmonic metasurfaces," Nano Lett. **12**(9), 4932–4936 (2012).
15. T. Čižmár and K. Dholakia, "Tunable bessel light modes: engineering the axial propagation," Opt. Express **17**(18), 15558–15570 (2009).
16. S. Orlov, A. Juršėnas, and E. Nacius, "Optical bessel-like beams with engineered axial phase and intensity distribution," J. Laser Micro/Nanoeng. **13**, 244–248 (2018).
17. R. Dharmavarapu, S. Bhattacharya, and S. Juodkazis, "Diffractive optics for axial intensity shaping of bessel beams," J. Opt. **20**(8), 085606 (2018).
18. S. Orlov, A. Juršėnas, J. Baltrukonis, and V. Jukna, "Controllable spatial array of bessel-like beams with independent axial intensity distributions for laser microprocessing," J. Laser Micro/Nanoeng. **13**, 324–329 (2018).
19. R. C. Jones, "A new calculus for the treatment of optical systemsi. description and discussion of the calculus," J. Opt. Soc. Am. **31**(7), 488–493 (1941).
20. C. P. Jisha, S. Nolte, and A. Alberucci, "Geometric phase in optics: From wavefront manipulation to waveguiding," Laser Photonics Rev. **2021**, 2100003 (2021).
21. J. C. Gutiérrez-Vega, "Optical phase of inhomogeneous jones matrices: retardance and ortho-transmission states," Opt. Lett. **45**(7), 1639–1642 (2020).
22. N. Yu and F. Capasso, "Flat optics with designer metasurfaces," Nat. Mater. **13**(2), 139–150 (2014).

23. Y. Bao, L. Wen, Q. Chen, C.-W. Qiu, and B. Li, "Toward the capacity limit of 2d planar jones matrix with a single-layer metasurface," Sci. Adv. **7**(25), eabh0365 (2021).
24. H.-T. Chen, A. J. Taylor, and N. Yu, "A review of metasurfaces: physics and applications," Rep. Prog. Phys. **79**(7), 076401 (2016).
25. M. K. Hedayati and M. Elbahri, "Review of metasurface plasmonic structural color," Plasmonics **12**(5), 1463–1479 (2017).
26. J. Hu, S. Bandyopadhyay, Y.-h. Liu, and L.-y. Shao, "A review on metasurface: From principle to smart metadevices," Front. Phys. **8**, 502 (2021).
27. J. Kim, Y. Li, M. N. Miskiewicz, C. Oh, M. W. Kudenov, and M. J. Escuti, "Fabrication of ideal geometric-phase holograms with arbitrary wavefronts," Optica **2**(11), 958–964 (2015).
28. Y. Shimotsuma, P. G. Kazansky, J. Qiu, and K. Hirao, "Self-organized nanogratings in glass irradiated by ultrashort light pulses," Phys. Rev. Lett. **91**(24), 247405 (2003).
29. M. Sakakura, Y. Lei, L. Wang, Y.-H. Yu, and P. G. Kazansky, "Ultralow-loss geometric phase and polarization shaping by ultrafast laser writing in silica glass," Light: Sci. Appl. **9**(1), 15 (2020).
30. R. Drevinskas and P. G. Kazansky, "High-performance geometric phase elements in silica glass," APL Photonics **2**(6), 066104 (2017).
31. S. Pancharatnam, "Generalized theory of interference and its applications, *Proceedings of the Indian Academy of Sciences-Section A*, vol. 44 (Springer, 1956), pp. 398–417.
32. M. V. Berry, "The adiabatic phase and pancharatnam's phase for polarized light," J. Mod. Opt. **34**(11), 1401–1407 (1987).
33. P. Gotovski, P. Šlevas, E. Nacius, V. Jukna, S. Orlov, J. Baltrukonis, O. Ulčinas, and T. Gertus, "Formation of optical needles by pancharatnam-berry phase element for laser-induced modifications in transparent materials," in *Laser-based Micro-and Nanoprocessing XIV*, vol. 11268 (International Society for Optics and Photonics, 2020), p. 112681Y.
34. J. Baltrukonis, O. Ulčinas, S. Orlov, and V. Jukna, "Void and micro-crack generation in transparent materials with high-energy first-order vector bessel beam," J. Opt. Soc. Am. B **37**(7), 2121–2127 (2020).
35. J. Baltrukonis, O. Ulčinas, S. Orlov, and V. Jukna, "High-order vector bessel-gauss beams for laser micromachining of transparent materials," Phys. Rev. Appl. **16**(3), 034001 (2021).
36. "Laser-induced damage threshold (ldt) measurement report," https://wophotonics.com/wp-content/uploads/2020/07/LIDT-result-fs-regime.pdf, accessed 2021-07-23.
37. M. Beresna, M. Gecevičius, and P. G. Kazansky, "Polarization sensitive elements fabricated by femtosecond laser nanostructuring of glass," Opt. Mater. Express **1**(4), 783–795 (2011).
38. M. Gecevičius, Polarization sensitive optical elements by ultrafast laser nanostructuring of glass, Ph.D. thesis, University of Southampton (2015).
39. C. De Boor and C. De Boor, *A practical guide to splines*, vol. 27 (springer-verlag, New York, 1978).

P3

Investigation of the Pancharatnam–Berry phase element for the generation of the top-hat beam

P. Gotovski, **P. Šlevas**, S. Orlov, O. Ulčinas, V. Jukna, A. Urbas

Journal of Optics, 24(3), 035607 (2022)
DOI: 10.1088/2040-8986/ac4317
https://iopscience.iop.org/article/10.1088/2040-8986/ac4317

IOP Publishing Journal of Optics
J. Opt. **24** (2022) 035607 (9pp) https://doi.org/10.1088/2040-8986/ac4317

Investigation of the Pancharatnam–Berry phase element for the generation of the top-hat beam

P Gotovski[1], P Šlevas[1,2], S Orlov[1,*], O Ulčinas[1,2], V Jukna[1,3] and A Urbas[1,2]

[1] Center for Physical Sciences and Technology, Sauletekio av. 3, LT-10257 Vilnius, Lithuania
[2] Workshop of Photonics, Mokslininku st. 6A, LT-08412 Vilnius, Lithuania
[3] Laser Research Center, Vilnius University, Saulėtekio Avenue 10, LT, 10223 Vilnius, Lithuania

E-mail: sergejus.orlovas@ftmc.lt

Received 18 August 2021, revised 9 December 2021
Accepted for publication 14 December 2021
Published 9 February 2022

Abstract
Within optics, the Pancharatnam–Berry phase enables the design and creation of various flat special optical elements such as top-hat converters. We present a study on engineering efficient vectorial top-hat converters inscribed in glass by high-power femtosecond laser pulses. We phase-encode a top-hat converter and demonstrate how its quality is influenced by various parameters. We investigate theoretically the generation of the top-hat beam under imperfect conditions such as the mismatch of the incident beam width or the misalignment of the center of the converter. Experimental verification of the concept is also presented.

Keywords: Pancharatnam–Berry phase, geometrical phase, beam shaping, centered optical systems

(Some figures may appear in colour only in the online journal)

1. Introduction

Optical elements are essential in transforming an optical beam for various applications. The traditional way of manufacturing such optical elements is to precisely polish the surface of a transparent material, which will transform the beam by refraction. An unconventional, but very promising, process for manufacturing optical elements is to controllably distribute small-scale structures on the surface or inside the volume of the element [1]. Spatial variation of size, shape, material and orientations of these small-scale structures results in changes to the local (geometrical) phase of a photonic element [2] and ultimately alters the incoming beam. The local geometrical phase is usually referred to as the Pancharatnam–Berry phase (PBP) [3, 4]. The PBP element finds its use in many areas such as metalenses with high numerical aperture [5], or special optics transforming the beam intensity to a top-hat beam [6–8]. Advancements in the fields of lithography, laser microprocessing, chemical etching, thin film deposition, etc have enabled a fine control of these small-scale structures over a large area and made possible the production of high-quality optical components [9, 10].

Such special optics are becoming highly functional due to the concept of so-called metasurfaces, where individual meta-atoms are arranged with a flexibly changing internal orientation (and the PBP) [11–13]. In most cases, such structures (meta-atoms) are smaller than the wavelength of the interacting optical field. The shape, material, orientation and other properties of meta-atoms can be changed fairly easily [14]. Under these conditions, light behaves non-intuitively, and phenomena such as slow light, chirality or birefringence are observed [15, 16]. Two-dimensional functional meta-surfaces suitable for different wavelengths are created by variation of the scale of the structures. This makes PBP elements advantageous in many implementations because they can be tuned for a broad spectrum of radiation sources ranging from ultraviolet [17] to THz [18, 19] and even radio frequencies [20]. An additional advantage of such elements is their flatness, which is caused by the fact that changes in the beam phase appear not

* Author to whom any correspondence should be addressed.

because of the locally different optical path but rather due to the locally induced phase difference between two orthogonal components of the electric field and the possibility to easily produce phase wrapping [21, 22].

In this work, we utilize PBP-based elements, based on the formation of nanogratings inside the volume of fused silica [23]. When an ultrashort linearly polarized laser beam is focused inside the sample with the fluence close to the damage threshold, a type II volume modification occurs and a birefringent nanograting is formed. Due to the repetitive nonlinear interaction of a laser and fused silica lattice a periodic volume structure is induced. The orientation and the depth of the nanogratings can be flexibly controlled via rotation of the pulse polarization and change of the pulse energy. This technology allows one to manufacture spatially distributed variable waveplates, with an S-plate [24] being a good example. Since the nanograting structure can be seen as a metasurface, it is convincingly described via a geometric phase or PBP [25, 26]. The actual optical elements with custom orientation of the nanograting and with custom retardance are usually called geometric phase optical elements (GPOEs). Those nanogratings act as meta-atoms and are applied for the spatial manipulation of amplitude, phase or polarization of the incoming beam [27–34]. The main advantage of such elements over other implementations is a high optical damage threshold, reaching 2.2 J cm^{-2} at 1030 nm wavelength (212 fs regime) or 63.4 J cm^{-2} at 1064 nm wavelength (10 ns regime) [35, 36]. The material optical damage threshold for fused silica is very close to that, therefore these optical PBP elements are flexible and reliable choices for beam shaping in laser micromachining [37–43].

The generation of various exotic vector electromagnetic beams—radially polarized light [44], optical vortices [45], Bessel beams [46], spin-dependent accelerating beams [47] and complex source vector vortices [48, 49]—is increasingly associated with PBP-related special optics [50], which opens up new possibilities for precise control of the wavefront and polarization state in various applications [35].

Here, we are interested in beam shaping elements for high-power laser microprocessing applications. It was already shown that it is beneficial to have a non-Gaussian irradiance profile in the microprocessing of transparent materials, such as Bessel beams [51], optical needles [32], knives [52] and shovels [53]. Most high-power interactions of laser light and matter are threshold-based [54]. Therefore, it is beneficial to form a profile of constant intensity over a given focal area (so-called top-hat beams) [6, 55, 56]. Top-hat beams are applied in the processing of transparent materials, semiconductor wafers and nonlinear frequency conversion [57]. More accurate and predictable laser microfabrication with cleaner cuts and sharper edges becomes possible [58]. However, additional system complexity and costs are introduced [59, 60]. In our previous work, we have proposed a new approach to generate top-hat beams via GPOE that enables a reduction of the number of optical elements in the scheme [8]. This element is based on transmittance (i.e. amplitude) modulation, therefore despite the high quality of the beam achieved, the energy loss is substantial.

In this publication, we introduce a phase-modulating PBP element based on the inscription of nanogratings inside the fused silica for the generation of the top-hat beam. We discuss its properties, study its performance and quality, and investigate its implementation. We devise a pair of top-hat generating PBP elements that are manufactured by our partner 'Altechna R&D' ('Workshop of Photonics', see Special Optics [35]). A systematic numerical and experimental investigation of the quality and feasibility of such elements is performed and results are presented. We study the behavior of the PBP element-generated beam under various imperfect conditions. Our main concern is the offset of the beamwidth of the laser beam impinging onto the PBP element and the transverse misplacement of the PBP element with respect to the beam propagation axis.

2. Theoretical methods

2.1. Gauss to top-hat transformation

The electric field E_{G} of the Gaussian beam is defined as

$$E_{\mathrm{G}}(\rho) = E_0 \mathrm{e}^{-\rho^2/w_0^2}, \tag{1}$$

where E_0 is the amplitude, ρ is the radial coordinate and w_0 is the beam waist. From an experimental point of view, it is easier to measure the beam waist $d_0 = w_0/\sqrt{2}$, which gives the beam radius at the $1/e$ level from the peak beam intensity. The action of a phase-modulating element that transforms the field of the incident beam into the electric field E_{TH} of a top-hat beam at distance z_0 from the phase element is depicted in figure 1. The optical element redistributes the intensity of the incident Gaussian beam into a top-hat beam, and this action can be understood as a change in the density of individual light rays that is achieved by the phase modulation of the input beam.

The derivation of the phase distribution required to achieve this action is based on the energy conservation law, which is defined as

$$\int_0^{2\pi}\int_0^{\rho_{\max}} I_{\mathrm{G}}\rho\,\mathrm{d}\rho\,\mathrm{d}\varphi = \int_0^{2\pi}\int_0^{R_{\max}} I_{\mathrm{TH}}R\,\mathrm{d}R\,\mathrm{d}\varphi, \tag{2}$$

where $I_{\mathrm{G}} = |E_{\mathrm{G}}(\rho)|^2$ is the incident Gaussian beam intensity, $I_{\mathrm{TH}} = |E_{\mathrm{TH}}(\rho)|^2$ is the intensity of the top-hat beam, $\rho_{\max} = 1.7\,w_0$ is the radius covering 95% of the total innermost incident Gaussian beam energy, $R_{\max}$ is the radius of the top-hat beam and φ is the azimuthal angle. The target function $I_{\mathrm{TH}}(R)$ in equation (2) is required to be a constant $I_{\mathrm{TH}}(R) = I_{\mathrm{TH}}$. The integration of both sides of equation (2) results in

$$I_{\mathrm{TH}} = |E_0|^2 \frac{w_0^2\left(1-\mathrm{e}^{-2\rho_{\max}^2/w_0^2}\right)}{2R_{\max}^2}. \tag{3}$$

For the sake of simplicity, we can define $|E_0|^2$ as equal to 1. In this case, the intensity I_{TH} is normalized to the maximum intensity of the incident Gaussian beam. Next, we integrate equation (2) with variable integral bounds for the second time

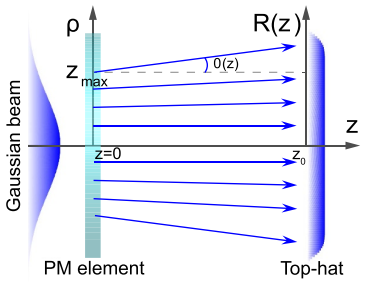

Figure 1. Depiction of a phase-modulating (PM) element that converts the electric field E_G of the Gaussian beam into a top-hat beam. $R(\rho)$ is the radial distance at which the light ray coming from the point $(\rho, z=0)$ arrives at the plane $(z=z_0)$. The angle $\beta(\rho)$ is the angle at which the ray crosses the z-axis.

and use the derived expression for I_{TH} to arrive at the following equation that defines the ray mapping from the initial plane at $z=0$ to the one placed at $z=z_0$ (see figure 1):

$$R(\rho) = \pm R_{max}\sqrt{\frac{1-e^{-2\rho^2/w_0^2}}{1-e^{-2\rho_{max}^2/w_0^2}}}. \quad (4)$$

The optical element performs spatially-dependent phase modulation of the incident beam so that immediately behind the optical element its complex amplitude distribution $E_G(\rho)$ is transformed to $E_t(\rho) = \exp[i\Phi(\rho)]E_G(\rho)$. The gradient of the phase modulation $\Phi(\rho)$ is

$$\frac{d\Phi(\rho)}{d\rho} = k\sin\beta(\rho), \quad (5)$$

where $\beta(\rho)$ is the angle of the ray coming from the initial plane at $z=0$ with respect to the z axis as presented in figure 1 and k is the wavenumber. By integrating equation (5) and using trigonometric identities, the phase modulation function $\Phi(\rho)$ is written in integral form as

$$\Phi(\rho) = \int_0^{\rho} k\sin\beta(r)\,dr, \quad (6)$$

where

$$\sin\beta(r) = \frac{\tan\beta(r)}{\sqrt{1+\tan^2\beta(r)}}, \quad (7)$$

and

$$\tan\beta(r) = \frac{R(r)-r}{z_0}. \quad (8)$$

The complex integration operation in equation (6) is approximated as

$$\Phi(\rho+d\rho) = \Phi(\rho) + k\sin\beta(\rho+d\rho)\,d\rho. \quad (9)$$

An example of the phase modulation profile and the simulated intensity distribution at $z=z_0$ is presented in figure 2.

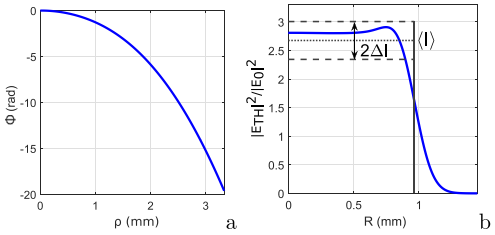

Figure 2. Phase profile of the PM element (a) and the diffraction intensity pattern at z_0 (b),which resembles the top-hat beam. Parameters are $z_0 = 0.06z_r$, $z_r = 2\pi d_0^2/\lambda$ (the Rayleigh length), $R_{max}/\rho_{max} = 0.25$, $d_0 = 1.7$ mm and $\lambda = 1$ μm.

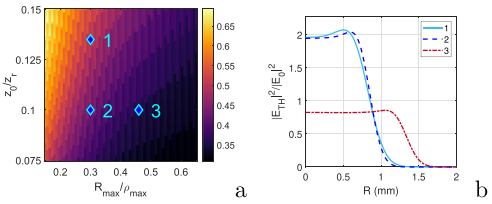

Figure 3. Distribution of the quality criterion μ (a) for the different R_{max}/ρ_{max} and z_0 values. 1D cross sections of the transverse intensity distribution $|E_{TH}|^2$ of the top-hat beam at $z=z_0$ (b). Cross-section numbers represent corresponding points in the graph on the left. $z_r = 2\pi w_0^2/\lambda$ (the Rayleigh length).

The intensity distribution is numerically calculated using the Fresnel diffraction theory [61]. The generated beam resembles the top-hat beam, i.e. has a sharp increase in intensity and almost constant intensity in the vicinity of the beam center.

2.2. Quality of the top-hat generation

The computed intensity profile presented in figure 2(b) deviates from the ideal top-hat profile. Its intensity varies in a certain range and the edge of the top-hat is not abrupt but has a slope. To define the quality of the beam and its dependence on the parameters R_{max}/ρ_{max} and z_0 we define a quality criterion as

$$\mu = \frac{\Delta I}{\langle I\rangle}, \quad (10)$$

where $\langle I\rangle$ is the mean intensity and ΔI is the standard deviation; both of them are evaluated in the most central part of the top-hat beam that constitutes 90% of the total beam energy (see figure 2(b)). After determining realistic ranges of R_{max}/ρ_{max} and z_0, the 2D plot in figure 3(a) depicts the distribution of the numerically obtained quality parameter μ of the diffracted beam. Three examples of the simulated diffracted beam's intensity distributions with different R_{max}/ρ_{max} and z_0 values are presented in figure 3(b) and their relative positions

in the graph determining the top-hat beam quality are depicted in figure 3(a).

2.3. Phase modulation using a PBP element

We implement the phase element using the PBP [3, 4]. Our approach is based on birefringent nanogratings induced by direct femtosecond micromachining in a glass volume [24]. Such nanogratings are self-assembling structures with the direction of the fast axis perpendicular to the incident beam polarization. The retardance of these structures is related to the length of nanogratings. Precise control of incident beam parameters allows for the creation of a beam-shaping element. This element is a space-variant phase retarder and is described using the Jones matrix formalism [62]. The general expression of the transmission matrix of the element is

$$M = \begin{bmatrix} \cos^2\alpha + \mathrm{e}^{\mathrm{i}k\sigma}\sin^2\alpha & \left(1-\mathrm{e}^{\mathrm{i}k\sigma}\right)\cos\alpha\sin\alpha \\ \left(1-\mathrm{e}^{\mathrm{i}k\sigma}\right)\cos\alpha\sin\alpha & \mathrm{e}^{\mathrm{i}k\sigma}\cos^2\alpha + \sin^2\alpha \end{bmatrix} \quad (11)$$

where α is the slow-axis angle of the local birefringent nanograting and σ is the retardance. In the case when the retardance is equal to $\lambda/2$ and the incident beam is circularly polarized, $\vec{E}_{\mathrm{inc}} = \begin{bmatrix} 1 \\ \mp\mathrm{i} \end{bmatrix}$, the output beam is also circularly polarized and

$$\vec{E}_{\mathrm{out}} = M\vec{E}_{\mathrm{inc}} = \mathrm{e}^{2\mathrm{i}\alpha}\begin{bmatrix} 1 \\ \pm\mathrm{i} \end{bmatrix}. \quad (12)$$

Local changes to the slow-axis angle α of the nanogratings modulate the phase front of the incident beam; see equation (12). In what follows, the linear phase modulation of the blazed grating is considered together with the phase Φ to separate the undiffracted beam from the desired intensity pattern at $z = z_0$,

$$\alpha(x,y) = \Phi(x,y)/2 + \gamma x, \quad (13)$$

where γ is the deflection coefficient of the grating.

3. Numerical simulation

In this section, we investigate the performance of the Gaussian to top-hat converter under various imperfect conditions. We are concentrating mainly on the two following situations: the width of the incoming beam is misadjusted and the PBP element is transversely misplaced with respect to the propagation axis.

3.1. Misadjustment of the width of the incident Gaussian beam

The phase distribution encoded in the PBP element defined as in equation (6) is valid only for a specific beam, i.e. centered at the element center and with given beam width w_0; see equation (6). Therefore, aligning the axes of optical elements as well as finding their proper diameter is a typical experimental challenge. For example, for some complex elements, treating $1/\mathrm{e}^2$ as the limit of beam diameter is not sufficient because distant edges, up to, say, $1/\mathrm{e}^3$, may have a significant influence on the result. It is natural to ask ourselves how sensitive the top-hat profile is to such imperfect conditions.

We have performed a numerical experiment in which we have designed PBP elements (to be used with $\lambda = 1030$ nm wavelength laser beams) for the generation of a top-hat profile having a radius of $R_{\max} = 1.38$ mm from a Gaussian beam of width $d_0 = 1.25$ mm at the distance $z_0 = 1$ m from the PBP element. This amounts to $R_{\max}/\rho_{\max} = 0.46$ and $z_0/z_{\mathrm{r}} = 0.1$. This situation is reflected in figure 3 (point 3). In this set of simulations, we have also determined the effect that the blazed grating (see equation (13)) has on the transverse profile of the top-hat. Interestingly, the profile of the top-hat does not change very much with small realistic changes of the deflection coefficient γ. The deflection must be by at least $R_{\max}$ at z_0 to be able to block the zero-order diffraction maximum coming from the discretization of the experimentally fabricated element. In our experiment, γ was 1.6 deg mm^{-1} so as to deflect the beam by a required amount at z_0. Of course, as the deflection angle increases, the resulting beam profile is affected. However, in further practical implementations, those situations are not observed. Therefore, for the sake of brevity, we omit here unnecessary discussion and consider what follows the performance of the phase profile of the top-hat generating element.

As expected, when the beam width of the incident Gaussian mode is matched with the expected beam width $d_0 = 1.25$ mm, our numerical simulation reveals that the PBP element acts as intended; see figures 4(c) and (d). We observe the transverse intensity profile, which resembles the target profile in figure 3(b) (curve 3). As we decrease the width of the incident beam to $d_0 = 1.05$ mm (approximately by 16%) the transverse top-hat profile becomes convex at $z = z_0$. Nevertheless, as the beam propagates, a slightly disturbed top-hat profile does appear further away (from the expected position z_0). We note that this behavior is observed also when the size of the beam increases. In this case, the top-hat profile is formed before the expected position.

This behavior can be well understood by a simple consideration of the Gaussian beam diffraction. Smaller beams grow during diffraction as they move away from the beam waist. They get additional positive wavefront curvature while propagating and the top-hat profile is further away. Larger beams have a negative wavefront curvature before the beam waist and thus the top-hat profile is formed before the expected position.

We conclude that the main influence from the mismatch of the incident beam sizes manifests itself in the longitudinal position of the top-hat profile.

3.2. Axial (transverse) misalignment of the PBP element

Yet another imperfection occurring during the alignment of the optical elements is the transverse displacement of the PBP element. As we did observe it during the experimentation (see a section 4.3 below) we have decided to investigate it numerically.

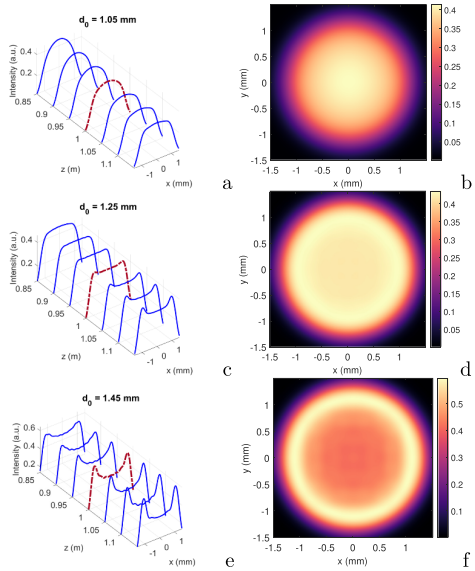

Figure 4. 1D cross sections of the transverse intensity profiles of propagating beams produced by the PBP element for different beam widths d_0 (a), (c), (e) and propagation distances z. The 2D intensity distributions (b), (d), (f) at the position where a top-hat beam profile is expected are marked in dashed red (on the left) and are depicted on the right. $d_0 = 1.05$ mm in the first row, $d_0 = 1.25$ mm in the middle row and $d_0 = 1.45$ mm in the last row.

In this set of simulations, we change the width of the incident Gaussian beam and the position of the PBP element with respect to the optical axis to obtain a full spectrum of variation. The transverse intensity profiles at the distance $z = z_0$ are depicted in figure 5. Here an array of transverse profiles is presented as a matrix, where the horizontal coordinate is the displacement Δx and the vertical coordinate is the beam width d_0. Underneath each beam, the intensity cross section is depicted by a light blue line.

These results showcase an interplay between two misalignments. In general, the axial misalignment of the PBP element introduces the intensity slope of the beam. However, when a Gaussian beam of smaller diameter impinges on the PBP element, the effect of the axial misalignment is not as pronounced as for the larger beam diameters. When a smaller Gaussian beam impinges on the PBP element the effect of large displacements is not so pronounced because of the convex shape of the beam profile. As the incident beam width increases, the distortion in the beam intensity profile due to the displacement of the PBP element is increasing—it becomes skewed, forming a C-shaped intensity modulation, with the slope being negative or positive depending on the direction of the displacement; see figure 5.

As our previous investigation has demonstrated, for beam widths that are larger than intended, the beam profile at the

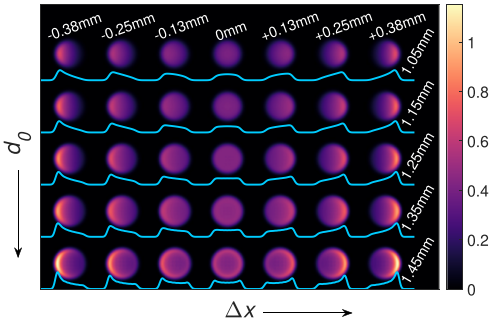

Figure 5. The transverse intensity distribution of beams produced by the PBP element at the distance $z = z_0$ for various displacements of the PBP element Δx (horizontally) and sizes of the incoming Gaussian beam d_0 (vertically).

distance z_0 demonstrates the appearance of horns in the 1D cross section. The transverse profile as a result has a distinct ring-like structure. Because of this, the transverse displacement results in a more pronounced horn appearing to the left or right depending on the sign of the displacement Δx.

4. Experimental verification

In this section, we report on the performance of the PBP element that was manufactured by Altechna R&D with the transmittance being higher than 90% over a broad spectral region [63]. This implementation of GPOE enables beam-shaping of high-energy beams because these elements can withstand pulses of 1.5 mJ energy and 158 fs FWHM duration at 1030 nm [41, 43]. Scaling optical elements and beam size would reduce the impinging beam fluence and would enable the transformation of even higher-energy pulses [36].

4.1. Optical setup

The optical setup used in the experiment is presented in figure 6. A femtosecond laser (Amplitude Systems, $\lambda = 1030$ nm) produced pulses of 500 fs FWHM duration at the rate of 200 kHz and 1 W power. The power of the pulses was attenuated to 100 mW by an external attenuator to avoid camera damage during the beam scan. The beam size was controlled using a variable beam expander (BE) placed in reverse to de-magnify the beam. The polarization of the Gaussian beam was converted to circular by a quarter-wave plate (QWP) and the beam phase front was modulated by a Pancharatnam–Berry phase element (PBPE) presented in figure 7. The resulting beam was recorded with a camera (CCD) placed on the linear translation stage.

For our experiments, we have devised two designs of PBP elements: with and without a blazed grating. Figure 7 shows the slow-axis angle distribution of the two fabricated PBP elements without (figure 7(a)) and with (figure 7(b)) the blazed grating. The retardance of both elements was fixed to

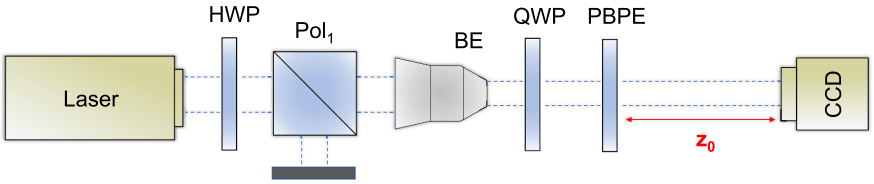

Figure 6. Scheme of the experimental setup comprising a half-wave plate (HWP), a beam expander (BE), a linearly polarizing cube (Pol_1), a quarter-wave plate (QWP), a PBP element (PBPE) and a camera (CCD). The laser is from Amplitude Systems, $\lambda = 1030$ nm.

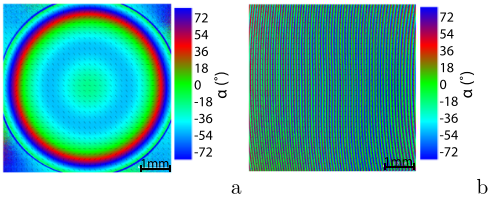

Figure 7. Experimentally obtained slow-axis angle distribution of the two manufactured PBP elements. (a) The PBP element has no blazed grating; (b) with a blazed grating, $\gamma = 1.6^\circ\ \mu m^{-1}$. Images were taken with the birefringence imaging microscope *Hinds Instruments Exicor MicroImager*.

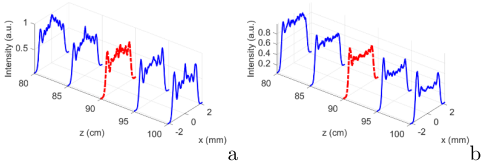

Figure 8. Cross sections of the experimentally obtained intensity profiles of the top-hat beam produced by PBP elements with (b) and without (a) a blazed grating. The red dotted-dashed line represents a top-hat beam, which has formed at $z_{0e} = 90$ cm.

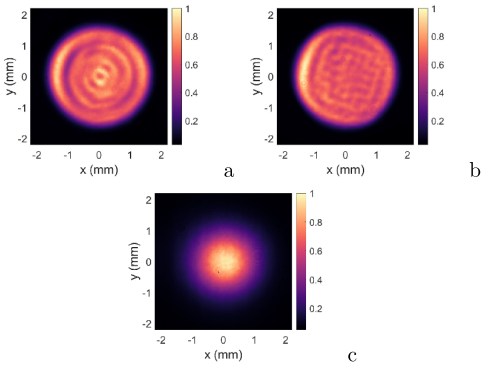

Figure 9. Experimentally obtained 2D intensity profiles of the top-hat beam at the distance $z_{0e} = 90$ cm produced by PBP elements (a) without and (b) with a blazed grating. The measured quality factor μ was equal to 0.216 and 0.195 for (a) and (b) respectively. (c) The intensity profile of the incident Gaussian beam.

$\lambda/2$ and its distribution over the full area of the element is almost constant, similar to the measurement made in [43]. Two PBP elements were necessary in order to prove our numerical hypothesis that the blazed grating does not perturb the top-hat profile as long as the deflection angle is relatively small (up to a few degrees), but enables the removal of the the zeroth-order diffraction beam, which is harmful to the quality of the resulting beam. The slow-axis distribution of the manufactured elements is depicted in figure 7. We confirm the good quality of the inscription of the element by comparing it with the theoretically calculated distribution (equation (6)).

We started our experiment by finding the location at which the top-hat beam forms. For this, we set the diameter of the incoming Gaussian beam to 2.5 mm and registered a transverse intensity distribution profile of the top-hat beam at several propagation distances close to $z_0 = 1$ m with a step of 2.5 cm. The experiment has largely validated our estimation. We observe the formation of the top-hat beam at the same distance using both PBP elements; see figure 8. Results show that both elements generate top-hat beams, which appear a bit closer to the element than intended ($z_0 = 1$ m). After theoretical investigation, we have noticed that the sign and value of the curvature radius of the incoming beam wavefront influence the position of the top-hat beam. Next, we notice a pronounced interference between the diffracted and undiffracted beams for the top-hat produced by the element without the blazed grating. This outcome is natural because in the simulations the phase and amplitude of the Gaussian beam impinging on the PBP element are ideal. In the experiment, the phase and amplitude of the incident Gaussian beam contain noise that is unavoidable (see figure 9(c)), and the PBP element has some imperfections due to the manufacturing.

Although the cross sections of the top-hat beam intensity in figure 8 seem to be nonuniform, the 2D beam profiles look more homogeneous; see figures 9(a) and (b). We notice the presence of additional ripples in the profile of the top-hat produced by an element without deflection. Some modulation of the brightness is also present. Even though the incident Gaussian beam appears to be clean prior to the element, it may possess an uneven phase distribution that may have an impact on

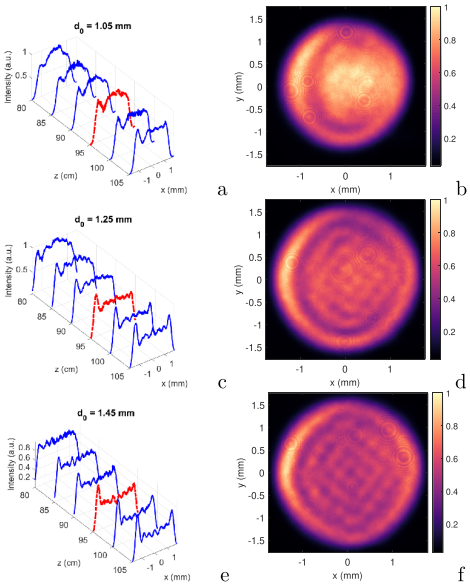

Figure 10. On the left (a), (c), (e), experimentally obtained cross sections of the propagating top-hat beams for different incident Gaussian beam waists and propagation distances z. On the right (b), (d), (f), beams whose profiles were registered 95 cm away from the PBP element.

the ring modulation. The modulation of the brightness at the same radius as the top-hat beam with the blazed grating is also evident, suggesting the same cause—the initial imperfection in the beam phase.

4.2. Imperfect incident beam waist

In the next set of experiments, we have fine-tuned parameters of the incident beam as well as possible, so the top-hat beam does appear near the expected point. We have registered formation of the top-hat beam at the distance $z_{0e} = 95$ cm from the element. The experimental difference of $\Delta z = 5$ cm in the position of the top-hat beam could be due to a nonideal incident Gaussian beam.

In this set of measurements, we investigate the effect caused by the imperfect incident beam waist (mismatch of the beam width d_0). The beam intensity profiles and cross sections are illustrated in figure 10. When beam waist was fixed to $d_0 = 1.25$ mm, at larger propagation distances the central part of the beam remains flat but a high-intensity ring starts to appear around the center. At distances smaller than $z_0 = 95$ cm, the intensity profile evolves into a convex one. Similar behavior was observed in the theoretical section; see figure 4.

We have chosen two imperfect incident Gaussian beams waists: $d_0 = 1.05$ mm and $d_0 = 1.45$ mm. If the waist of the incoming beam is smaller than that required by the element design, the top-hat beam forms at a larger distance from the PBP elemen't see figure 10(a). However, when the incident beam is larger, the top-hat beam forms closer to the PBP element; see figure 10(e). This is also in good agreement with the theoretical predictions; see figure 4.

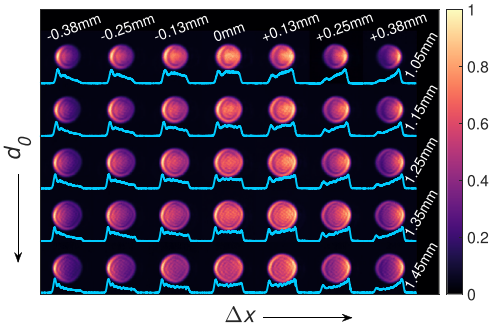

Figure 11. Experimentally obtained transverse intensity distribution of beams produced by the PBP element at the distance $z = z_{0e}$ for various displacements of the PBP element Δx (horizontally) and sizes of the incoming Gaussian beam d_0 (vertically).

4.3. Displacing the PBP element

Our last set of experiments investigates the influence of the imperfect placement of the PBP element with respect to the optical axis. Here, we note that we adjust the optical setup as much as possible for the top-hat to appear at the intended distance z_0. In doing so we have managed to record the top-hat at the distance $z_{0e} \approx 95$ cm; see figure 11. We fix the position of the camera so that the beam is imaged in the plane of the top-hat $z = z_{0e}$. The PBP element is laterally displaced with a step of 128 μm in both directions from the axis while the beam waist was changed with a step of 0.1 mm. Results are presented in figure 11.

As expected, the small misalignment of the PBP element does not change the beam profile significantly. Nevertheless, the larger shifts of the PBP element in the transverse plane cause pronounced changes in the top-hat intensity distribution. The intensity cross section becomes skewed either to the right or to the left depending on the sign of the displacement. In general, qualitative agreement between numerical simulation and experimental verification is evident. Slight deviations are present, possibly due to additional imperfections in the incident beam.

5. Conclusions

A method to control the incident beam amplitude via the Pancharatnam–Berry geometrical phase was presented and the application of a Gaussian to top-hat converter was analyzed. The phase profile required to generate a top-hat beam from a Gaussian beam was presented. The quality of the generated

top-hat beam was analyzed and it was demonstrated that this increases with the waist of the top-hat for distances closer to the PBP element. Thus, the most efficient generation is possible for a given range of distances from the element and top-hat sizes.

We have numerically investigated the formation dynamics of the top-hat beam with a PBP element. It turns out that a mismatch of the incident Gaussian beam waist by 16% will result mainly in a shift in the position where the top-hat beam forms either further from or closer to the element by $\approx 10\%$. The shape of the top-hat beam intensity profile becomes convex or ring-like near the designed formation distance depending on whether the beam waist is smaller or larger than intended. The good quality top-hat beam is either created at the distance z_0 or can be displaced azimuthally using an additional blazed grating phase. For small deflections, the quality of the top-hat is preserved.

The small transverse shift (around 10%) of the element does not affect the top-hat beam intensity profile. This tolerance to shifts is more pronounced if the incident Gaussian beam is smaller than intended. For larger incident beams the shift in the element produces a disctint C-shaped intensity modulation on the edge of the beam.

The PBP element was manufactured by Altechna R&D. The phase of the circularly polarized beam was modulated by the volume nanogratings inscribed in the glass of the optical element by femtosecond lasers. The manufactured PBP element was studied by the transformation of an intense Gaussian beam of 400 fs pulse duration to a top-hat beam, and its performance under imperfect conditions was also analysed. Results show that the sensitivity of the element to aberrations and imperfections is rather low. The element with a blazed grating increases the quality of the produced beam by removing interference coming from the zeroth-order diffracted beam. Experimental results do confirm theoretical expectations.

Data availability statement

The data that support the findings of this study are available upon reasonable request from the authors.

Acknowledgments

This project has received funding from European Social Fund (Project No. 09.3.3-LMT-K-712-01-0167) under a grant agreement with the Research Council of Lithuania (LMTLT).

ORCID iD

S Orlov https://orcid.org/0000-0003-1692-0189

References

[1] Herzig H P 1997 *Micro-Optics: Elements, Systems and Applications* (Boca Raton, FL: CRC Press)
[2] Lin D, Fan P, Hasman E and Brongersma M L 2014 *Science* **345** 298–302
[3] Pancharatnam S 1956 Generalized theory of interference and its applications *Proc. Indian Academy of Sciences, Section A* vol 44 (Springer) pp 398–417
[4] Berry M V 1987 *J. Mod. Opt.* **34** 1401–7
[5] Paniagua-Dominguez R *et al* 2018 *Nano Lett.* **18** 2124–32
[6] Hoffnagle J A and Jefferson C M 2000 *Appl. Opt.* **39** 5488–99
[7] Gertus T, Michailovas A, Michailovas K and Petrauskienė V 2015 Laser beam shape converter using spatially variable waveplate made by nanogratings inscription in fused silica *Laser Resonators, Microresonators and Beam Control XVII* vol 9343 (Int. Society for Optics and Photonics) p 93431S
[8] Gotovski P, Šlevas P, Nacius E, Jukna V, Orlov S, Ulcinas O, Baltrukonis J and Gertus T 2020 Design of efficient Gauss to top-hat converters using geometrical phase elements inscribed in the glass by femtosecond laser pulses *Laser Resonators, Microresonators and Beam Control XXII* vol 11266 (Int. Society for Optics and Photonics) p 112661J
[9] Chen H T, Taylor A J and Yu N 2016 *Rep. Prog. Phys.* **79** 076401
[10] Hu J, Bandyopadhyay S, Liu Y H and Shao L Y 2021 *Frontiers Phys.* **8** 502
[11] Bomzon Z, Kleiner V and Hasman E 2001 *Opt. Lett.* **26** 1424–6
[12] Bomzon Z, Biener G, Kleiner V and Hasman E 2002 *Opt. Lett.* **27** 1141–3
[13] Marrucci L, Manzo C and Paparo D 2006 *Appl. Phys. Lett.* **88** 221102
[14] Luo W, Sun S, Xu H X, He Q and Zhou L 2017 *Phys. Rev. Appl.* **7** 044033
[15] Laurinavičius K, Berškys J and Orlov S 2020 Tailoring response of a cluster of nanoparticles on a substrate and its application for design of geometrical phase elements *Photonic and Phononic Properties of Engineered Nanostructures X* vol 11289 (Int. Society for Optics and Photonics) p 112891Z
[16] Orlov S and Berškys J 2020 *Phys. Rev.* A **102** 063532
[17] Kanwal S, Wen J, Yu B, Kumar D, Chen X, Kang Y, Bai C and Zhang D 2020 *Nanomaterials* **10** 490
[18] Pacheco-Peña V, Engheta N, Kuznetsov S, Gentselev A and Beruete M 2017 *Phys. Rev. Appl.* **8** 034036
[19] Minkevičius L, Jokubauskis D, Kašalynas I, Orlov S, Urbas A and Valušis G 2019 *Opt. Express* **27** 36358–67
[20] Zhang L, Mei S, Huang K and Qiu C W 2016 *Adv. Opt. Mater.* **4** 818–33
[21] Page D N 1987 *Phys. Rev.* A **36** 3479
[22] Cohen E, Larocque H, Bouchard F, Nejadsattari F, Gefen Y and Karimi E 2019 *Nat. Rev. Phys.* **1** 437–49
[23] Shimotsuma Y, Kazansky P G, Qiu J and Hirao K 2003 *Phys. Rev. Lett.* **91** 247405
[24] Beresna M, Gecevičius M and Kazansky P G 2011 *Opt. Mater. Express* **1** 783–95
[25] Hasman E, Kleiner V, Biener G and Niv A 2003 *Appl. Phys. Lett.* **82** 328–30
[26] Cohen E, Larocque H, Bouchard F, Nejadsattari F, Gefen Y and Karimi E 2019 *Nat. Rev. Phys.* 1 437
[27] Beresna M 2012 Polarization engineering with ultrafast laser writing in transparent media *PhD Thesis* University of Southampton, UK
[28] Drevinskas R, Beresna M, Zhang J and Kazansky P 2016 *Adv. Opt. Mater.* **5** 1600575
[29] Sakakura M, Lei Y, Wang L, Yu Y and Kazansky P G 2020 *Light: Sci. Appl.* **9** 15
[30] Šlevas P, Orlov S, Nacius E, Ulčinas O, Gotovski G, Baltrukonis J and Jukna V *et al* 2020 Laser induced modifications in transparent materials using azimuthally modulated axicon beams *Laser Applications in Microelectronic and Optoelectronic Manufacturing (LAMOM) XXV* vol 11267, ed G Račiukaitis (Int. Society for Optics and Photonics (SPIE)) pp 17–23

[31] Šlevas P, Orlov S, Nacius E and Ulčinas O 2021 *Opt. Commun.* **505** 127509
[32] Gotovski P, Šlevas P, Nacius E, Jukna V, Orlov S, Baltrukonis J, Ulčinas O and Gertus T 2020 Formation of optical needles by Pancharatnam-Berry phase element for laser-induced modifications in transparent materials *Laser-Based Micro-and Nanoprocessing XIV* vol 11268 (Int. Society for Optics and Photonics) p 112681Y
[33] Gotovski P, Šlevas P, Orlov S, Ulčinas O and Urbas A 2021 *Opt. Express* **29** 33331–45
[34] Nacius E, Pavel G, Ulčinas O, Orlov S, Urbas A and Jukna V 2021 *J. Opt. Soc. Am.* B **38** 3886–95
[35] Products – workshop of photonics: femtosecond laser micromachining (available at: https://wophotonics.com/products/) (Accessed 23 July 2021)
[36] Laser-induced damage threshold (LIDT) measurement report (available at: https://wophotonics.com/wp-content/uploads/2020/07/LIDT-result-fs-regime.pdf) (Accessed 23 July 2021)
[37] Beresna M, Gecevicius M, Kazansky P and Gertus T 2011 *Appl. Phys. Lett.* **98** 201101
[38] Hnatovsky C, Shvedov V, Krolikowski W and Rode A 2011 *Phys. Rev. Lett.* **106** 123901
[39] Bao-Li Y, Shao-Hui Y, Tong Y and Wei Z 2010 *Chin. Phys. Lett.* **27** 108701
[40] Weber R, Michalowski A, Abdou-Ahmed M, Onuseit V, Rominger V, Kraus M and Graf T 2011 *Phys. Proc.* **12** 21–30 Lasers in Manufacturing 2011 - *Proc. Sixth Int. Conf. on Lasers in Manufacturing*
[41] Baltrukonis J, Ulčinas O, Orlov S and Jukna V 2020 *J. Opt. Soc. Am.* B **37** 2121–7
[42] Baltrukonis J, Ulcinas O, Gotovski P, Orlov S and Jukna V 2020 Realization of higher order vector Bessel beams for transparent material processing applications *Laser-Based Micro- and Nanoprocessing XIV* vol 11268, ed U Klotzbach, A Watanabe and R Kling (Int. Society for Optics and Photonics (SPIE)) pp 295–302
[43] Baltrukonis J, Ulčinas O, Orlov S and Jukna V 2021 *Phys. Rev. Appl.* **16** 034001
[44] Dorn R, Quabis S and Leuchs G 2003 *Phys. Rev. Lett.* **91** 233901
[45] Ma X *et al* 2015 *Sci. Rep.* **5** 1–7
[46] Pfeiffer C and Grbic A 2014 *Phys. Rev. Appl.* **2** 044012
[47] Wang H, Du J, Wang H, Lu Y and Wang P 2019 *Adv. Opt. Mater.* **7** 1900552
[48] Orlov S and Banzer P 2014 *Phys. Rev.* A **90** 023832
[49] Shen Z, Xiang Z, Wang Z, Shen Y and Zhang B 2021 *Appl. Opt.* **60** 4820–6
[50] Bauer T, Banzer P, Bouchard F, Orlov S, Marrucci L, Santamato E, Boyd R W, Karimi E and Leuchs G 2019 *New J. Phys.* **21** 053020
[51] Marcinkevičius A, Juodkazis S, Matsuo S, Mizeikis V and Misawa H 2001 *Jpn. J. Appl. Phys.* **40** L1197
[52] Vosylius V, Grabusovas A and Orlov S 2018 *Proc. CIRP* **74** 701–4
[53] Gotovski P, Baltrukonis J and Orlov S 2018 *Proc. CIRP* **74** 696–700
[54] Sugioka K, Meunier M and Piqué A 2010 *Laser Precision Microfabrication* vol 135 (Berlin: Springer)
[55] Hoffnagle J A and Shealy D L 2012 Optical and mechanical tolerances for two-lens plano-aspheric laser beam shapers *Laser Beam Shaping XIII* vol 8490 (Int. Society for Optics and Photonics) p 849004
[56] Han W, Cheng W and Zhan Q 2011 *Opt. Lett.* **36** 1605–7
[57] Rung S, Rexhepi M, Bischoff C and Hellmann R 2013 *J. Laser Micro Nanoeng.* **8** 309
[58] Le H, Penchev P, Henrottin A, Bruneel D, Nasrollahi V, Ramos-de Campos J A and Dimov S 2020 *Micromachines* **11** 221
[59] Möhl A and Fuchs U 2016 *Adv. Opt. Technol.* **5** 201–10
[60] Nodop D, Ruecker J, Waechter S and Kahle M 2019 *Opt. Lett.* **44** 2169–72
[61] Iizuka K 2013 *Engineering Optics* vol 35 (Berlin: Springer)
[62] Jones R C 1941 *J. Opt. Soc. Am.* **31** 488–93
[63] Gotovski P, Šlevas P, Orlov S, Ulčinas O and Urbas A 2021 Inscription in the glass of efficient Gauss to top-hat converters based on Pancharatnam-Berry phase by high power femtosecond laser pulses *Laser Applications in Microelectronic and Optoelectronic Manufacturing (LAMOM) XXVI* vol 11673 (Int. Society for Optics and Photonics) p 116730H

P4

An optical needle with elongated transversal profile created using Airy beams for laser processing of glasses

P. Šlevas, K. Mundrys, O. Ulčinas, S. Orlov

Optics & Laser Technology, 174, 110558 (2024)
DOI: 10.1016/j.optlastec.2024.110558
https://www.sciencedirect.com/science/article/pii/S0030399224000161

Supporting information: https://doi.org/10.1016/j.optlastec.2024.110558

Optics & Laser Technology 174 (2024) 110558

Contents lists available at ScienceDirect

Optics and Laser Technology

journal homepage: www.elsevier.com/locate/optlastec

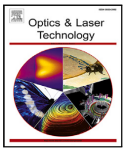

Full length article

An optical needle with elongated transversal profile created using Airy beams for laser processing of glasses

Paulius Šlevas [a,*], Karolis Mundrys [a], Orestas Ulčinas [a,b], Sergej Orlov [a]

[a] Center for Physical Sciences and Technology, Coherent Optics Laboratory, Sauletekio Ave. 3, Vilnius, Lithuania
[b] Workshop of Photonics, Mokslininku st. 6A, Vilnius, Lithuania

ARTICLE INFO

Keywords:
Airy beam
Binary phase mask
Beam shaping
Optical needle
Laser microprocessing
Elongated transverse beam profile

ABSTRACT

In recent decades, significant progress has been made in the field of laser beam shaping, driven by the growing demands in both scientific research and industrial applications. Notably, a class of beams known as nondiffracting beams, which exhibit such characteristics as self-healing and resistance to diffraction, has found practical utility in communication, imaging, and laser microprocessing. Although Bessel beams have become commonplace for various optical applications, further advances in beam engineering remain a need. One of the key requirements is the ability to control the elongation of the transverse profile of an optical needle, which is highly sought after for specific applications. In this study, we propose to achieve this control by utilizing nondiffracting Airy beams. The elongation of the optical needle's transverse profile is achieved through the implementation of a binary phase mask. We evaluate the performance of this method through both numerical simulations and experimental assessments, employing various metrics, such as the major-to-minor axis ratio, the length of the optical needle, and its stability. We present a specific case where a flat optical element is created using geometrical phase induced by nanogratings inscribed within the element's volume by means of a femtosecond laser. We validate the performance of this geometrical phase element through laser microprocessing of transparent glasses and report the results obtained from these experiments.

1. Introduction

Over the years, lasers have proved to be a versatile tool in a variety of fields, such as manufacturing [1], biomedicine [2,3], telecommunication [4,5] and more. A meticulous adaptation of laser parameters is key for realization of particular application, and the shape of the beam is one of them. The most common is the Gaussian beam, desirable for its ability to be focused to a small volume. However, recently nondiffracting beams have gained popularity due to their ability to retain shape over long distances compared to a Gaussian beam [6]. One of the examples is a Bessel beam [7] that has a focal zone with a high aspect ratio. This beam proved to be beneficial in laser material processing in applications such as nanochannel machining [8], through glass vias [9], glass refraction index modifications [10], glass dicing [11–13]. In other fields, it has been successfully used for THz imaging [14], particle manipulation [15], and microscopy [16].

Another example of a well-known nondiffracting beam is the Airy beam [17], which is interesting due to its main lobe propagation on a parabolic trajectory in the longitudinal plane [18]. Airy beams were successfully used for particle trapping and optical manipulation [19–21], for machining curved structures along the beam propagation path [22], multiphoton polymerization [23], and to image a sample around the obstacle in the THz wavelength [24].

In some applications, further focal zone engineering is desirable. The standard method to generate an Airy beam is a Fourier transform lens setup, which creates a caustic of light, having the shape of the Airy beam [25]. This association of the nondiffracting Airy beam with caustics of light has resulted in numerous works on the flexible shaping of Airy beam propagation trajectories [26,27] and has even been extended to the general family of propagation invariant optical fields [28]. Such a looming number of new optical beams has most importantly also resulted in the lensless generation of Airy beams with trajectories other than parabolic [29,30].

Bessel beams can be produced using circular slits in the Fourier plane [31], axicons, diffractive multilevel elements, or geometrical phase-based metasurfaces [32]. These generation methods have their advantages and drawbacks; for example, the axial intensity in the Bessel zone is not flat. This can be corrected by focal zone engineering that effectively converts the Bessel beam into an optical needle [33].

* Corresponding author.
E-mail address: paulius.slevas@ftmc.lt (P. Šlevas).

https://doi.org/10.1016/j.optlastec.2024.110558
Received 29 May 2023; Received in revised form 5 December 2023; Accepted 8 January 2024
Available online 15 January 2024

Yet another example is an introduction of ellipticity in the transverse intensity distribution of a Bessel beam [34]. Using such a beam to modify the bulk of the transparent glass results in directional cracking of the glass, which can improve the quality of the dicing [35–39]. This beam shaping can be performed by employing an additional optical element to shape the amplitude or phase in the spectrum of a Bessel beam [38] or by designing a specific geometrical phase optical element [40]. The phase of the Bessel beam can also be corrected to allow for the fabrication of tilted glass [41]. Further approaches to better directional cracking or other laser microprocessing requests can involve superpositions of Bessel beams with different vortical topologies [42] or polarizations [43,44].

To achieve various kinds of beam profiles, diffractive optical elements (DOEs) are often manufactured and used in optical setup. There are two main types of DOE: amplitude and phase contrast-based DOE [45]. Phase-only DOEs are more efficient than amplitude-based ones. Such elements are created by inscribing structures on the surface of glass, polymer, or other photosensitive, heat-sensitive material by means of high-precision processing such as plasma etching, direct laser writing, circular laser writing, etc. [46,47]. Ideally, material and structures should be able to tolerate high intensities in applications requiring ultrashort laser pulses [48]. Phase-only DOEs can be divided into binary or multilevel phase modulating elements [49]. One drawback of binary DOEs is the appearance of additional diffraction orders, because some energy is wasted. However, some applications require multiple beams and methods such as a combination of binary masks [50], binarization level adjustment [51], or multi-value phase grating design [50] allow control of the behavior of additional diffraction orders. For example, the introduction of a slope factor in Airy binary masks can control the distance between two diffraction orders [52].

In this work, we propose an approach to use two diffraction orders of easy-to-implement diffractive binary phase masks to create elongated in-transverse-plane optical needles. This concept is introduced into a high-power optical system to engineer an elliptical high-aspect ratio optical needle beam, which is useful for the aforementioned laser microprocessing scenarios. We demonstrate how the ellipticity of the resulting beam could be flexibly controlled by adjustments in the binary phase mask. We theoretically benchmarked a variety of phase masks to determine the best stability, the best homogeneity, and ellipticity of the resulting optical needle. Additionally, we pay attention to the quality parameters: ratio of energy in the main lobe compared to the entire beam, homogeneity length, and directionality length. Furthermore, we employ the spatial light modulator (SLM) to confirm the agreement between the theoretically simulated and experimentally obtained results.

In this work, we use a type 2 modification of bulk transparent dielectric material to create a geometrical phase element (GPE) [53–55]. As a femtosecond laser beam is raster-scanned over the glass, nanogratings are formed with slow axes aligned perpendicular to the polarization of the laser beam. A metasurface is created within fused silica glass with a geometric phase that continuously varies [56,57]. An element is designed and encoded as a GPE produced by the *Workshop of Photonics*. The transmittance of this element is higher than 90% in a broad spectral region [58]. Such GPEs generate high-quality beams and are used in high-power setups, to withstand up to 1.5 mJ energy, 158 fs FWHM duration pulses at 1030 nm [43,44].

Based on this approach, we manufactured one geometrical phase element for the generation of an elliptical Airy optical needle. We have systematically checked and verified its performance in a laser micro-machining setup to make surface and volume modifications in glass using varying pulse energy and duration. Our first findings have revealed the potential of this beam-shaping approach. Further improvements are expected by adjustment of the phase mask, laser parameters, and sample sizes.

2. Theoretical background

In 1979 Berry and Balaz noticed that a wavepacket described by the Airy function could be a solution to the Schrödinger equation for a free particle [17,59]:

$$i\frac{\partial u}{\partial \xi}+\frac{1}{2}\frac{\partial^2 u}{\partial s^2}=0. \tag{1}$$

It turns out that this equation is very similar to the paraxial diffraction equation when $u(s,\ \xi)$ is a function of the electrical field envelope, $s = x/x_0$ – dimensionless transverse coordinate, $\xi = z/(kx_0^2)$ – dimensionless longitudinal coordinate, x is transverse coordinate, z is longitudinal coordinate and $k = 2\pi/\lambda$ is the wave vector and λ is the wavelength. A generalized solution of this paraxial diffraction equation is a finite-energy Airy beam [59]:

$$u(s,0)=Ai(s)e^{qs}, \tag{2}$$

where $Ai()$ is the Airy function, and q is a damping parameter. Inserting this solution into Eq. (1) and integrating it gives [59]:

$$\begin{aligned} u(s,\xi) &= Ai\left(s-\frac{\xi^2}{4}+iq\xi\right)\\ &* \exp\left[qs-\frac{q\xi^2}{2}+i\left(\frac{q^2\xi}{2}-\frac{\xi^3}{12}+\frac{s\xi}{2}\right)\right]. \end{aligned} \tag{3}$$

We note here, that the way the Airy beam is defined, creates a caustic, which is constant in the normalized coordinates $s = \xi^2/4$. This means that the transverse size of the Airy beam quadratically scales the longitudinal dimension when $q = 0$. For the sake of brevity we stick to this definition, though we note that trajectory can be flexibly adjusted as described in the literature [30].

Using the Fourier transform of Eq. (3), we get the spatial spectrum of the wavepacket.

$$\tilde{u}\left(k_t\right)=\exp[\left(q_t+ik_t\right)^3/3], \tag{4}$$

where k_t denotes the normalized (i.e. proportional to x_0 or y_0) x or y component of the wave vector, q_t is the exponential truncation factor (either q_x or q_y), see Ref. [60]. Consequently, the spatial spectrum of the three-dimensional Airy beam is $\tilde{u}\left(k_x,k_y\right)=\tilde{u}\left(k_x\right)\tilde{u}\left(k_y\right)$.

So, the general expression of the spatial spectrum is

$$\begin{aligned} \tilde{u}\left(k_x,k_y\right) &= A_0\exp\left[-\left(q_xk_x^2+q_yk_y^2\right)\right]\\ &\times\exp\left[-i\frac{k_x^3+k_y^3}{3}+i\left(q_x^2k_x+q_y^2k_y\right)\right], \end{aligned} \tag{5}$$

It is important to keep in mind here that the spatial coordinates are normalized here with respect to x_0 and y_0, so in reality we have 3 pairs of parameters appearing in Eq. (5): $q_it_0^2$, $q_i^2t_0$ and t_0^3, where t denotes x or y.

The number of parameters in this expression is commonly reduced to achieve a Gaussian envelope with cubic phases [61]:

$$\tilde{u}\left(k_x,k_y\right)=A_0\exp\left[-q\left(k_x^2+k_y^2\right)\right]\exp\left(i\frac{k_x^3+k_y^3}{3}\right), \tag{6}$$

where A_0 is a constant, the physical meaning of q is clearly revealed as a number proportional to the square of the beam width of the Gaussian envelope. Thus, in order to generate an Airy beam, the Gaussian beam has to be modulated by a cubic phase and then Fourier transformed.

From an experimental point of view, the Fourier transformation is performed by a lens of focal length f. If a spatial phase mask is placed in the focal plane before the lens, then the Fourier image of an object is obtained in the focal plane after the lens. The spatial frequencies k_x, k_y can be found from the spatial coordinates x_{obj}, y_{obj} as $k_x = kx_{obj}/f$, $k_y = ky_{obj}/f$. These dependencies have a direct implication on the extent of the spatial spectrum. Larger focal lengths lead to narrower spatial spectra, and smaller focal lengths result in wider extent in the domain of spatial frequencies. We can recast Eq. (6) into an expression

of the electric field distribution in the object plane that will generate an Airy beam behind the lens of the focal length f as:

$$\tilde{u}\left(x_{obj}, y_{obj}\right) = A_0 \exp\left[-\frac{k^2 q}{f^2}\left(x_{obj}^2 + y_{obj}^2\right)\right] * \exp\left[i\frac{k^3(x_{obj}^3 + y_{obj}^3)}{3f^3}\right], \quad (7)$$

Here, we note that Eq. (7) contains two independent variables: the damping parameter q and the scale factor $p = f/k$. From the experimental point of view, the Gaussian beam of beam width d_0 that impinges on a cubic phase mask will produce the required distribution of the electric field. We note that the phase mask is influenced solely by the scale factor p, see Eq. (7). We now use the expression $d_0^2 = p^2/q$ and the casting damping factor as $q = (p/d_0)^2$. As the wave vector remains constant throughout the experiment, the properties of the Airy beam are experimentally controlled by a choice of focusing lenses and beam widths of Gaussian beams illuminating the phase mask.

The influence of the Gaussian aperture for pseudonondiffracting beams was extensively studied in Ref. [62]. It was revealed that the decreasing Gaussian apertures affect the length of the nondiffracting zone for the Bessel, Mathieu and parabolic nondiffracting beams, thus, making the spatial extent smaller for all cases. A similar situation we do observe also here.

As a natural outcome of the spatial spectrum scaling introduced by a focal lens, the spatial extent of the Airy beam is inversely scaled. Larger focal lengths will generate larger and longer Airy beams, and shorter focal lengths will result in more focused and shorter beam configurations. As is already known, the damping factor also influences the longitudinal extent of the Airy beam. Although Airy beams with controllable trajectories can be generated from phase masks directly without the lens, the cornerstone of the current investigation is phase mask, which is expressed as:

$$T(x, y) = A_0 e^{i\varphi(x,y)}, \quad (8)$$

where $\varphi(x, y)$ is a phase defined in the interval $\varphi(x, y) \in [-\pi, \pi]$. In this work, we discretize the mask from Eq. (8) and effectively turn it into a binary phase mask (i.e., phases are 0 or π) using these relations for the transmission:

$$T_B(x, y) = A_0 \begin{cases} e^{i\pi} = -1, & \text{for} \quad -\pi \le \varphi(x, y) \le -\pi/2, \\ & \quad \pi/2 < \varphi(x, y) \le \pi, \\ e^{i0} = 1, & \text{for} \quad -\pi/2 < \varphi(x, y) \le \pi/2. \end{cases} \quad (9)$$

The introduction of binary masks is known to result in the appearance of two diffraction maxima (+1 and −1 orders). The transverse position of these maxima can be controlled by adding an additional linear phase. To create an elliptical main lobe of the beam, we perform this displacement by introducing two independent coefficients b_1 and b_2 for the coordinates x and y, respectively. The second change in the transmission function is the introduction of two independent cubic phases in the x and y directions, compare to the Eq. (7). A transfer function becomes:

$$T = e^{-i(a_1 x^3 + a_2 y^3 + b_1 x + b_2 y)}, \quad (10)$$

where a_1 and a_2 are the independent aforementioned coefficients (compare Eqs. (6) and (10)). Different values of coefficients b_1 and b_2 effectively introduce a diffraction grating with a spatial period defined by these numbers. This operation results in the first positive and negative diffraction orders being spatially separated in the transverse plane. The exact position of the orders of +1 and −1 diffraction is governed by the numbers b_1 and b_2. The superposition of these diffraction orders results in a controllable elongation of the resulting Airy beam.

The phase mask in Eq. (10) contains 4 variables, which at first sight makes investigation of the parameter space difficult. We introduce new coordinates $x_1^3 = a_1 x^3$ and $y_1^3 = a_2 y^3$ and rewrite the expression as

$$T = e^{-i(x_1^3 + y_1^3 + b_1/\sqrt[3]{a_1} x_1 + b_2/\sqrt[3]{a_2} y_1)}, \quad (11)$$

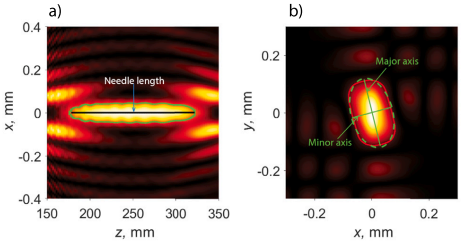

Fig. 1. Depiction to the definitions of (a) needle length (marked by a black line), (b) intensity in the main lobe (encircled by red), fitted ellipse (green dashed line) and its major and minor axes. The wavelength is $\lambda = 532$ nm. Intensity is normalized to the unity.

This way we have eliminated direct dependency on a_1 and a_2. However, there is still a hidden parameter a_2/a_1, as the scaling of the x and y coordinates is different. Thus, this indicates that the number of independent parameters can be reduced to three: $b_1/\sqrt[3]{a_1}$, $b_2/\sqrt[3]{a_2}$ and a_2/a_1.

We select an optical frequency with the wavelength of $\lambda = 532$ nm. The diameter of the mask is 5 mm, the beam width of the illuminating Gaussian beam is $d_0 = 2.5$ mm, and the focal length of the Fourier transform lens is $f = 250$ mm. This particular choice was caused by the initial experimental setup, which is not discussed here. This selection results in spatial frequencies k_x, k_y with paraxial numerical apertures up to $NA = 0.01$. A typical resulting optical needle is shown in Fig. 1. We note that because of the paraxiality, the length of the needle is up to tens of centimeters and the transverse size is up to tens of micrometers.

In order to characterize the resulting beam, we introduce parameters such as ellipticity, directionality, beam length in direction of propagation, length of the beam homogeneity, and the ratio of energy in the main lobe compared to the entire beam. We define the length of the optical needle at 50% of the maximum intensity (see Fig. 1(a)). We also calculate the energy ratio in the main peak compared to the surrounding side lobes. To do this, we encircle a contour around the main lobe in the XY plane at the intensity level $1/e^2$ as encircled in red in Fig. 1(b). We integrate the intensity in the located main peak and compare it with the integrated intensity in the XY plane. We select an average value of the energy ratio from XY planes between the start and the end of the optical needle. The directionality length is defined as follows. To find the direction of the semi-major and semi-minor axes, we fit an ellipse to a contour encircled around the main lobe (see the green dashed line in Fig. 1(b). Then the direction of the semi-major axis at the focal plane of the Fourier lens is taken as a reference. Next, the directions of the semi-major axes of the ellipse at different propagation distances are calculated and compared to the reference. If the difference exceeds 5 degrees, the beam is no longer considered directional. The mean square error (MSE) is used for the definition of homogeneity length. Comparisons are made between the reference cross section of the intensity distribution and the intensity distributions at different propagation distances. We calculate the MSE as $(\sum_{i=1}^{m}\sum_{j=1}^{n}|M_{i,j} - M_{i,j}^{ref}|^2)/(m * n)$, where $M_{i,j}^{ref}$ is an element of a reference image matrix at the focal point, $M_{i,j}$ is an element of a matrix at a particular position z, i, j are the indexes of the elements of the matrix, and m, n defines the size of a 2D matrix. The distance at which the MSE does not exceed 10^{-5} is defined as the homogeneity length.

In what follows, we will numerically estimate the influence of the aforementioned parameters on the optical needle by selecting $a_2/a_1 = 1.4$. The results are depicted in Fig. 2(a-e). Additionally, we provide animated sequences for different values of a_2/a_1 for readers as supplementary material. Please, note that some pixelated non-smoothness is present due to the numerical limitations. These sub-plots depict the

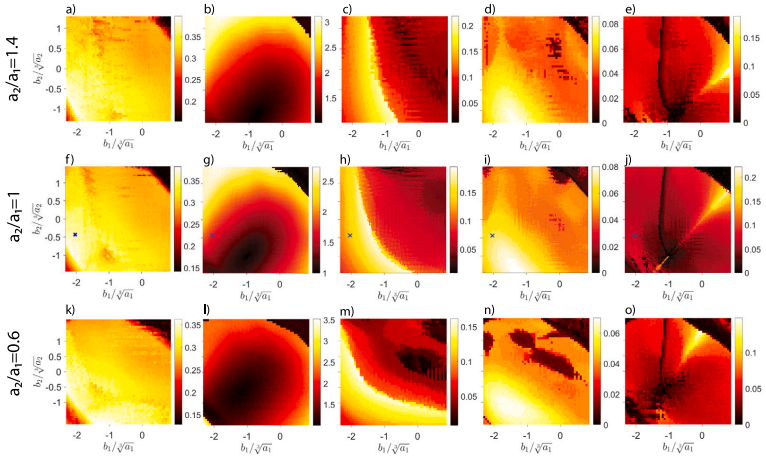

Fig. 2. (a), (f), (k) Ratio of energy in the main lobe compared to the energy of the entire beam, (b), (g), (l) Ratio of the semi-major and the semi-minor axes of the beam at the focal plane of the Fourier lens, (c), (h), (m) the length of the optical needle, (d), (i), (n) homogeneity length, (e), (j), (o) directionality length. Calculations performed for the lens of the focal length of $f = 250$ mm. The numbers in the color bar are given in meters in (c, h, m), (d, i, n), and (e, j, o). Each row of pictures contains results with different a_2/a_1 stated on the left.

dependencies of various parameters on the ratios $b_1/\sqrt[3]{a_1}$, $b_2/\sqrt[3]{a_2}$. In the first graph (see Fig. 2(a)), we observe a region where the power contained in the main lobe is the highest. The second Fig. 2(b) estimates the ellipticity of the transverse cross section of the beam. The third graph (Fig. 2(c)) is the dependence of the length of the optical needle on the ratios $b_1/\sqrt[3]{a_1}$, $b_2/\sqrt[3]{a_2}$. The last two graphs show the homogeneity and directionality lengths. We see that three dependencies have overlapping optimal conditions (Fig. 2(a, c, d)). The most optimal values for the energy ratio and homogeneity length are encountered when the ellipticity is close to unity. This also means that strongly elliptical shapes do not have high ratios of energies in the main lobe, but can be realized in relatively long and homogeneous optical needles. The optimal directionality is observed when $b_1/\sqrt[3]{a_1} > b_2/\sqrt[3]{a_2}$. This happens when the +1 and −1 diffraction orders are non-symmetrically displaced in the x and y directions. In this case, the resulting beam has no point symmetry with respect to the center, and parabolic trajectories of diffraction orders are oriented towards the center.

Next, we move on to the case where $a_1 = a_2$ (see Fig. 2(f-j)). First, the maximum energy ratio value in the main lobe is slightly decreased, and the maximum ellipticity of the optical needle has also decreased, although the general shape of the dependency is preserved (see Fig. 2(g)). The maximal length of the optical needle is also slightly affected, and those locations of the longest optical needle are slightly different now than in the previous case. Most notably, the directionality length has increased (see Fig. 2(j)). The optimal values for the energy ratio and homogeneity length are encountered when the ellipticity is close to unity. The optimal directionality is observed when $b_1 = b_2$. This happens when the +1 and −1 diffraction orders are symmetrically displaced in the x and y directions. In this case, the resulting beam has a point symmetry with respect to the center, and parabolic trajectories of diffraction orders are oriented towards the center. From these numerical estimates, we selected a particular set of parameters: $a_1 = 3.2 * 10^9\pi$ m^{-3}, $a_2 = 3.2 * 10^9\pi$ m^{-3}, $b_1 = -1400\pi$ m^{-1}, $b_2 = -300\pi$ m^{-1}. This selection results in an elliptical optical needle with a semi-major to semi-minor axes ratio of 1.7, see the "x" mark in Fig. 2.

The last case that we investigated is $a_2/a_1 = 0.6$. Numerical estimates are depicted in Fig. 2(k-o). The maximal energy ratio in the main lobe further decreases compared to the previous two cases. The ellipticity of the beam more or less preserves its dependence on the parameters (see Fig. 2(l)). The maximal length of the needle decreases and the homogeneity length decreases too (see Fig. 2(m) and (n)). The directionality length is also affected.

With these findings in mind, we calculate phase masks, which allow us to flexibly transform incident Gaussian beam profile into elliptical high aspect ratio beam. An example of numerically simulated transverse and longitudinal intensity distributions using the Fresnel diffraction integral [63] is given in Fig. 3, where the parameter b_2 displaces two diffraction orders in the y direction. We did perform simulations for a wide range of parameters. However, for the sake of brevity, we now select $a_1 = a_2 = 3.2\pi * 10^9$ m^{-3} and $b_1 = -1400\pi$ m^{-1} and are constant throughout the further investigation. Our aim here is to compare numerical simulations with experiments using a spatial light modulator. The following parameters were used; the diameter of the phase mask is now 8.6 mm (it was adjusted to match the size of the SLM matrix). The Fourier transform lens is now of focal length $f = 45$ mm. This selection results in numerical apertures up to 0.1. The beam width of the Gaussian illumination is now $d_0 = 6$ mm.

This selection of parameters mimics the experimental setup that we ended up using in the lab. Due to the scaling of spatial frequencies caused by the different focal length f, the length of the optical needle is now approximately 33 times smaller and its dimensions are expected to be approximately 5.7 times smaller (see Fig. 3) compared to the dimensions presented in Fig. 2.

From this set of numerical simulations we conclude that for a particular value of $b_2 = -1100\pi$ m^{-1} the center lobe in the transverse intensity distribution is symmetric. In the last case, when $b_2 = 500\pi$ m^{-1}, we observe the splitting of the resulting beam into two lobes. The intermediate values of the parameter b_2 enable the creation of an optical needle with various degrees of elongation. We note here that the elongation affects the intensity of the side lobes — it increases compared to the central intensity of the cross section when the two diffraction orders are displaced further apart (see Fig. 3).

Lastly, in Fig. 4, we choose the same parameters as in the calculation of Fig. 1 and demonstrate the lengths of the major and minor ellipse axes, as well as the evolution of the direction of the major axis during

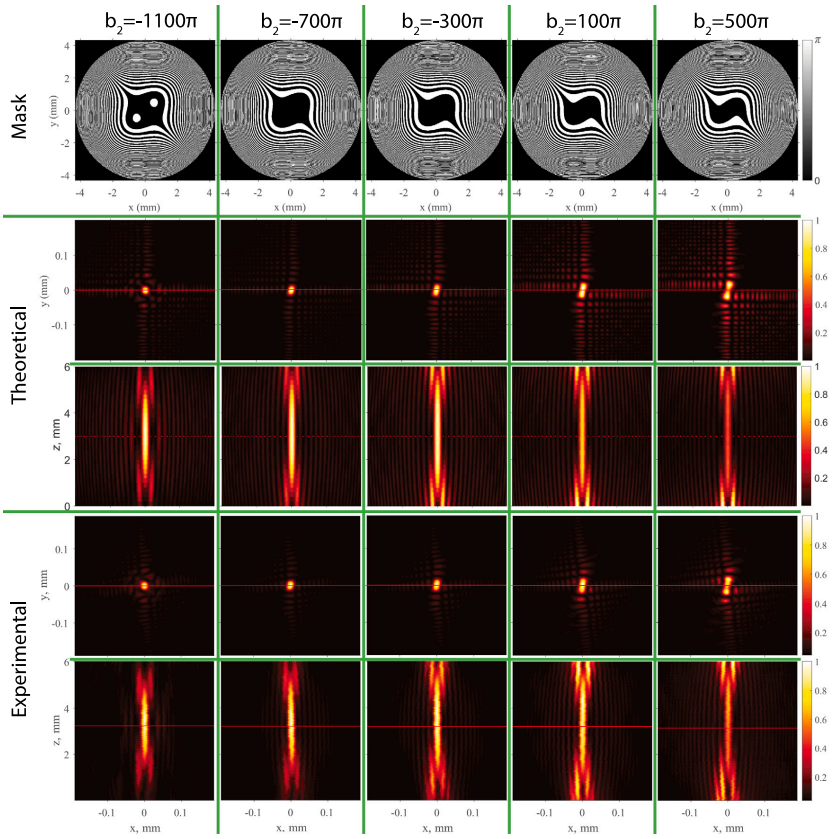

Fig. 3. Binary phase masks used in the numerical simulations and experiments (the first row). Numerically obtained transverse and longitudinal intensity distributions of the Airy needle beam, the second row, and the third row, respectively. Experimentally measured transverse and longitudinal intensity profiles, obtained using phase masks from the first row, fourth and fifth rows, respectively. The parameters are $a_1 = a_2 = 3.2 * 10^9\pi$ m^{-3} and $b_1 = -1400\pi$ m^{-1}. The red line marks the position of the cross section. Phase masks differ by the values of the parameter b_2, which is stated above the masks. The different columns correspond to different values of b_2.

propagation. The length of a long axis varies slightly (10%) in the zone of the optical needle. At the start and the end of the zone, the length of the long axis increases, and the angle of the major axis rapidly changes. This is due to the separation of two Airy beams from each other, whereas the algorithm still detects the ellipse in this transition stage.

3. Experimental verification of the concept

We start our experimentation with the verification of the proposed concept using a spatial light modulator. The optical setup is presented in Fig. 5. A laser beam of wavelength $\lambda = 532$ nm (DPSS laser) is attenuated, expanded to a diameter of around 5 mm ($1/e^2$), and sent to the phase-only reflective spatial light modulator (SLM *Holoeye Pluto*). Phase masks from Fig. 3 row 1 are loaded into the SLM. The angle between the beam incident on the SLM and the beam reflected from the SLM is small (3 deg). The reflected beam is imaged with a 4f set-up comprised of lenses with focal lengths $f_1 = 300$ mm, $f_2 = 125$ mm and focused with a $f_3 = 25$ mm lens. The resulting beam is captured by an imaging setup consisting of a 10x microscope objective (MO), a collimating lens (f_4), and a CCD camera, all assembled on a moving motorized stage. Images were captured every 30 μm of the camera position in the range of 6 mm. This measurement was repeated for every phase mask given in Fig. 3 row 1.

The experimental results are presented in the last two rows of Fig. 3. Row 4 contains experimentally obtained transverse intensity distributions, while in row 5 longitudinal intensity distributions are depicted. First of all, it was difficult to match the exact size of the incident Gaussian beam, so it is slightly smaller than expected. This has resulted in slightly shorter than in the calculations lengths of the optical needles. The transverse size was not affected by the illuminating aperture. Ideally, the larger phase mask, together with larger illuminating apertures, will result in the increase in the length of the optical needle. The experiment generally agrees well with the predictions from the numerical simulations. As in the numerics, the ellipticity of the main lobe of the transverse cross section increases in the experiment, when the parameter b_2 is large. The two diffraction orders are separated. As expected, the intensity of the side lobes increases as the separation between diffraction orders increases. The same effect is also observed in

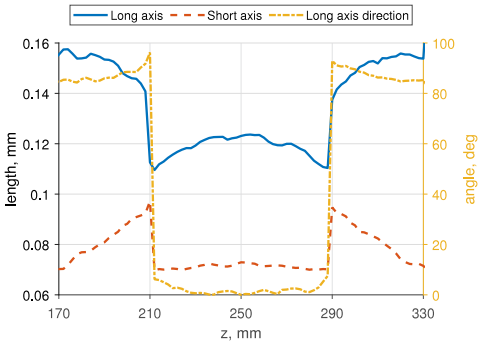

Fig. 4. Lengths of major and minor axes of the core of elliptical optical needle and an angle of a major axis relative to its angle at the focal point (f = 250 mm). Mask diameter of 5 mm and Gaussian beam width of d_0 = 2.5 mm were used in calculations.

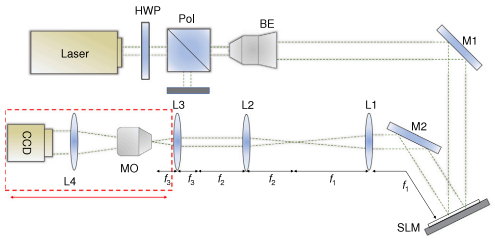

Fig. 5. Optical setup for the experimentation with SLM.

experimentally recorded longitudinal intensity distributions. An experimental evolution of the XY beam profile during propagation is shown in Fig. 6, where several XY intensity distributions are depicted at different propagation lengths. In Fig. 6(b) and (e) we see before and after the formation of the elliptical cross section that the main lobe is split into two parts, almost perpendicular to the direction of the elliptical central lobe. In conclusion, the results of the experiment have verified the claims made in the theoretical part.

4. Laser modification of glass

In the next set of experiments, we change the experimental setup, it is presented in Fig. 7(a). We use a high peak power *Pharos* laser (wavelength of 1030 nm) with the output of a Gaussian beam with 4.2 mm diameter. We control the output power using an external attenuator that is built from a $\lambda/2$ phase plate and a polarizer. We use the $\lambda/4$ phase plate to switch from linear to circular polarization and direct the beam to a geometric phase optical element (by *the Workshop of Photonics*).

The geometrical phase element (GPE) is implemented using the Pancharatnam– Berry phase (PBP) [56,57]. Birefringent nanogratings are induced by direct femtosecond micromachining in glass volume. This element is a space-variant phase retarder and is described using the Jones matrix formalism [64]. The general expression of the transmission matrix of the element is

$$M = \begin{bmatrix} \cos^2\alpha + e^{ik\sigma}\sin^2\alpha & \left(1-e^{ik\sigma}\right)\cos\alpha\sin\alpha \\ \left(1-e^{ik\sigma}\right)\cos\alpha\sin\alpha & e^{ik\sigma}\cos^2\alpha + \sin^2\alpha \end{bmatrix} \quad (12)$$

where α is the slow axis angle of the local birefringent nanograting and σ is the retardance. When the inscribed retardance is equal to $\lambda/2$ and the polarization of the incident beam to GPE is circular, the polarization of the output beam is also circular, and the phase front of the incoming beam is modulated according to the slow axis of the local birefringent nanograting [65]

$$E_{out} = M E_{inc} = e^{2i\alpha}\begin{bmatrix} 1 \\ \pm i \end{bmatrix}. \quad (13)$$

Therefore, the inscription of perpendicular nanogratings allows the construction of binary phase modulating optics. The element with Airy mask parameters $a_1 = a_2 = 3.2 * 10^9\pi$ m^{-3}, $b_1 = -1400\pi$ m^{-1}, $b_2 = -300\pi$ m^{-1} is produced by inscription of nanogratings within a fused silica sample (a part of this element is illustrated in Fig. 7 a). Though the GPE sustains high power, the production of large area elements is troublesome; because of that, we have reduced the size of the phase mask to 6 mm. Further, we recall that the diameter of the incident Gaussian beam is 4.2 mm. This further reduces the effective area of the phase mask.

The beam after the GPE is focused using the focal length lens f = 4 mm. The expected transverse size of the optical needle is expected to be approximately 63 times smaller than that in Fig. 1. Indeed, the recorded size of the optical needle is within the expected range, see Fig. 7(b). The longitudinal size is expected to be almost 4000 times smaller; additionally, it is influenced by the mismatch in the expected and realized sizes of Gaussian apertures. The longitudinal cross section is given in Fig. 7 c and is as long as expected. The length of the optical needle can be increased by using a larger Gaussian illumination or changes in the phase mask.

During the planning stage, we did realize that the optimal size of the phase mask inscribed in the GPE element should be relatively large, which should bring additional time costs to the creation of the GPE. Therefore, the current particular selection was motivated by the desire to capture the whole pattern of the beam within a particular glass sample. The transverse and longitudinal intensity distributions were obtained with a 60x microscope objective using a motorized stage, in 5 μm constitutive steps, and are shown in Fig. 7b and c. The resulting beam profiles are, as expected, similar to the profiles measured with the SLM. Their dimensions in the transverse and longitudinal directions are smaller because of a different focusing lens. This beam configuration (see Fig. 7) is used to induce modifications on the surface and in the bulk of 0.5 mm thick *Corning* EXG glass, which is a type of alkaline earth boro-aluminosilicate glass.

Having verified that the optical needle generated by the GPE acts as intended by the design, we proceed to laser microfabrication experiments. Our first task is to investigate surface modifications, induced by a single pulse with a spatial structure of the Airy optical needle. Different pulse durations ranging from 0.25 ps to 10 ps and energies from 145 μJ to 290 μJ are used. The surface modifications induced by focusing the laser wavepacket on the sample surface, are analyzed using an optical microscope (*Olympus BX51* with a 50x NA 0.75 objective, DoF 1.4 μm). The outcome of laser microprocessing with the beam focused on the surface is systematically presented in Fig. 8 for different pulse durations and pulse energies.

The shortest pulse duration of 0.25 ps creates modifications on the glass surface that resemble the beam structure, with many side lobes clearly visible for all pulse energies. A slight increase in pulse duration results in an effectively reduced pulse intensity. For this reason, we observe a reduction in the affected surface area of the glass sample, even when the pulse energy is constant.

In the particular case, when pulse durations are 6–10 ps and pulse energies are 145–174 μJ, only a few side lobes together with the main peak modify the surface of the glass. Most notably, for some particular pulse durations and pulse energies, for example, 203 μJ and 10 ps, a crack appears below the surface and it is directed along the semi-major axis of the elliptically shaped main lobe of the optical needle.

After investigating surface modifications, we proceed to the analysis of volume modifications produced using the same setup and focusing

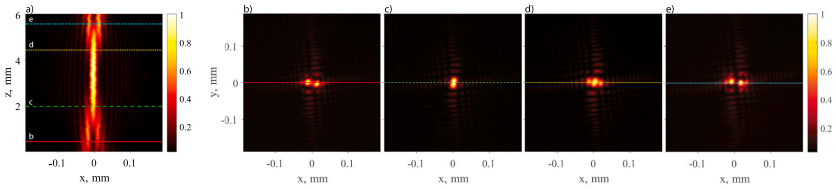

Fig. 6. (a) Experimental XZ intensity distribution of Airy optical with marked cross sections at which XY intensity distributions are provided in (b), (c), (d), (e). The lines in (b-e) mark the cross sections used to make the XZ distribution in (a). The parameters of the phase mask are $a_1 = a_2 = 3.2 * 10^9\pi$ m^{-3}, $b_1 = -1400\pi$ m^{-1}, $b_2 = -300\pi$ m^{-1}.

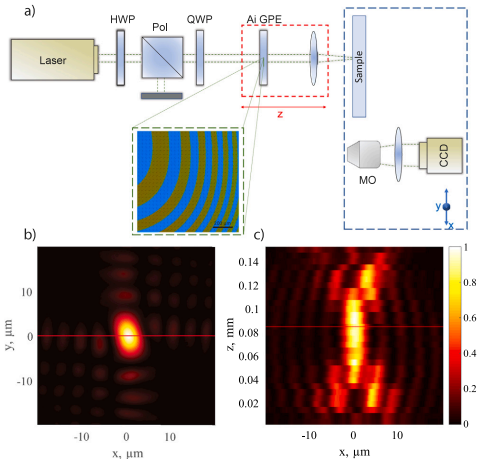

Fig. 7. (a) Optical setup for glass processing with GPE, (b) transverse intensity distribution of the Airy optical needle produced with GPE at the focus, and (c) longitudinal intensity distribution of the Airy optical needle produced with GPE at the focus. The red lines mark the positions at which cross sections were taken.

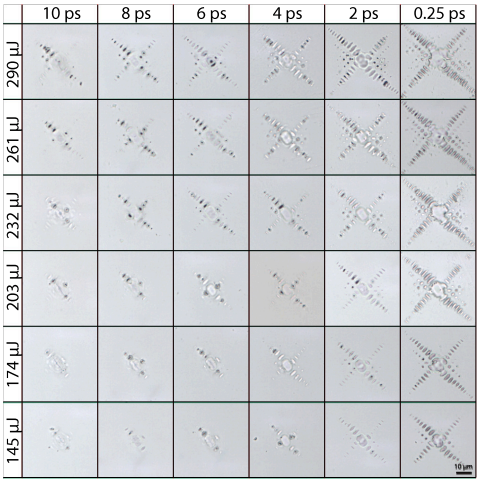

Fig. 8. Surface modifications of EXG glass, produced using a binary Airy beam with varying pulse energies and durations (both shown in first row and column of the picture).

the beam 80 µm below the surface. The set of pulse durations and energies is the same as in the aforementioned experiment, and the pictures are taken from a depth of 80 µm below the surface. The results of this experimentation are depicted in Fig. 9. In general, we observed that longer pulse durations result in clearly pronounced microcracks, as longer pulses induce larger material stress. Lower energy pulses produce less noticeable modifications compared to those obtained with high-energy pulses. We point out that in this particular scenario most microcracks at sample depth are directed along the semi-major axis of the elongation of the optical needle. No microcracks were detected within the bulk of the material when short pulses (0.25 ps, 2 ps) with energies ranging from 145 µJ to 290 µJ were used. Possibly this is related to the fact that large surface damage is induced in this regime (see Fig. 8).

From previous experiments, we deduce that the direction of the microcracks is the same (see Fig. 9). For this reason, we further investigate whether its orientation is controlled by the beam-shaping element. The GPE has its own internal orientation, which is related to the elongation direction of the optical needle. Thus, the mechanical rotation of the GPE is expected to control the orientation of the microcracks. In this experiment, we fix the laser pulse energy at 290 µJ and pulse duration at 10 ps. For each single orientation of the GPE, we scan the optical needle line-wise over the sample. In each constitutive line scan, we rotate the GPE by 15 deg. The distance between pulse shots in a single line is 50 µm. A picture of a glass sample taken at a particular depth with a 20x microscope objective is presented in Fig. 10. The directions of the microcracks depend on the orientation of the GPE. Thus, we verify that the orientation of the microcracks can be controlled by rotation of the GPE. We note that in some cases the microcracks do not maintain orientation throughout the sample.

Lastly, we study in detail the structure of the volume modification produced by the entire optical beam under investigation. This experiment is motivated by facts that: (a) the optical beam entering the glass sample is affected through the refraction law (which can be accounted for, see Ref. [66–68]) and (b) the focused optical beam is in the air smaller than the thickness of the glass sample. The propagation from optically thin material to optically denser material causes aberrations to appear, so we study these effects by recording volume modifications throughout the sample. For this purpose, we image (50x) the modification in glass from different depths. The overall damage structure appears to be more complex (Fig. 11). On the surface of the sample, multiple side lobes of the beam have enough energy to modify the glass, even though the beam structure has not developed. Microscope images obtained from below the surface (up to depths around $z = 75$ µm) reveal that the microcracks are not well defined. They seem to interconnect through the side lobes of the beam. Images taken further into the sample (depths between 75 µm to 120 µm) expose that the microcrack is now directed along the elongated axis of the

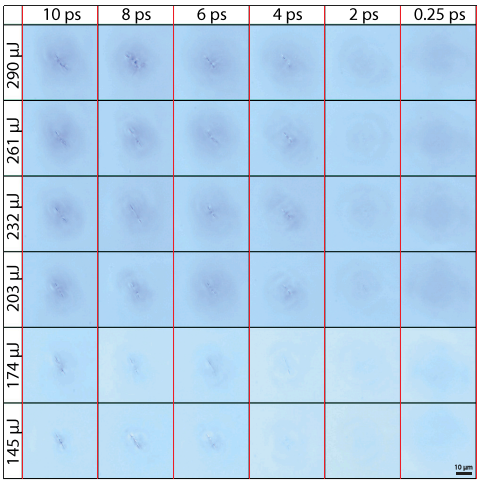

Fig. 9. Bulk modifications inside EXG glass induced by an Airy optical needle with varying pulse energies and durations (both shown in first row and column of the picture).

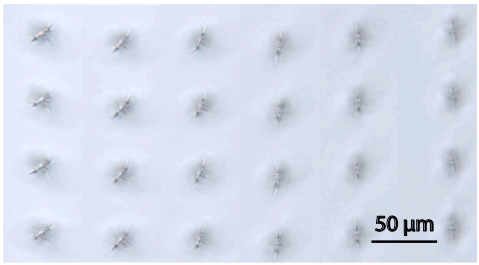

Fig. 10. Directional cracks obtained with the Airy binary beam inside EXG glass. The rotation of the GPE changed by 15 degrees every column. Microscope picture of a single plane. Modifications made with 10 ps, 290 µJ pulses.

beam. This is expected as at this depth the elongated beam profile is well developed. Imaging deeper from the surface of the sample (depths below 120 µm) microcracks become less defined, and their direction is changing. Different direction of microcrack close to the surface and deep in the sample could be attributed to the beam profile at the start and end of the optical needle where the two diffraction maxima begin to split from each other (see Fig. 6). Finally, at the end of the optical needle, multiple damage is detected due to intense side lobes (see Figs. 11, z =165 µm).

This experiment has revealed modifications produced by an elongated optical needle throughout the volume of the 0.5 mm thick EXG glass. As expected, the volume modifications largely resemble the internal structure of the optical beam. The last experiment has revealed the importance of aberration corrections for proper control of the beam structure within a glass sample. Ideally, a phase mask should be properly further optimized to account for the defocusing of the beam due to the air–glass interface.

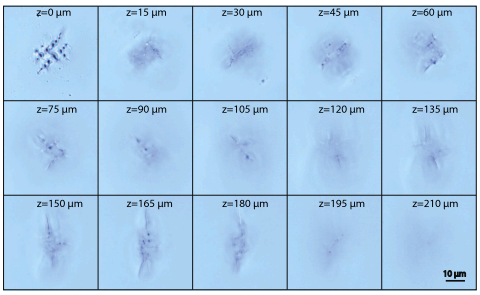

Fig. 11. Modifications inside the bulk of EXG glass sample produced by the Airy optical needle and imaged by a Microscope from different depths of the sample. The depth is defined as the distance from the surface of the sample (z =0 µm) and is given at the top of every inset. The pulse duration is 10 ps and pulse energy is 290 µJ.

5. Conclusions

In conclusion, a method was proposed to create an elliptical optical needle with controllable elongation in the transverse profile using binary phase masks, which contain cubic and linear phases. Variation of independent linear phase terms with respect to x and y coordinates allows us to control the positions of two diffraction orders created by a binary phase mask. Independent x and y cubic phases produce a bent trajectory of an individual Airy beam. Such a binary mask produces Airy beams in the +1 and −1 diffraction orders, and the linear phases flexibly control individual positions of those diffraction orders.

We study the three-dimensional parameter space around the point where an elongated transverse profile is created and introduce different metrics such as ratio of energy in the main lobe compared to the entire beam, ratio of the semi-major and semi-minor axes of the main lobe, length of the optical needle, homogeneity length, directionality length. An optical needle with good propagation distance and homogeneity is possible when the ratio of the semi-major and semi-minor axes is close to 1.

We experimentally test the formation of the optical needle beam by modulating the phase of the incoming Gaussian beam according to a binary phase mask applied to the SLM. We report a good agreement between the numerical calculations and the experimental results. We also chose a phase mask that allows us to create a beam with a major to minor axis ratio of 1.7, good homogeneity, propagation length, and inscribe it into a fused silica sample to create a geometrical phase element.

We employ this GPE inside an optical setup with a high-energy laser to produce modifications inside a glass sample using various pulse energies and pulse lengths. The most pronounced surface modifications are obtained using a short pulse duration, whereas the most pronounced volume modifications are obtained with longer pulses. A directional cracking of the glass was observed around the center of the optical needle, where an elliptical main lobe is formed.

The direction of the microcrack is controlled through the mechanical rotation of the GPE. However, in situations where the sample is thicker than the length of the optical needle, we observe, because of the abberations, uncontrolled directions of microcracks outside the zone of the optical needle. As expected, this indicates an importance of fine-tuning the phase mask to the optical setup and to the thickness of the sample which is to be laser microprocessed.

The presented implementation has its drawbacks — due to the size of the possible parameter space, for the sake of brevity we did consider Airy beams with classical propagation trajectory. Further enhancements to the presented method are expected by adjusting the phase masks to

introduce independent control of the longitudinal and transverse sizes of the resulting optical needle, which has been reported to be achieved in the literature [29,30].

CRediT authorship contribution statement

Paulius Šlevas: Conceptualization, Data curation, Investigation, Methodology, Resources, Supervision, Validation, Visualization, Writing – original draft, Writing – review & editing. **Karolis Mundrys:** Investigation, Methodology, Software, Validation, Data curation, Visualization. **Orestas Ulčinas:** Investigation, Validation. **Sergej Orlov:** Conceptualization, Data curation, Funding acquisition, Methodology, Resources, Software, Supervision, Validation, Writing – review & editing.

Declaration of competing interest

The authors declare that they have no known competing financial interests or personal relationships that could have appeared to influence the work reported in this paper.

Data availability

Data will be made available on request.

Acknowledgment

This research received funding from the Research Council of Lithuania (Lietuvos Mokslo Taryba) within the Eurostars 2 program, project No. RapidFAB/25/Ae.

Appendix A. Supplementary data

Supplementary material related to this article can be found online at https://doi.org/10.1016/j.optlastec.2024.110558.

References

[1] L. Orazi, L. Romoli, M. Schmidt, L. Li, Ultrafast laser manufacturing: from physics to industrial applications, CIRP Ann. 70 (2021) 543–566.
[2] W. Sibbett, A.A. Lagatsky, C.T.A. Brown, The development and application of femtosecond laser systems, Opt. Express 20 (2012) 6989–7001.
[3] A. Sussulini, J.S. Becker, J.S. Becker, Laser ablation icp-ms: Application in biomedical research, Mass Spectrom. Rev. 36 (2017) 47–57.
[4] W. Knox, Ultrafast technology in telecommunications, IEEE J. Sel. Top. Quantum Electron. 6 (2000) 1273–1278.
[5] Y. Weng, E. Ip, Z. Pan, T. Wang, Advanced spatial-division multiplexed measurement systems propositions—from telecommunication to sensing applications: A review, Sensors 16 (2016).
[6] F. Courvoisier, Nonstandard Light for Ultrafast Laser Microstructuring and Nanostructuring, Springer International Publishing, Cham, 2023, pp. 581–621.
[7] J. Durnin, Exact solutions for nondiffracting beams. I. The scalar theory, J. Opt. Soc. Amer. A 4 (1987) 651–654.
[8] M.K. Bhuyan, F. Courvoisier, P.A. Lacourt, M. Jacquot, R. Salut, L. Furfaro, J.M. Dudley, High aspect ratio nanochannel machining using single shot femtosecond Bessel beams, Appl. Phys. Lett. 97 (2010) 081102.
[9] L. Chen, D. Yu, Investigation of low-cost through glass vias formation on borosilicate glass by picosecond laser-induced selective etching, J. Mater. Sci., Mater. Electron. 32 (2021) 16481–16493.
[10] M. Mikutis, T. Kudrius, G. Šlekys, D. Paipulas, S. Juodkazis, High 90% efficiency bragg gratings formed in fused silica by femtosecond Gauss-Bessel laser beams, Opt. Mater. Express 3 (2013) 1862–1871.
[11] R. Meyer, L. Froehly, R. Giust, J. Del Hoyo, L. Furfaro, C. Billet, F. Courvoisier, Extremely high-aspect-ratio ultrafast Bessel beam generation and stealth dicing of multi-millimeter thick glass, Appl. Phys. Lett. 114 (2019) 201105.
[12] L. Rapp, R. Meyer, L. Furfaro, C. Billet, R. Giust, F. Courvoisier, High speed cleaving of crystals with ultrafast Bessel beams, Opt. Express 25 (2017) 9312–9317.
[13] A. Feuer, J.-U. Thomas, C. Freitag, R. Weber, T. Graf, Single-pass laser separation of 8 mm thick glass with a millijoule picosecond pulsed Gaussian–Bessel beam, Appl. Phys. A 125 (2019) 332.
[14] L. Minkevičius, D. Jokubauskis, I. Kašalynas, S. Orlov, A. Urbas, G. Valušis, Bessel terahertz imaging with enhanced contrast realized by silicon multi-phase diffractive optics, Opt. Express 27 (2019) 36358–36367.
[15] D. McGloin, V. Garcés-Chávez, K. Dholakia, Interfering Bessel beams for optical micromanipulation, Opt. Lett. 28 (2003) 657–659.
[16] L. Gao, L. Shao, B.-C. Chen, E. Betzig, 3D live fluorescence imaging of cellular dynamics using Bessel beam plane illumination microscopy, Nat. Protoc. 9 (2014) 1083–1101.
[17] M.V. Berry, N.L. Balazs, Nonspreading wave packets, Amer. J. Phys. 47 (1979) 264–267.
[18] G.A. Siviloglou, J. Broky, A. Dogariu, D.N. Christodoulides, Observation of accelerating Airy beams, Phys. Rev. Lett. 99 (2007) 213901.
[19] J. Baumgartl, M. Mazilu, K. Dholakia, Optically mediated particle clearing using Airy wavepackets, Nature Photonics 2 (2008) 675–678.
[20] H. Cheng, W. Zang, W. Zhou, J. Tian, Analysis of optical trapping and propulsion of Rayleigh particles using Airy beam, Opt. Express 18 (2010) 20384–20394.
[21] Z. Zheng, B.-F. Zhang, H. Chen, J. Ding, H.-T. Wang, Optical trapping with focused Airy beams, Appl. Opt. 50 (2011) 43–49.
[22] A. Mathis, F. Courvoisier, L. Froehly, L. Furfaro, M. Jacquot, P.A. Lacourt, J.M. Dudley, Micromachining along a curve: Femtosecond laser micromachining of curved profiles in diamond and silicon using accelerating beams, Appl. Phys. Lett. 101 (2012) 071110.
[23] M. Manousidaki, D.G. Papazoglou, M. Farsari, S. Tzortzakis, Abruptly autofocusing beams enable advanced multiscale photo-polymerization, Optica 3 (2016) 525–530.
[24] R. Ivaškevičiūtė-Povilauskienė, P. Kizevičius, E. Nacius, D. Jokubauskis, K. Ikamas, A. Lisauskas, N. Alexeeva, I. Matulaitienė, V. Jukna, S. Orlov, L. Minkevičius, G. Valušis, Terahertz structured light: nonparaxial Airy imaging using silicon diffractive optics, Light: Sci. Appl. 11 (2022) 326.
[25] M. Berry, Stable and unstable Airy-related caustics and beams, J. Opt. 19 (2017) 055601.
[26] L. Froehly, F. Courvoisier, A. Mathis, M. Jacquot, L. Furfaro, R. Giust, P. Lacourt, J. Dudley, Arbitrary accelerating micron-scale caustic beams in two and three dimensions, Opt. Express 19 (2011) 16455–16465.
[27] L. Zhu, Z. Yang, S. Fu, Z. Cao, Y. Wang, Y. Qin, A. Koonen, Airy beam for free-space photonic interconnection: Generation strategy and trajectory manipulation, J. Lightwave Technol. 38 (2020) 6474–6480.
[28] A. Zannotti, C. Denz, M.A. Alonso, M.R. Dennis, Shaping caustics into propagation-invariant light, Nature Commun. 11 (2020) 3597.
[29] Y. Guo, Y. Huang, X. Li, M. Pu, P. Gao, J. Jin, X. Ma, X. Luo, Polarization-controlled broadband accelerating beams generation by single catenary-shaped metasurface, Adv. Opt. Mater. 7 (2019) 1900503.
[30] Y. Qian, S. Zhang, Quasi-Airy beams along tunable propagation trajectories and directions, Opt. Express 24 (2016) 9489–9500.
[31] J. Durnin, J.J. Miceli, J.H. Eberly, Diffraction-free beams, Phys. Rev. Lett. 58 (1987) 1499–1501.
[32] S.N. Khonina, N.L. Kazanskiy, P.A. Khorin, M.A. Butt, Modern types of axicons: New functions and applications, Sensors 21 (2021).
[33] P. Gotovski, P. Šlevas, S. Orlov, O. Ulčinas, A. Urbas, Generation of an optical needle beam with a laser inscribed pancharatnam-berry phase element under imperfect conditions, Opt. Express 29 (2021) 33331–33345.
[34] R. Meyer, M. Jacquot, R. Giust, J. Safioui, L. Rapp, L. Furfaro, P.-A. Lacourt, J.M. Dudley, F. Courvoisier, Single-shot ultrafast laser processing of high-aspect-ratio nanochannels using elliptical Bessel beams, Opt. Lett. 42 (2017) 4307–4310.
[35] J. Dudutis, P. Gečys, G. Račiukaitis, Non-ideal axicon-generated Bessel beam application for intra-volume glass modification, Opt. Express 24 (2016) 28433–28443.
[36] J. Dudutis, R. Stonys, G. Račiukaitis, P. Gečys, Glass dicing with elliptical Bessel beam, Opt. Laser Technol. 111 (2019) 331–337.
[37] M. Jenne, D. Flamm, K. Chen, M. Schäfer, M. Kumkar, S. Nolte, Facilitated glass separation by asymmetric Bessel-like beams, Opt. Express 28 (2020) 6552–6564.
[38] J. Dudutis, M. Mackevičiūtė, J. Pipiras, R. Stonys, V. Stankevič, G. Račiukaitis, P. Gečys, Transversal and axial modulation of axicon-generated Bessel beams using amplitude and phase masks for glass processing applications, Opt. Express 30 (2022) 1860–1874.
[39] R. Meyer, R. Giust, M. Jacquot, J.M. Dudley, F. Courvoisier, Submicron-quality cleaving of glass with elliptical ultrafast Bessel beams, Appl. Phys. Lett. 111 (2017) 231108.
[40] E. Nacius, P. Gotovski, O. Ulčinas, S. Orlov, A. Urbas, V. Jukna, Spatially displaced and superposed Bessel beams for transparent material laser microprocessing, J. Opt. Soc. Amer. B 38 (2021) 3886–3895.
[41] C. Ungaro, N. Kaliteevskiy, P. Sterlingov, V.V. Ivanov, A.B. Ruffin, R.J. Terbrueggen, N. Savidis, Using phase-corrected Bessel beams to cut glass substrates with a chamfered edge, Appl. Opt. 60 (2021) 714–719.
[42] P. Šlevas, S. Orlov, E. Nacius, O. Ulčinas, Azimuthally modulated axicon vortical beams for laser microprocessing, Opt. Commun. 505 (2022) 127509.
[43] J. Baltrukonis, O. Ulčinas, S. Orlov, V. Jukna, Void and micro-crack generation in transparent materials with high-energy first-order vector Bessel beam, J. Opt. Soc. Amer. B 37 (2020) 2121–2127.

[44] J. Baltrukonis, O. Ulčinas, S. Orlov, V. Jukna, High-order vector Bessel-Gauss beams for laser micromachining of transparent materials, Phys. Rev. A 16 (2021) 034001.
[45] M. Kusko, D. Cojoc, D. Apostol, R. Muller, E. Manea, C. Podaru, Design and fabrication of diffractive optical elements, in: 2003 International Semiconductor Conference. CAS 2003 Proceedings (IEEE Cat. No. 03TH8676), Vol. 1, IEEE, 2003, pp. 167–170.
[46] M. Sparvoli, R.D. Mansano, J.F.D. Chubaci, Diffractive optical elements based in brand glass, ECS Trans. 14 (2008) 521.
[47] A.G. Poleshchuk, V.P. Korolkov, R.K. Nasyrov, Diffractive optical elements: fabrication and application, in: 7th International Symposium on Advanced Optical Manufacturing and Testing Technologies: Design, Manufacturing, and Testing of Micro- and Nano-Optical Devices and Systems, Vol. 9283, International Society for Optics and Photonics, SPIE, 2014, 928302.
[48] A. Larkin, D. Pushkarev, S. Degtyarev, S. Khonina, A. Savel'ev, Generation of Hermite – Gaussian modes of high-power femtosecond laser radiation using binary-phase diffractive optical elements, Quantum Electron. 46 (2016) 733.
[49] L. Zhu, M. Sun, M. Zhu, J. Chen, X. Gao, W. Ma, D. Zhang, Three-dimensional shape-controllable focal spot array created by focusing vortex beams modulated by multi-value pure-phase grating, Opt. Express 22 (2014) 21354–21367.
[50] P. García-Martínez, M.M. Sánchez-López, J.A. Davis, D.M. Cottrell, D. Sand, I. Moreno, Generation of Bessel beam arrays through Dammann gratings, Appl. Opt. 51 (2012) 1375–1381.
[51] P.A. Khorin, V.V. Podlipnov, S.N. Khonina, Generation of scalable wavefront for testing optical systems, in: Optical Technologies for Telecommunications 2019, Vol. 11516, International Society for Optics and Photonics, SPIE, 2020, p. 115161K.
[52] Y. Fan, J. Wei, J. Ma, Y. Wang, Y. Wu, Tunable twin Airy beams induced by binary phase patterns, Opt. Lett. 38 (2013) 1286–1288.
[53] Y. Shimotsuma, P.G. Kazansky, J. Qiu, K. Hirao, Self-organized nanogratings in glass irradiated by ultrashort light pulses, Phys. Rev. Lett. 91 (2003) 247405.
[54] M. Sakakura, Y. Lei, L. Wang, Y.-H. Yu, P.G. Kazansky, Ultralow-loss geometric phase and polarization shaping by ultrafast laser writing in silica glass, Light: Sci. Appl. 9 (2020) 1–10.
[55] R. Drevinskas, P.G. Kazansky, High-performance geometric phase elements in silica glass, APL Photonics 2 (2017) 066104.
[56] S. Pancharatnam, Generalized theory of interference, and its applications: Part I. Coherent pencils, in: Proceedings of the Indian Academy of Sciences-Section A, Vol. 44, Springer, 1956, pp. 247–262.
[57] M.V. Berry, The adiabatic phase and pancharatnam's phase for polarized light, J. Modern Opt. 34 (1987) 1401–1407.
[58] P. Gotovski, P. Šlevas, E. Nacius, V. Jukna, S. Orlov, J. Baltrukonis, O. Ulčinas, T. Gertus, Formation of optical needles by pancharatnam-berry phase element for laser-induced modifications in transparent materials, in: Laser-based Micro-and Nanoprocessing XIV, Vol. 11268, International Society for Optics and Photonics, 2020, p. 112681Y.
[59] G.A. Siviloglou, D.N. Christodoulides, Accelerating finite energy Airy beams, Opt. Lett. 32 (2007) 979–981.
[60] J. Beršys, S. Orlov, Accelerating Airy beams with particle-like polarization topologies and free-space bimeronic lattices, Opt. Lett. 48 (2023) 1168–1171.
[61] B.-Y. Wei, P. Chen, W. Hu, W. Ji, L.-Y. Zheng, S.-J. Ge, Y. Ming, V. Chigrinov, Y.-Q. Lu, Polarization-controllable Airy beams generated via a photoaligned director-variant liquid crystal mask, Sci. Rep. 5 (2015) 17484.
[62] C. Lopez-Mariscal, M.A. Bandres, J.C. Gutiérrez-Vega, Observation of the experimental propagation properties of Helmholtz-Gauss beams, Opt. Eng. 45 (2006) 068001.
[63] D.G. Voelz, Computational Fourier Optics: A MATLAB Tutorial, SPIE press Bellingham, Washington, 2011.
[64] R.C. Jones, A new calculus for the treatment of optical systemsi. Description and discussion of the calculus, J. Opt. Soc. Amer. 31 (1941) 488–493.
[65] P. Gotovski, P. Šlevas, S. Orlov, O. Ulčinas, V. Jukna, A. Urbas, Investigation of the Pancharatnam–Berry phase element for the generation of the top-hat beam, J. Opt. 24 (2022) 035607.
[66] S. Orlov, A. Gajauskaite, A. Juršenas, Propagation of vector nondiffracting and nondispersive pulsed beams through an air-dielectric planar interface, Procedia CIRP 74 (2018) 585–588.
[67] M. Jenne, D. Flamm, T. Ouaj, J. Hellstern, J. Kleiner, D. Grossmann, M. Koschig, M. Kaiser, M. Kumkar, S. Nolte, High-quality tailored-edge cleaving using aberration-corrected Bessel-like beams, Opt. Lett. 43 (2018) 3164–3167.
[68] H. Cheng, C. Xia, S.M. Kuebler, X. Yu, Aberration correction for slm-generated Bessel beams propagating through tilted interfaces, Opt. Commun. 475 (2020) 126213.

P5

Braiding of vortices in superpositions of Bessel–Gaussian beams for creation of high-contrast intensity structures

P. Šlevas, S. Orlov

Optik, 300, 171676 (2024)
DOI: 10.1016/j.ijleo.2024.171676
https://www.sciencedirect.com/science/article/pii/S0030402624000743

Supporting information: https://doi.org/10.1016/j.ijleo.2024.171676

Optik - International Journal for Light and Electron Optics 300 (2024) 171676

Contents lists available at ScienceDirect

Optik - International Journal for Light and Electron Optics

journal homepage: www.elsevier.com/locate/ijleo

Original research article

Braiding of vortices in superpositions of Bessel–Gaussian beams for creation of high-contrast intensity structures

Paulius Šlevas *, Sergej Orlov

Center for Physical Sciences and Technology, Sauletekio Ave. 3, Vilnius, Lithuania

ARTICLE INFO

Keywords:
Optical vortex
Bessel beam
Non-diffracting beam
Structured fields
Beam shaping
Complex topologies
High-contrast structures

ABSTRACT

Bessel vortices are well-known for their long focal region and the unique property of carrying angular momentum. These characteristics are desired in applications such as laser micromachining, optical trapping, and imaging. Interference of several non-diffracting vortical beams results in light fields with complex intensity distribution structure — many single charged positive and negative vortices appear and experience complex dynamics under propagation. The trajectory of single-charged vortices creates braided structures as they move, annihilate, or are created during propagation. This influences the dynamics of the high intensity regions of the combined beam: high-contrast symmetrical structures are created in the intensity profile. We demonstrate an experimental generation of such complex fields by superimposing several higher-order vortical Bessel beams. We introduce different cone angles of the interfering beams and study modifications of the resulting beam profile. We analyze the vortical structure of the combined beam, track its evolution, and observe the creation of complex high-contrast structures. We implement a convenient technique for generating superimposed higher-order Bessel beams of different spatial frequencies and topologies using diffractive phase masks. We employ a spatial light modulator to experimentally realize these structured fields and to verify theoretical and numerical predictions.

1. Introduction

The structure and properties of the electromagnetic field are crucial for modern optics and its applications [1–4]. One example of structured illumination is non-diffracting beams, in particular Bessel beams [5,6]. Their main feature is a long focal line instead of a focal point, along with their ability to self-reconstruct [7,8]. Similar characteristics are also achieved by other non-diffracting structured light: Mathieu–Gaussian [9,10] and parabolic-Gaussian (Weber–Gaussian) [11,12] beams.

The axial behavior of the laser beam is another aspect of beam shaping that has been rapidly developing [7,13,14] since the introduction of non-diffracting Bessel beams [6], which have a large ratio between the transverse and longitudinal widths of the focal line [5]. The discovery of other non-diffracting beams such as Mathieu [9], Weber [15], and Airy beams [16] further stimulated research on focal line engineering and resulted in the creation of optical needles [17–21].

An additional degree of freedom is related to the azimuthal phase dependence of higher-order non-diffracting Bessel beams J_m, which can be expressed as $\exp(im\phi)$, where m is a topological charge. This dependence leads to a phase singularity, also called an optical vortex [22–24], which manifests itself as a helical wave front with m nested screw dislocations [25,26]. Optical vortices are commonly observed in electromagnetics because they carry orbital angular momentum [27]. The first such example of optical engineering using cylindrical beams was reported in Ref. [28] where a coherent superposition of the Bessel and Neumann beams was

* Corresponding author.
E-mail address: paulius.slevas@ftmc.lt (P. Šlevas).

https://doi.org/10.1016/j.ijleo.2024.171676
Received 12 July 2023; Received in revised form 14 January 2024; Accepted 30 January 2024
Available online 2 February 2024

considered, although the Neumann beam possesses an amplitude singularity on the axis. Implying the periodicity of the transverse beam pattern in the infinite sum of the Bessel eigenmodes has resulted in the appearance of rotating patterns realized using binary diffractive element [29,30]. An alternative approach to rotating scale-invariant fields was presented in [31].

The generation of beams with a high aspect ratio and complex transverse intensity distribution is enabled by a linear superposition of several Bessel vortices [32,33]. They can be successfully applied in high-power applications [34]. In general, superposition of the vortical Bessel beam with the Laguerre–Gaussian vortex also results in explosion of the vortical structure of the combined beam [35]. These vortically rich structures evolve during the beam propagation – individual single charged positive and negative vortices move in the field, rotate under diffraction, are being created, and are being annihilated. Such vortice braiding was reported in Bessel beams superposed in Gaussian mode [36].

A single vortex is a dark spot of light with a phase singularity in its core. Thus, its three-dimensional trajectory can be considered as a single entity, especially given the fact that the time reversal would change signs of single vortices in the beam. For this reason, a negatively charged optical vortex can be interpreted as a backward propagating positively charged vortex, and the creation and annihilation of positive and negative vortices in pairs under diffraction can be seen as a dark knot of light [37–39]. This interpretation of the complex evolution of vortical structures with rich topologies has caused the appearance of terminology such as knots, braids, and bundles of dark light [40].

In this work, we build up on our previous research on azimuthaly modulated axicon beams [41], where we investigated the influence of the vortical structure with rich topology on the intensity profile of the combined beam, with the aim of applying it for laser microprocessing purposes. We extend the previous discussion by considering individual Bessel vortices with different cone angles. We start the paper by analyzing and tracking individual single-charged vortices in the combined beam. Our main interest in this investigation is the influence of the vortical dynamics on the three-dimensional pattern of the combined beam. We do observe an appearance of high-contrast intensity structures in the resulting optical beam, which is flexibly controlled by adjusting individual amplitudes, topological charges, and cone angles of Bessel vortices. We report on controllable braiding of this high-contrast intensity structure, where the angular rotation of the intensity pattern is influenced by the difference in topological charges and cone angles.

We create diffractive phase masks and experimentally verify our numerical predictions. Additionally, we confirm the presence of individual vortices in these high-contrast intensity structures using interference of the combined beam with a plane wave. Our study has revealed how the controlled knotting and braiding of individual single-charged optical vortices in the superposition of Bessel vortices influence the diffraction of the high-contrast intensity structures. This finding is especially interesting for laser microprocessing applications where such structures are desired.

2. Theoretical background

A Bessel–Gaussian beam represents an example of an apertured non-diffracting beam with finite energy, which maintains its properties over the length of the so-called Bessel zone [5–8]. The complex amplitude of a scalar Bessel–Gaussian beam is obtained in the paraxial approximation from the parabolic diffraction equation

$$E(\rho,\varphi,z,t)=\frac{1}{Z}J_m\left(\frac{k_\rho\rho}{Z}\right)\exp\left(-\frac{\rho^2}{d_0^2Z}\right)\exp\left(-\mathrm{i}\frac{k_\rho^2}{2k}\frac{z}{Z}\right)\exp(\mathrm{i}m\varphi+\mathrm{i}k_z z-\mathrm{i}\omega t), \tag{1}$$

where ρ,φ,z,t are cylindrical coordinates and time, $Z=1+\mathrm{i}z/z_0$, $z_0=kd_0^2/2$ is the Rayleigh length, d_0 is the radius of Gaussian aperture, m is the topological charge and the wave vector is $\mathbf{k}=(k_\rho,0,k_z)$. The individual components of the wave vector can be expressed by the cone angle θ as $k_\rho=k\sin\theta$ and $k_z=k\cos\theta$.

We suppose next that the light field consists of two different Bessel–Gaussian singular beams, the charges of which are m and n, and two different cone angles θ_1 and θ_2, correspondingly

$$\begin{aligned}E(\rho,\varphi,z,t)=&\left[a_mJ_m\left(\frac{k_{\rho1}\rho}{Z}\right)\exp\left(-\mathrm{i}\frac{k_{\rho1}^2}{2k}\frac{z}{Z}\right)\exp(\mathrm{i}m\varphi+\mathrm{i}k_{z1}z)\right.\\&\left.+\ a_nJ_n\left(\frac{k_{\rho2}\rho}{Z}\right)\exp\left(-\mathrm{i}\frac{k_{\rho2}^2}{2k}\frac{z}{Z}\right)\exp(\mathrm{i}n\varphi+\mathrm{i}k_{z2}z)\right]\times\frac{1}{Z}\exp\left(-\frac{\rho^2}{d_0^2Z}\right)\exp(-\mathrm{i}\omega t).\end{aligned} \tag{2}$$

A particular case of $\theta_1=\theta_2$ was studied extensively to reveal a rich vortical structure containing a matrix of single-charged positive and negative vortices [32]. The presence of such a matrix results in symmetric intensity patterns, which are applicable for laser microprocessing [41]. The matrix is stable through the Bessel zone, except for the rotation of individual vortices due to diffraction, which leads to their annihilation to the end of the Bessel zone [32]. This diffraction-induced rotation and annihilation of single charged vortices effectively creates the so-called knots and braids of darkness carved into the resulting light intensity profile of the beam [37,38,42–44].

The general paraxial case was theoretically and numerically discussed in Ref. [33], to reveal that the general vortical structure of the combined beam is more complicated and includes a complicated dynamics of vortical braids and knots. Most importantly, the rotation of individual vortices was analytically described to be controlled not only by diffraction but also by the choice of individual cone angles θ_1,θ_2.

In this work, we extend the discussion of Ref. [33] to include nonparaxial effects, staying within the almost (i.e., no significant z components) scalar approach. We recall that the vortical structure of the combined beam can be resolved by solving a system of the following equations [33]

$$F\left(\rho_l, z\right) = b, \quad l = 0, 1, 2, \ldots \tag{3}$$

$$\varphi_k = \frac{\Theta\left(\rho_l, z\right)}{m-n}, \quad k = 2, 4, \ldots, 2(m-n). \tag{4}$$

Here, $b = a_m/a_n$ is a real number and

$$\begin{aligned} F(\rho, z) &= \left| f\left(\frac{\rho}{Z}\right)\right| \exp\left[\left(\frac{k_{\rho 2}^2}{2k} - \frac{k_{\rho 1}^2}{2k}\right)\frac{z^2/z_0}{1+(z/z_0)^2}\right] \\ \Theta(\rho, z) &= \left(\frac{k_{\rho 2}^2}{2k} - \frac{k_{\rho 1}^2}{2k}\right)\frac{z}{1+(z/z_0)^2} + z\left(k_{z2} - k_{z1}\right) - \arg\left[f\left(\frac{\rho}{Z}\right)\right] \\ f\left(\frac{\rho}{Z}\right) &= J_m\left(\frac{k_{\rho 1}\rho}{Z}\right) \Big/ J_n\left(\frac{k_{\rho 2}\rho}{Z}\right). \end{aligned} \tag{5}$$

In general, we can interpret the Eq. (2) as the equation governing the transformation of the vortex $x + \mathrm{i}y = \rho\exp(\mathrm{i}\varphi)$ into a rich vortical field. This results in a local coordinate frame at the positions of single vortices with vectors $\overrightarrow{e_u}$ and $\overrightarrow{e_v}$ defined as

$$\begin{aligned} \overrightarrow{e_u} &= \overrightarrow{e_\rho}\left\{\frac{\partial F}{\partial \rho}\cos\Phi - F\frac{\partial \Theta}{\partial \rho}\sin\Phi\right\} - \overrightarrow{e_\phi}\frac{m-n}{\rho}F\sin\Phi, \\ \overrightarrow{e_v} &= \overrightarrow{e_\rho}\left\{\frac{\partial F}{\partial \rho}\sin\Phi + F\frac{\partial \Theta}{\partial \rho}\cos\Phi\right\} + \overrightarrow{e_\phi}\frac{m-n}{\rho}F\cos\Phi, \end{aligned} \tag{6}$$

where $\Phi = (m-n)\varphi - \Theta(\rho, z)$. The determinant of this transformation is

$$\begin{vmatrix} \frac{\partial F}{\partial \rho}\cos\Phi - F\frac{\partial \Theta}{\partial \rho}\sin\Phi & -\frac{m-n}{\rho}F\sin\Phi \\ \frac{\partial F}{\partial \rho}\sin\Phi + F\frac{\partial \Theta}{\partial \rho}\cos\Phi & \frac{m-n}{\rho}F\cos\Phi \end{vmatrix} = \frac{b}{\rho}\frac{\partial F}{\partial \rho}(m-n). \tag{7}$$

which means that the local frame of coordinates is either left handed or right handed, i.e. the sign of individual vortices is determined by that value.

We use Eq. (3) and substitute the expressions for F and Φ in Eq. (6). The trigonometric functions become now $\cos\Phi = 1$ and $\sin\Phi = 0$. The local coordinate frame from Eq. (6) becomes now

$$\begin{aligned} \overrightarrow{e_u} &= \overrightarrow{e_\rho}\frac{\partial F}{\partial \rho}, \\ \overrightarrow{e_v} &= \overrightarrow{e_\rho}b\frac{\partial \Theta}{\partial \rho} + \overrightarrow{e_\phi}\frac{m-n}{\rho}b, \end{aligned} \tag{8}$$

which leads to the fact that the single charged vortices are not canonical [45,46]. Their phase-winding pace is not linear with respect to their cores, and the intensity isosurfaces are elliptical in the vicinity of the core.

We note that the positions of individual vortex cores depend on the angles of the individual cones $\theta_{1,2}$, the topological charges m, n, and the Rayleigh length of the Gaussian envelope z_0. The radial positions of these individual single charged vortices of opposite signs were discussed briefly in Ref. [33]. Here, we pay attention to their azimuthal positions. The length of the Bessel zone of the individual Bessel vortex is $z_B = d_0/\tan\theta$. Let us assume that we remain in the Rayleigh zone of the Gaussian envelope, that is, $z \in [-z_0, z_0]$. For distances close to the focal plane, the change in radial position can be neglected [32]. In this case, the azimuthal positions of the individual vortices near the focal plane ($z \approx 0$) are determined by equations [32]

$$\varphi_k(z) \approx \varphi_k + \gamma z \tag{9}$$

where $\varphi_k \equiv \varphi_k(0)$. Most notable is that the vortical structure will experience a constant rotation with a speed determined by $\mathrm{d}\varphi_k/\mathrm{d}z = \gamma$. We evaluate the rotation speed from Eqs. (5) as

$$(m-n)\gamma = \left(\frac{k_{\rho 2}^2}{2k} - \frac{k_{\rho 1}^2}{2k}\right) + \left(k_{z2} - k_{z1}\right) - \frac{\rho_l f'(\rho_l)}{z_0 b}. \tag{10}$$

We note that the rotation speed depends on the difference in the cone angles explicitly via the first two terms, and the third term expresses the dependency on the different cone angles inexplicitly together with the dependency on the radial positions of the individual vortices. The first two terms cause a constant rotation, whereas the third term describes the diffraction of the structure, and its direction depends on the sign of the single-charged vortex. The influence of the angles can be estimated more precisely from the following expression

$$(m-n)\gamma = k\left(\frac{\sin^2\theta_2}{2} - \frac{\sin^2\theta_1}{2}\right) + k\left(\cos\theta_2 - \cos\theta_1\right) - \frac{\rho_l f'(\rho_l)}{z_0 b}. \tag{11}$$

In the paraxial approximation $\sin\theta \approx \theta$ and $\cos\theta \approx 1 - \theta^2/2$, these relations remove the first two terms from the Eq. (11), and they can be neglected in the paraxial regime, see Ref. [33]. The third term represents the braiding of the vortices due to diffraction. For small

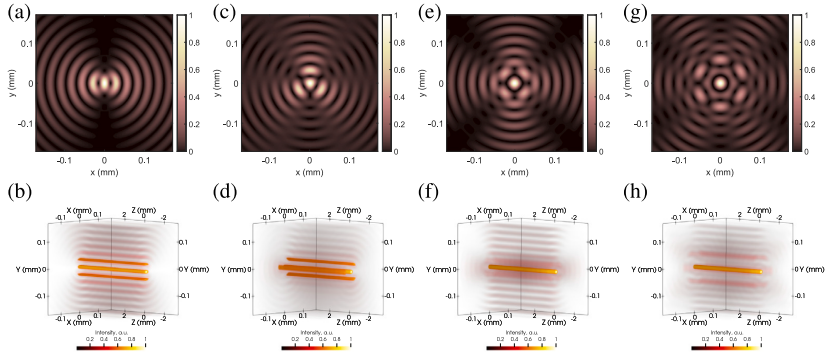

Fig. 1. Intensity distributions (transverse in the upper row and 3d in the lower row) of the Bessel beam superpositions with the same cone angles $\theta_1 = \theta_2$. Topological charge of the first beam $n = 0$, topological charges of the second beam $m = 2$, $m = 3$, $m = 4$, $m = 6$ in (a,b), (c,d), (e,f) and (g,h) respectively.

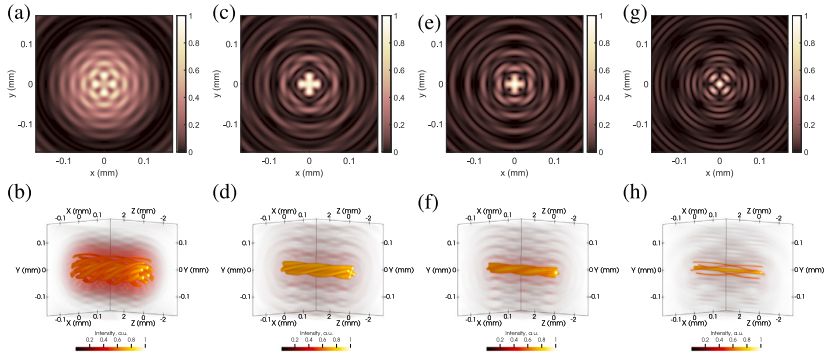

Fig. 2. Intensity distributions (transverse in the upper row and 3d in the lower row) of the superpositions of Bessel beams of the topological pair $n = 0$ and $m = 4$. The ratio of cone angles θ_1/θ_2 is 17.3, 4, 2.8 and 1.49 in (a,b), (c,d), (e,f) and (g,h) respectively.

paraxial angles, it is zero in the center of the beam if the difference $|m|-|n|$ of the topological charges is greater than three. However, in the periphery of the beam, this term causes clockwise and counterclockwise rotation of the vortices due to diffraction [32,33]. As it depends on the sign of the vortex, it causes the annihilation or creation of single-charged vortices in situations involving two Bessel vortex beams [32,33] or Bessel and Gaussian vortices [35].

Taking into account higher Taylor expansion terms in the Eq. (11) reveals that the first term that causes rotation at a constant pace is quartic and proportional to the difference $\theta_1^4 - \theta_2^4$. This means that for small cone angles, the higher ratio of angles is required to observe braiding of single vortex paths. For larger cone angles, when we move out of the paraxial approximation, this rotation is always observed, and the speed of braiding is influenced by the ratio of the cone angles, not in a proportional way. We note that some similarities are observed under coherent superpositions of Laguerre–Gaussian beams; however, the rotation speed depends on the propagation distance z [47].

Next, we introduce the results of numerical simulations performed using Eq. (2) where we use $d_0 = 2.5$ mm, $\lambda = 532$ nm, $a_m = a_n$ and vary the topological charges m from 2 to 6 and n from -1 to 13. The cone angles change as follows: θ_1 from 0.6° to 1.2° and θ_2 from 0.18° to 0.9°. In a further discussion, we introduce the cone angle ratio θ_1/θ_2.

The presentation of numerical results begins with the case $\theta_1/\theta_2 = 1$ and is presented in Fig. 1. Expectantly, the transverse beam cross section ($z = 0$) is split into $|m-n|$ parts in the azimuth direction, and the vortical structure is stable throughout the center of the Bessel zone. Such behavior was previously observed in superpositions of Bessel vortices with the same cone angle; see Ref. [32,41].

As a next step, we move on to the case of uneven cone angles. For small propagation distances z the radial positions of the single vortex cores barely change; see Eq. (9); however, the azimuthal positions experience linear dependence; see Eqs. (9), (11). This means that single charged positive and negative optical vortices will rotate at a constant pace defined by the difference in the cone angles. Here, the interaction between rotation caused by the mismatch of the individual cone angles and diffraction is

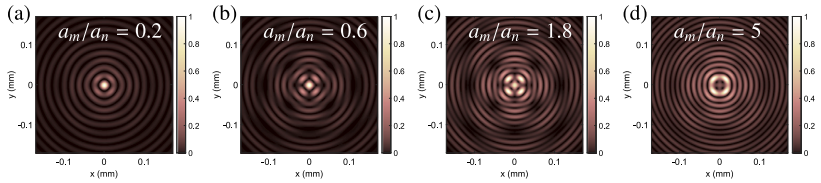

Fig. 3. Transverse intensity distribution of superpositions of Bessel beams of topological pair $n = 0$, $m = 4$, cone angle ratio $\theta_1/\theta_2 = 1.49$ and different amplitude ratios of 0.2, 0.6, 1.8 and 5 in (a), (b), (c) and (d) respectively.

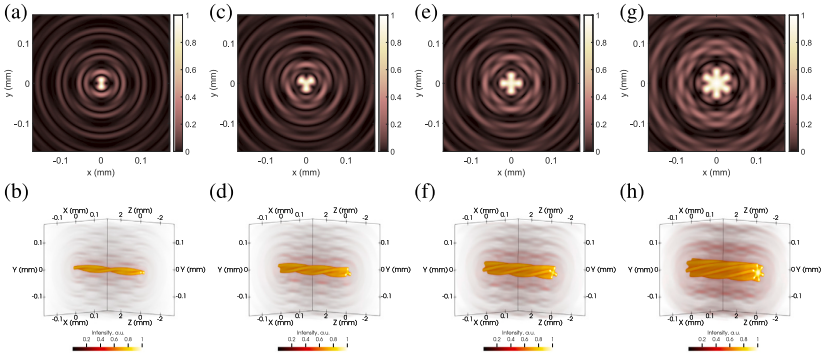

Fig. 4. Intensity distributions (transverse in the top row and 3d in the bottom row) of the superposition of Bessel beams. Cone angle of the first beam θ_1 and topological charge of the second beam $n = 0$ are constant. Topological charges of the first beam are $m = 2$, $m = 3$, $m = 4$, $m = 6$ in (a,b), (c,d), (e,f), (g,h), respectively, while ratio of cone angles θ_1/θ_2 are 2, 3, 4 and 6.5 in (a,b), (c.d), (e,f) and (g,h), respectively.

important. Diffraction causes single charged vortices to rotate in different directions, thus it is crucial to select such a combination of cone angles that diffraction effects are comparatively small. In this case, since individual vortices located at the same distance from the center of the beam are separated by high-intensity regions, this will lead to a similar rotation of high-intensity regions. In Fig. 2 we show the results of the numerical simulation for a few particular cases, when $n = 0$, $m = 4$ are constant, and θ_1/θ_2 is changing. Because the cone angles are not equal, we expect the high-intensity regions to rotate during diffraction with different azimuthal velocity. As these regions rotate, a braided structure is clearly revealed in the 3d beam representation; see Fig. 2(b, d, f, h). As expected, we note a higher rotation speed of the high-contrast structure when the cone angle ratio is large. Rotation is less noticeable when θ_1/θ_2 is closer to unity (compare Fig. 2(b) and (h)). The transverse intensity profile of the combined beam is also affected by the cone angle mismatch between the two beams. The lower contrast structure is obtained when $\theta_1/\theta_2 = 17.3$ (Fig. 2(a)). A reduction in this cone angle ratio results in a uniform cross-shaped intensity peak in the center (see Fig. 2(c) and (e)), which starts to split when θ_1/θ_2 approaches 1 (see Fig. 2(g)).

Another question worth considering is the influence of the amplitude ratio a_m/a_n on the intensity patterns of the superposed beam. The impact of this parameter on the vortical structure was investigated [33] and it was revealed that it changes the radial coordinates of the single charged vortices present in the beam. Until now, we have assumed the same amplitudes of the individual beams, so we are asking ourselves how different amplitudes of individual Bessel–Gaussian beams will manifest themselves on the intensity distribution. A particular example is presented in Fig. 3. In the first example, the amplitude of the Bessel beam with topological charge m is five times smaller than the amplitude of the beam with topological charge n (see Fig. 3(a)). Although a rich vortical structure is present in the combined beam, the intensity pattern largely resembles the zeroth-order Bessel beam with slight distortions present. Thus, the intensity pattern obtains a low-contrast structure. Decreasing the amplitude of the zeroth-order Bessel beam, we observe an appearance of a four-lobe pattern in the transverse plane (see Fig. 3(b)). The central part of the interference pattern is still dominated by the zeroth-order Bessel beam. Making the amplitudes equal results in the side lobes, obtaining intensities comparable to those of the central lobe (see Fig. 2(g)). An increase in the amplitude of the Bessel beam with topological charge m enhances the side lobes even more. When the amplitude of the Bessel beam with topological charge m is five times larger than the amplitude of the zeroth order beam, resulting intensity pattern largely resembles the first beam, however, the addition of the second beam results in the splitting of the central vortex into four single charged vortices, which cause the first ring to become modulated. Additional examples are provided as supplementary animated sequences for selection of topological charges m and n and cone angles $theta_1$ and $theta_2$.

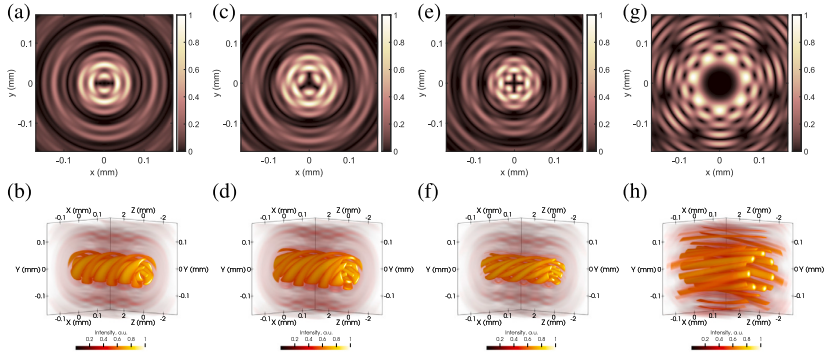

Fig. 5. Intensity distributions (transverse in the top row and 3d in the bottom row) of various superimposed beams Bessel beams. (a,b) $\theta_1/\theta_2 = 5.8$, $m = 3$ and $n = 1$, (c,d) $\theta_1/\theta_2 = 5.8$, $m = 4$ and $n = 1$, (e,f) $\theta_1/\theta_2 = 5.2$, $m = 3$ and $n = -1$, (g,h) $\theta_1/\theta_2 = 0.7$, $m = 6$ and $n = 13$.

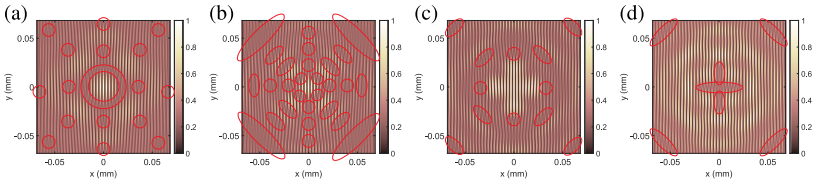

Fig. 6. Interference pattern of the structured Bessel beam and a plane wave. Phase dislocations are marked in the pictures. Bessel beam superposition parameters: (a) $\theta_1 = \theta_2$, $m = 4$ and $n = 0$, (b) $\theta_1/\theta_2 = 1.49$, $m = 4$ and $n = 0$ (c) $\theta_1/\theta_2 = 4$, $m = 4$ and $n = 0$, (d) $\theta_1/\theta_2 = 5.2$, $m = 3$ and $n = -1$.

When investigating the general trends in the creation of high contrast intensity patterns, we observed an interaction between the difference in topological charges $|m - n|$ and the ratio of the cone angles of Bessel vortices in the superposition. The difference in topological charges influences the azimuthal dependence of the high contrast structure, but the condition for the most pronounced shape requires the ratio of the cone angles to depend on $|m - n|$. Therefore, we display this interaction between topological charges and the cone angle ratio of the constituent beams as the next step. A careful choice of parameters enables the creation of high-contrast structures similar to the one presented in Fig. 2(c), but with a desirable number of high-intensity spikes around the center. Few exemplary cases of this procedure are given in Fig. 4. Here, we chose $n = 0$ and changed the topological charge m, and the ratio of cone angles θ_1/θ_2 also varies. The reason why the difference between topological charges in a high-contrast structure is related to a ratio of cone angles becomes apparent by looking at the right column of Fig. 4. The speed at which the high-contrast structure experiences rotation during diffraction is more or less similar for all the cases considered. As expected, this rotation of the high intensity pattern is caused by the rotation of single charged vortices located near the center of the beam.

Yet another interesting situation occurs when the topological charge of the second Bessel beam n is nonzero. In this case, the conservation of the topological charge requires the appearance of the optical vortex with the topological charge, whose absolute value is $\min(|m|, |n|)$. The presence of the central vortex, together with the control of the positions of a single charged vortices, allows us to create high-contrast inverted structures, where the central dark part of the beam is azimuthaly modulated, see Fig. 5. These superpositions of individual Bessel vortices result in the creation of more complex entwined and braided high-intensity regions within the Bessel zone. In all cases, this is caused by the presence of braided vortex lines in the propagating combined beam. Another important point is that regions with comparable intensities occupy larger volumes compared to the situations investigated previously ($n = 0$). As expected, larger differences between the topological charges cause a slower pace of structure rotation.

We finalize the theoretical section and prepare ourselves for the experimental detection of the vortical structure. One of the experimental techniques used for detection of optical vortices is a plane wave interferometry when interfering waves propagate at an angle in respect to each other. In this case, a fine fringe structure is created on the top of the brightest intensity pattern. The presence of the optical vortex can be distinguished by the appearance of a screwed fork dislocation, which is oriented straight or upside down, depending on the sign of the topological charge of the vortex [48,49]. We calculate such interference patterns between the combined beam and a plane wave (see Fig. 6) for a few particular cases. In these interference patterns, we encircle points with a fork shape, which correspond to the positions of phase dislocations in the beam.

For this particular preparation, we chose the case in which $|m - n| = 4$ and several different cone angle ratios θ_1/θ_2 are considered. The vortex positions determined by a fine look onto the interference pattern are in line with those predicted analytically from Eq. (5).

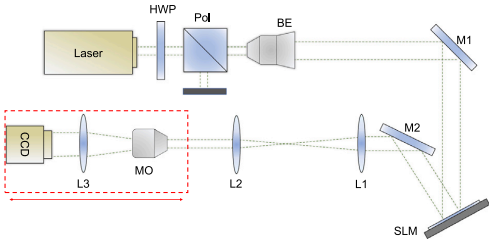

Fig. 7. Experimental setup. HWP — half wave plate, BP — beam polarizer, BE — beam expander, M1, M2 — mirrors, SLM — spatial light modulator, L1, L2, L3 — lenses of focal length f = 300 mm, f = 100 mm, f = 200 mm respectively, MO — microscope objective (10x).

For equal cone angles of the two constituent beams (Fig. 6(a)), a ring of four phase dislocations is observed around the central peak. Phase dislocations on the ring are more difficult to resolve because of the small separation between them in the vicinity of the beam center. As we look into the regions of the combined beam located further away, we observe two patterns of screwed fork dislocations: a diagonal one and a crest-like one. As expected, the topological charges of vortices in these patterns are the opposite. Most importantly, this simulation shows the pitfalls of the interferometric detection technique, which seems to be very sensitive to the angle at which the plane wave impinges on the focal plane of the combined beam.

In the next numerical experiment, we set $\theta_1/\theta_2 = 1.49$ (see Fig. 6(b)). In this case, the angle between the propagation directions of the combined beam and the plane wave seems to be optimally selected. The ring of the suboptimally resolved phase dislocations is no longer present. As expected from Eq. (5), the locations of individual vortex cores, together with charges, are clearly detected. In the next step, we set $\theta_1/\theta_2 = 4$, (Fig. 6(c)), vortices are detected outside the main intensity peak. This results in a flat, cross-shaped intensity distribution in the center. Lastly, we investigate a scenario when the difference of the topological charges is the same, but the combined beam is an interference of two nonzero Bessel vortices (see Fig. 6(d)). Consequently, the position of the vortices is in the center of the structured beam and forms a cross of darkness, contrary to the cross of light in Fig. 6(c).

3. Experimental setup

The formation of the vortical structure and the high contrast intensity regions within the combined beam, see Section 2, was experimentally observed using a setup presented in Fig. 7. A 532 nm CW DPSS laser beam is attenuated by a half-waveplate (HWP) and polarizer (Pol) pair and is directed to a phase-only reflective spatial light modulator (SLM, PLUTOVIS-006-A, HOLOEYE) at a small angle (<5 deg). A phase mask is prepared numerically and loaded onto the SLM and the modulated reflected phase beam is directed into a $4f$ lens system composed of the lenses L1 (f = 300 mm) and L2 (f = 100 mm). The resulting beam is scanned along its propagation direction using an imaging setup, containing a 10x microscope objective (MO), a collimating lens L3 (f = 200 mm) and a CCD camera, placed on a motorized stage. The phase mask applied to the SLM is calculated using the following transfer function

$$T(\rho, \theta_1, \theta_2) = \exp(\mathrm{i}k\theta_1\rho)\exp(\mathrm{i}m\varphi) + \exp(\mathrm{i}k\theta_2\rho)\exp(\mathrm{i}n\varphi), \tag{12}$$

where ρ is radial coordinate, θ_1 and θ_2 are the cone angles of the two beams, m and n are the topological charges of the superimposed beams. In what follows, all calculated phase masks are provided as insets in Figs. 8 to 11, which are discussed in the next section.

4. Experimental results

In this section, we experimentally verify the formation of various composite beams composed of individual Bessel vortices with various topological charges and cone angles. The experiments were carried out using the setup described in Section 3. In a fashion similar to that in the theoretical section, we superimpose Bessel vortices with the same cone angle. In this experiment, we vary only the topological charge m, while maintaining the topological charge $n = 0$. The resulting intensity profiles near the center of the Bessel zone are presented in Fig. 8. The phase masks used for the generation of these patterns are given as inlets on the upper right side of the picture. Except for a slight rotation of the pattern due to misalignment, the results closely resemble the theoretical expectations of Fig. 1. In all cases, there are central intensity maxima formed due to a topological charge beam $n = 0$ around which side intensity peaks are arranged due to interference with the first beam. The number of side intensity peaks is $|m - n|$ and they are located around the main maxima, as predicted in the numerical simulations. We have checked the behavior of these intensity structures under propagation, and, as expected, we did not observe any changes in the center of the Bessel zone.

In the next set of experiments, we chose a single pair of topological charges for superimposed beams and varying the cone angles of individual Bessel vortices. Here, in particular, the topological charges are $n = 0$, $m = 4$. The experimental results are depicted in Fig. 9. As expected from our numerical investigation, the large ratio θ_1/θ_2 results in a low contrast transverse intensity distribution being recorded (Fig. 9a). The decrease in the ratio of the cone angles creates a cross in the transverse plane with an almost flat intensity in the main peak, clearly visible in Fig. 9(b) and (c). For the lowest ratio $\theta_1/\theta_2 = 1.49$ considered in the experiment, the

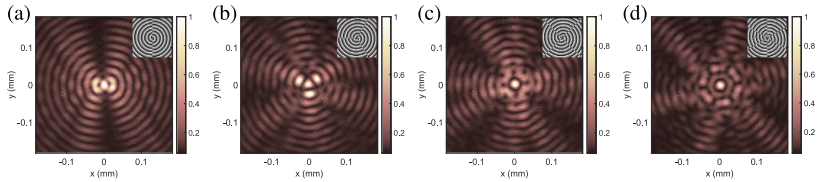

Fig. 8. Experimentally obtained transverse intensity distribution profiles of superpositions of Bessel beams with constant ratio of cone angles $\theta_1/\theta_2 = 1$. Topological charge of the first beam $n = 0$ topological charges of the second beam $m = 2$, $m = 3$, $m = 4$, $m = 6$ in (a), (b), (c) and (d), respectively.

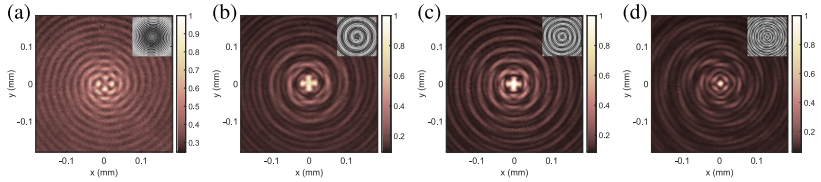

Fig. 9. Experimentally obtained transverse intensity distribution profiles of superpositions of Bessel beams with topological pairs $n = 0$ and $m = 4$. The ratios of the cone angles are θ_1/θ_2 are 17.3, 4, 2.8 and 1.49 in (a), (b), (c) and (d), respectively.

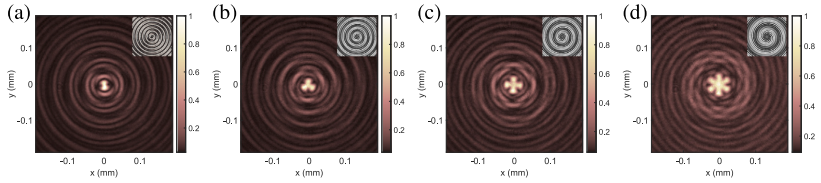

Fig. 10. Experimentally obtained transverse intensity distribution profiles of superpositions of Bessel beams. The cone angle of the first beam θ_1 and the topological charge of the second beam $n = 0$ are constant. The topological charges of the first beam are $m = 2$, $m = 3$, $m = 4$, $m = 6$ in (a), (b), (c), (d), respectively, while the ratio of cone angles θ_1/θ_2 is 2, 3, 4 and 6.5 in (a), (b), (c), and (d), respectively.

phase mask creates a structure with central intensity maxima and four side peaks around it. Overall, these findings are in line with the numerically predicted beams, see Fig. 2.

We move on to verify a set of parameters which, according to the theoretical expectations, should result in a fine-defined high-contrast structure. For this purpose, we generate a set of phase masks and test them experimentally. These experiments reproduce a situation similar to that in Fig. 9(b), where a structured central peak of the beam has a flat intensity. It can be realized using different topological charges as well, but some fine adjustments to the ratio of the cone angles have to be introduced. In this set of experiments, we maintain a constant cone angle of the first superimposed beam ($\theta_1 = const$) and a constant topological charge of the second beam ($n = 0$). We vary the topological charge m of the first component and the cone angle θ_2 of the second. The resulting intensity profiles are given in Fig. 10. As predicted, the number of merged peaks around the center is the same as the topological charge of the first constituent beam (m). The transversely elongated light structure is obtained when $\theta_1/\theta_2 = 2$ and $m = 2$ (Fig. 10 a), while more complex structures that resemble a screw and have a nearly flat intensity distribution in the main peak are generated when $m = 3$, $m = 4$, $m = 6$ and $\theta_1/\theta_2 = 3$, $\theta_1/\theta_2 = 4$, $\theta_1/\theta_2 = 6.5$ which are presented in Fig. 10(b), (c) and (d), respectively. These experimentally obtained high-contrast structures behave as expected compared to numerically determined intensity distributions shown in Fig. 4. In all cases, these high-contrast intensity patterns rotate in a manner similar to that in the numerical predictions. For the sake of brevity and to not repeat ourselves, we omit these figures and direct the reader to the theoretical section.

Our experiments continue with tests of the last set of parameters that were discussed in the theoretical part; see Fig. 5. The experimentally captured results of the beams diffracted from a set of phase masks shown in Fig. 11, together with the resulting transverse intensity distributions, show a high degree of similarity to expectations. Here, in all cases, the individual Bessel vortices have non-zero topological charges. Due to the presence of the central vortex, the vicinity of the center of the beam is hollow. We note that the shape of the minimum is similar to the shape of the intensity maxima in Fig. 10. In general, the experimentally determined transverse intensity patterns seen in Fig. 11(a) to (c) closely match the theoretical estimates. However, the combined beam presented in Fig. 11(d) has less contrast than the one determined numerically. Here, also, the intensity minimum is slightly distorted. In this case, we were unable to find a better position in the Bessel zone where the beam would behave as expected. In all cases, we fine-tuned the position of the recording camera to best match the center of the Bessel zone. However, some artifacts may

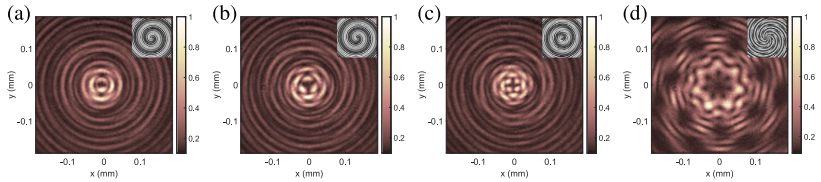

Fig. 11. Experimentally obtained transverse intensity distribution profiles of various superimposed beams Bessel beams. (a) $\theta_1/\theta_2 = 5.8$, $m = 3$ and $n = 1$, (b) $\theta_1/\theta_2 = 5.8$, $m = 4$ and $n = 1$, (c) $\theta_1/\theta_2 = 5.2$, $m = 3$ and $n = -1$, (d) $\theta_1/\theta_2 = 0.7$, $m = 6$ and $n = 13$.

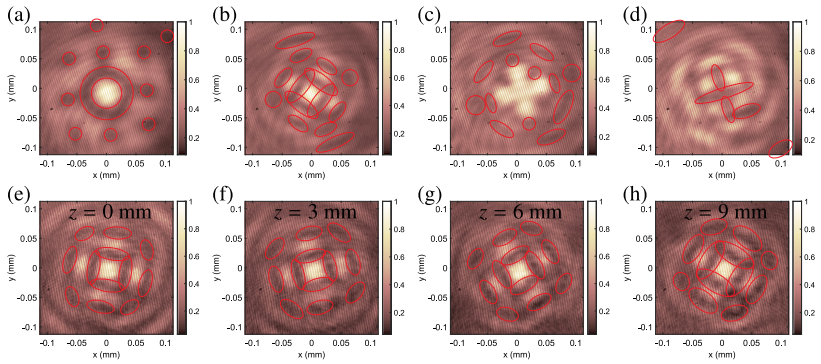

Fig. 12. Experimentally obtained interference patterns of the combined Bessel beam and a plane wave. Phase dislocations are marked in the pictures by red ellipses. The parameters of the Bessel beam superposition are: (a) $\theta_1 = \theta_2$, $m = 4$ and $n = 0$, (b) $\theta_1/\theta_2 = 1.49$, $m = 4$ and $n = 0$ (c) $\theta_1/\theta_2 = 4$, $m = 4$ and $n = 0$, (d) $\theta_1/\theta_2 = 5.2$, $m = 3$ and $n = -1$. (e–h) Pattern (b) at different propagation distances.

appear due to slight misalignments, the complexity of phase masks, or difficulties related to the realization of high-order optical vortices [50].

From an experimental standpoint, the detection of very rich topological structures is not an easy task. First of all, as we have discussed in the theoretical part, individual vortices are located at very different distances from each other. Their individual strengths such parameters as elipticities and orientations of the main axis for non-canonical vortices may make it difficult to select optimal conditions for the best resolving power. In order to optimally resolve non-canonical vortices in the presence of a large amount of nearby vortices of the same or opposite charge, the angle at which the plane wave is impinging the transverse plane of the combined beam has to be carefully selected.

Another peculiarity to the validation of the rich vortical structure is the rotation of the intensity pattern of the combined beam during diffraction. Here, we interfere superimposed Bessel beams with a Gaussian beam (of large diameter) to experimentally determine the positions of individual vortices.

For this purpose, we modify the setup presented in Fig. 7 as follows: lens L2 is now $f = 200$ mm, microscope objective (MO) is 40x, and the reference beam is directed into the Bessel zone at a small angle (approx. 5 deg). For this particular experiment, we select 4 masks that produce superpositions of beams with topological charge difference $|m - n| = 4$ and various cone angle ratios θ_1/θ_2 and record the result of two beam interference.

The results of these experiments are shown in Fig. 12, where the positions of the optical vortices are determined from the position of screwed fork dislocations in the interference fringes. These are enclosed by red ellipses in Fig. 12. In general, the arrangement of individual vortex positions is similar to that numerically determined and presented in Fig. 6. Some vortex positions do not seem to be detected because of the low contrast of interference fringes in the regions with low intensity. Furthermore, the positions of some vortices were not found in the places numerically predicted in Fig. 12(c and d). This could be caused by some imperfect experimental conditions — improperly detected focal plane, curved wavefront of the reference beam, effects caused by the mismatch between the angles of incidence and reflection from the SLM, etc. Fig. 12(e–h) show the interference patterns of Fig. 12(b) at different propagation distances starting from an arbitrarily chosen position $z = 0$ mm. These figures confirm the rotation of the vortical structure. We note that the angle of the reference wave had to be adjusted at every plane to produce interference patterns.

5. Conclusions

In conclusion, we have discussed how superpositions of vortical Bessel beams with different topological charges and cone angles create singular braided structures in the combined beam. We have investigated both theoretically and experimentally the impact of

the topological charge and cone angle of each constituent beam on the topology of the vortical structure and the overall shape of the superposition. The difference in the modulus of topological charges $|m - n|$ controls the number of single charged optical vortices created in ever increasing circles around the central peak or the central vortical void. The presence of the azimuthally symmetric vortical matrix influences the shape of the high-intensity regions. Various high-contrast symmetric areas do appear in the combined beam.

The ratio of cone angles influences the angular rotation of the vortical structure and the accompanying high-contrast intensity shapes. On the other hand, it also affects the individual position of these vortices and the contrast of the intensity areas surrounding them. The creation of braided vortical and intensity structures in the Bessel zone is possible only for uneven cone angles. For equal cone angles the braiding naturally occurs during the diffraction as individual single charged vortices are annihilating pair-vise and the far field is being created. The number of braids in the combined beam depends on the difference in topological charges $m - n$, and the rotation speed is lower for higher differences $m - n$. For very small cone angles the constant rotation is observable only when the quartic term $\theta_1^4 - \theta_2^4$ is sufficiently large in the on-axis region of interest. Moreover, it has to also be comparatively large in comparison to the rotation caused by beam diffraction. The larger angle ratios lead not only to faster rotations of the vortical and high-intensity braids in the combined beam but also enable one to overcome diffraction effects in the center of the Bessel zone.

Our numerical and experimental findings were verified using interference with a plane wave. We confirmed the presence of optical vortices and determined their positions, which are in line with the theoretical predictions.

Such high-contrast braided structures have potential in fields as direct laser microprocessing of transparent materials using scalar [10,41,51] or vector [34,52,53] Bessel vortices. Another promising field for the application of such high-contrast structures is processes such as laser-induced polymerization [54,55]. The superpositions of higher-order Bessel beams were also employed to measure the refractive index of fluids [56]. Given the wide number of applications for structured light that has orbital angular momentum and manifests non-diffracting properties [3,4], the reported findings are promising for similar areas of research and applications.

CRediT authorship contribution statement

Paulius Šlevas: Conceptualization, Data curation, Investigation, Methodology, Project administration, Software, Validation, Visualization, Writing – original draft, Writing – review & editing. **Sergej Orlov:** Conceptualization, Funding acquisition, Methodology, Project administration, Resources, Supervision, Writing – review & editing, Software.

Declaration of competing interest

The authors declare that they have no known competing financial interests or personal relationships that could have appeared to influence the work reported in this paper.

Data availability

Data will be made available on request.

Acknowledgments

This research has received funding from the Research Council of Lithuania (LMTLT), agreement No [S-MIP-23-71].

Appendix A. Supplementary data

Supplementary material related to this article can be found online at https://doi.org/10.1016/j.ijleo.2024.171676.

References

[1] H. Rubinsztein-Dunlop, A. Forbes, M.V. Berry, M.R. Dennis, D.L. Andrews, M. Mansuripur, C. Denz, C. Alpmann, P. Banzer, T. Bauer, et al., Roadmap on structured light, J. Opt. 19 (2016) 013001.
[2] O.V. Angelsky, A.Y. Bekshaev, S.G. Hanson, C.Y. Zenkova, I.I. Mokhun, Z. Jun, Structured light: ideas and concepts, Front. Phys. 8 (2020) 114.
[3] F. Courvoisier, Nonstandard light for ultrafast laser microstructuring and nanostructuring, in: Ultrafast Laser Nanostructuring: The Pursuit of Extreme Scales, 2023, pp. 581–621.
[4] A. Porfirev, S. Khonina, A. Kuchmizhak, Light–matter interaction empowered by orbital angular momentum: Control of matter at the micro-and nanoscale, Prog. Quantum Electron. (2023) 100459.
[5] J. Durnin, Exact solutions for nondiffracting beams. i. the scalar theory, J. Opt. Soc. Amer. A 4 (1987) 651–654.
[6] J. Durnin, J. Miceli Jr., J.H. Eberly, Diffraction-free beams, Phys. Rev. Lett. 58 (1987) 1499.
[7] S.N. Khonina, N.L. Kazanskiy, S.V. Karpeev, M.A. Butt, Bessel beam: Significance and applications—a progressive review, Micromachines 11 (2020) 997.
[8] R. Grunwald, M. Bock, Needle beams: a review, Adv. Phys.: X 5 (2020) 1736950.
[9] J.C. Gutiérrez-Vega, M. Iturbe-Castillo, S. Chávez-Cerda, Alternative formulation for invariant optical fields: Mathieu beams, Opt. Lett. 25 (2000) 1493–1495.
[10] P. Slevas, S. Orlov, E. Nacius, O. Ulcinas, P. Gotovski, J. Baltrukonis, V. Jukna, Laser induced modifications in transparent materials using azimuthally modulated axicon beams, in: Laser Applications in Microelectronic and Optoelectronic Manufacturing (LAMOM) XXV, Vol. 11267, SPIE, 2020, pp. 17–23.
[11] M.A. Bandres, B. Rodríguez-Lara, Nondiffracting accelerating waves: Weber waves and parabolic momentum, New J. Phys. 15 (2013) 013054.

[12] S. Orlov, V. Vosylius, P. Gotovski, A. Grabusovas, J. Baltrukonis, T. Gertus, Vector beams with parabolic and elliptic cross-sections for laser material processing applications, J. Laser Micro Nanoeng. 13 (2018) 280–286.
[13] M. Duocastella, C.B. Arnold, Bessel and annular beams for materials processing, Laser Photonics Rev. 6 (2012) 607–621.
[14] R. Stoian, M.K. Bhuyan, G. Zhang, G. Cheng, R. Meyer, F. Courvoisier, Ultrafast Bessel beams: advanced tools for laser materials processing, Adv. Opt. Technol. 7 (2018) 165–174.
[15] M.A. Bandres, J.C. Gutiérrez-Vega, S. Chávez-Cerda, Parabolic nondiffracting optical wave fields, Opt. Lett. 29 (2004) 44–46.
[16] G. Siviloglou, J. Broky, A. Dogariu, D. Christodoulides, Observation of accelerating airy beams, Phys. Rev. Lett. 99 (2007) 213901.
[17] J. Wang, W. Chen, Q. Zhan, Engineering of high purity ultra-long optical needle field through reversing the electric dipole array radiation, Opt. Express 18 (2010) 21965–21972.
[18] E.T. Rogers, S. Savo, J. Lindberg, T. Roy, M.R. Dennis, N.I. Zheludev, Super-oscillatory optical needle, Appl. Phys. Lett. (102) (2013).
[19] S. Orlov, A. Juršėnas, E. Nacius, Optical Bessel-like beams with engineered axial phase and intensity distribution, J. Laser Micro Nanoeng. 13 (2018) 244–248.
[20] S. Orlov, A. Juršėnas, J. Baltrukonis, V. Jukna, Controllable spatial array of Bessel-like beams with independent axial intensity distributions for laser microprocessing, J. Laser Micro Nanoeng. 13 (2018) 324–329.
[21] P. Gotovski, P. Šlevas, E. Nacius, V. Jukna, S. Orlov, J. Baltrukonis, O. Ulčinas, T. Gertus, Formation of optical needles by pancharatnam-berry phase element for laser-induced modifications in transparent materials, in: Laser-Based Micro-and Nanoprocessing XIV, Vol. 11268, International Society for Optics and Photonics, 2020, 112681Y.
[22] P. Coullet, L. Gil, F. Rocca, Optical vortices, Opt. Commun. 73 (1989) 403–408.
[23] K. Gahagan, G.J. Swartzlander, Optical vortex trapping of particles, Opt. Lett. 21 (1996) 827–829.
[24] G. Molina-Terriza, J.P. Torres, L. Torner, Twisted photons, Nat. Phys. 3 (2007) 305–310.
[25] Y. Shen, X. Wang, Z. Xie, C. Min, X. Fu, Q. Liu, M. Gong, X. Yuan, Optical vortices 30 years on: Oam manipulation from topological charge to multiple singularities, Light: Sci. Appl. 8 (2019) 1–29.
[26] A.P. Porfirev, A.A. Kuchmizhak, S.O. Gurbatov, S. Juodkazis, S.N. Khonina, Y.N. Kulchin, Phase singularities and optical vortices in photonics, Phys.-Usp. 65 (2022) 789–811.
[27] L. Allen, M.W. Beijersbergen, R.J.C. Spreeuw, J.P. Woerdman, Orbital angular momentum of light and the transformation of Laguerre-Gaussian laser modes, Phys. Rev. A 45 (1992) 8185–8189.
[28] S. Chávez-Cerda, G. McDonald, G. New, Nondiffracting beams: travelling, standing, rotating and spiral waves, Opt. Commun. 123 (1996) 225–233.
[29] V. Kotlyar, V. Soifer, S. Khonina, An algorithm for the generation of laser beams with longitudinal periodicity: rotating images, J. Modern Opt. 44 (1997) 1409–1416.
[30] S. Khonina, V. Kotlyar, V. Soifer, J. Lautanen, M. Honkanen, J. Turunen, Generating a couple of rotating nondiffracting beams using a binary-phase doe, Opt.-Int. J. Light Electron Opt. 110 (1999) 137–144.
[31] J. Tervo, J. Turunen, Rotating scale-invariant electromagnetic fields, Opt. Express 9 (2001) 9–15.
[32] S. Orlov, K. Regelskis, V. Smilgevičius, A. Stabinis, Propagation of Bessel beams carrying optical vortices, Opt. Commun. 209 (2002) 155–165.
[33] S. Orlov, A. Stabinis, Propagation of superpositions of coaxial optical Bessel beams carrying vortices, J. Opt. A: Pure Appl. Opt. 6 (2004) S259.
[34] J. Baltrukonis, O. Ulčinas, S. Orlov, V. Jukna, High-order vector Bessel-Gauss beams for laser micromachining of transparent materials, Phys. Rev. A 16 (2021) 034001.
[35] S. Orlov, A. Stabinis, Free-space propagation of light field created by Bessel–Gauss and Laguerre–Gauss singular beams, Opt. Commun. 226 (2003) 97–105.
[36] A.A. Voitiv, J.M. Andersen, M.E. Siemens, M.T. Lusk, Optical vortex braiding with Bessel beams, Opt. Lett. 45 (2020) 1321–1324.
[37] J. Leach, M.R. Dennis, J. Courtial, M.J. Padgett, Knotted threads of darkness, Nature 432 (2004) 165.
[38] M.R. Dennis, R.P. King, B. Jack, K. O'holleran, M.J. Padgett, Isolated optical vortex knots, Nat. Phys. 6 (2010) 118–121.
[39] D. Sugic, M.R. Dennis, Singular knot bundle in light, J. Opt. Soc. Amer. A 35 (2018) 1987–1999.
[40] B. Bode, M.R. Dennis, D. Foster, R.P. King, Knotted fields and explicit fibrations for lemniscate knots, Proc. R. Soc. A 473 (2017) 20160829.
[41] P. Šlevas, S. Orlov, E. Nacius, O. Ulčinas, Azimuthally modulated axicon vortical beams for laser microprocessing, Opt. Commun. 505 (2022) 127509.
[42] M.V. Berry, M.R. Dennis, Knotted and linked phase singularities in monochromatic waves, Proc. R. Soc. Lond. Ser. A Math. Phys. Eng. Sci. 457 (2001) 2251–2263.
[43] J. Leach, M.R. Dennis, J. Courtial, M.J. Padgett, Vortex knots in light, New J. Phys. 7 (2005) 55.
[44] M.J. Padgett, K. O'holleran, R.P. King, M.R. Dennis, Knotted and tangled threads of darkness in light beams, Contemp. Phys. 52 (2011) 265–279.
[45] G. Molina-Terriza, E.M. Wright, L. Torner, Propagation and control of noncanonical optical vortices, Opt. Lett. 26 (2001) 163–165.
[46] F.S. Roux, Coupling of noncanonical optical vortices, J. Opt. Soc. Amer. B 21 (2004) 664–670.
[47] S. Khonina, V. Kotlyar, V. Soifer, M. Honkanen, J. Lautanen, J. Turunen, Generation of rotating Gauss—Laguerre modes with binary-phase diffractive optics, J. Modern Opt. 46 (1999) 227–238.
[48] J.F. Nye, M.V. Berry, Dislocations in wave trains, Proc. R. Soc. Lond. Ser. A Math. Phys. Eng. Sci. 336 (1974) 165–190.
[49] I. Basistiy, M. Soskin, M. Vasnetsov, Optical wavefront dislocations and their properties, Opt. Commun. 119 (1995) 604–612.
[50] A. Kumar, P. Vaity, J. Bhatt, R. Singh, Stability of higher order optical vortices produced by spatial light modulators, J. Modern Opt. 60 (2013) 1696–1700.
[51] P. Šlevas, E. Kozlovskis, S. Orlov, P. Gotovski, O. Ulčinas, Creation of high-contrast structures in superpositions of higher order Bessel beams for laser processing of glasses, in: 2021 Conference on Lasers and Electro-Optics Europe & European Quantum Electronics Conference, CLEO/Europe-EQEC, IEEE, 2021, p. 1.
[52] J. Baltrukonis, O. Ulcinas, P. Gotovski, S. Orlov, V. Jukna, Realization of higher order vector Bessel beams for transparent material processing applications, in: Laser-Based Micro-and Nanoprocessing XIV, Vol. 11268, International Society for Optics and Photonics, 2020, 112681D.
[53] J. Baltrukonis, O. Ulčinas, S. Orlov, V. Jukna, Void and micro-crack generation in transparent materials with high-energy first-order vector Bessel beam, J. Opt. Soc. Amer. B 37 (2020) 2121–2127.
[54] L. Yang, D. Qian, C. Xin, Z. Hu, S. Ji, D. Wu, Y. Hu, J. Li, W. Huang, J. Chu, Two-photon polymerization of microstructures by a non-diffraction multifoci pattern generated from a superposed Bessel beam, Opt. Lett. 42 (2017) 743–746.
[55] H. Cheng, P. Golvari, C. Xia, M. Sun, M. Zhang, S.M. Kuebler, X. Yu, High-throughput microfabrication of axially tunable helices, Photon. Res. 10 (2022) 303–315.
[56] A.H. Dorrah, M. Zamboni-Rached, M. Mojahedi, Experimental demonstration of tunable refractometer based on orbital angular momentum of longitudinally structured light, Light: Sci. Appl. 7 (2018) 40.

P6

Creating an Array of Parallel Vortical Optical Needles

P. Šlevas, S. Orlov

Photonics, 11(3), 203 (2024)
DOI: doi.org/10.3390/photonics11030203
https://www.mdpi.com/2304-6732/11/3/203

Supporting information:
137

photonics

MDPI

Article

Creating an Array of Parallel Vortical Optical Needles

Paulius Šlevas † and Sergej Orlov *,†

Center for Physical Sciences and Technology, Coherent Optics Laboratory, Sauletekio Ave. 3, LT-10257 Vilnius, Lithuania; paulius.slevas@ftmc.lt

* Correspondence: sergejus.orlovas@ftmc.lt

† These authors contributed equally to this work.

Abstract: We propose a method for creating parallel Bessel-like vortical optical needles with an arbitrary axial intensity distribution via the superposition of different cone-angle Bessel vortices. We analyzed the interplay between the separation of individual optical vortical needles and their respective lengths and introduce a super-Gaussian function as their axial profile. We also analyzed the physical limitations to observe well-separated optical needles, as they are influenced by the mutual interference of the individual beams. To verify our theoretical and numerical results, we generated controllable spatial arrays of individual Bessel beams with various numbers and spatial separations by altering the spectrum of the incoming laser beam via the spatial light modulator. We demonstrate experimentally how to implement such beams using a diffractive mask. The presented method facilitates the creation of diverse spatial intensity distributions in three dimensions, potentially finding applications in specific microfabrication tasks or other contexts. These beams may have benefits in laser material processing applications such as nanochannel machining, glass via production, modification of glass refractive indices, and glass dicing.

Keywords: diffraction; optical engineering; spatial light modulator; Bessel beam; optical vortex; optical needle; focal line; translation of Bessel beams

Citation: Šlevas, P.; Orlov, S. Creating an Array of Parallel Vortical Optical Needles. *Photonics* **2024**, *11*, 203. https://doi.org/10.3390/photonics11030203

Received: 23 January 2024
Revised: 13 February 2024
Accepted: 22 February 2024
Published: 24 February 2024

1. Introduction

Over time, lasers have proven to be a versatile tool across various domains, including manufacturing [1], biomedicine [2,3], telecommunication [4,5], and more. Precise adjustment of laser parameters is crucial for achieving specific applications, with the beam shape being a critical factor. The Gaussian beam is the most-common due to its ability to be focused to a small volume.

The structure and properties of the electromagnetic field play a vital role in modern optics and its applications [6–9]. However, non-diffracting beams have recently gained traction due to their capacity to maintain shape over long distances compared to Gaussian beams [8]. One example of structured illumination is non-diffracting beams, such as Bessel beams [10,11], known for their elongated focal line and self-reconstruction capability [12,13]. Laser beams with a long depth of focus and a narrow transverse intensity distribution [14] are useful for laser applications. These beams can be generated by axicons [15,16]. They have shown benefits in laser material processing applications like nanochannel machining [17], glass via production [18], modification of glass refractive indices [19], and glass dicing [20–22]. In other fields, they have been used successfully for THz imaging [23], particle manipulation [24], and microscopy [25].

They have a fixed bell-shaped axial intensity distribution in the Bessel zone [26]. However, this distribution may not be optimal for some applications, such as laser micromachining [17,27–30] and optical tweezers [31]. For some applications, such as surface patterning, Bessel beams can provide a less-sensitive process to surface height variations [32–34], but shaping the focal region could improve stability even further. Several methods to create non-diffractive beams with a flat longitudinal intensity distribution

have been suggested, for example the implementation of a logarithmic axicon [35,36], modulating the spatial spectrum of the Bessel beam [37,38], or using diffractive optical elements [29,39].

Similar characteristics are exhibited by other types of structured light without diffraction, such as Mathieu-Gaussian [40] and parabolic-Gaussian (Weber-Gaussian) beams [41,42]. Another well-known non-diffracting beam is the Airy beam [43], notable for its main lobe propagating along a parabolic trajectory in the longitudinal plane [44]. Airy beams have been used for particle trapping, optical manipulation [45–47], machining curved structures along the beam path [48], multiphoton polymerization [49], and imaging around obstacles in the THz wavelength [50].

In some applications, additional engineering of the focal zone is desirable. The axial behavior of the laser beam, another aspect of beam shaping, has been rapidly evolving [12,51,52] since the introduction of non-diffracting Bessel beams [11], which have a large ratio between the transverse and longitudinal widths of the focal line [10]. The discovery of axial engineering has further stimulated research on focal line engineering, leading to the development of optical needles [38,53–55].

Another degree of freedom is associated with the azimuthal phase dependence of higher-order non-diffracting Bessel beams J_m, expressed as $\exp(im\phi)$, where m is a topological charge. This dependence results in a phase singularity, also known as an optical vortex [56–58], which presents as a helical wavefront with m nested screw dislocations [59,60]. Optical vortices, commonly observed in electromagnetics, carry orbital angular momentum [61]. The first instance of optical engineering using cylindrical beams was reported in Ref. [62], where a coherent superposition of the Bessel and Neumann beams was considered, despite the Neumann beam having an amplitude singularity on the axis. By implying the periodicity of the transverse beam pattern in the infinite sum of Bessel eigenmodes, rotating patterns were realized using binary diffractive elements [63,64]. An alternative approach to generating rotating scale-invariant fields was presented in [65].

A single vortex is a dark spot of light with a phase singularity at its core. Consequently, its three-dimensional trajectory can be considered as a unified entity, especially considering that time reversal would change the signs of single vortices in the beam. Therefore, a negatively charged optical vortex can be interpreted as a positively charged vortex propagating backwards, and the creation and annihilation of positive and negative vortices in pairs under diffraction can be viewed as a dark knot of light [66–68]. This interpretation of the intricate evolution of vortical structures with various topologies has led to the emergence of terminology such as knots, braids, and bundles of dark light [69].

Multispot beam splitting is another attractive topic in the field. Various techniques are used to create an array of Gaussian beams, for instance direct laser interference [70,71], beam shaping by a free-form surface lens array [72], by an SLM and a phase mask created by iterative algorithms [73], or by diffractive optical elements [74,75]. The generation of a Bessel beam array has also been reported in the literature. The superposition of multiple shifted axicon holograms in an SLM [76] or the illumination of the axicon with a phase-modulated beam [77] can lead to the formation of multiple Bessel beams. A particular microstructure array can also be used for this purpose [78]. Furthermore, when using these elaborate intensity distributions, aberrations can have positive effects on these beams [79] or can suffer negative aberrations when they pass through a planar dielectric material interface (e.g., air–bulk material) [38,55,80], which affects their performance and efficiency and requires correction [81].

In this work, we propose a method for creating parallel Bessel-like optical needles with adjustable individual axial intensity patterns and individual topological charges. We used a superposition of vortical Bessel beams with specific axicon angles and complex amplitudes, as suggested in Refs. [37,38,77,82–84]. We also demonstrate experimentally how to implement such beams using a spatial light modulator. We studied the interaction of the topological charge and transverse displacements of individual vortical Bessel-like needles of different topological charges. This investigation is important for practical

applications, as it improves the laser energy deposition and the axial intensity distribution of the optical needles [77,85].

2. Axial Intensity Control in an Vortical Optical Needle and Translation of Optical Needles

In this section, we outline the theoretical foundation for generating arrays of parallel Bessel-like vortical optical needle beams characterized by a controlled axial intensity pattern. Our approach involves employing ideal Bessel vortices as fundamental basis functions, derived from an angular spectrum described by Dirac's delta function [86]. These non-diffracting beams serve as sufficiently accurate approximations of intensity distributions experimentally observed in the vicinity of the Fourier lens's focal point.

2.1. Axial Intensity Control in an Optical Needle

A non-diffracting Bessel vortex is a solution of the scalar Helmholtz equation in the cylindrical coordinates:

$$\psi(\rho, \varphi, z) = J_m(k_\rho \rho) \exp(im\varphi + izk_z), \tag{1}$$

where ψ is the electric field, J_m is the m-th order Bessel function, ρ, φ, z are cylindrical coordinates, m is the topological charge, and k_ρ, k_z are the radial and longitudinal components of the wavevector $\mathbf{k} = (k_\rho, 0, k_z)$. The components of the independent wave vectors are defined through the cone angle θ of the Bessel beam as $k_\rho = k \sin\theta$ and $k_z = k \cos\theta$ [86].

Every solution to the scalar Helmholtz equation can be expressed through a 3D integral comprising plane waves with distinct wave vectors. This integral can be simplified to a 2D form when dealing with axisymmetric fields, as outlined by Stratton [86]. This two-dimensional representation is based on a Fourier–Bessel transform and can be modified for our specific needs by adjusting the integration variables from k_ρ to k_z. The axial component of the wave vector becomes the coordinate of the Fourier transform within the integral expression.

A comprehensive discussion on this method for designing axial profiles can be found in extensive detail in [37,38,82]. When the radial coordinate ρ is zero, the expression of the combined electric field becomes a Fourier series with respect to the axial coordinate z, achieved through the superposition of the Bessel beams, see Equation (1). In this context, a Fourier integral is explicitly defined as

$$\Psi(\mathbf{r}) = \int_{-\infty}^{\infty} A(K_z + k_{z0}) \psi(\mathbf{r}; K_z) dK_z \tag{2}$$

where $k_z = k_{z0} + K_z$, where k_{z0} is a carrier wave vector and $A(k_z)$ is the spatial spectral amplitude of the combined beam. The carrier wave vector k_{z0} restricts K_z to forward propagating waves only by shifting the spectral coordinates k_z to positive values. A specific case of $m = 0$ was discussed in Ref. [55]; here, we investigated the general case. Near the optical axis $\rho \approx 0$, we can rewrite Equation (1) as

$$\psi(\rho, \varphi, z) = \frac{1}{m!} \left(\frac{k_\rho \rho}{2} \right)^m \exp(im\varphi + izk_z), \tag{3}$$

so, using Equation (3) in Equation (2) results in

$$\Psi(\mathbf{r}) = \frac{1}{m!} \left(\frac{k_\rho \rho}{2} \right)^m \exp(im\varphi + izk_{z0}) \int_{-\infty}^{\infty} A(K_z + k_{z0}) \exp(izK_z) dK_z \tag{4}$$

Thus, finally, we arrive at the expression:

$$\Psi(\mathbf{r}) = \frac{1}{m!} \left(\frac{k_\rho \rho}{2} \right)^m \exp(im\varphi + izk_{z0}) f(z), \tag{5}$$

where $f(z)$ is the axial distribution of the combined vortical beam with the engineered axial profile, and this profile is expressed as

$$f(z) = \int_{-\infty}^{\infty} A(K_z + k_{z0}) \exp(\mathrm{i}zK_z) dK_z. \tag{6}$$

Alternatively, knowing the axial profile $f(z)$ of the vortical optical needle, we can arrive at the spatial spectra $A(k_z)$ as

$$A(k_z) = \frac{1}{2\pi} \int_{-\infty}^{+\infty} f(z) e^{-\mathrm{i}K_z z} dz. \tag{7}$$

Therefore, the continuous superposition of Bessel beams $\Psi(\mathbf{r})$, as defined in Equation (2) with a spatial spectrum (Equation (3)), is capable of axial intensity properties resembling those defined by a function $f(z)$.

An optical needle (or an optical bottle) is created when the axial profile $f(z)$ is a constant step function. The step function with abrupt start and ending points will cause undesired effects due to the Gibbs phenomenon. Therefore, our aim is to mimic this desired profile by selecting the function $f(z)$ to be a super-Gaussian function:

$$f(z) = \exp\left[-\left(\frac{z - z_0}{z_0}\right)^{2N}\right] \tag{8}$$

where $z_0 = L/\left[2\log\left(2/2^{1/2N}\right)\right]$ is a some control parameter of the profile at the full-width at half-maximum (FWHM), N is the order of a super-Gaussian beam, and L is the length at the FWHM. This choice enables smoother axial intensity profiles; see Figure 1.

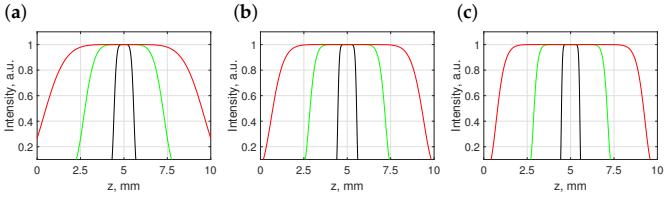

Figure 1. Examples of axial profiles used for both numerical simulations and experimental measurements; the order of the super-Gaussian function is $N = 3, 5, 7$ in (**a**–**c**), respectively. The lengths L of the axial profile function $f(z)$ are 1 mm (black), 4 mm (green), and 8 mm (red).

2.2. Translation of the Vortical Optical Needle

The control of the transverse position of an optical needle can be performed with the help of the addition theorem of Bessel beams [86]:

$$J_n(k_\rho \rho_2) e^{\mathrm{i}n\varphi_2} = \sum_{m=-\infty}^{\infty} J_m(k_\rho \rho_{12}) J_{n+m}(k_\rho \rho_1) e^{\mathrm{i}m(\varphi_1 - \varphi_{12})}. \tag{9}$$

Here, the indices 1 and 2 indicate the coordinates of the first and second cylindrical coordinate systems, n is an index, and ρ_{12} and φ_{12} are the coordinates of the translated origin O_1 with respect to the untranslated origin O; see Figure 2. The spatial spectrum of individual Bessel beam (see Equation (1)) is the Dirac delta function multiplied by the azimuthal phase term; therefore, the shifted coordinates becomes

$$\hat{\psi}(k_\rho, \varphi_k) = \sum_{m=-\infty}^{\infty} J_m(k_\rho \rho_{12}) e^{-\mathrm{i}m\varphi_{12}} \frac{\mathrm{i}^m e^{\mathrm{i}m\varphi_k} \delta(k \sin\theta - k_\rho)}{k_\rho}, \tag{10}$$

where φ_k is the azimuth of the spatial spectral coordinates. In this way, the Bessel beam with the origin at the shifted point is expressed as a superposition of Bessel beams in the non-shifted origin; see Figure 2.

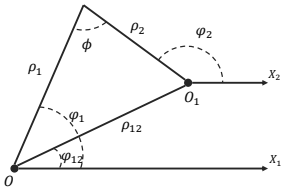

Figure 2. Depiction of the original and translated cylindrical coordinates. O is the original coordinate (x_1, ρ_1, φ_1), and O_1 is the center of the translated coordinate (x_2, ρ_2, φ_2).

Our intention here is to have a number $p = 1, 2, \ldots, P$ of independent parallel vortical needles, each with its own axial profile $f_p(z)$ and individual position x_p, y_p in the transverse plane. According to the superposition principle, the resulting spatial spectrum of the combined beam is

$$\hat{\Psi}(k_x, k_y) = \sum_p \int_{-\infty}^{\infty} A_p(K_z + k_{z0}) \hat{\psi}_p(k_x, k_y) dK_z. \tag{11}$$

where

$$A_p(k_z) = \frac{1}{2\pi} \int_{-\infty}^{+\infty} f_p(z) e^{-\mathrm{i}K_z z} dz. \tag{12}$$

and $\hat{\psi}_p$ is given in Equation (10) for translation to the coordinate center located at x_p, y_p.

3. Experimental Results

3.1. Optical Setup

The optical setup used throughout the experiment is displayed in Figure 3. A $\lambda = 532$ nm DPSS laser beam is attenuated by a half-waveplate (HWP) and a Brewster's polarizer (BP) and, then, expanded by 40×, with an $NA = 0.65$ microscope objective (MO1), and the beam is collimated by the lens L1 ($f = 125$ mm). The beam is then directed to a spatial light modulator (SLM) (PLUTOVIS-006-A, HOLOEYE Photonics AG, 8 bit, 1920 × 1080 pixels, 8 µm pitch) by means of a non-polarizing beam splitter (BS) at a 0 deg angle. The correct polarization direction is set by the polarizer (BP). The size of the beam (~8.5 mm diameter) is selected by an aperture (A1) to fill the SLM screen (8.64 mm). The SLM shapes the beam spectrum, which is directed to a 3× demagnifying optical setup $4f$ comprised of lenses L2 ($f = 150$ mm) and L3 ($f = 50$ mm). This demagnifies the transverse coordinates three times and the longitudinal coordinates nine times. In the focal plane of lens L2, additional diffraction maxima created by the checkerboard mask are filtered out by aperture A2. Lastly, the spectrum is focused by a Fourier lens L4 ($f = 25.4$ mm). The dimensions of the central lobe would be too small to register directly by a camera; therefore, the beam is captured by an optical imaging setup assembled on a motorized stage. This setup contains a 10× microscope objective (MO2), a collimating lens L5 ($f = 200$ mm), and a CCD camera. The entire beam is scanned using 0.05 mm steps.

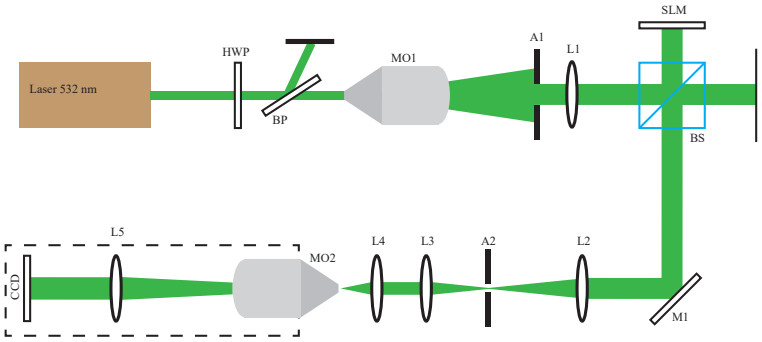

Figure 3. Optical setup of the experiments. HWP is the half-wave plate; BP is the Brewster polarizer; MO1, MO2 are the microscope objectives; L1, L2, L3, L4, and L5 are the lenses; A1 and A2 are the apertures; SLM is a spatial light modulator; BS is a beam splitter; M1 is a mirror; CCD is a charge-coupled device camera.

3.2. Creation of Single Vortical Needles

The optical setup used in this work is a bit different from that used in our previous research [38,55]. This time, a different set of lenses was used for magnification. Therefore, we begin with experiments to verify the concept of single vortical needles with controllable axial profiles $f(z)$, described in Equation (8). The spatial spectra of the engineered beams are found using Equation (7) and encoded in a phase-only mask using a checkerboard method [87]. The parameters for the axial profiles $f(z)$ used in the experiments were the same as in the theoretical section; see Figure 1.

Our intention here is to reproduce optical needles without topological charge (i.e. $m = 0$) to ensure the smooth operation of the optical setup before proceeding to the masks with topological charges. For this purpose, we selected three different lengths of optical needles $L = 1$ mm, $L = 4$ mm, and $L = 8$ mm and experimentally verified their creation (see Figure 4). We performed experiments with various orders N of the super-Gaussian function, but our experimentation identified the number $N = 7$ as optimal, which is in line with previous work [38,55].

The optical needle with the shortest length L = 1 mm has a central spike that is ~7.3 µm in diameter (at the intensity level $1/e^2$) and two detectable rings in the transverse intensity pattern; see Figure 4a. This is an expected outcome given its small longitudinal dimension. As the length L decreases, the properties of the optical needle are not similar to the properties of a Bessel beam, but are more like those of a Gaussian beam. Moving on to the four-time longer optical needle with $L = 4$ mm, we observed the appearance of additional rings (seven in total) around the central spike. The size of the central spike remained the same within the experimental tolerance, and the transverse profile largely resembles a Bessel-Gaussian beam with a significant number of concentric rings surrounding the center of the beam. Lastly, we increased the length of the optical needle twice more to $L = 8$ mm; see Figure 4c. The system of concentric rings becomes more pronounced, and the central lobe is not significantly affected. We verified the propagation of these optical needles by measuring the intensity of the central lobes for various positions of the z coordinate; see Figure 4d. In general, the behavior was detected to be as expected from numerical simulations, with no sharp oscillations on the edges; the intensity drop was smooth, as desired. However, we did observe some axial oscillations, which might be caused by inaccuracies in the positioning of the translation stage and some possible misalignment in the optical system.

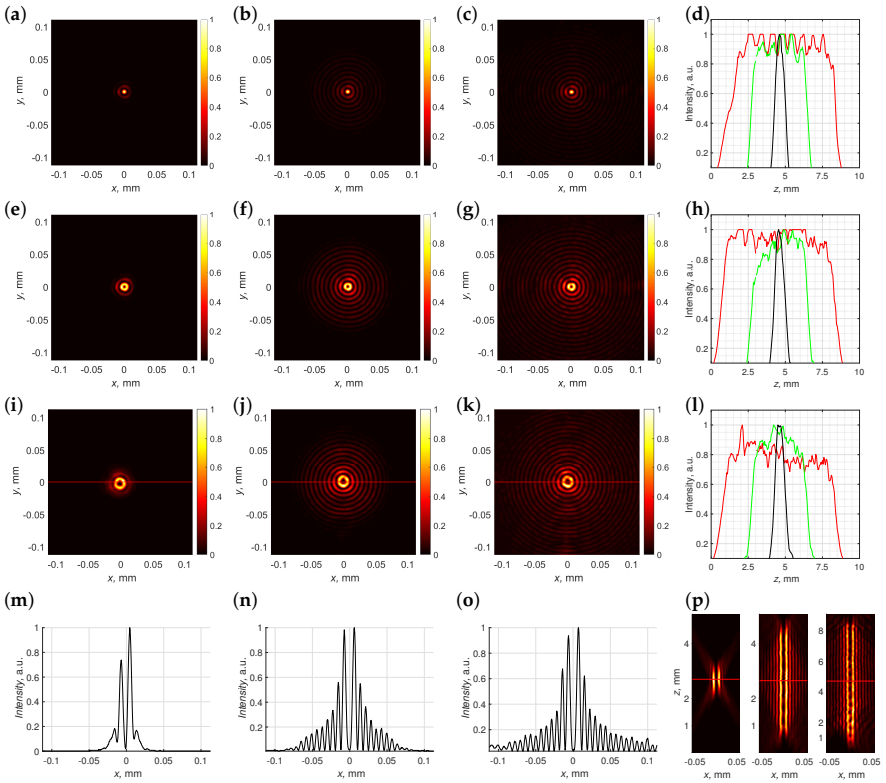

Figure 4. Transverse intensity distributions for vortical needles with topological charges $m = 0$ (**a**–**c**), $m = 1$ (**e**–**g**) and $m = 2$ (**i**–**k**) and lengths of the axial super-Gaussian profile $L = 1$ mm (**a**,**e**,**i**), $L = 4$ mm (**b**,**f**,**j**), and $L = 8$ mm (**c**,**g**,**k**). Longitudinal axial profiles of vortical optical needles, measured in the brightest ring (or central lobe) for topological charges $m = 0$ (**d**), $m = 1$ (**h**), and $m = 2$ (**l**) and different lengths $L = 8$ mm (red), $L = 4$ mm (green), and $L = 1$ mm (black). Intensity distributions (**m**–**o**) of cross-sections marked by a red line in (**i**–**k**), respectively. Longitudinal intensity distributions for optical needles with topological charge $m = 2$ (**p**).

Having verified that the optical setup acts at an intended level of performance, we now introduce nonzero topological charges $m = 1$ and $m = 2$; see Figure 4. Starting with the shortest vortical needle with a length of $L = 1$ mm, we observed similarities with the previous case; compare Figure 4e,i to Figure 4a. We observed two pronounced rings, the first ring with the vortical core inside and the second one surrounding it. The third ring was weak in both cases. In the expected manner, the radii of the first rings were different: the higher topological charge resulted in a larger central ring; compare Figure 4e to Figure 4i. In the case of the topological charge $m = 1$, the size of a dark spot inside the first ring was ~5.6 µm, measured at a $(1 - 1/e^2)$ intensity level. Setting the length of the axial profile to four-times larger values $L = 4$ mm immediately resulted in the appearance of a good pronounced concentric structure with nine rings in it for both topological charges. The sizes of the central rings surrounding the vortex cores with topological charges $m = 1$ (Figure 4f) and $m = 2$ (Figure 4j) did not change significantly. Lastly, setting the length of the super-Gaussian axial profile to $L = 8$ mm gave us the transverse intensity patterns depicted

in Figure 4g,k. In a similar fashion to the non-vortical optical needle (see Figure 4c), the ring-like structure of the field became more pronounced. We verified the intended action of the phase mask by measuring the intensity on the first ring while performing a z scan; see Figure 4h,l. In both cases, the axial profile of the vortical beams with the shortest length $L = 1$ mm resembled our expectation well; see the black curves in Figure 4h,l. Longer axial profiles had the expected lengths, but were somehow distorted; see the green curves in Figure 4h,l. This might happen due to the azimuthal intensity fluctuations on the first ring; compare to Figure 4 f,j. We might have used a non-optimal detection method or some misalignment was present in the optical setup. The situation improved for axial profiles designed with length $L = 8$ mm; see the red curves in Figure 4h,l. For the topological charge $m = 1$, we were able to measure the intended axial profile. The axial profile of the topological charge $m = 2$ was flat enough, but some spikes appeared. As we did not integrate azimuths into a ring, but measured them at a single azimuthal angle, this might have occurred due to the coherent addition of a small background, which caused splitting of the central vortex and the appearance of single charged vortices [88,89]. Figure 4m–o show the cross-sections of the $m = 2$ beams marked by a red line in Figure 4i–k, respectively.

As stated above, the main ring was intensity dominant for the shortest optical needle. The first side ring was less than 20% of the maximum (Figure 4). Side rings appeared with the increasing length of the optical needle. For the case of $L = 4$ mm, the first side ring was 55% while for the case of $L = 8$ mm, it was 65%. Both of these values were higher compared to the second ring intensity of the ideal second-order Bessel beam, which would be 42% of the maximum. The size of the dark central spot was ~11.2 µm, which was twice as large compared to the intensity minima of the vortical optical needle of topological charge $m = 1$. Lastly, in Figure 4p, we present the xz distributions of the optical needles of lengths $L = 1$, $L = 4$, and $L = 8$ mm and with topological charge $m = 2$. Smooth intensity distributions were generated for optical needles with $L = 1$ mm and $L = 4$ mm. In the case of $L = 8$ mm, axial modulation was present, which might have occurred due to the splitting of the central vortex into single charged vortices [88,89], as mentioned before.

3.3. Creation of an Array of Optical Needles

Having ensured ourselves that single vortical Bessel-like beams with a controllable axial profile can be created similarly as optical vortices, we proceeded to the experimental verification of the creation of an array of independent optical needles using Equation (11). In our previous study, we already investigated this question (see Ref. [55]), but as the optical setup differed from that used in those studies, we will briefly verify that those results are still valid under different conditions.

For this purpose, we created four different phase masks for a set of three optical needles with topological charges $m = 0$, angles $\varphi_{12} = -\pi/4$, and $\varphi_{13} = 3\pi/4$ having four distinct values of $\rho_{12} = \rho_{13}$; see Figure 5. In the first case, we wished to create an array where two adjacent optical needles are separated by $\rho_{12} = 20\lambda$; see Figure 5a. We observed a homogeneous rod-shaped structure, which appeared in the combined beam, with a transverse length similar to the combined distance $\rho_{12} + \rho_{13} = 40\lambda$. However, the side lobes in the direction perpendicular to the axis of the array were comparatively strong, making the spatial lobe of the combined beam complex. This was an expected outcome, as we estimated $f/\# \approx 9$. This implies a classical diffraction limit of approximately 11.5 µm or approximately 22.1λ, so the individual objects are not resolvable in Figure 5a. Moving on to the next case, when $\rho_{12} = \rho_{13} = 40\lambda$ (see Figure 5b), we observed a separation of the rod-shaped structure in the center of the array into three distinct lobes, located in the engineered positions and separated by less-intense rod-shaped intensity patterns. This is a minimal separation distance, which we detected to have a distinct three-spike pattern. A further increase in the separation parameter to $\rho_{12} = \rho_{13} = 60\lambda$ resulted in visibly enhanced central lobes of individual optical needles and reduced the intensity of the side lobes; see Figure 5c. Most notably, though individual objects had only one to two intense rings in the transverse plane (see Figure 4a), the structure of the side lobe appeared to be spatially larger

than that of a single needle. Moving on to even larger spatial separation $\rho_{12} = \rho_{13} = 80\lambda$ resulted in a clearly pronounced array of three optical needles with additional interference patterns; see Figure 5d.

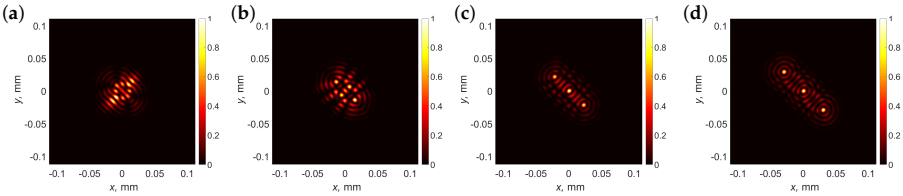

Figure 5. Transverse intensity distributions for an array of three optical needles with topological charges $m = 0$ and the length of the axial super-Gaussian profile $L = 1$ mm. The spatial separation of the individual optical needles is $\rho_{12} = 20\lambda$ (**a**), $\rho_{12} = 40\lambda$ (**b**), $\rho_{12} = 60\lambda$ (**c**), and $\rho_{12} = 80\lambda$ (**d**).

Thus, we have confirmed that the optical setup in use acted as intended.

3.4. Creation of an Array of Vortical Needles with Individual Topological Charges

In this section, we introduce into the array individual topological charges m. We start with a particular example of three optical vortical needles with topological charges $m_1 = 1$, $m_2 = 2$, and $m_3 = 0$. We investigated how the lengths L of individual super-Gaussian axial profiles together with separation distances ρ_{12} and ρ_{13} influence the resulting intensity profile of the combined beam; see Figure 6.

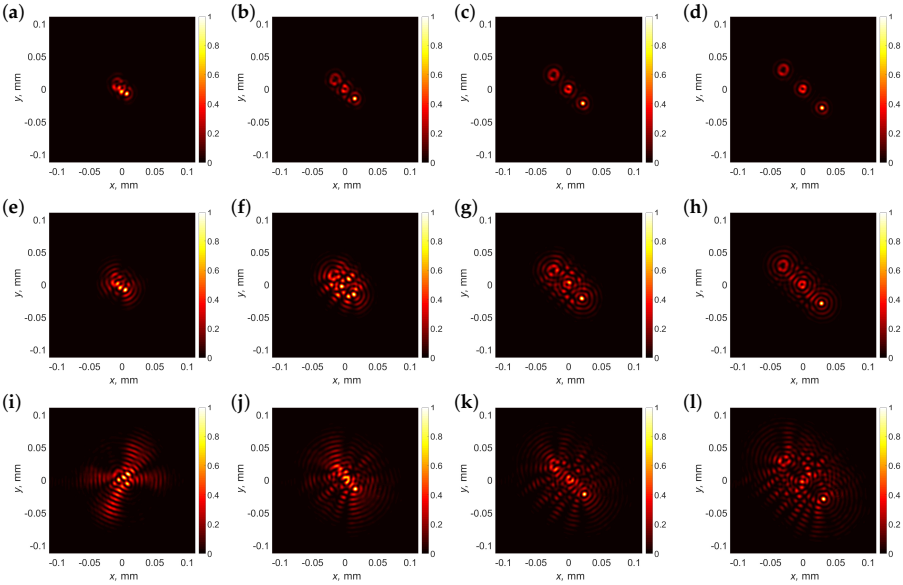

Figure 6. Transverse intensity distributions for an array of three optical needles with topological charges $m_1 = 1$, $m_2 = 2$, and $m_3 = 0$ and the length of the axial super-Gaussian profile $L = 1$ mm (**a**–**d**), $L = 2$ mm (**e**–**h**), and $L = 4$ mm (**i**–**l**). The spatial separation of individual optical needles is $\rho_{12} = 20\lambda$ (**a**,**e**,**i**), $\rho_{12} = 40\lambda$ (**b**,**f**,**j**), $\rho_{12} = 60\lambda$ (**c**,**g**,**k**), and $\rho_{12} = 80\lambda$ (**d**,**h**,**l**).

The first case that we studied was the case where the azimuthal locations of adjacent vortical structures are given by the angles $\varphi_{12} = -\pi/4$ and $\varphi_{13} = 3\pi/4$. The separation distances were $\rho_{12} = \rho_{13}$ in all cases. We note that the interference pattern of overlapping Laguerre-Gaussian vortices was studied in Ref. [90], so in the case of coaxial Bessel vortices, we should expect some similar effects. In the first case, we wished to create an array where two adjacent optical needles are separated by $\rho_{12} = 20\lambda$; see Figure 6a,e,i. In general, we see that, for all axial profile lengths L, the introduction of vorticity resulted in a largely skewed and distorted profile, although needles with charges $m_3 = 0$ and $m_2 = 2$ can be recognized in the profile of the combined beam for the smallest length $L = 1$ mm. Longer structures were unrecognizable; see Figure 6e,i.

As a next step, we increased the separation lengths $\rho_{12} = \rho_{13}$ to 40λ; see Figure 6b,f,j. For the case with the shortest lengths $L = 1$ mm, we observed an almost complete separation of individual profiles; see Figure 6b. The increase in the length of the optical vortical needle distorted the combined beam; see Figure 6f,j. A further increase in the separation of individual optical beams to $\rho_{12} = \rho_{13} = 60\lambda$ is shown in Figure 6c,g,k. We see that, for $L = 1$ mm, the individual transverse profiles were now fully separated; see Figure 6c. A twofold increase in the length of individual objects was induced as multiple interference patterns adjacent to the individual center rings, but the structure was recognizable and looked as expected; see Figure 6g. A further twofold increase in the length of the optical needles induced stronger interference distortions (see Figure 6k), and as expected, the central optical needle was the most-distorted. Lastly, we further increased the separation distance to $\rho_{12} = \rho_{13} = 80\lambda$; see Figure 6d,h,l. The first two cases were distinctly pronounced (see Figure 6d,h), while the array of the three longest needles showed the main distorted features of the central and upper structure in the transverse plane (see Figure 6l).

Lastly, we were curious whether the order of the topological charges in the combined array had any influence on the quality of the combined beam; see Figure 7. For this investigation, we chose an intermediate length of an individual structure $L = 2$ mm, and the individual topological charges were now $m_1 = 2$, $m_2 = 1$, and $m_3 = 0$. The general idea behind this experiment was that the spatial extent of the higher-order vortex was larger, so the change in the spatial position of the vortex with topological charge $m = 2$ will have an immediate effect on the intensity pattern of the combined beam.

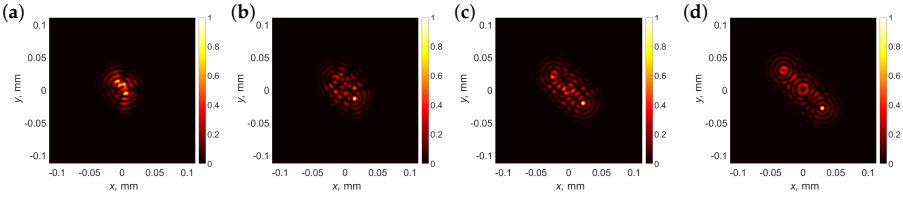

Figure 7. Transverse intensity distributions for an array of three optical needles with topological charges $m_1 = 2$, $m_2 = 1$, and $m_3 = 0$ and the length of the axial super-Gaussian profile $L = 2$ mm. The spatial separation of individual optical needles was $\rho_{12} = 20\lambda$ (**a**), $\rho_{12} = 40\lambda$ (**b**), $\rho_{12} = 60\lambda$ (**c**), and $\rho_{12} = 80\lambda$ (**d**).

As expected, the spatial separation $\rho_{12} = \rho_{13} = 20\lambda$ did not show improvement; see Figure 7a. The slight increase of $\rho_{12} = \rho_{13}$ to 40λ (see Figure 7b) demonstrated that only the non-vortical spike was recognized. However, most notably, when $\rho_{12} = \rho_{13} = 60\lambda$ (see Figure 7c), we observed that the topological charge needle $m = 2$ being central affected adjacent beams more than in the previous case, compared to Figure 6g. This means that the choice of the optimal separation distance depended not only on the individual topological charges, but also on the local position of that structure within an array. Lastly, we selected $\rho_{12} = \rho_{13} = 80\lambda$; see Figure 6d. When comparing this combined beam with the previous case (see Figure 6h), we observed that, due to the larger spatial extent, the vortical

needle with topological charge $m = 2$ was now more distorted due to the presence of the two adjacent optical needles.

3.5. Creation of an Array of Vortical Needles with Complex Positions and Axial Profiles

Lastly, given we found an optimal separation distance of $\rho_{12} = 80\lambda$, we aimed to create a more-complex array of vortical Bessel-like needles with individual positions in the space around the focal point; see Figure 8.

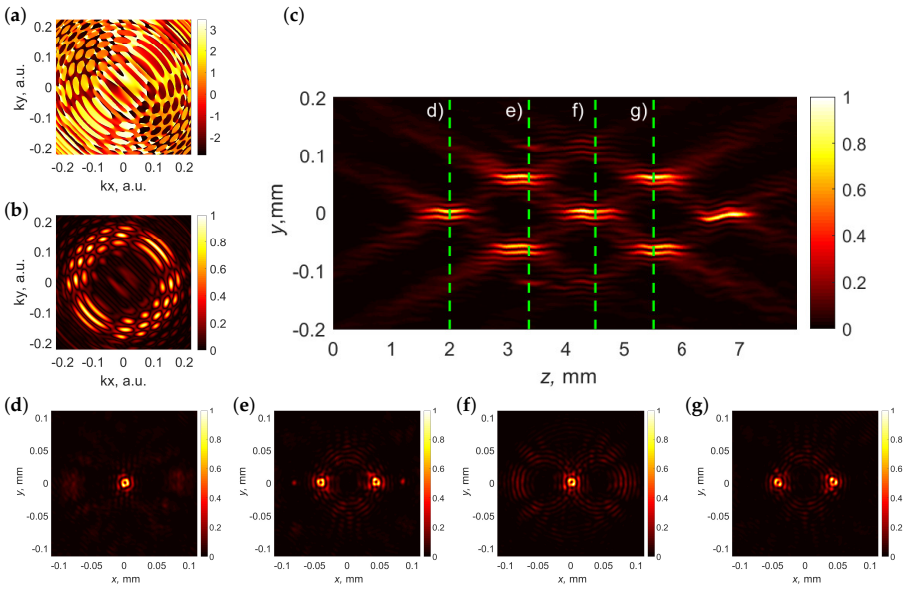

Figure 8. Phase (**a**) and amplitude (**b**) of the spatial spectra of a complex array of vortical needles. Longitudinal intensity distribution of an array of seven vortical optical needles with individual positions and topological charges (**c**). Transverse intensity distributions of an array and the particular positions in (**c**), marked green; see (**d**–**g**).

In this case, we created a structure of seven independent vortical-needle-like structures. For convenience, we selected their lengths to be the same, that is $L = 1$ mm and topological charges $m = 1$; however, the positions of those individual vortex needles were different.

The amplitude and phase distribution of the mask are shown in Figure 8a,b. The longitudinal intensity profile is shown in Figure 8c. We observed the intended propagation of the combined beam, although the vortical cores with topological charges $m = 1$ were not optimally resolved. This effect was caused by the fact that the resolution of the SLM in use was somehow pushed to the limit, and the z scan quality, blur, appeared due to scan inhomogeneities and some inevitable inaccuracies. The signal-to-noise ratio in this case was estimated from Figure 8e comparing the minimal value in the center to the maximum value, and it was $SNR = 200$.

The inspection of the array at four individual positions z is presented in Figure 8d–g. We observed some side lobes in parts peripheral to the vortex cores, but the main vortical pairs of vortical needles seemed to be intact, though slightly distorted.

4. Discussion and Conclusions

We discussed the creation of complex structures consisting of a number of individual vortical optical needles with individual topological charges.

We introduced a versatile method that empowers the controlled creation of arrays of parallel optical vortical needles with independent axial intensity profiles and topological charges. Our analysis delved into the interplay between the separation of individual optical vortical needles and their respective lengths. We observed that destructive interference between adjacent needles was less pronounced when they varied in length. The preliminary findings suggest that this phenomenon arose from the distinct spatial modulation in the Fourier space associated with optical needles of different lengths. The distortion between neighboring optical needles was the result of spatial overlap, emphasizing the importance of minimizing such overlap for optimal results. However, this technique imposes limitations on the smallest separation between the beams, the length of the needle, the topological charge, or the width of the beam.

Additionally, we introduced a step-like axial intensity profile described using a super-Gaussian function. This choice mitigated issues related to the Gibbs phenomenon, ensuring a smooth varying profile and sharp edges. Our experimentation identified the optimal parameter for the super-Gaussian function as $N = 7$.

In conclusion, the presented method facilitates the creation of diverse spatial intensity distributions in three dimensions, potentially finding applications in specific microfabrication tasks or other contexts.

Author Contributions: Conceptualization, S.O.; methodology, S.O.; software, S.O. and P.Š.; validation, P.Š.; formal analysis, S.O.; investigation, P.Š.; resources, S.O.; data curation, P.Š.; writing—original draft preparation, S.O.; writing—review and editing, S.O. and P.Š.; visualization, P.Š.; supervision, S.O.; project administration, S.O.; funding acquisition, S.O. All authors have read and agreed to the published version of the manuscript.

Funding: This research received funding from the Research Council of Lithuania (LMTLT) via agreement No. [S-MIP-23-71].

Institutional Review Board Statement: Not applicable.

Informed Consent Statement: Not applicable.

Data Availability Statement: The data will be made available upon request.

Conflicts of Interest: The authors declare no conflicts of interest.

Abbreviations

The following abbreviations are used in this manuscript:

SLM	spatial light modulator
FWHM	full-width at half-maximum
CCD	charge-coupled device

References

1. Orazi, L.; Romoli, L.; Schmidt, M.; Li, L. Ultrafast laser manufacturing: From physics to industrial applications. *CIRP Ann.* **2021**, *70*, 543–566. [CrossRef].
2. Sibbett, W.; Lagatsky, A.A.; Brown, C.T.A. The development and application of femtosecond laser systems. *Opt. Express* **2012**, *20*, 6989–7001. [CrossRef].
3. Sussulini, A.; Becker, J.S.; Becker, J.S. Laser ablation ICP-MS: Application in biomedical research. *Mass Spectrom. Rev.* **2017**, *36*, 47–57. [CrossRef].
4. Knox, W. Ultrafast technology in telecommunications. *IEEE J. Sel. Top. Quantum Electron.* **2000**, *6*, 1273–1278. [CrossRef].
5. Weng, Y.; Ip, E.; Pan, Z.; Wang, T. Advanced Spatial-Division Multiplexed Measurement Systems Propositions—From Telecommunication to Sensing Applications: A Review. *Sensors* **2016**, *16*, 1387. [CrossRef].
6. Rubinsztein-Dunlop, H.; Forbes, A.; Berry, M.V.; Dennis, M.R.; Andrews, D.L.; Mansuripur, M.; Denz, C.; Alpmann, C.; Banzer, P.; Bauer, T.; et al. Roadmap on structured light. *J. Opt.* **2016**, *19*, 013001.

7. Angelsky, O.V.; Bekshaev, A.Y.; Hanson, S.G.; Zenkova, C.Y.; Mokhun, I.I.; Jun, Z. Structured light: Ideas and concepts. *Front. Phys.* **2020**, *8*, 114.
8. Courvoisier, F. Nonstandard Light for Ultrafast Laser Microstructuring and Nanostructuring. In *Ultrafast Laser Nanostructuring: The Pursuit of Extreme Scales*; Springer: Cham, Switzerland, 2023; pp. 581–621.
9. Porfirev, A.; Khonina, S.; Kuchmizhak, A. Light–matter interaction empowered by orbital angular momentum: Control of matter at the micro-and nanoscale. *Prog. Quantum Electron.* **2023**, *88*, 100459.
10. Durnin, J. Exact solutions for nondiffracting beams. I. The scalar theory. *JOSA A* **1987**, *4*, 651–654.
11. Durnin, J.; Miceli, J., Jr.; Eberly, J.H. Diffraction-free beams. *Phys. Rev. Lett.* **1987**, *58*, 1499.
12. Khonina, S.N.; Kazanskiy, N.L.; Karpeev, S.V.; Butt, M.A. Bessel Beam: Significance and Applications—A Progressive Review. *Micromachines* **2020**, *11*, 997.
13. Grunwald, R.; Bock, M. Needle beams: A review. *Adv. Phys. X* **2020**, *5*, 1736950.
14. Misawa, H.; Juodkazis, S. *3D Laser Microfabrication: Principles and Applications*; John Wiley & Sons: Hoboken, NJ, USA, 2006.
15. Jarutis, V.; Paškauskas, R.; Stabinis, A. Focusing of Laguerre–Gaussian beams by axicon. *Opt. Commun.* **2000**, *184*, 105–112.
16. Khonina, S.N.; Kazanskiy, N.L.; Khorin, P.A.; Butt, M.A. Modern types of axicons: New functions and applications. *Sensors* **2021**, *21*, 6690.
17. Bhuyan, M.K.; Courvoisier, F.; Lacourt, P.A.; Jacquot, M.; Salut, R.; Furfaro, L.; Dudley, J.M. High aspect ratio nanochannel machining using single shot femtosecond Bessel beams. *Appl. Phys. Lett.* **2010**, *97*, 081102. [CrossRef].
18. Chen, L.; Yu, D. Investigation of low-cost through glass vias formation on borosilicate glass by picosecond laser-induced selective etching. *J. Mater. Sci. Mater. Electron.* **2021**, *32*, 16481–16493. [CrossRef].
19. Mikutis, M.; Kudrius, T.; Šlekys, G.; Paipulas, D.; Juodkazis, S. High 90% efficiency Bragg gratings formed in fused silica by femtosecond Gauss-Bessel laser beams. *Opt. Mater. Express* **2013**, *3*, 1862–1871. [CrossRef].
20. Meyer, R.; Froehly, L.; Giust, R.; Del Hoyo, J.; Furfaro, L.; Billet, C.; Courvoisier, F. Extremely high-aspect-ratio ultrafast Bessel beam generation and stealth dicing of multi-millimeter thick glass. *Appl. Phys. Lett.* **2019**, *114*, 201105. [CrossRef].
21. Rapp, L.; Meyer, R.; Furfaro, L.; Billet, C.; Giust, R.; Courvoisier, F. High speed cleaving of crystals with ultrafast Bessel beams. *Opt. Express* **2017**, *25*, 9312–9317. [CrossRef].
22. Feuer, A.; Thomas, J.U.; Freitag, C.; Weber, R.; Graf, T. Single-pass laser separation of 8 mm thick glass with a millijoule picosecond pulsed Gaussian–Bessel beam. *Appl. Phys. A* **2019**, *125*, 332.
23. Minkevičius, L.; Jokubauskis, D.; Kašalynas, I.; Orlov, S.; Urbas, A.; Valušis, G. Bessel terahertz imaging with enhanced contrast realized by silicon multi-phase diffractive optics. *Opt. Express* **2019**, *27*, 36358–36367. [CrossRef].
24. McGloin, D.; Garcés-Chávez, V.; Dholakia, K. Interfering Bessel beams for optical micromanipulation. *Opt. Lett.* **2003**, *28*, 657–659. [CrossRef].
25. Gao, L.; Shao, L.; Chen, B.C.; Betzig, E. 3D live fluorescence imaging of cellular dynamics using Bessel beam plane illumination microscopy. *Nat. Protoc.* **2014**, *9*, 1083–1101. [CrossRef].
26. Zhu, M.; Cao, Q.; Gao, H. Creation of a 50,000 λ long needle-like field with 0.36 λ width. *JOSA A* **2014**, *31*, 500–504.
27. Lightman, S.; Gvishi, R.; Hurvitz, G.; Arie, A. Shaping of light beams by 3D direct laser writing on facets of nonlinear crystals. *Opt. Lett.* **2015**, *40*, 4460–4463.
28. Courvoisier, F.; Zhang, J.; Bhuyan, M.; Jacquot, M.; Dudley, J.M. Applications of femtosecond Bessel beams to laser ablation. *Appl. Phys. A* **2013**, *112*, 29–34.
29. Gotovski, P.; Šlevas, P.; Orlov, S.; Ulčinas, O.; Urbas, A. Generation of an optical needle beam with a laser inscribed Pancharatnam-Berry phase element under imperfect conditions. *Opt. Express* **2021**, *29*, 33331–33345.
30. Šlevas, P.; Mundrys, K.; Ulčinas, O.; Orlov, S. An optical needle with elongated transversal profile created using Airy beams for laser processing of glasses. *Opt. Laser Technol.* **2024**, *174*, 110558.
31. Orlov, S.; Stabinis, A. Propagation of superpositions of coaxial optical Bessel beams carrying vortices. *J. Opt. Pure Appl. Opt.* **2004**, *6*, S259.
32. Doan, D.H.; Iida, R.; Kim, B.; Satoh, I.; Fushinobu, K. Bessel beam laser-scribing of thin film silicon solar cells by ns pulsed laser. *J. Therm. Sci. Technol.* **2016**, *11*, JTST0011.
33. Wetzel, B.; Xie, C.; Lacourt, P.A.; Dudley, J.M.; Courvoisier, F. Femtosecond laser fabrication of micro and nano-disks in single layer graphene using vortex Bessel beams. *Appl. Phys. Lett.* **2013**, *103*, 241111.
34. Li, X.; Xu, Z.; Jiang, L.; Shi, Y.; Wang, A.; Huang, L.; Wei, Q. Creating a three-dimensional surface with antireflective properties by using femtosecond-laser Bessel-beam-assisted thermal oxidation. *Opt. Lett.* **2020**, *45*, 2989–2992.
35. Jaroszewicz, Z.; Sochacki, J.; Kołodziejczyk, A.; Staronski, L.R. Apodized annular-aperture logarithmic axicon: Smoothness and uniformity of intensity distributions. *Opt. Lett.* **1993**, *18*, 1893–1895.
36. Golub, I.; Chebbi, B.; Shaw, D.; Nowacki, D. Characterization of a refractive logarithmic axicon. *Opt. Lett.* **2010**, *35*, 2828–2830.
37. Čižmár, T.; Dholakia, K. Tunable Bessel light modes: Engineering the axial propagation. *Opt. Express* **2009**, *17*, 15558–15570.
38. Orlov, S.; Juršėnas, A.; Nacius, E. Optical Bessel-like beams with engineered axial phase and intensity distribution. *J. Laser Micro Nanoeng.* **2018**, *13*, 244–248.
39. Dharmavarapu, R.; Bhattacharya, S.; Juodkazis, S. Diffractive optics for axial intensity shaping of Bessel beams. *J. Opt.* **2018**, *20*, 085606.

40. Gutiérrez-Vega, J.C.; Iturbe-Castillo, M.; Chávez-Cerda, S. Alternative formulation for invariant optical fields: Mathieu beams. *Opt. Lett.* **2000**, *25*, 1493–1495.
41. Bandres, M.A.; Rodríguez-Lara, B. Nondiffracting accelerating waves: Weber waves and parabolic momentum. *New J. Phys.* **2013**, *15*, 013054.
42. Orlov, S.; Vosylius, V.; Gotovski, P.; Grabusovas, A.; Baltrukonis, J.; Gertus, T. Vector beams with parabolic and elliptic cross-sections for laser material processing applications. *J. Laser Micro Nanoeng.* **2018**, *13*, 280–286.
43. Berry, M.V.; Balazs, N.L. Nonspreading wave packets. *Am. J. Phys.* **1979**, *47*, 264–267. [CrossRef].
44. Siviloglou, G.A.; Broky, J.; Dogariu, A.; Christodoulides, D.N. Observation of Accelerating Airy Beams. *Phys. Rev. Lett.* **2007**, *99*, 213901. [CrossRef].
45. Baumgartl, J.; Mazilu, M.; Dholakia, K. Optically mediated particle clearing using Airy wavepackets. *Nat. Photonics* **2008**, *2*, 675–678. [CrossRef].
46. Cheng, H.; Zang, W.; Zhou, W.; Tian, J. Analysis of optical trapping and propulsion of Rayleigh particles using Airy beam. *Opt. Express* **2010**, *18*, 20384–20394. [CrossRef].
47. Zheng, Z.; Zhang, B.F.; Chen, H.; Ding, J.; Wang, H.T. Optical trapping with focused Airy beams. *Appl. Opt.* **2011**, *50*, 43–49. [CrossRef].
48. Mathis, A.; Courvoisier, F.; Froehly, L.; Furfaro, L.; Jacquot, M.; Lacourt, P.A.; Dudley, J.M. Micromachining along a curve: Femtosecond laser micromachining of curved profiles in diamond and silicon using accelerating beams. *Appl. Phys. Lett.* **2012**, *101*, 071110. [CrossRef].
49. Manousidaki, M.; Papazoglou, D.G.; Farsari, M.; Tzortzakis, S. Abruptly autofocusing beams enable advanced multiscale photo-polymerization. *Optica* **2016**, *3*, 525–530. [CrossRef].
50. Ivaškevičiūtė-Povilauskienė, R.; Kizevičius, P.; Nacius, E.; Jokubauskis, D.; Ikamas, K.; Lisauskas, A.; Alexeeva, N.; Matulaitienė, I.; Jukna, V.; Orlov, S.; et al. Terahertz structured light: Nonparaxial Airy imaging using silicon diffractive optics. *Light. Sci. Appl.* **2022**, *11*, 326. [CrossRef].
51. Duocastella, M.; Arnold, C.B. Bessel and annular beams for materials processing. *Laser Photonics Rev.* **2012**, *6*, 607–621.
52. Stoian, R.; Bhuyan, M.K.; Zhang, G.; Cheng, G.; Meyer, R.; Courvoisier, F. Ultrafast Bessel beams: Advanced tools for laser materials processing. *Adv. Opt. Technol.* **2018**, *7*, 165–174.
53. Wang, J.; Chen, W.; Zhan, Q. Engineering of high purity ultra-long optical needle field through reversing the electric dipole array radiation. *Opt. Express* **2010**, *18*, 21965–21972.
54. Rogers, E.T.; Savo, S.; Lindberg, J.; Roy, T.; Dennis, M.R.; Zheludev, N.I. Super-oscillatory optical needle. *Appl. Phys. Lett.* **2013**, *102*.
55. Orlov, S.; Juršėnas, A.; Baltrukonis, J.; Jukna, V. Controllable spatial array of Bessel-like beams with independent axial intensity distributions for laser microprocessing. *J. Laser Micro Nanoeng.* **2018**, *13*, 324–329.
56. Coullet, P.; Gil, L.; Rocca, F. Optical vortices. *Opt. Commun.* **1989**, *73*, 403–408.
57. Gahagan, K.; Swartzlander, G.J. Optical vortex trapping of particles. *Opt. Lett.* **1996**, *21*, 827–829.
58. Molina-Terriza, G.; Torres, J.P.; Torner, L. Twisted photons. *Nat. Phys.* **2007**, *3*, 305–310.
59. Shen, Y.; Wang, X.; Xie, Z.; Min, C.; Fu, X.; Liu, Q.; Gong, M.; Yuan, X. Optical vortices 30 years on: OAM manipulation from topological charge to multiple singularities. *Light. Sci. Appl.* **2019**, *8*, 1–29.
60. Porfirev, A.P.; Kuchmizhak, A.A.; Gurbatov, S.O.; Juodkazis, S.; Khonina, S.N.; Kulchin, Y.N. Phase singularities and optical vortices in photonics. *Phys. Usp.* **2022**, *65*, 789–811. [CrossRef].
61. Allen, L.; Beijersbergen, M.W.; Spreeuw, R.J.C.; Woerdman, J.P. Orbital angular momentum of light and the transformation of Laguerre-Gaussian laser modes. *Phys. Rev. A* **1992**, *45*, 8185–8189. [CrossRef].
62. Chávez-Cerda, S.; McDonald, G.; New, G. Nondiffracting beams: Travelling, standing, rotating and spiral waves. *Opt. Commun.* **1996**, *123*, 225–233.
63. Kotlyar, V.; Soifer, V.; Khonina, S. An algorithm for the generation of laser beams with longitudinal periodicity: Rotating images. *J. Mod. Opt.* **1997**, *44*, 1409–1416.
64. Khonina, S.; Kotlyar, V.; Soifer, V.; Lautanen, J.; Honkanen, M.; Turunen, J. Generating a couple of rotating nondiffracting beams using a binary-phase DOE. *Opt.-Int. J. Light Electron Opt.* **1999**, *110*, 137–144.
65. Tervo, J.; Turunen, J. Rotating scale-invariant electromagnetic fields. *Opt. Express* **2001**, *9*, 9–15.
66. Leach, J.; Dennis, M.R.; Courtial, J.; Padgett, M.J. Knotted threads of darkness. *Nature* **2004**, *432*, 165–165.
67. Dennis, M.R.; King, R.P.; Jack, B.; O'holleran, K.; Padgett, M.J. Isolated optical vortex knots. *Nat. Phys.* **2010**, *6*, 118–121.
68. Sugic, D.; Dennis, M.R. Singular knot bundle in light. *JOSA A* **2018**, *35*, 1987–1999.
69. Bode, B.; Dennis, M.R.; Foster, D.; King, R.P. Knotted fields and explicit fibrations for lemniscate knots. *Proc. R. Soc. A Math. Phys. Eng. Sci.* **2017**, *473*, 20160829.
70. Lasagni, A.F.; Gachot, C.; Trinh, K.E.; Hans, M.; Rosenkranz, A.; Roch, T.; Eckhardt, S.; Kunze, T.; Bieda, M.; Günther, D.; et al. Direct laser interference patterning, 20 years of development: From the basics to industrial applications. In Proceedings of the Laser-Based Micro-and Nanoprocessing XI, SPIE, San Francisco, CA, USA, 7 March 2017; Volume 10092, pp. 186–196.
71. Zabila, Y.; Perzanowski, M.; Dobrowolska, A.; Kąc, M.; Polit, A.; Marszałek, M. Direct laser interference patterning: Theory and application. *Acta Phys. Pol. A* **2009**, *115*, 591–593.

72. Si, J.; Feng, Z.; Cheng, D.; Wang, Y. Freeform beam splitting system design for generating an array of identical sub-beams. *Opt. Express* **2021**, *29*, 29918–29935.
73. Kahle, M.; Nodop, D.; Rücker, J. Beam shaping and splitting for high-power USP-lasers. *Procedia CIRP* **2020**, *94*, 807–811.
74. Katz, S.; Kaplan, N.; Grossinger, I. Using Diffractive Optical Elements: DOEs for beam shaping–fundamentals and applications. *Opt. Photonik* **2018**, *13*, 83–86.
75. Brodsky, A.; Kaplan, N. Laser surface texturing using a single diffractive optical element as an alternative for direct laser interference patterning. *J. Laser Appl.* **2020**, *32*, 032011.
76. Bowman, R.; Muller, N.; Zambrana-Puyalto, X.; Jedrkiewicz, O.; Di Trapani, P.; Padgett, M. Efficient generation of Bessel beam arrays by means of an SLM. *Eur. Phys. J. Spec. Top.* **2011**, *199*, 159–166.
77. Lutz, C.; Schwarz, S.; Marx, J.; Esen, C.; Hellmann, R. Multi-Bessel Beams Generated by an Axicon and a Spatial Light Modulator for Drilling Applications. *Photonics* **2023**, *10*, 413. [CrossRef].
78. Stankevicius, E.; Garliauskas, M.; Raciukaitis, G. Bessel-like beam array generation using round-tip microstructures and their use in the material treatment. *J. Laser Micro Nanoeng.* **2016**, *11*, 352.
79. Dudutis, J.; Stonys, R.; Račiukaitis, G.; Gečys, P. Aberration-controlled Bessel beam processing of glass. *Opt. Express* **2018**, *26*, 3627–3637.
80. Novotny, L.; Hecht, B. *Principles of Nano-Optics*; Cambridge University Press: Cambridge, UK, 2012.
81. Jenne, M.; Flamm, D.; Ouaj, T.; Hellstern, J.; Kleiner, J.; Grossmann, D.; Koschig, M.; Kaiser, M.; Kumkar, M.; Nolte, S. High-quality tailored-edge cleaving using aberration-corrected Bessel-like beams. *Opt. Lett.* **2018**, *43*, 3164–3167.
82. Zamboni-Rached, M.; Recami, E.; Hernández-Figueroa, H.E. Theory of "frozen waves": Modeling the shape of stationary wave fields. *JOSA A* **2005**, *22*, 2465–2475.
83. Yan, W.; Gao, Y.; Yuan, Z.; Wang, Z.; Ren, Z.C.; Wang, X.L.; Ding, J.; Wang, H.T. Non-diffracting and self-accelerating Bessel beams with on-demand tailored intensity profiles along arbitrary trajectories. *Opt. Lett.* **2021**, *46*, 1494–1497.
84. Zeng, Y.; Yu, Y.; Wu, P.; Chen, M.; Zheng, S.; Pan, M.; Zhan, Q. Generation of a linear array of focal spots with prescribed characteristic using the radiation pattern from a tapered line source antenna. *Opt. Commun.* **2023**, *534*, 129329.
85. Lutz, C.; Schwarz, S.; Rung, S.; Marx, J.; Esen, C.; Hellmann, R. Optical system for multi Bessel beam high power ultrashort pulsed laser processing using a spatial light modulator. In Proceedings of the Lasers in Manufacturing-LiM 2021, Munich, Germany (virtual), 21–24 June 2021.
86. Stratton, J.A. *Electromagnetic Theory*; John Wiley & Sons: Hoboken, NJ, USA, 2007; Volume 33.
87. Wang, Y.; Potoček, V.; Barnett, S.M.; Feng, X. Programmable holographic technique for implementing unitary and nonunitary transformations. *Phys. Rev. A* **2017**, *95*, 033827.
88. Orlov, S.; Regelskis, K.; Smilgevičius, V.; Stabinis, A. Propagation of Bessel beams carrying optical vortices. *Opt. Commun.* **2002**, *209*, 155–165.
89. Orlov, S.; Stabinis, A. Free-space propagation of light field created by Bessel–Gauss and Laguerre–Gauss singular beams. *Opt. Commun.* **2003**, *226*, 97–105.
90. Pyragaite, V.; Stabinis, A. Free-space propagation of overlapping light vortex beams. *Opt. Commun.* **2002**, *213*, 187–191.

NOTES

NOTES

NOTES

Vilniaus universiteto leidykla
Saulėtekio al. 9, III rūmai, LT-10222 Vilnius
El. p. info@leidykla.vu.lt, www.leidykla.vu.lt
bookshop.vu.lt, journals.vu.lt
Tiražas 15 egz.